

PAPER

Variation of electric properties across the grain boundaries in BiFeO₃ film

To cite this article: Bojan Stojadinovi *et al* 2016 *J. Phys. D: Appl. Phys.* **49** 045309

View the [article online](#) for updates and enhancements.

Related content

- [Local electrical conduction in polycrystalline La-doped BiFeO₃ thin films](#)
Ming-Xiu Zhou, Bo Chen, Hai-Bin Sun *et al.*
- [The 2016 oxide electronic materials and oxide interfaces roadmap](#)
M Lorenz, M S Ramachandra Rao, T Venkatesan *et al.*
- [Effect of Ni substitution on the optical properties of BiFeO₃ thin films](#)
Govind N Sharma, Shankar Dutta, Sushil Kumar Singh *et al.*



IOP | ebooks™

Bringing you innovative digital publishing with leading voices to create your essential collection of books in STEM research.

Start exploring the collection - download the first chapter of every title for free.

Variation of electric properties across the grain boundaries in BiFeO₃ film

Bojan Stojadinović¹, Borislav Vasić¹, Dimitrije Stepanenko¹, Nenad Tadić², Radoš Gajić¹ and Zorana Dohčević-Mitrović¹

¹ Center for Solid State Physics and New Materials, Institute of Physics Belgrade, University of Belgrade, Pregrevica 118, 11080 Belgrade, Serbia

² Faculty of Physics, University of Belgrade, Studentski trg 12-16, 11000 Belgrade, Serbia

E-mail: bvasic@ipb.ac.rs and zordoh@ipb.ac.rs

Received 13 October 2015, revised 3 December 2015

Accepted for publication 8 December 2015

Published 29 December 2015



CrossMark

Abstract

Stark differences in charge transport properties between the interior and the boundary regions of grains in an undoped BiFeO₃ thin film have been found. The material is ferroelectric and each grain is a single domain. A spatial resolution that distinguishes between the grain interior and the boundary between the grains has been achieved by using piezoelectric force microscopy and conductive atomic force microscopy measurements. The local electric properties, as well as the local band gap show hysteresis only when probed in the grain interior, but do not show hysteresis when probed in the region around the boundary between two grains. The leakage current is more pronounced at the grain boundaries, and the region that carries significant current increases with the applied voltage.

Keywords: multiferroics, thin films, electrical properties, grain boundaries, scanning probe microscopy

 Online supplementary data available from stacks.iop.org/JPhysD/49/045309/mmedia

(Some figures may appear in colour only in the online journal)

1. Introduction

Multiferroic materials exhibit at least two ferroic properties among magnetic, electric, and elastic responses. Simultaneous presence of at least two hysteretic responses and interaction between the associated orders has spurred interest in the mechanisms that govern the phase transitions in multiferroics [1–3]. The explanation of the multiferroic order remains an interesting open problem of condensed matter physics. A pair of ferroic properties causes nonlinear and nonstandard responses, e.g. a material will produce electric polarization when exposed to an external magnetic field. Such responses make the multiferroics interesting from a practical point of view by allowing for novel forms of control. The most sought-after applications of multiferroics are electrically controlled magnetic memories [4], and emerging spintronic devices based on the simultaneous use of electric polarization, based on the orbital order, and magnetization, based on the spin order [2, 5].

The properties of multiferroic materials structured at the nanoscale can be drastically different from the corresponding properties of the bulk. Integration of materials into current semiconductor technology requires fabrication and structuring of thin films, leading to the interest in variation of the material properties with the nanoscale structure, as well as to the development of methods for their synthesis [6, 7]. In addition to reduced dimension, the thin films often show granular structure on the characteristic length scale of the order of 10 nm. Details of the grain structure contribute to the variation of the properties of both the material and the devices.

One of the most well-known multiferroic materials is the bismuth ferrite (BiFeO₃). It shows high critical temperatures, both for the ferroelectric ordering below 1104 K [8] and the antiferromagnetic ordering below 643 K [9]. The interest in BiFeO₃ stems from the possibility of having all the technologically desirable properties of multiferroics at and above the room temperature. A major obstacle for the applications of BiFeO₃ is the existence of relatively large leakage currents

which severely limit the electric fields that a material can sustain. The leakage currents have been explained by the existence of charge defects, for example the oxygen and bismuth vacancies [10]. Attempts at minimizing the leakage currents in BiFeO₃ thin films drive the interest in their electronic transport properties and their modification either by doping [11–14] or by modifying the conditions of film growth [15, 16].

The properties of multiferroic BiFeO₃ granular thin film strongly depend on the grain size. The Neel temperature was shown to correlate with the volume of the grains which affects the polar displacements of cations and changes in polarization [17]. The mechanical properties also depend on the grain size [18]. Therefore, the regions in proximity to the grain boundaries may play an important role in determining the material properties.

We have studied a film of an undoped, single crystallographic phase, BiFeO₃. The film has been produced by sol–gel spin coating. The film has shown granular structure, and we have probed the variation of the electronic properties on the spatial scale commensurate with the grain size. Our film did not have any holes and all the measured grains lied on the top of the film, and not on the substrate. The variation at probed length scale are therefore properties of the grain morphology and independent of the thickness or large-scale roughness of the film.

In our measurements, the local electric properties of the film have varied on two characteristic length scales, corresponding to the sizes of grains and boundary regions. In scanning probe measurements, we have found mild variations between the interiors of different grains when probing their band structure. On the other hand, the differences between the grain interiors and the grain boundaries have been drastic. We have measured the local electric properties of the BiFeO₃ film across the grain boundary, and have found that the boundary regions differ from the grain interior in the density of states, charge transport mechanism, and the absence of hysteresis in the I–V curves. Remarkably, all the measured properties have shown a hysteresis when measured in the grain interior, but there were no signs of hysteresis when probed at the boundary.

2. Experimental procedure

BiFeO₃ thin film was prepared via the sol–gel spin coating method. The details of preparation are presented in the supplementary material (stacks.iop.org/JPhysD/49/045309/mmedia).

Structural characterization was carried out using x-ray diffraction (XRD) with Cu–K α radiation on a Rigaku Ultima IV diffractometer ($2\theta = 20^\circ$ – 60°). Raman spectroscopy was used to study the vibrational properties of BiFeO₃ thin film. Micro-Raman spectra were collected using a Jobin Yvon T64000 spectrometer with a liquid-nitrogen-cooled CCD camera.

The morphology and phenomena at short length scales were recorded by atomic force microscopy (AFM). AFM imaging was performed using tapping mode on NT-MDT system Ntegra Prima and silicon NSG01 probes with the tip curvature radius of 6 nm. The phase lag of the cantilever oscillation was recorded simultaneously with the topography image.

We have investigated the electromechanical response of our sample by piezoresponse force microscopy (PFM). During PFM measurements, an AC bias with the amplitude of 10V and frequency of 150kHz has been applied between the tip and the substrate on which the BiFeO₃ film is grown. PFM measurements were done using TiN coated NSG01 probes with a tip curvature radius of 35 nm, a typical force constant of 5.1 N m^{-1} and typical resonant frequency of 150kHz. The conductive tip was scanning the surface of the sample in contact mode while AC bias was applied to the tip. The AC bias was inducing the contraction and expansion of the sample, and these changes of the shape were monitored by the tip deflection. This local piezoelectricity of BiFeO₃ thin film was recorded in out-of-plane and in-plane polarization.

The local electrical conductivity of a BiFeO₃ film was probed by conductive atomic force microscopy (C-AFM). During C-AFM measurements, a DC bias voltage (from +2 to +6 volts) was applied between the tip and the substrate. Surface topography and current maps were obtained simultaneously by using a conducting probe in contact with the sample. The measurements were performed with the DCP20 probe of a nominal curvature radius of 50–70 nm and typical force constant of 48 N m^{-1} . In the same mode, the electrical measurements of current-voltage (I–V) characteristics were recorded in the bias voltage range from -10V to $+10\text{V}$. The I–V curves were measured using C-AFM at the points within the grain interior and at the points on the grain boundary. We have determined the band gap value of BiFeO₃ film according to the same procedure as in references [20–22]. Thus, we have measured the local density of states and the local band gap in BiFeO₃ film using C-AFM. At each point we have repeated the measurements a few times, and therefore proved the reproducibility. Differential conductance spectra were obtained by averaging and differentiating five current-voltage curves measured on an individual grain of BiFeO₃ film. All AFM measurements were performed at ambient conditions (room temperature and air atmosphere).

3. Results and discussion

The crystallographic phase and structure of our sample have been determined by XRD. The XRD pattern of the BiFeO₃ thin film is shown in figure 1(a). The XRD peaks of BiFeO₃ film with a rhombohedrally distorted BiFeO₃ perovskite structure, belonging to the R3c space group have been indexed. No peaks originating from the secondary phase were observed. The absence of the impurity phase signal from XRD measurement does not imply that the sample itself is ultra pure. However, it does imply that there are no regions of impurity phase of appreciable size. From the Williamson–Hall plot [19], we have estimated the grain size in our film to $\sim 38 \text{ nm}$ and the microstrain to $\sim 0.3\%$, as shown in figure 1(b). The diffraction peaks corresponding to the perovskite structure have been clearly observed. Figure 1(c) shows the histogram of the grain size distribution from the AFM measurement of the BiFeO₃ film. Raman spectrum of BiFeO₃ film has confirmed the rhombohedrally distorted structure without the presence

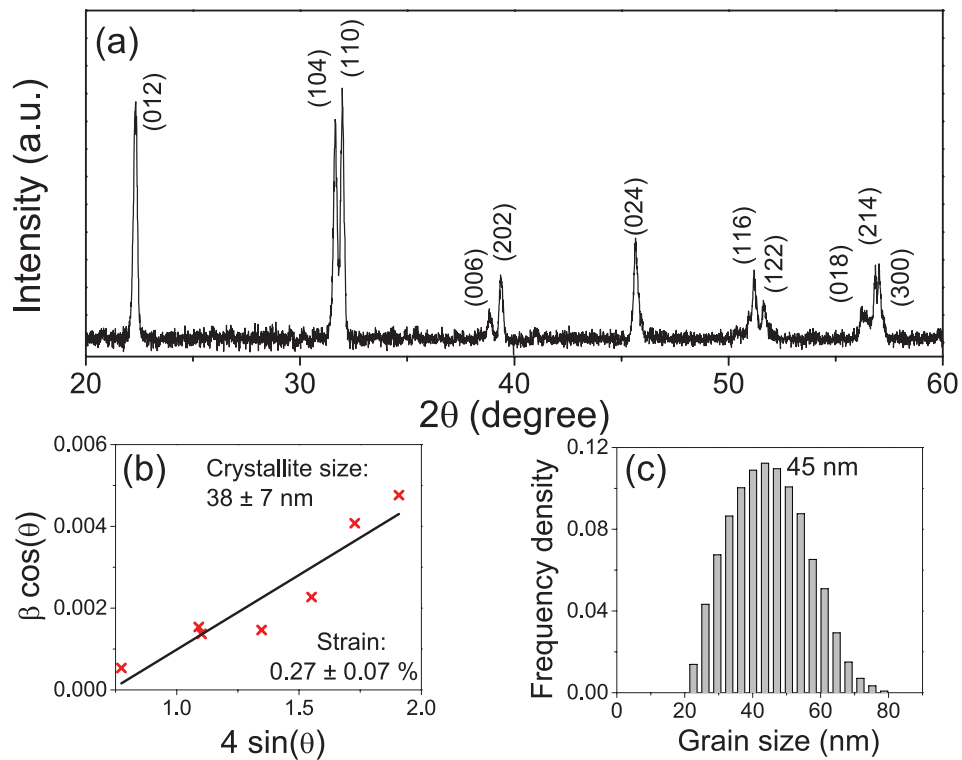


Figure 1. (a) X-ray diffraction pattern of the BiFeO_3 film fabricated by the sol-gel method, (b) Williamson-Hall plot for BiFeO_3 film with calculated crystallite size and strain, and (c) histogram of grain size distribution of BiFeO_3 film obtained from AFM image (see supplementary material (stacks.iop.org/JPhysD/49/045309/mmedia)).

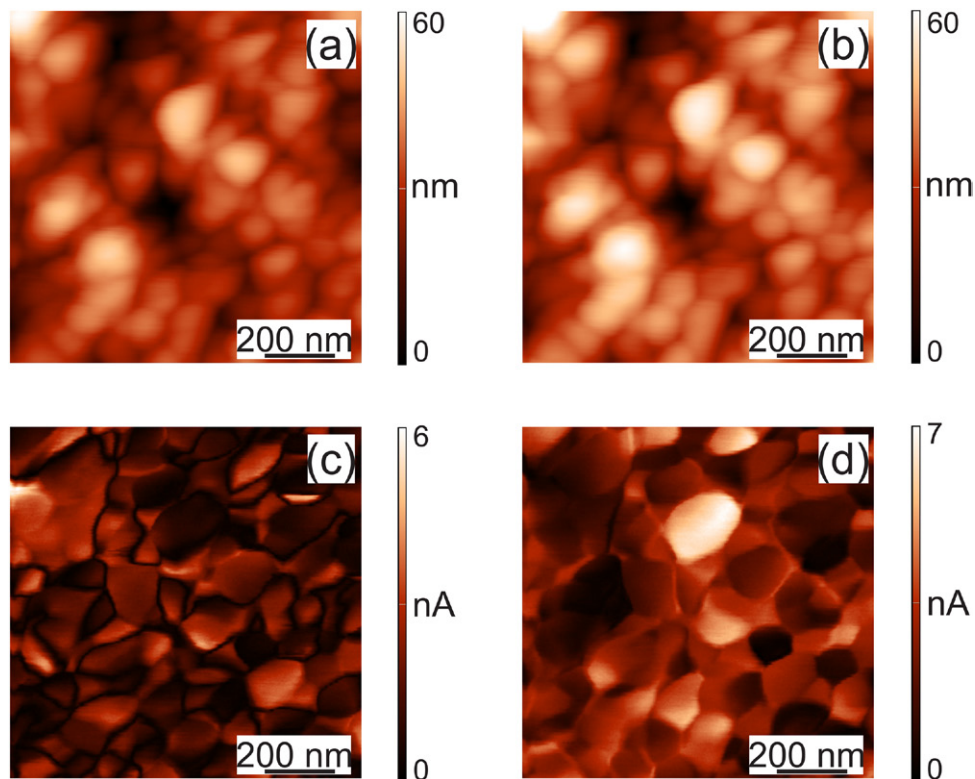


Figure 2. Topography (a) and out-of-plane PFM magnitude (c), topography (b) and in-plane PFM magnitude (d), showing the polarization components of BiFeO_3 film. The grains, visible on the topography images (a) and (b), correspond to the ferroelectric domain captured by the PFM magnitudes in (c) and (d).

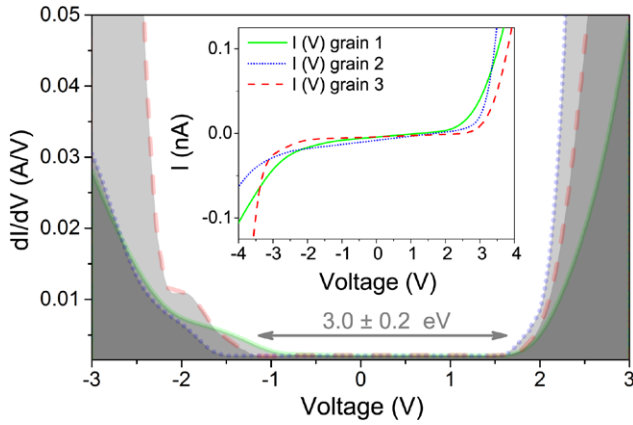


Figure 3. Representative differential conductance spectra measured on interior points of three different grains on BiFeO₃ film. Arrow shows the averaged band gap value. The corresponding I–V curves are shown in the inset in a wider voltage range, from –4 to 4 V.

of secondary phase. Raman scattering spectrum of the BiFeO₃ film is presented in supplementary material (stacks.iop.org/JPhysD/49/045309/mmedia).

Ferroelectric domains occur when the minimization of the electrostatic and elastic energy favors an inhomogeneous distribution in a material with unsaturated bulk electric polarization. The domain shapes and sizes are governed by various stresses that appear in the process of thin film growth [23, 24]. The granular structure of the BiFeO₃ film is dictated by lattice, morphology and thermal expansion coefficient mismatch between the BiFeO₃ film and the substrate [25, 26], the film thickness, and the temperature [27]. We have measured the polarization domains in the film, and found that they change on the characteristic length scale of ~ 40 nm. We have measured both the out-of-plane and the in-plane polarization, based on normal and lateral deflection of the AFM cantilevers during PFM measurements (figures 2(c) and (d)). Therefore, we have identified both the in-plane and out-of-plane polarization components. Comparison with the sample topography, figures 2(a) and (b), has shown that the domain boundaries coincide with the grain boundaries. Therefore, each grain in the film has been a single-domain particle. This kind of the domain distribution is characteristic for the small grains, while larger grains generically show a multi-domain structure [24]. In our film, we could not identify any multi-domain grains.

Knowledge of the charge transport mechanism is essential in the design of memory devices based on BiFeO₃ film. The granular film contains rough surfaces that cause an inhomogeneous behavior of conductivity [28]. We have investigated the spatial distribution of the density of states and of the band gap. We have achieved high resolution by measuring the I–V characteristics locally using C-AFM, and by extracting the corresponding differential conductances.

Figure 3 shows the characteristic spectra of local differential conductance as a function of voltage. The measurements have been performed on interior points of different grains, far away from any boundaries with the neighboring grains. The density of states has varied slightly between the grains. The estimated band gap is $E_g = 3.0 \pm 0.2$ eV, in agreement with the optical measurements [29–31]. Conduction at negative bias

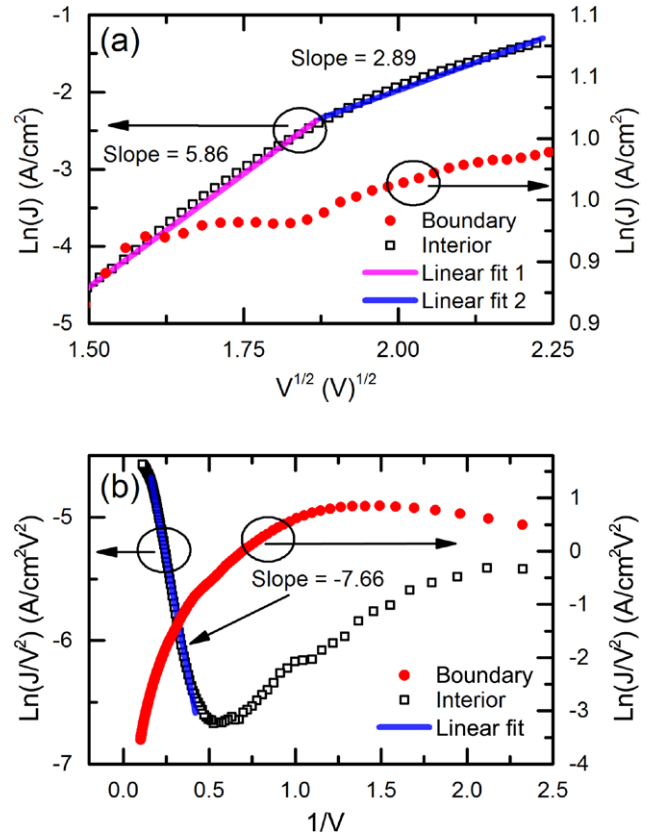


Figure 4. (a) Schottky thermionic emission plot, $\ln(J)$ versus $V^{1/2}$ and (b) Fowler–Nordheim plot, $\ln(J/V^2)$ versus $1/V$ at positive bias curves of the grain interior (left scale) and grain boundary (right scale) of the BiFeO₃ film.

voltages corresponds to the states in the valence band, while the conduction at the positive bias corresponds to the states in the conduction band. The flat plateau around zero voltage represents the band gap. These results show that the grain interiors are very similar, even though the grain’s immediate surroundings vary. Therefore, we claim that the properties at the length scale of the grain size are not influenced by the distant regions of the film, and therefore should not depend on the film thickness, as long as it is larger than the grain dimension.

We have observed a difference between the grain boundary and the grain interior in the local measurements of the current as a function of bias voltage. In the resulting I–V curves the conduction has been higher at the boundary. Conduction through semiconductor heterostructures is well researched, and various transport mechanisms have been proposed and observed [32, 33]. In our case, the distribution of electric polarization (see figure 2), and the typical gap sizes (see figure 3), suggest that the interior of the grain behaves as a semiconductor of fairly large band gap, ~ 3 eV. In the grain interior, the transport has been consistent with the tunneling through a barrier, either via Schottky or Fowler–Nordheim mechanism [32–34]. We have fitted the I–V curves in the spatial region of the grain interior, and in the voltage region $V > 2$ V, to the predictions of the tunneling transport theory. Up to $V \approx 5$ V, the Schottky mechanism of thermal excitations across the barrier explains the observed behavior. At larger voltages,

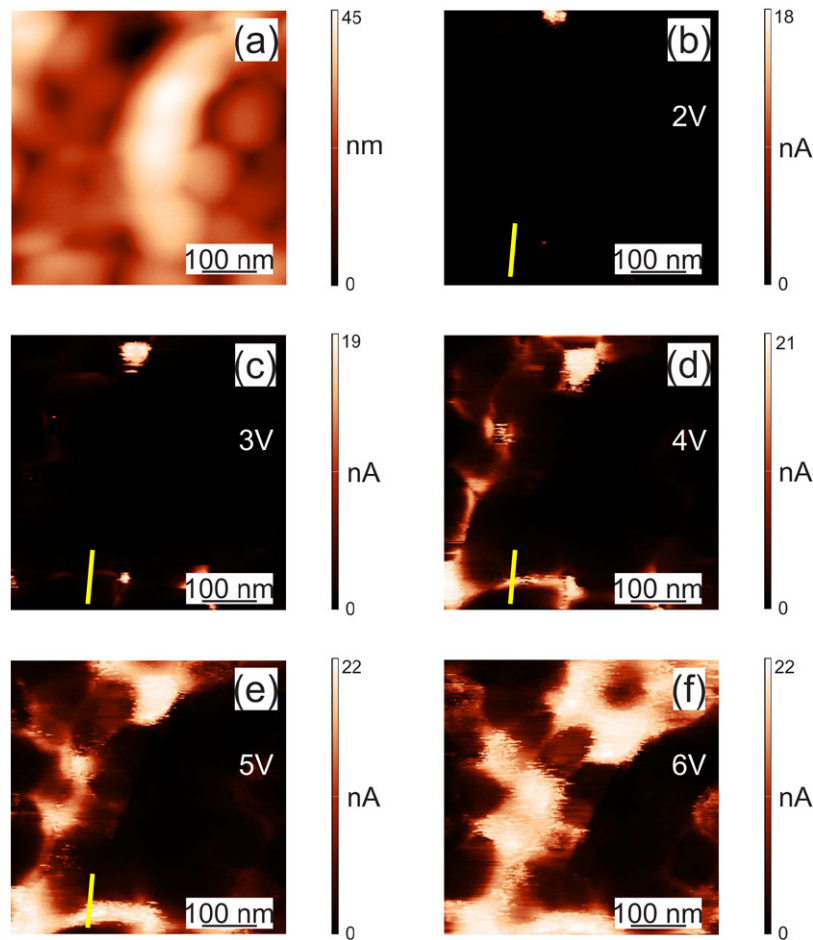


Figure 5. (a) Topography and ((b)–(f)) current maps (C-AFM images) according to bias voltages $V = 2, 3, 4, 5, 6$ V respectively. Bright regions means higher current. Notice the enhanced conductivity at grain boundaries and no conductivity regions in the grains interior. Bright line indicates the places between two grains where we have measured the current as a function of the position (shown in figure 6).

the results are consistent with the Fowler–Nordheim mechanism. Figure 4(a) shows the plot of $\ln(J)$ versus $V^{1/2}$ measured at various points in the BiFeO_3 film in the voltage range from 2 to 5 V. For the leakage current governed by the tunneling, $\ln(J/V^2)$ versus $1/V$ plot shows linearity for bias voltage well below the gap, i.e. $V < 2$ V (figure 4(b)), as we have observed in our film. At low fields, $V < 1.5$ V the grain interior has shown a plain Ohmic behavior (see supplementary material (stacks.iop.org/JPhysD/49/045309/mmedia)). As opposed to the grain interior, I–V curves of the grain boundary have not followed any standard transport model.

The local current distributions and the I–V characteristic of the BiFeO_3 film have been studied by the C-AFM. Current maps (C-AFM images) and topography images have been probed in the same spatial region of the sample. In C-AFM images, figure 5, the bright parts are conducting regions, while the dark regions are non-conducting. From the morphological and PFM measurements we have found that the BiFeO_3 film is inhomogeneous. A difference in electric transport properties between the grain interior and its boundary can appear for several reasons. Due to the different crystal orientation of the grains and the possible strain between the grains, the polarizations of neighboring grains are not equal and generically point in different directions. Furthermore, different polarizations

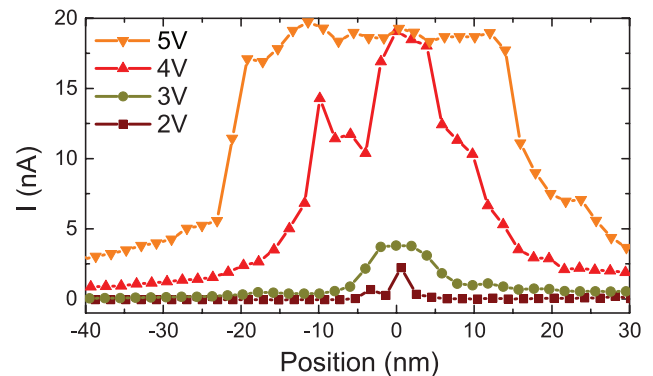


Figure 6. The current profiles of cross-sectional analysis along the bright solid line in figure 5.

of the neighboring grains cause strong electric fields in the region of the boundary between the grains. A similar phenomenon was observed in HoMnO_3 [35].

Our measurements have demonstrated that the local conduction pathways of the BiFeO_3 film coincide with the grain boundaries, while the interior of the grains remain insulating [36], as indicated in figure 5, and consistent with the measurements on the interior points of various grains, presented in figure 3. The charge transport of BiFeO_3 film has been

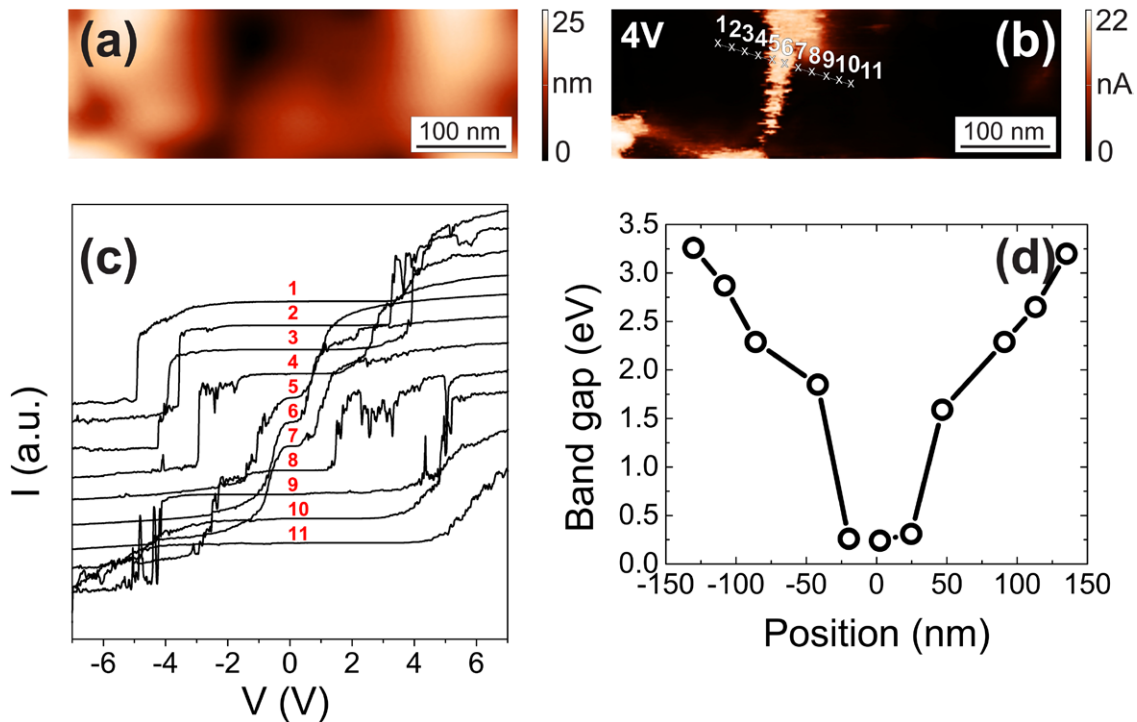


Figure 7. (a) Topography, (b) C-AFM image with line across the grain boundary, (c) I–V characteristics for 11-points across grain boundary and (d) behavior of the band gap as a function of the position of the grain boundary.

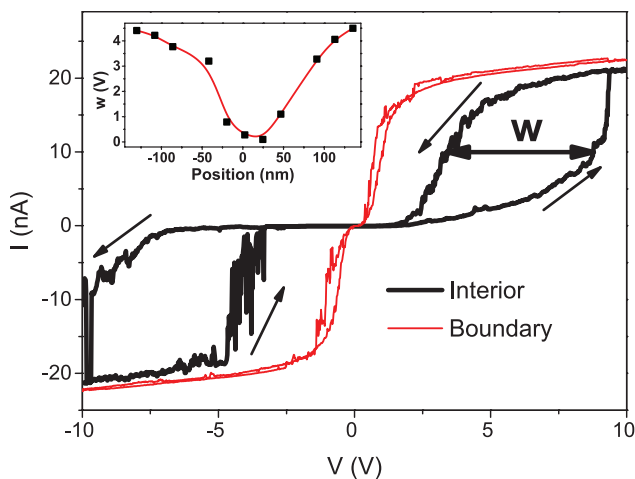


Figure 8. Dramatic I–V hysteresis in the grain interior (heavy line) and the absence of the hysteresis in the grain boundaries (thin line) of the BiFeO₃ film. In the inset, the width of the hysteresis curve (w) is shown as a function of the position across the grain boundary. Solid line in the inset is a guide to the eye.

investigated at different applied bias voltages, both slightly smaller and larger than the band gap. Topography image (figure 5(a)) and the corresponding C-AFM images at bias voltage ranged from 2 to 6 V (figures 5(b)–(f)) have confirmed high correlation between the granular structure of the film and the shape of the conduction pathways. Under low bias voltages, narrow charge transport pathways form (figures 5(b) and (c)) at the places that are low in the topographic image of the film, and are barely visible. As the bias voltage increases, both the width of the conduction pathways and the intensity of the current that flows through them increases.

The evolution of the conduction pathways with the increasing bias voltage is shown in figure 6. The current through the film has been measured at the points that lie both near the grain boundaries and deep within the grain, along line that crosses the grain boundary at the right angle. The measurements were repeated for various bias voltages. The geometry is indicated by the bright solid line in figures 5(b)–(e). With the increase of the bias voltage, the conduction path broadens. Initial broadening is slow, the currents are weak, and the path is narrow as long as the bias voltage is below the band gap. At the bias voltage of about 4 V, which is larger than the band gap, the path suddenly broadens dramatically, and the local currents increase. At such high biases, the interior of the grain also begins to conduct. Similar behavior was previously observed in doped BiFeO₃ film [28].

In order to better understand the microscopic charge transport process in the grain boundaries, we have measured the I–V characteristics across the grain boundary and observed the changes in the conduction. A pair of particularly large grains and the boundary between them have been chosen, so that we can reach a relatively high spatial resolution when compared to the dimensions of the grains. Figure 7 shows topography (a) and C-AFM image (b) under the 4 V bias with a line across the grain boundary and 11 points on it. The I–V characteristics taken at these points are shown in figure 7(c). As a general trend, the grain boundaries have almost Ohmic behavior, but at the point in the grain interior, the I–V characteristics are typical of semiconductors. Figure 7(d) shows the evolution of the band gap across the grain boundary. We have found the band gap of about 3.2 eV on the grain interior, consistent with the measurements on other grains, see figure 3. As the probe approaches the boundary, the band gap narrows down. At the

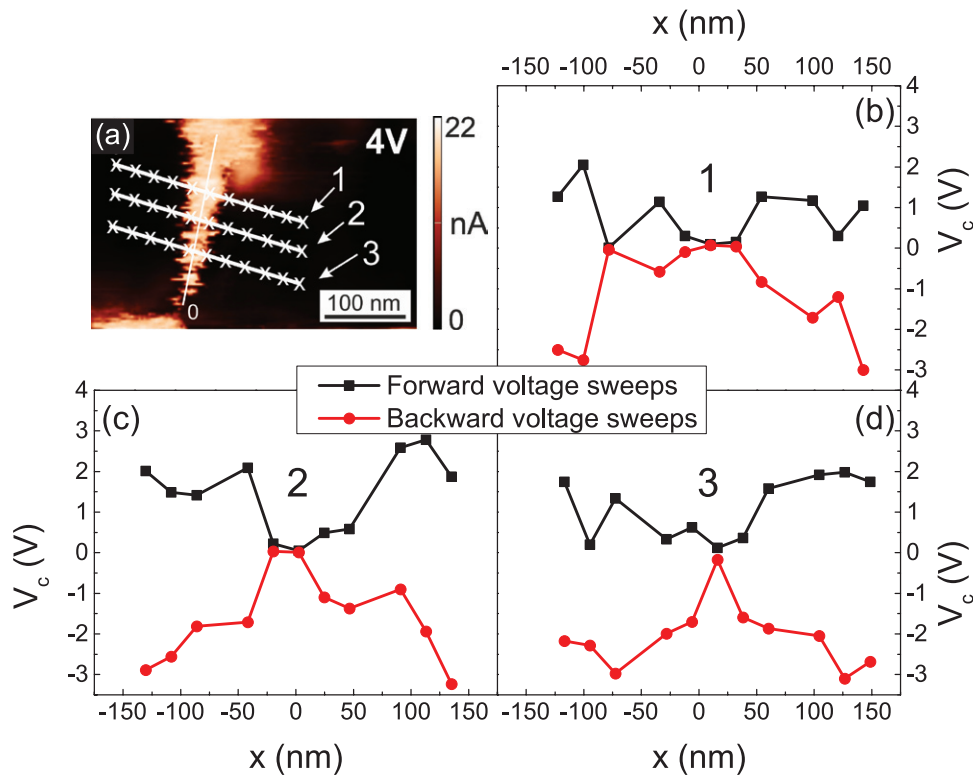


Figure 9. (a) C-AFM image with 3 lines across grain boundary and ((b)–(d)) center of band gap across lines 1, 2, and 3 in the C-AFM image. Solid lines are a guide to the eye.

three points located at the grain boundary (5, 6, and 7) the band gap is very narrow, and the material behaves similarly to a conductor. The fact that we do not find the band gap to be constant across the sample suggests that, at the level of single grains, the film is not homogeneous with well-defined and constant band structure throughout the sample.

The hysteretic dependence of polarization on the external electric field is well known in bulk ferroelectric BiFeO₃. The hysteretic phenomena are necessary for the applications of BiFeO₃ films in memory devices. Reorganization of charge associated with the variation of electric polarization causes strong internal fields in the sample, and we may expect similar hysteretic behavior in the quantities related to the charge transport. The I–V characteristics and the phenomenon of resistive switching in polycrystalline thin films shows some signatures of the hysteresis [37–39]. However, the hysteresis of electric polarization in the electric field exists only in insulators, whereas the conductors cannot support the electric fields in the interior. We have studied the local hysteresis in the I–V curves, and have probed both the region where the grain is insulating, i.e. the grain interior, and the region where the grain is conductive, i.e. the grain boundary. We have defined the hysteresis width, w , as the difference of voltage that produces a 10 nA current in forward- and backward voltage sweep, see figure 8. The hysteresis width vanishes at the grain boundary, and turns on in the interior with the characteristic length scale of 50 nm, see inset of figure 8. The measured points are presented in figure 7(b). Figure 8 shows the I–V curves in the forward and backward sweep at the grain interior (thick line) and at the grain boundary (thin line). Note that the typical grain diameter is 40 nm.

The bulk BiFeO₃ shows both the ferroelectric and the anti-ferromagnetic order. Both orders are characterized by hysteretic response to external fields. We have found the hysteresis in conductivity in the interior of the grain, but not at the grain boundary (see figure 8). Another property of the grain that can be studied locally is the density of states. We have measured the local density of states across the grain boundary and have found, again, the hysteretic behavior within the grain interior, but not on the boundary. We have chosen the center of the band gap as a representative quantity that describes the band structure. The definition of the center of band gap is illustrated graphically in the supplementary material (stacks.iop.org/JPhysD/49/045309/mmedia). In a series of C-AFM measurements, we have measured the density of states in a forward- and backward voltage sweeps at a set of points that extends across the grain boundary.

Figure 9(a) shows a C-AFM image of grain boundary. Within this region, we have recorded 11 I–V curves through three different lines (see picture). Three representative lines (1–3) across the leakage current pathways of different widths are selected for detailed study of the local density of states. The center of flat plateau in the I–V characteristics is defined as the center of the band gap. Figures 9(b)–(d) show the potential at the band gap centers, V_c , across marked lines 1–3 in figure 9(a).

The density of states is hysteretic, and the center of the band gap is hysteretic within the grain, but not within the boundary layer, see figure 9. The motion of the center of the band gap, V_c , as the probe position x moves in real space across the grain boundary is more pronounced in the backward voltage sweeps,

and less in the forward ones. The local hysteresis is manifested by the difference in the positions of the band gap centers as measured in the forward- and backward voltage sweeps while the position of the probe within the sample is kept fixed. Comparison of the $V_c(x)$ curves from the figures 9(b)–(d) with the image of conductivity obtained by C-AFM shows that the narrower boundary region as defined by conductivity (figure 9(a)) also implies a narrower region with the absent hysteresis in $V_c(x)$ (figures 9(b)–(d)). Note, however that the boundary region as would naively be defined from $I(V)$ is much narrower than the absence of hysteresis would imply.

In thin BiFeO₃ films, a similar shift of the band gap was observed at the ferroelectric domain boundaries [40]. Discontinuity in polarization and the consequent charge accumulation on the surface causes potential discontinuity and moves the band gap. Such a potential difference should enhance the electrical conductivity by causing carriers in the material to accumulate at the domain wall to screen the polarization discontinuity [41, 42]. In our sample, the grains are single domains, see above, and a similar charge accumulation appears at the boundaries between the grains.

4. Conclusions

We have observed a difference in electrical properties between the grain interior and the grain boundary in BiFeO₃ thin film obtained by sol–gel spin coating process. Leakage current was more pronounced at the grain boundaries. The onset of large leakage current with the increasing bias voltage happens as the region of large conductivity expands from the grain boundaries towards the grain interiors. The leakage mechanism in grain interior have been identified with Schottky and Fowler–Nordheim processes, while the leakage current through the grain boundaries does not appear to be dominated by any standard mechanism of conduction. In the measurement with the local probes, we have also found that the band gap varies slightly among the different grains, but varies strongly between the grain boundary and the grain interior. In the grain interior, we have observed hysteresis in various properties of the material connected to the charge transport. The shape of the density of states is itself hysteretic. As a consequence, the conductivity as a function of slowly varying voltage is also hysteretic. As opposed to the grain interior, no hysteresis was observed with the local probe at the grain boundary.

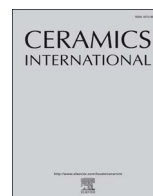
Acknowledgments

This work was financially supported by the Ministry of Education, Science and Technological Development of the Republic of Serbia under the projects OI171032, OI171005, III45018 and SNF through SCOPES IZ73Z0152500.

References

- [1] Sergienko I A and Dagotto E 2006 Role of the Dzyaloshinskii–Moriya interaction in multiferroic perovskites *Phys. Rev. B* **73** 094434
- [2] Cheong S W and Mostovoy M 2007 Multiferroics: a magnetic twist for ferroelectricity *Nat. Mater.* **6** 13
- [3] Picozzi S, Yamauchi K, Sergienko I A, Sen C, Sanyal B and Dagotto E 2008 Microscopic mechanisms for improper ferroelectricity in multiferroic perovskites: a theoretical review *J. Phys.: Condens. Matter* **20** 434208
- [4] Catalan G and Scott J F 2009 Physics and applications of bismuth ferrite *Adv. Mater.* **21** 2463
- [5] Ramesh R and Spaldin N A 2007 Multiferroics: progress and prospects in thin films *Nat. Mater.* **6** 21
- [6] Ren X R, Tan G Q, Miao H Y and Li Z Y 2012 Controllability study on the preparation of pure phase BiFeO₃ thin films by liquid phase self-assembled method *Appl. Surf. Sci.* **258** 8040
- [7] Schwartz R W 1997 Chemical solution deposition of perovskite thin films *Chem. Mater.* **9** 2325
- [8] Roginskaya Y E, Tomashpol’Skii Y Y, Venevtsev Y N, Petrov V M and Zhdanov G S 1966 Nature of dielectric and magnetic properties of BiFeO₃ *Sov. Phys.—JETP* **23** 47
- [9] Kiselev S V, Ozerov R P and Zhdanov G S 1963 Detection of magnetic order in ferroelectric BiFeO₃ by neutron diffraction *Sov. Phys.—Dokl.* **7** 742
- [10] Wang Y and Nan C W 2006 Enhanced ferroelectricity in Ti-doped multiferroic BiFeO₃ thin films *Appl. Phys. Lett.* **89** 052903
- [11] Mao W *et al* 2014 Effect of Ln (Ln = La, Pr) and Co co-doped on the magnetic and ferroelectric properties of BiFeO₃ nanoparticles *J. Alloys Compd.* **584** 520
- [12] Pradhan S K and Roul B K 2011 Effect of Gd doping on structural, electrical and magnetic properties of BiFeO₃ electroceramic *J. Phys. Chem. Solids* **72** 1180
- [13] Liu J, Li M, Pei L, Wang J, Yu B, Wang X and Zhao X 2010 Structural and multiferroic properties of the Ce-doped BiFeO₃ thin films *J. Alloys Compd.* **493** 544
- [14] Qi X, Dho J, Tomov R, Blamire M G and MacManus-Driscoll J L 2005 Greatly reduced leakage current and conduction mechanism in aliovalent-ion-doped BiFeO₃ *Appl. Phys. Lett.* **86** 062903
- [15] Jang H W *et al* 2009 Domain engineering for enhanced ferroelectric properties of epitaxial (001) BiFeO₃ thin films *Adv. Mater.* **21** 817
- [16] Lu H X, Zhao J L, Sun J R, Wang J and Shen B G 2011 Ferroelectric domain structure of the BiFeO₃ film grown on different substrates *Physics B* **406** 305
- [17] Selbach S M, Tybell T, Einarsrud M A and Grande T 2007 Size-dependent properties of multiferroic BiFeO₃ nanoparticles *Chem. Mater.* **19** 6478
- [18] Armstrong R W 1970 The influence of polycrystal grain size on several mechanical properties of materials *Metall. Mater. Trans. B* **1** 1169
- [19] Williamson G K and Hall W H 1953 X-ray line broadening from filed aluminium and wolfram *Acta Metall. Mater.* **1** 22
- [20] Alpers B, Cohen S, Rubinstein I and Hodes G 1995 Room-temperature conductance spectroscopy of CdSe quantum dots using a modified scanning force microscope *Phys. Rev. B* **52** R17017
- [21] Alpers B, Rubinstein I and Hodes G 2001 Identification of surface states on individual CdSe quantum dots by room-temperature conductance spectroscopy *Phys. Rev. B* **63** 081303
- [22] Kwon S, Lee S J, Kim S M, Lee Y, Song H and Park J Y 2015 Probing the nanoscale Schottky barrier of metal/semiconductor interfaces of Pt/CdSe/Pt nanodumbbells by conductive-probe atomic force microscopy *Nanoscale* **7** 12297
- [23] Johann F, Morelli A, Biggemann D, Arredondo M and Vrejoiu I 2011 Epitaxial strain and electric boundary condition effects on the structural and ferroelectric properties of BiFeO₃ films *Phys. Rev. B* **84** 094105

- [24] Castillo M E, Shvartsman V V, Gobeljic D, Gao Y, Landers J, Wende H and Lupascu D C 2013 Effect of particle size on ferroelectric and magnetic properties of BiFeO₃ nanopowders *Nanotechnology* **24** 355701
- [25] Speck J S and Pompe W 1994 Domain configurations due to multiple misfit relaxation mechanisms in epitaxial ferroelectric thin films. I. Theory *J. Appl. Phys.* **76** 466
- [26] Speck J S, Seifert A, Pompe W and Ramesh R 1994 Domain configurations due to multiple misfit relaxation mechanisms in epitaxial ferroelectric thin films. II. Experimental verification and implications *J. Appl. Phys.* **76** 477
- [27] Kwak B S, Erbil A, Budai J D, Chisholm M F, Boatner L A and Wilkens B J 1994 Domain formation and strain relaxation in epitaxial ferroelectric heterostructures *Phys. Rev. B* **49** 14865
- [28] Zhou M X, Chen B, Sun H B, Wan J G, Li Z W, Liu J M, Song F Q and Wang G H 2013 Local electrical conduction in polycrystalline La-doped BiFeO₃ thin films *Nanotechnology* **24** 225702
- [29] Allibe J *et al* 2010 Optical properties of integrated multiferroic BiFeO₃ thin films for microwave applications *Appl. Phys. Lett.* **96** 182902
- [30] Kumar A *et al* 2008 Linear and nonlinear optical properties of BiFeO₃ *Appl. Phys. Lett.* **92** 121915
- [31] Chen X, Zhang H, Wang T, Wang F and Shi W 2012 Optical and photoluminescence properties of BiFeO₃ thin films grown on ITO-coated glass substrates by chemical solution deposition *Phys. Status Solidi A* **209** 1456
- [32] Yan F, Lai M O, Lu L and Zhu T J 2011 Variation of leakage mechanism and potential barrier in La and Ru co-doped BiFeO₃ thin films *J. Phys. D: Appl. Phys.* **44** 435302
- [33] Chen Z, He L, Zhang F, Jiang J, Meng J, Zhao B and Jiang A 2013 The conduction mechanism of large on/off ferroelectric diode currents in epitaxial (1 1 1) BiFeO₃ thin film *J. Appl. Phys.* **113** 184106
- [34] Chiu F C 2014 A review on conduction mechanisms in dielectric films *Adv. Mater. Sci. Eng.* **2014** 578168
- [35] Wu W, Horibe Y, Lee N, Cheong S W and Guest J R 2012 Conduction of topologically protected charged ferroelectric domain walls *Phys. Rev. Lett.* **108** 077203
- [36] Cheng Z, Bin C, Xiao-Jian Z, Zheng-Hu Z, Yi-Wei L, Yuan-Fu C, Qing-Feng Z and Run-Wei L 2011 Local leakage current behaviours of BiFeO₃ films *Chin. Phys. B* **20** 117701
- [37] Yang C H *et al* 2009 Electric modulation of conduction in multiferroic Ca-doped BiFeO₃ films *Nat. Mater.* **8** 485
- [38] Yin K, Li M, Liu Y, He C, Zhuge F, Chen B, Lu W, Pan X and Li R W 2010 Resistance switching in polycrystalline BiFeO₃ thin films *Appl. Phys. Lett.* **97** 042101
- [39] Wang C, Jin K J, Xu Z T, Wang L, Ge C, Lu H B, Guo H Z, He M and Yang G Z 2011 Switchable diode effect and ferroelectric resistive switching in epitaxial BiFeO₃ thin films *Appl. Phys. Lett.* **98** 192901
- [40] Seidel J *et al* 2010 Domain wall conductivity in la-doped BiFeO₃ *Phys. Rev. Lett.* **105** 197603
- [41] Seidel J *et al* 2009 Conduction at domain walls in oxide multiferroics *Nat. Mater.* **8** 229
- [42] Maksymovych P, Seidel J, Chu Y H, Wu P, Baddorf A P, Chen L Q, Kalinin S V and Ramesh R 2011 Dynamic conductivity of ferroelectric domain walls in BiFeO₃ *Nano Lett.* **11** 1906



Dielectric and ferroelectric properties of Ho-doped BiFeO₃ nanopowders across the structural phase transition



Bojan Stojadinović^a, Zorana Dohčević-Mitrović^{a,*}, Dimitrije Stepanenko^a, Milena Rosić^b, Ivan Petronijević^c, Nikola Tasić^d, Nikola Ilić^d, Branko Matović^b, Biljana Stojanović^d

^a Center for Solid State Physics and New Materials, Institute of Physics Belgrade, University of Belgrade, Pregrevica 118, 11080 Belgrade, Serbia

^b Institute for Nuclear sciences, Centre of Excellence-CextremeLab "Vinča", University of Belgrade, 11000 Belgrade, Serbia

^c Faculty of Physics, University of Belgrade, Studentski trg 12-16, 11000 Belgrade, Serbia

^d Institute for Multidisciplinary Research, University of Belgrade, Kneza Višeslava 1, 11000 Belgrade, Serbia

ARTICLE INFO

Keywords:

Sol-gel processes
X-ray methods
Dielectric properties
Ferroelectric properties
Perovskites

ABSTRACT

We have studied Ho-doped BiFeO₃ nanopowders (Bi_{1-x}Ho_xFeO₃, x = 0–0.15), prepared via sol-gel method, in order to analyse the effect of substitution-driven structural transition on dielectric and ferroelectric properties of bismuth ferrite. X-ray diffraction and Raman study demonstrated that an increased Ho concentration (x ≥ 0.1) has induced gradual phase transition from rhombohedral to orthorhombic phase. The frequency dependent permittivity of Bi_{1-x}Ho_xFeO₃ nanopowders was analysed within a model which incorporates Debye-like dielectric response and dc and ac conductivity contributions based on universal dielectric response. It was shown that influence of leakage current and grain boundary/interface effects on dielectric and ferroelectric properties was substantially reduced in biphasic Bi_{1-x}Ho_xFeO₃ (x > 0.1) samples. The electrical performance of Bi_{0.85}Ho_{0.15}FeO₃ sample, for which orthorhombic phase prevailed, was significantly improved and Bi_{0.85}Ho_{0.15}FeO₃ has sustained strong applied electric fields (up to 100 kV/cm) without breakdown. Under strong external fields, the polarization exhibited strong frequency dependence. The low-frequency remnant polarization and coercive field of Bi_{0.85}Ho_{0.15}FeO₃ were significantly enhanced. It was proposed that defect dipolar polarization substantially contributed to the intrinsic polarization of Bi_{0.85}Ho_{0.15}FeO₃ under strong electric fields at low frequencies.

1. Introduction

Multiferroics, materials which simultaneously exhibit at least two ferroic properties among electric, magnetic, and elastic responses, are quite rare. They are of great interest for both fundamental physics and potential applications. Among multiferroic materials, bismuth ferrite (BiFeO₃) possesses unique property, i.e. exhibits multiferroic behavior at room temperature. Having high ferroelectric (T_C ~ 1100 K) and antiferromagnetic (T_N ~ 640 K) transition temperatures, BiFeO₃ is a promising material for the applications in spintronic devices, electrically controlled magnetic memories and functional sensors [1,2]. Nevertheless, problems of low resistivity and sinterability and appearance of secondary phases present a serious obstacle for the application of BiFeO₃ (BFO) in devices. BFO suffers from high leakage current which causes large dielectric loss and degradation of the ferroelectric properties. The main cause of leakage is disorder, usually in the form of charge defects, like oxygen or bismuth vacancies and secondary phases. Attempts at minimizing the leakage current density through doping

with rare earth ions at Bi sites, have led to improvement of electric and magnetic properties of BFO [3–6]. These studies have demonstrated that substitution of Bi sites with rare-earth ions effectively controls the volatility of Bi³⁺ ions and the amount of defects, while suppressing the secondary phase appearance.

Despite a significant body of work dealing with rare-earth doped BFO [3,4,7–10], BFO doped with Ho is less investigated. There are several studies dealing with the influence of Ho doping on leakage current, and on magnetic or ferroelectric properties of BFO, for which BFO is either phase stabilized [11–16] or exhibits biphasic character with increased Ho doping [17–20]. Among these studies, only Song and coauthors [20] showed that dielectric constant was significantly increased with small amount of Ho substitution (x = 0.05, 0.10) for which BFO retained rhombohedral structure and then decreased when the orthorhombic phase appeared with higher doping (x = 0.15, 0.20). They also deduced that the dielectric loss of doped samples behaves in a complicated manner, probably influenced by the conductivity of material. Song and coauthors did not analyse the reasons of obtaining

* Corresponding author.

E-mail address: zordoh@ipb.ac.rs (Z. Dohčević-Mitrović).

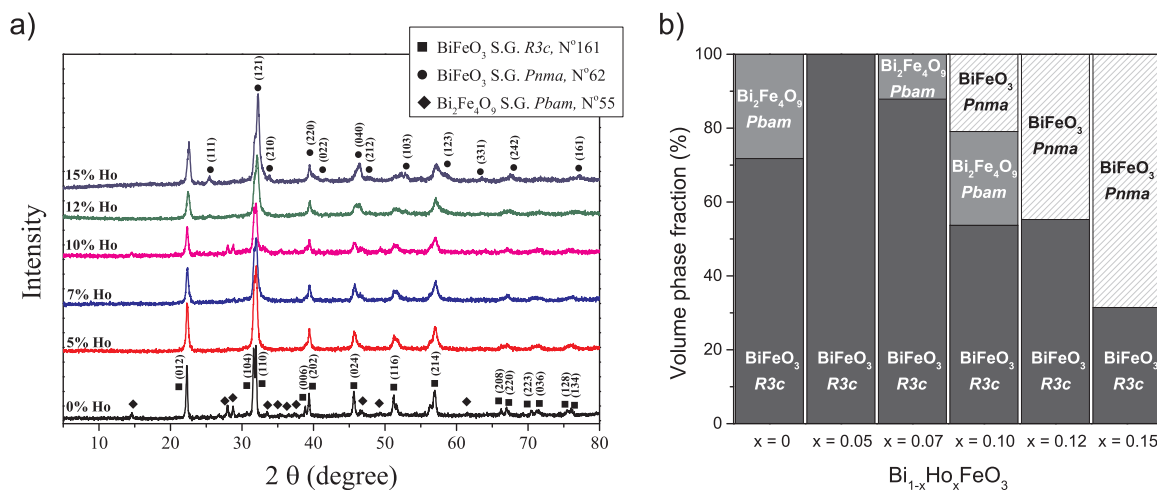


Fig. 1. a) X-ray diffraction patterns and b) volume phase fraction analysis of the Bi_{1-x}Ho_xFeO₃ (0 ≤ x ≤ 0.15) samples.

colossal dielectric constant, nor assumed that quite often these phenomena can be explained by Maxwell-Wagner-type contributions of depletion layers at the interface between sample and contacts or at grain boundaries. Furthermore, it is quite reasonable to assume that various polarization mechanisms can appear in biphasic BFO and influence the dielectric and ferroelectric properties of BFO. To the best of our knowledge, influence of structural phase transformation caused by Ho doping on polarization mechanisms, which can exert a strong influence on the dielectric and ferroelectric properties of BFO, has not been studied.

Herein, we investigated how the structural phase transformation induced by Ho doping influenced the dielectric and ferroelectric properties of Bi_{1-x}Ho_xFeO₃ nanopowders. Detailed analysis of the frequency dependent permittivity, using combined model which incorporated Debye-like dielectric relaxation, as well as dc and ac conductivity contributions, was performed. This analysis enabled us to estimate the influence of leakage current and grain boundary/interface effects on the dielectric and ferroelectric properties of single phase and biphasic Bi_{1-x}Ho_xFeO₃ nanopowders. Origin of improved electric performances of biphasic Bi_{1-x}Ho_xFeO₃ nanostructures, for which orthorhombic phase prevailed, was discussed in detail. These results may provide new insight into modified electrical properties of BiFeO₃ by Ho doping, which can be important for potential applications.

2. Experimental procedure

2.1. Materials synthesis

Bi_{1-x}Ho_xFeO₃ (x = 0, 0.05, 0.07, 0.10, 0.12, and 0.15) powders were synthesized by a sol-gel method. The stoichiometric amounts of bismuth nitrate (Bi(NO₃)₃·6H₂O), iron nitrate (Fe(NO₃)₃·9H₂O), and holmium nitrate (Ho(NO₃)₃·5H₂O) were used. 2-Methoxyethanol and acetic acid (CH₃COOH) were mixed and stirred for 30 min, before adding the nitrates. Obtained solutions were stirred and heated at 80 °C. After a partial liquid evaporation, the solutions have turned into brown gels. The gels were dried for 45 min at 150 °C. Dried samples were calcinated at 650 °C for 6 h. The pristine and doped samples were named according to the Ho content as BFO, BHFO5, BHFO7, BHFO10, BHFO12 and BHFO15.

2.2. Materials characterization

The phase composition and crystal structure of Bi_{1-x}Ho_xFeO₃ samples were analysed using X-ray diffractometer Rigaku Ultima IV with nickel filtered Cu K_α radiation in the 2θ range of 10–80° with the step of 0.02° and the scanning rate of 0.5°/min. XRD pattern analysis

was performed using Powder Cell programme (<http://powdercell-for-windows.software.informer.com/2.4/>) [21]. The TCH pseudo-Voigt profile function gave the best fit to the experimental data. The surface morphology was studied by scanning electron microscopy (SEM, TESCAN SM-300). The micro-Raman spectra were measured at room temperature using a Jobin Yvon T64000 spectrometer equipped with a nitrogen-cooled CCD detector. The λ = 532 nm line of solid state Nd:YAG laser was used as an excitation source with an incident laser power less than 40 mW in order to minimize the heating effects. The dielectric properties of the samples were examined in the frequency range of 80 Hz to 8 MHz. The Digital Programmable LCR Bridge HM8118 (Hameg) was used in the range 80 Hz–120 kHz, and the Digital LCR Meter 4285 A (HP/Agilent) was used in the range 80 kHz–8 MHz. Each sample was placed in a closed capacitor cell housed in a Faraday cage with an AC signal of 1.5 V applied across the cell. The disk-shaped samples had a diameter close to the diameter of the cell electrodes (8 mm). Standard bipolar measurements in the frequency range 1 Hz–1 kHz were performed on Precision Multiferroic Test System (Radiant Technologies, Inc.), using a triangular electric field waveform. All measurements were performed at room temperature.

3. Results and discussion

Fig. 1(a) shows XRD patterns of the Bi_{1-x}Ho_xFeO₃ (0 ≤ x ≤ 0.15) samples. The XRD pattern of pristine BFO matches the rhombohedral R3c structure with a presence of weak diffraction peaks which correspond to the orthorhombic Bi₂Fe₄O₉ secondary phase of Pbam space group (N° 55, ICSD #20067). XRD spectra of the BHFO5 and BHFO7 samples maintain R3c structure. No secondary peaks were detected in BHFO5 sample, whereas the traces of secondary phase were observed in the BHFO7 sample. Addition of Ho dopant induced a gradual broadening of XRD peaks and their shifts towards higher angles. These changes suggest structural distortion of BFO lattice and can be attributed to the unit cell contraction due to the substitution of Bi³⁺ ions with smaller Ho³⁺ dopant. Significant changes with increased Ho concentration were observed in doublet (104) and (110) diffraction peaks at 2θ ~ 32°. These peaks were shifted towards larger 2θ values, and in the samples with higher Ho content (x > 0.07) they gradually merged into a single broad peak (BHFO15 sample). In addition, the (006), (116) and (202) diffraction peaks of R3c phase became weak and disappeared in the samples with higher Ho concentration (x > 0.1). In the spectra of BHFO12 and BHFO15 samples, a new single peak appeared at 2θ ~ 38°, whereas additional peak at 2θ ~ 25° was found in BHFO15 sample.

Such changes have already been seen in the XRD spectra of doped

Table 1The lattice parameters (Å), volume of the unit cell (Å³) and volume phase fraction (vol%).

Phase	BFO	BHFO5	BHFO7	BHFO10	BHFO12	BHFO15
BiFeO ₃ rhombohedral <i>R3c</i>	a = 5.5722 c = 13.8511 V = 372.45 71.75%	a = 5.5636 c = 13.8216 V = 370.51 100.00%	a = 5.5575 c = 13.8145 V = 369.51 87.86%	a = 5.5651 c = 13.8143 V = 370.51 53.72%	a = 5.5675 c = 13.8542 V = 371.91 55.27%	a = 5.5441 c = 13.8127 V = 367.68 31.45%
Bi ₂ Fe ₄ O ₉ orthorhombic <i>Pbam</i>	a = 7.9477 b = 8.4582 c = 6.0050 V = 403.68 28.25%	/	a = 7.9769 b = 8.5299 c = 5.9448 V = 404.50 12.14%	a = 7.9501 b = 8.4580 c = 5.9976 V = 403.29 25.36%	/	/
BiFeO ₃ orthorhombic <i>Pnma</i>	/	/	/	a = 5.5830 b = 7.8825 c = 5.4192 V = 238.49 20.92%	a = 5.5993 b = 7.8679 c = 5.4540 V = 240.27 44.73%	a = 5.5907 b = 7.8129 c = 5.4297 V = 237.17 68.55%
Rp	5.81	6.27	5.94	4.86	6.18	5.42
Rwp	7.44	7.92	7.60	6.14	7.92	6.91
Rexp	0.11	0.12	0.09	0.06	0.07	0.09

BiFeO₃ nanoparticles [17,22], ceramics [23–25] and films [26], and were ascribed to the presence of orthorhombic phase. All these notable changes in the XRD spectra indicate structural phase transformation from rhombohedral to orthorhombic phase in the samples doped with higher Ho content ($x = 0.10, 0.12$ and 0.15). Bi₂Fe₄O₉ phase is still present in the BHFO10 sample, but with further increase of Ho doping (BHFO12 and BHFO15 samples) the secondary Bi₂Fe₄O₉ phase is completely suppressed. Furthermore, the absence of diffraction peaks which correspond to Ho oxides, even at higher concentrations, implies that Ho ions have entered substitutionally into BFO lattice.

The measured XRD patterns were further refined using PowderCell programme in order to calculate the structural parameters and estimate the volume fraction of each phase. The best fits of the measured data were obtained using rhombohedral *R3c* structure for BHFO5 and BHFO7 samples. The orthorhombic phase appeared in BHFO10 samples and with further Ho doping this phase becomes dominant in BHFO15 sample. Unit cell parameters and the estimated volume fractions of different phases are presented in Table 1 for pristine and Ho-doped BFO samples. The decreasing trend in lattice constants and the unit cell contraction of *R3c* phase confirm that Bi³⁺ ions are substituted with smaller Ho³⁺ ions. A similar behavior has been reported in Tb-doped BiFeO₃ [10] as well as in rare-earth doped BiFeO₃ ceramics [27,28]. The slight increase of *R3c* phase lattice parameters in BHFO10 and BHFO12 samples can be ascribed to increased strain at phase boundary between rhombohedral and orthorhombic crystal structure. Levin et al. have also found abrupt expansion of the *R3c* unit cell volume at the rhombohedral-orthorhombic phase transition in Nd-substituted BiFeO₃ [29]. The results of quantitative phase analysis of the Bi_{1-x}Ho_xFeO₃ samples are presented in Fig. 1(b).

The influence of structural changes on surface morphology of BFO is illustrated in Fig. 2, where the SEM images of pristine and BHFO15 samples are shown for comparison. Changes in the surface morphology are clearly visible. Certain amount of intergranular porosity and non-uniformity of particles can be observed in the BFO sample, including very small spherical particles and big clumps. With incorporation of Ho³⁺ ions in BFO, the particles became more uniform and compact, whereas the particle size was reduced, as seen in 10% Ho-doped BFO [30]. In the enlarged images (Fig. 2c and d) it can be seen that pure and Ho-doped BFO samples consist of small particles and large irregularly shaped agglomerates.

Changes of Bi_{1-x}Ho_xFeO₃ crystal structure are reflected in the changes of BiFeO₃ vibrational properties, i.e. through the changes in intensity, position, and width of the Raman modes. Fig. 3 shows the room-temperature Raman spectra of Bi_{1-x}Ho_xFeO₃ samples. Raman spectrum of undoped BiFeO₃ was deconvoluted using Lorentzian profiles and all 13 Raman active modes (4A₁ + 9E) of the rhombohedral

BiFeO₃ [31] are observed. The most prominent Raman modes for *R3c* structure (marked as E-1, A₁-1, A₁-2, and A₁-3) are positioned at 75, 140, 171, and 218 cm⁻¹, respectively and are related to Bi–O bonds. The A₁-4 mode at 430 cm⁻¹ and eight E modes at 124, 274, 344, 369, 468, 520, 550 and 598 cm⁻¹ with quite weak scattering intensity are related to Fe–O bonds.

Raman spectroscopy is sensitive to atomic displacements. The A₁-1, A₁-2 and A₁-3 modes are blue-shifted due to the substitution of Bi³⁺ ions with smaller Ho³⁺ ions. Modes E-1, A₁-1, A₁-2 and A₁-3 became broader and of reduced intensity, whereas higher frequency E modes (E-4, E-5) have almost disappeared. The peak broadening and reduced intensities of Raman modes imply the distortion of rhombohedral structure with incorporation of Ho. With increasing Ho concentration ($x \geq 0.1$), further changes in the Raman spectra are the result of decreased stereochemical activity of Bi lone electron pair. The intensities of A₁ and E modes are drastically reduced in BHFO10 and BHFO12 samples. These modes are barely visible in the Raman spectra of BHFO15 sample. Moreover, in BHFO12 sample three new modes approximately at 300, 400, and 510 cm⁻¹, are observed. Reduced intensities of phonon modes, characteristic for rhombohedral phase, and the presence of additional modes suggest the appearance of new crystalline phase. In the Raman spectrum of BHFO15 sample which is significantly different from the spectrum of pristine BFO, the most prominent modes are at $\sim 300, 400,$ and 510 cm⁻¹. These modes are characteristic for orthorhombic perovskite LaMnO₃ and YMnO₃ structures [32] and are also observed in doped BFO powders [17]. All notable changes in the Raman spectra of BHFO12 and BHFO15 samples are consistent with the results of XRD analysis, confirming a structural transformation from rhombohedral to orthorhombic paraelectric phase. Hence, Raman spectroscopy is powerful tool for detecting changes of Bi–O covalent bonds during the phase transition.

Fig. 4(a) and (b) illustrate the frequency dependence of real (ϵ') and imaginary (ϵ'') part of the complex permittivity ϵ of Bi_{1-x}Ho_xFeO₃ samples. In the lower frequency range, both ϵ' and ϵ'' decrease with increasing frequency and become nearly constant at higher frequencies. Among the samples with *R3c* structure, BHFO5 sample has shown pronounced dispersion at lower frequencies and higher values of ϵ' and ϵ'' than BFO. The BHFO7 sample displayed almost no dispersion over the whole frequency range. Among the samples with higher Ho content in which orthorhombic phase appears, BHFO10 sample displayed more dispersive characteristic than BHFO12 and BHFO15 samples for which permittivity dispersions were negligible.

BFO nanostructures in the form of nanopowders or thin films usually suffer from large leakage current due to the presence of oxygen vacancies, Fe²⁺ ions or some other impurities. The inhomogeneity of BFO microstructure and composition originates from the regions with

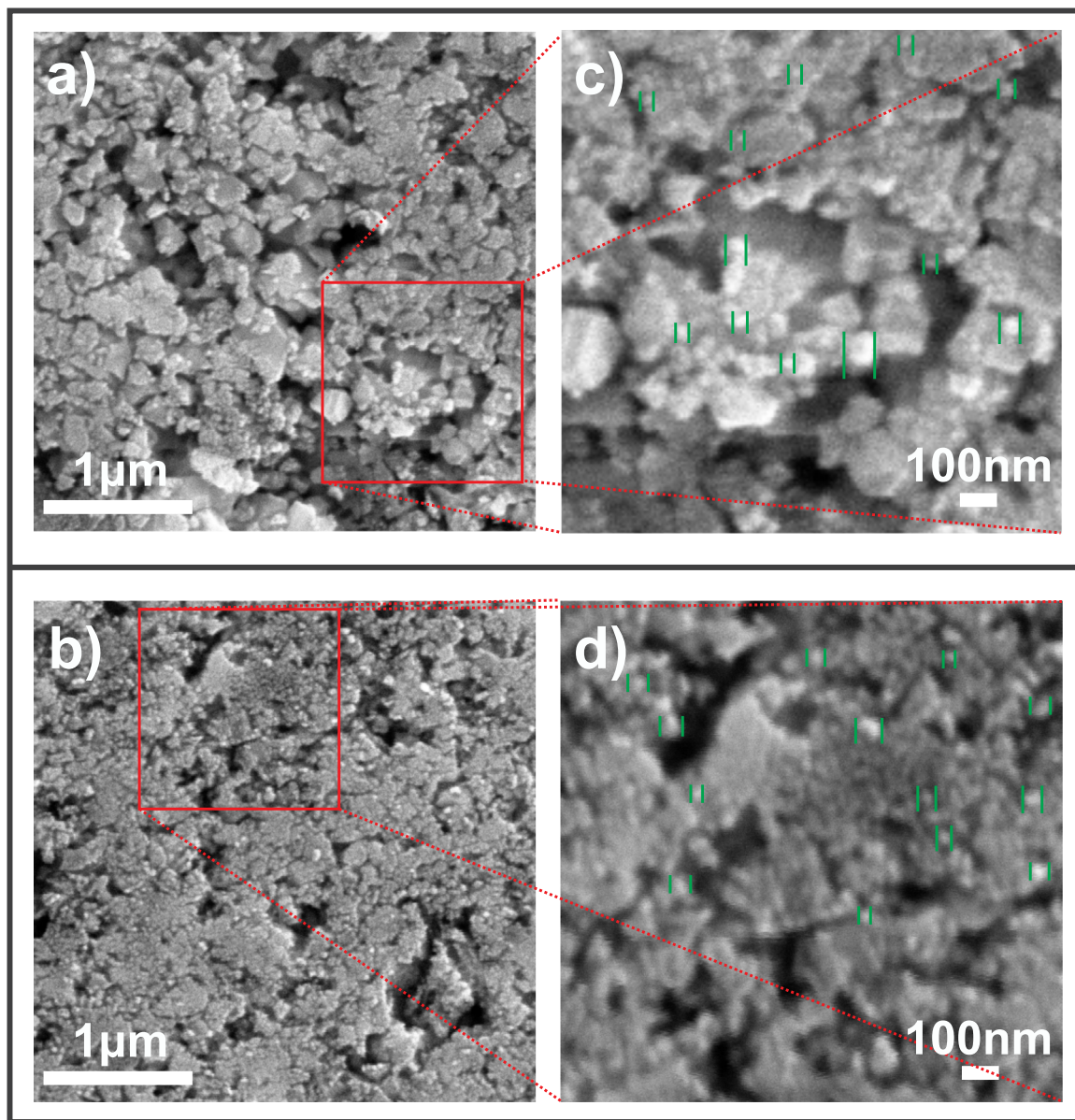


Fig. 2. SEM images of a) BiFeO₃ and b) Bi_{0.85}Ho_{0.15}FeO₃ samples. High-magnification SEM images of the c) BiFeO₃ and d) Bi_{0.85}Ho_{0.15}FeO₃ samples.

different conductivity, for example bulk and grain boundaries or from depletion layers formed at the interface of the electrode/sample surface. In addition to the dipolar or orientational polarization which occurs in the frequency range of 10³–10⁶ Hz, the grain boundary or interface effects give rise to the Maxwell-Wagner polarization which can substantially contribute to the permittivity and its dispersion at lower frequencies [3].

The dielectric relaxation processes in pure and Ho-doped BFO nanopowders were analysed within a model which includes Cole-Cole empirical expression, dc and ac conductivity terms. This model describes dielectric relaxation processes due to dipole relaxation, and the contributions from leakage current and grain boundary/interface effects. The advantages of this model for analyzing the dielectric properties of pristine BiFeO₃ films have been shown by Li and coworkers [33]. The total complex permittivity is of the form [33,34]:

$$\varepsilon = \varepsilon' + i\varepsilon'' = \frac{\varepsilon_s - \varepsilon_\infty}{1 + (i\omega\tau)^{1-\alpha}} + \frac{\sigma_0}{\varepsilon_0} \tan\left(\frac{\pi s}{2}\right) \omega^{s-1} + i\left(\frac{\sigma_{DC}}{\omega\varepsilon_0} + \frac{\sigma_0}{\varepsilon_0} \omega^{s-1}\right) \quad (1)$$

The first term in Eq. (1) corresponds to the Cole-Cole formula, where ε_s and ε_∞ are static and high frequency dielectric permittivity, τ is

the relaxation time, and α , taking the value between 0 and 1, describes the distribution of relaxation times. For an ideal Debye relaxation $\alpha = 0$. For $\alpha < 0$ the loss peaks are broader and deviate in shape from the symmetric Debye peak [35]. The frequency-independent dc conductivity contributes only to the imaginary part of permittivity (ε'') through the term $\sigma_{DC}/\omega\varepsilon_0$, whilst the frequency-dependent ac conductivity represented by UDR ansatz [34,35], influences both ε' and ε'' through terms $(\sigma_0/\varepsilon_0) \tan\left(\frac{\pi s}{2}\right) \omega^{s-1}$ and $(\sigma_0/\varepsilon_0) \omega^{s-1}$, where σ_0 is a pre-power term and s is a frequency exponent which takes values between 0 and 1.

The fits of $\varepsilon'(\omega)$ and $\varepsilon''(\omega)$, based on Eq. (1), are presented with solid lines on Figs. 4(a) and 4(b) and the values of fit parameters for Bi_{1-x}Ho_xFeO₃ samples are summarized in Table 2. The values of σ_{DC} and σ_0 for Bi_{1-x}Ho_xFeO₃ samples, based on the fitting results, are presented in Fig. 4(d). BFO sample has relatively high σ_{DC} value of $6.1 \cdot 10^{-9} \Omega^{-1} \text{ cm}^{-1}$, whereas the value of σ_0 is an order of magnitude lower. These values are comparable with reported data [15,33,36]. It can be concluded that the permittivity of BFO sample is dominated by the leakage current contribution, whereas the ac dependent mechanisms are less prominent. Among the Ho-doped samples with R3c

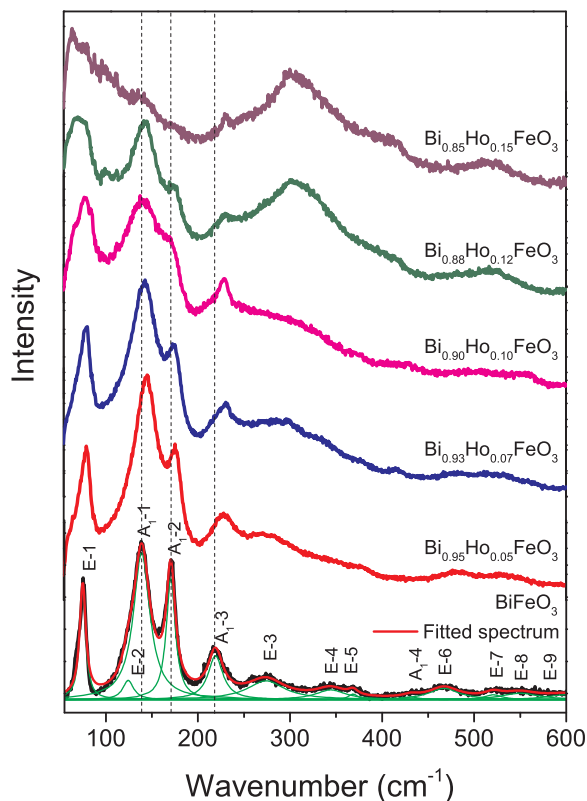


Fig. 3. Room-temperature Raman spectra of the $\text{Bi}_{1-x}\text{Ho}_x\text{FeO}_3$ ($0 \leq x \leq 0.15$) samples together with the deconvoluted Raman spectrum of pristine BiFeO_3 .

structure, the highest dc and ac conductivity exhibits the BHFO5 sample, meaning that leakage current and grain boundary or interface effects can be a cause of permittivity dispersion and its higher value at lower frequencies. This finding offers an explanation for the colossal dielectric constant of Ho doped samples found by Song et al. [20]. The σ_{DC} and σ_0 values of BHFO7 sample are much lower than in BFO and BHFO5 samples. Despite the fact that the amount of secondary phase in BHFO7 is almost the same as in pristine BFO and having in mind that BHFO5 sample is phase pure, it seems that BHFO5 and BFO samples are more conductive than BHFO7 sample. This fact can explain the flat frequency dependence of $\epsilon'(\omega)$ and $\epsilon''(\omega)$ (Figs. 4(a) and (b)) of BHFO7 sample and imply that the presence of secondary phase has no great influence on the BFO conductivity, but defects in the form of oxygen vacancies and grain boundary or interface effects play a major role in the conductivity of BHFO5 and BFO samples. A significant increase of σ_{DC} value, which is almost twice as large as in pristine BFO and BHFO5 samples, was found in a case of BHFO10. Although it is expected that increased Ho doping reduces the leakage current due to the suppressed concentration of oxygen and bismuth vacancies, this sample seems to be more leaky than the pristine BFO. The σ_{DC} value, higher than in all the other samples, and pronounced dispersion of $\epsilon''(\omega)$ implies that the leakage current affects the dielectric properties of BHFO10 to a great extent.

The changes in dielectric properties of BHFO10 sample can be related to the appearance of orthorhombic phase, because the dielectric properties are dependent on the sample structure and therefore can be modified near the phase transformation boundary [3]. The dc and ac conductivities were significantly reduced in BHFO12 sample, whereas BHFO15 sample, for which orthorhombic phase prevails, had an order of magnitude lower dc conductivity ($5.7 \cdot 10^{-10} \Omega^{-1} \text{cm}^{-1}$) than the BFO ($6.1 \cdot 10^{-9} \Omega^{-1} \text{cm}^{-1}$). Therefore, we argue that higher Ho content reduces the leakage current, and weakens the ac conductivity contribution to the dielectric response. The frequency dependence of dielectric loss ($\tan \delta$) of $\text{Bi}_{1-x}\text{Ho}_x\text{FeO}_3$ samples is presented in Fig. 4(c).

The dielectric loss follows a trend similar to the permittivity in the frequency range of 100 Hz to 8 MHz, i.e. it decreases with increasing frequency. The BFO, BHFO5 and BHFO10 samples have higher $\tan \delta$ value than other Ho-doped samples with pronounced dispersion at lower frequencies. There is an indication of dielectric relaxation peak in conductive BFO and BHFO10 samples at frequency of 5 kHz, which can be ascribed to the carrier hopping process between Fe^{2+} and Fe^{3+} ions inside the particles [37] or to the hopping along the $\text{Fe}^{2+} \cdot \text{V}_O \cdot \text{Fe}^{3+}$ chain [38]. This peak is slightly shifted to lower frequency in BHFO5 sample. This low frequency relaxation can be attributed to the grain boundary conduction [39]. Reduced $\tan \delta$ values and the absence of relaxation peaks in BHFO7, BHFO12 and BHFO15 samples point at an increased resistivity of these samples.

Polarization-electric field (P-E) hysteresis loops of $\text{Bi}_{1-x}\text{Ho}_x\text{FeO}_3$ samples, measured at frequency of 100 Hz, are presented in Fig. 5(a). The BFO sample has an unsaturated P-E loop due to non negligible contribution of leakage current ($\sigma_{DC} = 6.1 \cdot 10^{-9} \Omega^{-1} \text{cm}^{-1}$). The maximal polarization, remnant polarization (P_r), and coercive field (E_c) reached the highest values in BFO sample and decreased with Ho-doping. The BHFO5 sample has a pinched P-E loop, characteristic for leaky materials. The permittivity analysis has shown that BHFO5 is less resistive than BFO and that grain boundary effects and leakage current dominate its dielectric properties. Therefore, the degraded ferroelectric properties can be attributed to the presence of oxygen vacancies and valence fluctuations of Fe ions (between Fe^{3+} and Fe^{2+}), because the appearance of oxygen vacancies and Fe^{2+} ions, especially at grain boundaries, is unfavorable for the polarization switching. The study of dielectric properties has shown that BHFO7 is more resistive than BFO and BHFO5. This fact explains slightly improved P-E loop compared to BHFO5 sample, but still lower P_r and E_c values than in BFO can originate from a decrease in stereochemical activity of Bi lone electron pair with increase of Ho content. P-E loops of the BHFO10, BHFO12 and BHFO15 samples are very similar to the P-E loops of BHFO5 sample. The degraded ferroelectricity of BHFO10 mainly originates from the contribution of dc conductivity (σ_{DC}) which is the highest among all analysed samples (see Fig. 4(d) and Table 2). Although BHFO12 and BHFO15 samples are more resistive than BFO and all the other Ho-doped samples, their ferroelectric properties are degraded because of the possible appearance of paraelectric phase regions in highly Ho doped BFO. This is supported by the changes noticed in the Raman spectra of these samples. Near the ferroelectric-paraelectric phase transition, the intensities of the Raman modes characteristic for Bi-O bonds [28] were reduced in BHFO12 sample and have almost disappeared in BHFO15 sample.

Furthermore, the presence of orthorhombic phase increases the breakdown field strength of $\text{Bi}_{1-x}\text{Ho}_x\text{FeO}_3$ samples (inset of Fig. 5(a)). The breakdown in BFO and $\text{Bi}_{1-x}\text{Ho}_x\text{FeO}_3$ samples with rhombohedral structure ($x < 0.1$) happens at the applied electric fields of around 20 kV/cm. The BHFO10 and BHFO12 samples, in which rhombohedral and orthorhombic phase coexist, withstand applied fields that are approximately twice as high. The BHFO15 sample in which orthorhombic phase prevails, withstands even higher electric fields (> 50 kV/cm) without breakdown (marked with arrow on the inset). The reason can be found in reduced dc conductivity of BHFO15 and in increasing number of Ho-O bonds with large bond energy, almost two times larger than the Bi-O bond [15]. Knowing that BHFO15 sample withstands high external fields without breakdown, the P-E loops of BHFO15 sample were measured at different testing frequencies from 2 Hz to 100 Hz under the applied field of 50 kV/cm, as shown in Fig. 5(b). It is obvious that P-E loops exhibit frequency-dependent behavior by showing rapid increase of P_r , E_c and maximal polarization at lower frequencies. Frequency dependence of the $2P_r$ for BHFO15 sample is presented in the top-left inset of Fig. 5(b), from which it is clear that $2P_r$ has the highest value of $0.21 \mu\text{C}/\text{cm}^2$ at 2 Hz and rapidly decreases to $0.07 \mu\text{C}/\text{cm}^2$ at 20 Hz. The P-E loops of BHFO15 measured in a high amplitude electric field of 100 kV/cm and at low frequencies of 1 Hz

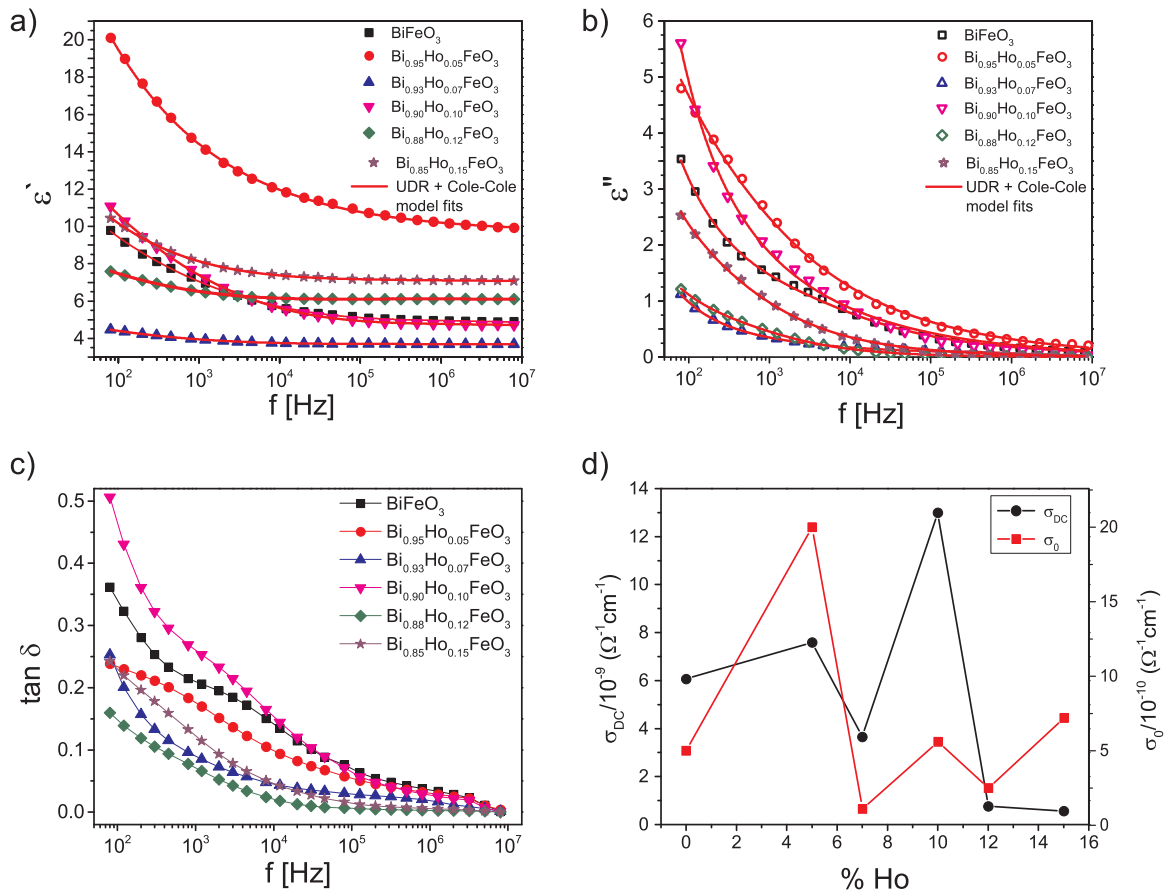


Fig. 4. Room-temperature (a) real (ϵ') and (b) imaginary (ϵ'') part of the complex permittivity. Full lines present the corresponding fits applying the combined model (Eq. 1), (c) loss tangent ($\tan \delta$) and (d) the dependence of σ_{DC} and σ_0 values on Ho content for $\text{Bi}_{1-x}\text{Ho}_x\text{FeO}_3$ samples.

and 2 Hz are presented in the right-bottom inset of Fig. 5(b). The $2P_r$ value is larger by a factor of two than the one obtained at the same frequency in the field of 50 kV/cm. Such a behavior can be explained by the effect of external field on the reorientation of defect dipoles and their role in domain wall switching in BFO. The presence of mobile, single defects (like V_{Bi}'' , V_{O}^* or V_{Fe}'') or defect complexes (oxygen vacancy associated dipoles) in BFO plays an important role in the domain wall pinning. It leads to the deterioration of polarization-switching properties by suppression of intrinsic polarization and increase of leakage current. The ferroelectric domain depinning can be achieved by applying high electric field or can be favoured at elevated temperatures and a secondary re-oxidation annealing [40–43]. On the other hand, in high electric fields the defect complexes can orient along the direction of spontaneous polarization and follow the domain switching, enhancing polarization properties of BFO [42–45]. Inherent defect dipoles are expected not to switch during fast field cycling, since their reorientation takes more time than the domain switching process. Therefore, the influence of defect dipole polarization on the overall polarization can be seen in high fields at low frequencies, as defect complexes can keep up with reversal of the field and contribute to the bulk ferroelectric

polarization [40,44]. It is plausible to suppose that inherent defect complexes like $V_{\text{Bi}}'' - V_{\text{O}}^*$, $Fe_{\text{Fe}^{2+}}' - V_{\text{O}}^*$ or $Fe_{\text{Fe}^{2+}}' - V_{\text{O}}^*$ form during the crystallization process in $\text{Bi}_{1-x}\text{Ho}_x\text{FeO}_3$ samples. Among all $\text{Bi}_{1-x}\text{Ho}_x\text{FeO}_3$ samples, only BHFO15 sample has supported high external field of 50 kV/cm which can induce defect dipole reorientation. By applying strong external field at low frequencies, defect dipoles can orient along the direction of spontaneous polarization following the domain switching. With increasing of the field strength to 100 kV/cm and by lowering the frequency to 1 Hz, the effect of defect dipolar polarization was more pronounced. Therefore, the reorientation of internal defect complexes under high external field gives rise to the enhancement of intrinsic polarization of BHFO15 sample.

4. Conclusions

In summary, the phase transformation from rhombohedral to orthorhombic phase induced by increased Ho substitution, affected to a great extent the dielectric and ferroelectric properties of $\text{Bi}_{1-x}\text{Ho}_x\text{FeO}_3$ nanopowders. The frequency dependent permittivity was analysed using combined model which incorporated Debye-like dielectric

Table 2
The fitting parameters for $\text{Bi}_{1-x}\text{Ho}_x\text{FeO}_3$ samples obtained from combined model.

Parameter	BFO	BHFO5	BHFO7	BHFO10	BHFO12	BHFO15
α	0.55	0.69	0.65	0.69	0.60	0.67
τ (s)	$5.3 \cdot 10^{-6}$	$2.2 \cdot 10^{-6}$	$5.2 \cdot 10^{-5}$	$1.2 \cdot 10^{-5}$	$5.6 \cdot 10^{-5}$	$3.2 \cdot 10^{-5}$
s	0.79	0.66	0.80	0.85	0.78	0.75
σ_0 ($\Omega^{-1} \text{cm}^{-1}$)	$5.0 \cdot 10^{-10}$	$1.8 \cdot 10^{-9}$	$1.1 \cdot 10^{-10}$	$5.6 \cdot 10^{-10}$	$2.5 \cdot 10^{-10}$	$7.2 \cdot 10^{-10}$
σ_{DC} ($\Omega^{-1} \text{cm}^{-1}$)	$6.1 \cdot 10^{-9}$	$7.6 \cdot 10^{-9}$	$3.6 \cdot 10^{-9}$	$1.3 \cdot 10^{-8}$	$7.7 \cdot 10^{-10}$	$5.7 \cdot 10^{-10}$

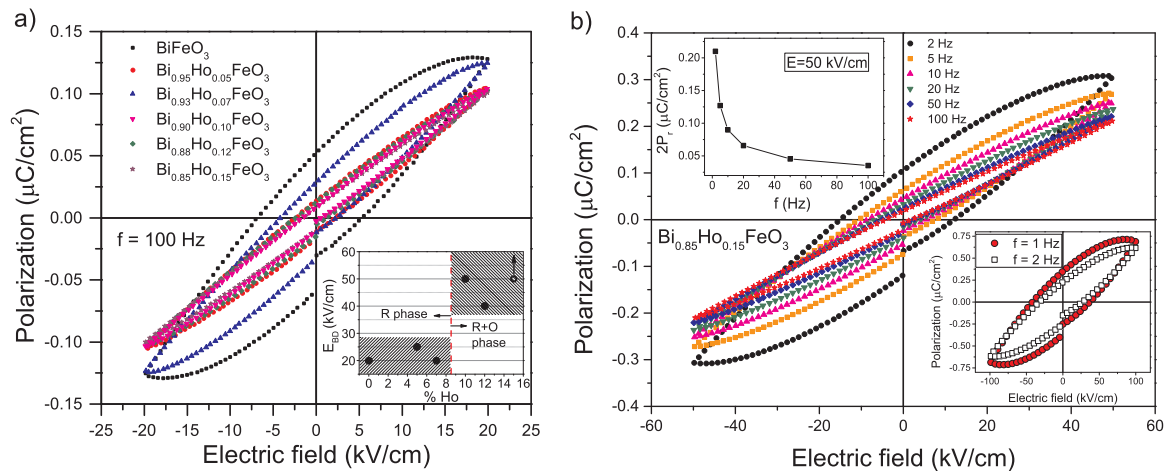


Fig. 5. a) Room-temperature P-E loops of $\text{Bi}_{1-x}\text{Ho}_x\text{FeO}_3$ samples. Inset presents breakdown fields for all samples except for BHFO15. b) P-E loops of BHFO15 sample taken at different frequencies. The frequency dependence of $2P_r$ is shown in the top-left corner inset, and the P-E loops in the field of large amplitude at low frequencies are shown in the bottom-right corner inset.

response and dc and ac conductivity contributions. It was shown that not only dc conductivity, but also grain boundary and interfacial effects were much reduced in biphasic $\text{Bi}_{1-x}\text{Ho}_x\text{FeO}_3$ ($x > 0.1$) samples. The dominant presence of orthorhombic phase in $\text{Bi}_{0.85}\text{Ho}_{0.15}\text{FeO}_3$ sample has stabilized the perovskite structure of BFO, significantly increased the breakdown field and improved BFO electrical performances. In high external electric fields (50 kV/cm and 100 kV/cm), P-E loops of $\text{Bi}_{0.85}\text{Ho}_{0.15}\text{FeO}_3$ sample manifested strong frequency dependence and abrupt increase of remnant polarization and coercive field at low frequencies. It was proposed that defect dipoles were oriented along the direction of spontaneous polarization, following the domain switching, and were therefore a primary cause of the enhanced polarization properties of $\text{Bi}_{0.85}\text{Ho}_{0.15}\text{FeO}_3$ sample. Although it is well established opinion that appearance of orthorhombic paraelectric phase degrades ferroelectricity of BFO, our study contributes to better understanding of polarization mechanisms in biphasic bismuth ferrite.

Acknowledgments

This work was financially supported by the Ministry of Education, Science and Technological Development of the Republic of Serbia under the projects ON171032 and III45018.

References

- G. Catalan, J.F. Scott, Physics and applications of bismuth ferrite, *Adv. Mater.* 21 (2009) 2463–2485.
- R. Ramesh, N.A. Spaldin, Multiferroics: progress and prospects in thin films, *Nat. Mater.* 6 (2007) 21–29.
- S.K. Pradhan, B.K. Roul, Effect of Gd doping on structural, electrical and magnetic properties of BiFeO_3 electroceramic, *J. Phys. Chem. Solids* 72 (2011) 1180–1187.
- G.L. Yuan, Siu Wing Or, J.M. Liu, Z.G. Liu, Structural transformation and ferroelectromagnetic behavior in single-phase $\text{Bi}_{1-x}\text{Nd}_x\text{FeO}_3$ multiferroic ceramics, *Appl. Phys. Lett.* 89 (2006) 052905.
- G.L. Yuan, S.W. Or, H.L.W. Chan, Reduced ferroelectric coercivity in multiferroic $\text{Bi}_{0.825}\text{Nd}_{0.175}\text{FeO}_3$ thin film, *J. Appl. Phys.* 101 (2007) 024106.
- J. Liu, M. Li, L. Pei, J. Wang, B. Yu, X. Wang, X. Zhao, Structural and multiferroic properties of the Ce-doped BiFeO_3 thin films, *J. Alloy. Compd.* 493 (2010) 544–548.
- K.S. Nalwa, A. Gart, A. Upadhyaya, Effect of samarium doping on the properties of solid-state synthesized multiferroic bismuth ferrite, *Mater. Lett.* 62 (2008) 878–881.
- W. Sun, J.F. Li, Q. Yu, L.Q. Cheng, Phase transition and piezoelectricity of sol-gel-processed Sm-doped BiFeO_3 thin films on Pt(111)/Ti/SiO₂/Si substrates, *J. Mater. Chem. C* 3 (2015) 2115–2122.
- D. Varshney, P. Sharma, S. Satapathy, P.K. Gupta, Structural, magnetic and dielectric properties of Pr-modified BiFeO_3 multiferroic, *J. Alloy. Compd.* 584 (2014) 232–239.
- Y. Wang, C.W. Nan, Effect of Tb doping on electric and magnetic behavior of BiFeO_3 thin films, *J. Appl. Phys.* 103 (2008) 024103.
- S. Chaturvedi, R. Bag, V. Sathe, S. Kulkarni, S. Singh, Holmium induced enhanced functionality at room temperature and structural phase transition at high temperature in bismuth ferrite nanoparticles, *J. Mater. Chem. C* 4 (2016) 780–792.
- P. Suresh, P.D. Babu, S. Srinath, Effect of Ho substitution on structure and magnetic properties of BiFeO_3 , *J. Appl. Phys.* 115 (2014) 17D905.
- S.K. Pradhan, B.K. Roul, D.R. Sahu, Enhancement of ferromagnetism and multiferroicity in Ho doped Fe rich BiFeO_3 , *Solid State Commun.* 152 (2012) 1176–1180.
- S.K. Pradhan, J. Das, P.P. Rout, V.R. Mohanta, S.K. Das, S. Samantray, D.R. Sahu, J.L. Huang, S. Verma, B.K. Roul, Effect of holmium substitution for the improvement of multiferroic properties of BiFeO_3 , *J. Phys. Chem. Solids* 71 (2010) 1557–1564.
- N. Jeon, D. Rout, W. Kim, S.-J.L. Kang, Enhanced multiferroic properties of single-phase BiFeO_3 bulk ceramics by Ho doping, *Appl. Phys. Lett.* 98 (2011) 072901.
- H. Singh, K.L. Yadav, Enhanced magnetization with unusual low temperature magnetic ordering behaviour and spin reorientation in holmium-modified multiferroic BiFeO_3 perovskite ceramics, *J. Phys. D: Appl. Phys.* 48 (2015) 205001.
- Y. Wu, J. Zhang, X.-K. Chen, X.-J. Chen, Phase evolution and magnetic property of $\text{Bi}_{1-x}\text{Ho}_x\text{FeO}_3$ powders, *Solid State Commun.* 151 (2011) 1936–1940.
- Z.L. Hou, H.F. Zhou, L.B. Kong, H.B. Jin, X. Qi, M.S. Cao, Enhanced ferromagnetism and microwave absorption properties of BiFeO_3 nanocrystals with Ho substitution, *Mater. Lett.* 84 (2012) 110–113.
- Y.Q. Liu, Y.J. Wang, J. Zhang, M. Gao, Y.J. Zhang, M.B. Wei, J.H. Yang, Effect of Ho substitution on structure and magnetic property of BiFeO_3 prepared by sol-gel method, *Mater. Sci. Semicond. Proc.* 40 (2015) 787–795.
- G.L. Song, G.J. Ma, J. Su, T.X. Wang, H.Y. Yang, F.G. Chang, Effect of Ho³⁺ doping on the electric, dielectric, ferromagnetic properties and TC of BiFeO_3 ceramics, *Ceram. Int.* 40 (2014) 3579–3587.
- W. Kraus, G. Nolze, POWDER CELL – a program for the representation and manipulation of crystal structures and calculation of the resulting X-ray powder patterns, *J. Appl. Cryst.* 29 (1996) 301.
- L. Chen, L. Zheng, Y. He, J. Zhang, Z. Mao, X. Chen, The local distortion and electronic behavior in Mn doped BiFeO_3 , *J. Alloy. Compd.* 633 (2015) 216–219.
- V. Singh, S. Sharma, M. Kumar, R.K. Kotnala, R.K. Dwivedi, Structural transition, magnetic and optical properties of Pr and Ti co-doped BiFeO_3 ceramics, *J. Magn. Mater.* 349 (2014) 264–267.
- P.C. Sati, M. Arora, S. Chauhan, M. Kumar, S. Chhoker, Structural, magnetic, vibrational and impedance properties of Pr and Ti codoped BiFeO_3 multiferroic ceramics, *Ceram. Int.* 40 (2014) 7805–7816.
- B. Stojadinović, Z. Dohčević-Mitrović, N. Paunović, N. Ilić, N. Tasić, I. Petronijević, D. Popović, B. Stojanović, Comparative study of structural and electrical properties of Pr and Ce doped BiFeO_3 ceramics synthesized by auto-combustion method, *J. Alloy. Compd.* 657 (2016) 866–872.
- V.A. Khomchenko, D.V. Karpinsky, A.L. Kholkin, N.A. Sobolev, G.N. Kazakei, J.P. Araujo, I.O. Troyanchuk, B.F.O. Costa, J.A. Paixão, Rhombohedral-to-orthorhombic transition and multiferroic properties of Dy-substituted BiFeO_3 , *J. Appl. Phys.* 108 (2010) 074109.
- P.C. Sati, M. Kumar, S. Chhoker, M. Jewariya, Influence of Eu substitution on structural, magnetic, optical and dielectric properties of BiFeO_3 multiferroic ceramics, *Ceram. Int.* 41 (2015) 2389–2398.
- P. Pandit, S. Satapathy, P. Sharma, P.K. Gupta, S.M. Yusuf, V.G. Sathe, Structural, dielectric and multiferroic properties of Er and La substituted BiFeO_3 ceramics, *B. Mater. Sci.* 34 (2011) 899–905.
- I. Levin, M.G. Tucker, H. Wu, V. Provenzano, C.L. Dennis, S. Karimi, T. Comyn, T. Stevenson, R.I. Smith, I.M., Reaney displacive phase transitions and magnetic structures in Nd-substituted BiFeO_3 , *Chem. Mater.* 23 (2011) 2166–2175.
- X. Xue, G. Tan, W. Liu, H. Ren, Comparative study on multiferroic ($\text{Bi}_{0.9}\text{RE}_{0.1}$) ($\text{Fe}_{0.97}\text{Co}_{0.03}$) $\text{O}_{3-\delta}$ (RE = Ce and Ho) thin films: structural, electrical and optical properties, *Ceram. Int.* 40 (2014) 6247–6254.
- P. Hermet, M. Goffinet, J. Kreisel, P. Ghosez, Raman and infrared spectra of multiferroic bismuth ferrite from first principles, *Phys. Rev. B* 75 (2007) 220102.
- M. Iliev, M. Abrashev, H.G. Lee, V. Popov, Y. Sun, C. Thomsen, R. Meng, C. Chu,

- Raman spectroscopy of orthorhombic perovskitelike YMnO_3 and LaMnO_3 , Phys. Rev. B 57 (1998) 2872–2877.
- [33] Y.W. Li, Z.G. Hu, F.Y. Yue, P.X. Yang, Y.N. Qian, W.J. Cheng, X.M. Ma, J.H. Chu, Oxygen-vacancy-related dielectric relaxation in BiFeO_3 films grown by pulsed laser deposition, J. Phys. D: Appl. Phys. 41 (2008) 215403.
- [34] P. Lunkenheimer, V. Bobnar, A.V. Pronin, A.I. Ritus, A.A. Volkov, A. Loidl, Origin of apparent colossal dielectric constants, Phys. Rev. B 66 (2002) 052105.
- [35] A.K. Jonscher, The universal dielectric response, Nature 267 (1977) 673–679.
- [36] Q. Yun, Y. Bai, J. Chen, W. Gao, A. Bai, S. Zhao, Improved ferroelectric and fatigue properties in Ho doped BiFeO_3 thin films, Mater. Lett. 129 (2014) 166–169.
- [37] E. Markiewicz, B. Hilczner, M. Blaszyk, A. Pietraszko, E. Talik, Dielectric properties of BiFeO_3 ceramics obtained from mechanochemically synthesized nanopowders, J. Electroceram. 27 (2011) 154–161.
- [38] Q. Ke, X. Lou, Y. Wang, J. Wang, Oxygen-vacancy-related relaxation and scaling behaviors of $\text{Bi}_{0.9}\text{La}_{0.1}\text{Fe}_{0.98}\text{Mg}_{0.02}\text{O}_3$ ferroelectric thin films, Phys. Rev. B 82 (2010) 024102.
- [39] S. Mukherjee, R. Gupta, A. Garg, V. Bansal, S. Bhargava, Influence of Zr doping on the structure and ferroelectric properties of BiFeO_3 thin films, J. Appl. Phys. 107 (2010) 123535.
- [40] B. Li, G. Li, Q. Yin, Z. Zhu, A. Ding, W. Cao, Pinning and depinning mechanism of defect dipoles in PMnNPZT ceramics, J. Phys. D: Appl. Phys. 38 (2005) 1107–1111.
- [41] I. Bretos, R. Jiménez, C. Gutiérrez-Lázaro, I. Montero, L. Calzada, Defect-mediated ferroelectric domain depinning of polycrystalline BiFeO_3 multiferroic thin films, Appl. Phys. A 104 (2014) 092905.
- [42] D. Guo, C. Wang, Q. Shen, L. Zhang, M. Li, J. Liu, Effect of measuring factors on ferroelectric properties of $\text{Bi}_{3.15}\text{Nd}_{0.85}\text{Ti}_3\text{O}_{12}$ thin films prepared by sol-gel method for non-volatile memory, Appl. Phys. A 97 (2009) 877–881.
- [43] J. Lv, X. Lou, J. Wu, Defect dipole-induced poling characteristics and ferroelectricity of quenched bismuth ferrite-based ceramics, J. Mater. Chem. C 4 (2016) 6140–6151.
- [44] L. Zhang, E. Erdem, X. Ren, R.-A. Eichel, Reorientation of $(Mn_{Ti}^{2+}V_O^{\bullet})X$ defect dipoles in acceptor-modified BaTiO_3 single crystals: an electron paramagnetic resonance study, Appl. Phys. Lett. 93 (2008) 202901.
- [45] Y. Chirshima, Y. Noguchi, Y. Kitanaka, M. Miyayama, Defect control for polarization switching in BiFeO_3 single crystals, IEEE Trans. Ultrason. Ferroelectr. Freq. Control 57 (2010) 2233–2236.

Coherent manipulation of single electron spins with Landau-Zener sweeps

Marko J. Rančić*

Department of Physics, University of Konstanz, D-78457 Konstanz, Germany

Dimitrije Stepanenko†

Institute of Physics Belgrade, University of Belgrade, Pregrevica 118, 11080 Belgrade, Serbia

(Received 23 August 2016; revised manuscript received 3 November 2016; published 12 December 2016)

We propose a method to manipulate the state of a single electron spin in a semiconductor quantum dot (QD). The manipulation is achieved by tunnel coupling a QD, labeled L , and occupied with an electron to an adjacent QD, labeled R , which is not occupied by an electron but having an energy linearly varying in time. We identify a parameter regime in which a complete population transfer between the spin eigenstates $|L\uparrow\rangle$ and $|L\downarrow\rangle$ is achieved without occupying the adjacent QD. This method is convenient due to the fact that manipulation can be done electrically, without precise knowledge of the spin resonance condition, and is robust against Zeeman level broadening caused by nuclear spins.

DOI: [10.1103/PhysRevB.94.241301](https://doi.org/10.1103/PhysRevB.94.241301)

Introduction. The initialization, manipulation, and readout of single electron spins in an efficient way are necessary for the implementation of single electron spin qubits [1]. Spin-orbit interactions and stray magnetic fields of micromagnets provide a necessary toolkit to control the single electron spin [2–7]. In electric dipole spin resonance (EDSR), microwaves drive an electron to oscillate in the spin-orbit field and/or the magnetic field gradient, producing a coherent spin rotation.

The Landau-Zener-Stückelberg-Majorana (LZSM) model [8–11] is one of the few analytically solvable time-dependent problems in quantum mechanics. It has found applications modeling nanoelectromechanical systems [12], optomechanical systems [13], Bose liquids [14], molecular magnets [15], Rydberg atoms [16], superconducting qubits [12, 17–20], and semiconductor singlet-triplet qubits [21–23]. In the LZSM model the energy difference between two coupled states is varied linearly in time, while the coupling between the states is time independent. This results in a transition between the states with the probability determined by the coupling constant and the rate of the sweep.

Unlike the two-level LZSM problem, multilevel LZSM problems are not exactly analytically solvable for a general case [24–30]. Chirped Raman adiabatic passage (CHIRAP) [31, 32, 32–34] and similar techniques [35–41] allow for the efficient transfer of populations between two uncoupled levels. In order to utilize CHIRAP, the energy of the radiatively decaying state is varied linearly in time with laser pulses having chirped frequencies.

Equivalently to CHIRAP, the goal of our scheme is to transfer the population between two uncoupled levels $|L\uparrow\rangle$ and $|L\downarrow\rangle$ by coupling the levels of the L electrostatically defined quantum dot (QD) in a time-independent manner to an adjacent electrostatically defined quantum dot, whose energy is linearly varying in time [42]. It should be noted that, as the probability to occupy the adjacent quantum dot R remains negligible in this scheme, the states in the R QD can be extremely

susceptible to relaxation without influencing the efficiency of our scheme. The scheme under study is also applicable to coupled donors [43] and coupled donor-dot systems [44].

We discuss two possible realizations of our scheme. In the first realization the R quantum dot has significantly larger Zeeman splitting than the L quantum dot. Then, the scheme operates even in the case when the rate of non-spin-conserving tunneling events is significantly smaller than the rate of spin-conserving events. This regime is often present in GaAs double quantum dots. In the second realization the Zeeman splittings of the left L and right R quantum dots are comparable in magnitude but the rates of spin-conserving and non-spin-conserving tunneling events must be comparable. This regime can be reached for electrons in InAs double quantum dots and holes in GaAs double quantum dots.

The Hamiltonian. We model a situation where the electron spin is localized in the L quantum dot. The energy of the R quantum dot is varied linearly in time (Fig. 1),

$$H(t) = \sum_c \sum_\sigma E_{c,\sigma}(t) |c\sigma\rangle \langle c\sigma| + \tau \sum_\sigma \sum_{c \neq \bar{c}} |c\sigma\rangle \langle \bar{c}\sigma| + \tau_\Delta \sum_{\sigma \neq \bar{\sigma}} \sum_{c \neq \bar{c}} |c\sigma\rangle \langle \bar{c}\bar{\sigma}|. \quad (1)$$

The sum over the charge states runs over the left and the right quantum dots, $c = L, R$, and the sum over spin states runs over spin-up and spin-down states $\sigma = \uparrow, \downarrow$. Furthermore, $E_{c\sigma}$ represents the energy with charge state c and spin state σ . The energies of the L quantum dot are time independent, $E_{L\uparrow} = \Delta E_L/2$, $E_{L\downarrow} = -\Delta E_L/2$, where ΔE_L is the Zeeman splitting in the left quantum dot. The energies of the R quantum dot are time dependent with a linear time dependence, $E_{R\uparrow} = \Delta E_R + \beta t$, and $E_{R\downarrow} = \beta t$, where ΔE_R is the Zeeman splitting in the right quantum dot, t is time, and β the Landau-Zener velocity (see Fig. 1).

The off-diagonal terms in the Hamiltonian are the spin-conserving tunneling amplitude τ , and the non-spin-conserving tunneling amplitude τ_Δ . The non-spin-conserving tunneling can appear due to spin-orbit interaction or be induced by the stray field of the micromagnet, which is inhomogeneous in the tunneling direction [45, 46].

*marko.rancic@uni-konstanz.de

†dimitrije.stepanenko@ipb.ac.rs

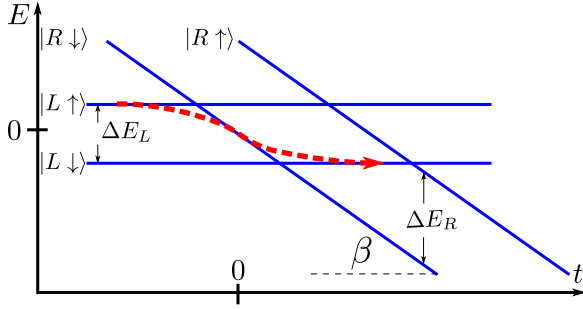


FIG. 1. The energy diagram. We initialize the electron in the $|L\uparrow\rangle$ state, with the R quantum dot being higher in energy. We ramp the energies of the states in R quantum dot with a Landau-Zener velocity β . In the figure, $\beta < 0$. The goal of our scheme is to find a parameter regime in which the adiabatic evolution path is followed (red dashed arrow). The Zeeman splittings of the L and R quantum dots are marked as ΔE_L and ΔE_R , respectively.

Different Zeeman splittings. We initialize the system in the $|L\uparrow\rangle$ state, at a negative instance of time $-T/2$. If the product of the Landau-Zener velocity β and the total duration of the Landau-Zener sweep T is smaller than the Zeeman splitting of the right quantum dot $\Delta E_R > \beta T$, and if the R quantum dot is initially positively detuned with respect to the L quantum dot, our system behaves as an effective three-level system. Furthermore, if the evolution of the system is adiabatic ($\tau^2, \tau_\Delta^2 \gg \beta\hbar$), the system will remain in the instantaneous eigenstate of the Hamiltonian for the entire duration of the Landau-Zener sweep T . Given all these assumptions, we can calculate the adiabatic eigenvectors, and therefore the time evolution of our three state probabilities,

$$P_{L\uparrow} = \tau_\Delta^2 \frac{|\lambda(t) + \Delta E_L/2|^2}{N(t)^2}, \quad P_{L\downarrow} = \tau_\Delta^2 \frac{|\lambda(t) - \Delta E_L/2|^2}{N(t)^2},$$

$$P_{R\downarrow} = \frac{|\lambda(t)^2 - \Delta E_L^2/4|^2}{N(t)^2}, \quad (2)$$

where $\lambda(t)$ is the appropriate adiabatic eigenvalue [see the Supplemental Material [47] for the expression for $\lambda(t)$] and $N(t)$ is the normalization of the adiabatic eigenvectors. For simplicity, we have omitted to explicitly state that $\lambda(t)$ is also a function of ΔE_L , β , τ , τ_Δ . Depending on the values of τ and τ_Δ , $\lambda(t) = 0$ close to $t = 0$ (for $\tau = \tau_\Delta$), $\lambda(t) = 0$ at $t > 0$ (for $\tau > \tau_\Delta$), and $\lambda(t) = 0$ at $t < 0$ (for $\tau < \tau_\Delta$). Furthermore, the adiabatic eigenvalue takes the following values, $\lambda(t = \mp\infty) = \pm\Delta E_L/2$, $-\Delta E_L/2 \leq \lambda(t) \leq \Delta E_L/2$, for every t . Therefore, the maximal possible occupation probabilities are $P_{L\uparrow}^{\max} \sim \tau_\Delta^2 \Delta E_L^2$, $P_{R\downarrow}^{\max} \sim \Delta E_L^4$, $P_{L\downarrow}^{\max} \sim \tau^2 \Delta E_L^2$. If $\tau, \tau_\Delta \gg \Delta E_L$, no significant population will occupy the R quantum dot, $P_R \approx 0$ at every instance of time (see Fig. 2), and a complete population transfer between the spin eigenstates $|L\uparrow\rangle$ and $|L\downarrow\rangle$ occurs.

In contrast to EDSR techniques, our scheme does not require precise knowledge of the spin resonance condition ΔE_L and operates without microwaves. However, in order for our scheme to be successful, a necessary requirement is that the quantum dots have significantly different Zeeman splittings $\Delta E_L \ll \Delta E_R$. For a typical double quantum dot system

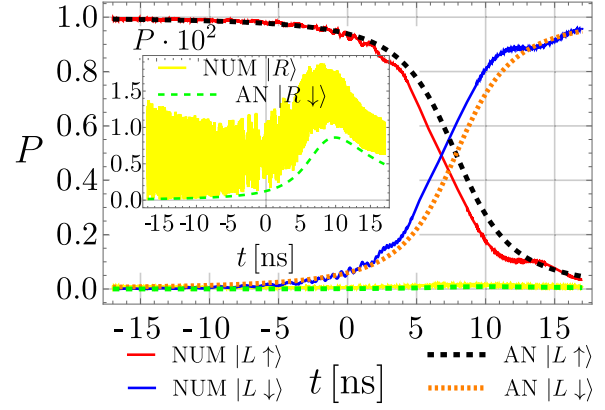


FIG. 2. The comparison between the numerically computed probabilities [obtained from evolving the state using the Hamiltonian of Eq. (1)] (Num) and analytic adiabatic three-level probabilities Eq. (2) (An). The parameters of the plot are the Landau-Zener velocity $\beta = 5 \times 10^3$ eV/s, the tunnel coupling $\tau = 6.5$ μ eV, corresponding to an interdot separation of $l = 179$ nm (for more information, see the Supplemental Material [47]), the non-spin-conserving tunnel coupling $\tau_\Delta = 0.25\tau$, the external magnetic field Zeeman splitting in the left QD $\Delta E_L = 1$ μ eV, and Zeeman splitting in the right quantum dot $\Delta E_R = 200\Delta E_L$. The inset represents the magnification of the occupation probabilities of the states in the R quantum dot.

where the distance between the quantum dots is ~ 200 nm, the required gradient would be $dB_z/dx \sim 10$ T/ μ m, which is for a factor of 10 larger than the currently maximally achieved experimental value [6,48]. A possible way to induce a large enough difference of Zeeman energies between quantum dots is to engineer the g factor of one of the quantum dots L to be almost zero, and engineer the g factor of the R QD to be significantly larger [49–52]. This could be achieved by locally inducing different content of Al in the GaAs mixture [50].

Equal Zeeman splittings. Again we initialize the system in the $|L\uparrow\rangle$ state, at a negative instance of time $-T/2$. Another way for our scheme to be successful is that the magnitude of spin-conserving and non-spin-conserving tunnelings are comparable, $\tau \approx \tau_\Delta$. The requirement for our scheme to work is $\tau/\tau_\Delta \sim 4l/3\Lambda_{SO} \approx 1$ can be fulfilled in InAs [53]. Here, l is the interdot separation and Λ_{SO} is the spin-orbit length, defined by [54,55] $\Lambda_{SO} = \hbar/m^* \sqrt{\cos^2\phi(\beta - \alpha)^2 + \sin^2\phi(\beta + \alpha)^2}$, for a two-dimensional electron gas (2DEG) in the (001) plane. Here, m^* is the effective electron mass, ϕ is the angle between the [110] crystallographic axis and the interdot connection axis, and β and α are Dresselhaus and Rashba spin-orbit constants, respectively. Possible ways of controlling the spin-orbit interaction is the variation of angle between the external magnetic field and the spin-orbit field [56], variation of the direction in which the double quantum dot (DQD) is grown [57] (and therefore maximizing $\cos\phi$), isotopic control of indium in InGaAs, or electric field control of the Rashba constant [58,59].

In the adiabatic limit ($\tau^2 = \tau_\Delta^2 \gg \beta\hbar$), the system will remain in the instantaneous eigenstate of the Hamiltonian for the entire duration of the Landau-Zener sweep T . In that limit, we can calculate the adiabatic eigenvectors, and therefore the

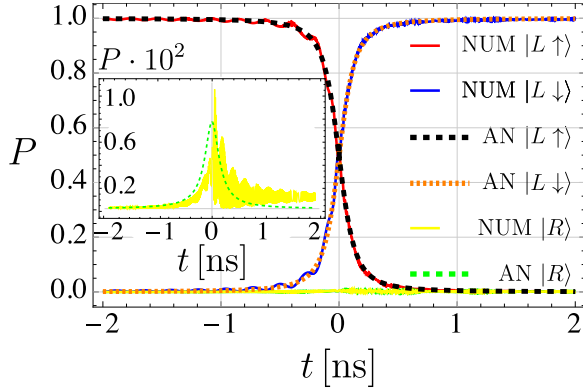


FIG. 3. Comparison between the numerically computed probabilities [obtained from evolving the state using the Hamiltonian of Eq. (1)] (Num) and analytic adiabatic four-level probabilities Eq. (3) (An). The inset represents the magnification of the probability to occupy the R quantum dot. The parameters of the plot are the Landau-Zener velocity $\beta = 4 \times 10^6$ eV/s, the tunnel hopping $\tau = 50$ μ eV, corresponding to interdot distance of $l = 280$ nm for $m^* = 0.023m_e$ (for more information, see the Supplemental Material [47]), the Zeeman energies $\Delta E_L = \Delta E_R = 17$ μ eV.

time evolution of our four state probabilities,

$$P_{L\uparrow} = \tau^2 \frac{|\Lambda(t) + \Delta E_L/2|^2}{\tilde{N}(t)^2}, \quad P_{L\downarrow} = \tau^2 \frac{|\Lambda(t) - \Delta E_L/2|^2}{\tilde{N}(t)^2},$$

$$P_{R\downarrow} = P_{R\uparrow} = \frac{|\Lambda(t)^2 - \Delta E_L^2/4|^2}{2\tilde{N}(t)^2}, \quad (3)$$

where $\Lambda(t)$ is the corresponding adiabatic eigenvalue and $\tilde{N}(t)$ the wave-function normalization.

The requirement that spin-conserving and non-spin-conserving tunnel couplings are equal is due to the fact that when $\Delta E_L = \Delta E_R$, the adiabatic eigenfunctions have only a vanishing contribution of the two states of the R quantum dot when $\tau \approx \tau_\Delta$ is fulfilled. In the case of $\tau \gg \tau_\Delta$, the adiabatic eigenfunctions have only a small component in the $|R\downarrow\rangle$ state when $\Delta E_L \ll \tau, \tau_\Delta$, and the $|R\uparrow\rangle$ state is detuned during the duration of the Landau-Zener sweep T .

Similarly to the previous implementation of our scheme, the appropriate adiabatic eigenvalue spans between $\Lambda(t = \mp\infty) = \pm\Delta E_L/2$, $-\Delta E_L/2 \leq \Lambda(t) \leq \Delta E_L/2$, for every t , with $\Lambda(t) = 0$ for $t \approx 0$. The maximal possible occupations of states for the case $\Delta E_L = \Delta E_R$ are $P_{L\uparrow}^{\max} \sim \tau^2 \Delta E_L^2$, $P_{L\downarrow}^{\max} \sim \tau^2 \Delta E_L^2$, and $P_{R\uparrow}^{\max} = P_{R\downarrow}^{\max} \sim \Delta E_L^4/2$. Equivalently to CHIRAP, the probabilities to occupy the $|R\downarrow\rangle$ and $|R\uparrow\rangle$ states are negligible at all instances of time $P_R \approx 0$ in the case when $\tau \gg \Delta E_L$ (see Fig. 3), and a complete population transfer between the spin eigenstates $|L\uparrow\rangle$ and $|L\downarrow\rangle$ occurs.

Experimental realizations. Our control scheme works optimally when the Zeeman splitting of the L QD is small. Furthermore, different signs of the Landau-Zener velocity and initial detunings need to be used for different initial spin states. We will address the problem of initializing and measuring electron spin states when the Zeeman splitting in the L QD is small in the remaining part of this section.

If the thermal broadening of the lead is smaller than the Zeeman splitting of the electron spin states $k_B T_e \ll \Delta E_L$, the state of the spin qubit can be initialized by tuning the chemical potential of a nearby lead close to the $|\downarrow\rangle$ state of the spin qubit. When lead-to-dot relaxation occurs, the only possible state to which the electron can relax from the lead is the $|\downarrow\rangle$ state. Furthermore, single-shot measurement of the electron spin state can be achieved in a similar manner [60], by tuning the chemical potential of the lead in such a way so that only one of the states can tunnel out of the quantum dot to the lead.

As our scheme operates optimally in low magnetic fields $k_B T_e > \Delta E_L$, the initialization and readout, validating the efficiency of our scheme, must be done in an alternative way, via the R QD. The chemical potential of the lead coupled to the R QD can be tuned between the spin states of the R QD.

After successful initialization of the $|R\downarrow\rangle$ state, the spin is shuttled to the $|L\downarrow\rangle$ state, followed by a manipulation of the spin according to our scheme.

After the manipulation stage, the modification in the current of a quantum point contact (QPC) near R is monitored. If the current of the QPC is unchanged, this means that the manipulation stage did not produce any leakage to the R quantum dot and that the spin measurement stage can follow. In the spin measurement stage, states $|L\downarrow\rangle$ and $|R\downarrow\rangle$ are aligned in energy one more time. If the electron spin was in the $|L\downarrow\rangle$ state, a tunneling event occurs and a nearby QPC modifies its current accordingly [61,62]. On the other hand, if the electron spin was in the $|L\uparrow\rangle$ state, the current of the QPC would remain unchanged.

In the case of $\Delta E_L = \Delta E_R$ (and therefore $\tau \approx \tau_\Delta$) and when $\Delta E_L < k_B T_e$, the initialization could still be achieved by waiting a sufficiently long time for the electron spin to relax to the thermal equilibrium state. However, spin readout would need to be done with alternative methods, because both spin eigenstates are energetically allowed to tunnel to the R QD when $|L\downarrow\rangle$ and $|R\downarrow\rangle$ are aligned in energy. This is why we consider the case $\Delta E_L \ll \Delta E_R$ to be more likely to implement in future experiments, and only consider the influence of nuclear spin noise for this realization.

Errors due to nuclear spins. We model the influence of nuclear spins as a distribution of the magnetic field in the L and R quantum dot, centered around the external magnetic field in the left and the right dot $\Delta E_L, \Delta E_R$, with standard deviations $\sigma = g_L \mu_B B_N$, $\chi = g_R \mu_B B_N$, where $g_{L(R)}$ is the electron g factor in the left (right) quantum dot, μ_B is the Bohr magneton, and B_N is the root mean square of the distribution of the nuclear magnetic field [63]. The influence of nuclear spins on our manipulation scheme can be estimated by averaging the probabilities of all relevant states over a distribution of nuclear spins,

$$\bar{P}_{c\sigma} = \iint_{-\infty}^{\infty} \frac{P_{c\sigma}}{2\pi\chi\sigma} e^{-\frac{(\Delta E - \Delta E_L)^2 + (\beta\tilde{t} - \beta t)^2}{4\sigma^2\chi^2}} d(\Delta E)d(\beta\tilde{t}), \quad (4)$$

where $c = L, R$, $\sigma = \uparrow, \downarrow$, with the exclusion of the detuned $|R\uparrow\rangle$ state.

In Fig. 4 we show how the nuclear spins influence our control scheme in the case of no uncertainty of the magnetic field in the right quantum dot, $\chi = 0$. If the random nuclear field is parallel with the external magnetic field, this gives rise

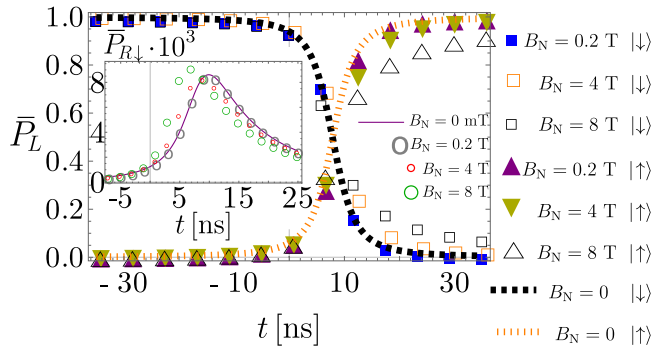


FIG. 4. Spin manipulation in the presence of nuclear spins. The parameters of the plot are the Landau-Zener velocity $\beta = 5 \times 10^3$ eV/s, the tunnel coupling $\tau = 6.5 \mu\text{eV}$, corresponding to an interdot separation of $l = 179$ nm (for more information, see the Supplemental Material [47]), the non-spin-conserving tunnel coupling $\tau_\Delta = 0.25\tau$, the Zeeman energy in the left quantum dot $\Delta E_L = 1 \mu\text{eV}$, the standard deviation in the right quantum dot $\chi = 0$, and the g factor in the left quantum dot $g_L = 1.2 \times 10^{-3}$. The inset represents occupation of the states in the R quantum dot.

to more leakage into the $|R\downarrow\rangle$ state. However, if the random nuclear field is antiparallel with the external magnetic field, this gives rise to less leakage into the $|R\downarrow\rangle$ state, and these two effects (less and more leakage to $|R\rangle$) cancel first order in ΔE_L .

In Fig. 5 we present the behavior of our control scheme under an influence of random nuclear spins in both quantum dots. Other than the already mentioned mechanism of additional leakage, the uncertainties in the nuclear field in the right quantum dot (and therefore the position of the level $|R\downarrow\rangle$) lead to reduced maximal probability to occupy the $|R\downarrow\rangle$ state (Fig. 5, inset, dark gray versus green circles). In contrast to EDSR, we are able to achieve a full transfer of population between the spin eigenstates, even when the uncertainty in the energy difference between spin eigenstates is large (Fig. 5, black open squares and triangles).

An effective nuclear magnetic field of unknown intensity in the z direction is going to change the instance of time in which the energy of the state $|R\downarrow\rangle$ is located between the energies of the states $|L\uparrow\rangle$ and $|L\downarrow\rangle$. For a nuclear magnetic field parallel with the external field, the energy of the state $|R\downarrow\rangle$ is located between the energy of the states $|L\uparrow\rangle$ and $|L\downarrow\rangle$ at a time $t < 0$. In contrast to that, for a nuclear magnetic field antiparallel with the external field, the energy of the state $|R\downarrow\rangle$ is located between the energies of the states $|L\uparrow\rangle$ and $|L\downarrow\rangle$ at a time $t > 0$. A process such as this is described with a Gaussian distribution, centered around βt with a standard deviation $\chi = g_R \mu_B B_N$, where g_R is the g

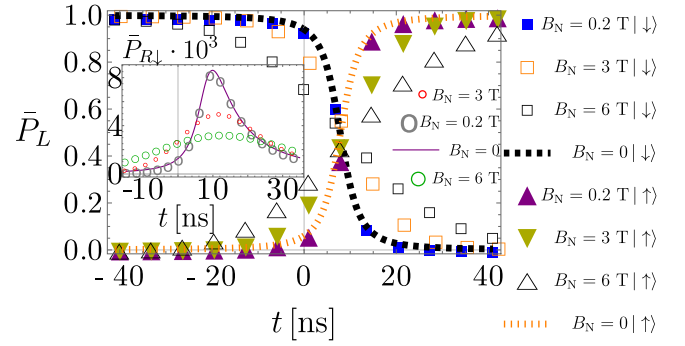


FIG. 5. Spin manipulation in the presence of nuclear spins. The parameters of the plot are the Landau-Zener velocity $\beta = 5 \times 10^3$ eV/s, the tunnel coupling $\tau = 6.5 \mu\text{eV}$, corresponding to an interdot separation of $l = 179$ nm (for more information, see the Supplemental Material [47]), the non-spin-conserving tunnel coupling $\tau_\Delta = 0.25\tau$, the Zeeman splitting in the left quantum dot $\Delta E_L = 1 \mu\text{eV}$, the g factor in the left quantum dot $g_L = 1.2 \times 10^{-3}$, and the g factor in the right quantum dot $g_R = 200g_L$. The inset represents occupation of the states in the R quantum dot.

factor in the right quantum dot, $g_R \gg g_L$. This leads to a reduced maximal value of the occupation of the $|R\downarrow\rangle$ state, without changing the averaged occupation of the $|R\downarrow\rangle$ per unit time $\bar{P}_{R\downarrow}(T) = \int_{-T/2}^{T/2} \bar{P}_{R\downarrow}(t) dt / T = \text{const}$ for a large enough T . Since the nuclear spins do not affect the final probabilities, our scheme can be operated in the presence of nuclear spin induced decoherence, as long as the total sweep time (in our case ~ 80 ns) is shorter than the characteristic time of nuclear spin evolution ($1 \mu\text{s}$) [63]. It should be noted that quasistatic detuning noise yields the same effect as having an uncertain nuclear spin distribution in the R quantum dot, and therefore we do not address this issue separately in this Rapid Communication.

Conclusions and final remarks. To conclude, we have proposed a method to manipulate a single electron spin by using Landau-Zener sweeps. Our control method is robust against the uncertainties of the nuclear field and static charge noise, and operates without microwaves and without precise knowledge of the spin resonance condition.

Note added. In the process of preparing this Rapid Communication, we became aware of an article [42] implementing similar ideas for double quantum dot $S - T_+$ qubits.

Acknowledgments. We thank Marko Milivojević, Guido Burkard, Maximilian Russ, Alexander Pearce, and Ferdinand Kuemmeth for fruitful discussions. This work is funded from MPNTR Grant No. OI171032, DAAD Grant No. 451-03-01858201309-3, and European Union within the S³nano initial training network.

- [1] D. Loss and D. P. DiVincenzo, *Phys. Rev. A* **57**, 120 (1998).
- [2] C. Flindt, A. S. Sørensen, and K. Flensberg, *Phys. Rev. Lett.* **97**, 240501 (2006).
- [3] K. Nowack, F. Koppens, Y. V. Nazarov, and L. Vandersypen, *Science* **318**, 1430 (2007).

- [4] S. Nadj-Perge, S. Frolov, E. Bakkers, and L. P. Kouwenhoven, *Nature (London)* **468**, 1084 (2010).
- [5] Y. Tokura, W. G. van der Wiel, T. Obata, and S. Tarucha, *Phys. Rev. Lett.* **96**, 047202 (2006).
- [6] M. Pioro-Ladriere, T. Obata, Y. Tokura, Y.-S. Shin, T. Kubo, K. Yoshida, T. Taniyama, and S. Tarucha, *Nat. Phys.* **4**, 776 (2008).

- [7] E. Kawakami, P. Scarlino, D. Ward, F. Braakman, D. Savage, M. Lagally, M. Friesen, S. Coppersmith, M. Eriksson, and L. Vandersypen, *Nat. Nanotechnol.* **9**, 666 (2014).
- [8] L. Landau, *Phys. Z. Sowjetunion* **2**, 46 (1932).
- [9] C. Zener, *Proc. R. Soc. London, Ser. A* **137**, 696 (1932).
- [10] E. C. G. Stueckelberg, *Helv. Phys. Acta (Basel)* **5**, 369 (1932).
- [11] E. Majorana, *Il Nuovo Cimento (1924-1942)* **9**, 43 (1932).
- [12] M. LaHaye, J. Suh, P. Echternach, K. C. Schwab, and M. L. Roukes, *Nature (London)* **459**, 960 (2009).
- [13] G. Heinrich, J. G. E. Harris, and F. Marquardt, *Phys. Rev. A* **81**, 011801 (2010).
- [14] Y.-A. Chen, S. D. Huber, S. Trotzky, I. Bloch, and E. Altman, *Nat. Phys.* **7**, 61 (2011).
- [15] W. Wernsdorfer, R. Sessoli, A. Caneschi, D. Gatteschi, and A. Cornia, *Europhys. Lett.* **50**, 552 (2000).
- [16] J. R. Rubbmark, M. M. Kash, M. G. Littman, and D. Kleppner, *Phys. Rev. A* **23**, 3107 (1981).
- [17] W. D. Oliver, Y. Yu, J. C. Lee, K. K. Berggren, L. S. Levitov, and T. P. Orlando, *Science* **310**, 1653 (2005).
- [18] M. Sillanpää, T. Lehtinen, A. Paila, Y. Makhlin, and P. Hakonen, *Phys. Rev. Lett.* **96**, 187002 (2006).
- [19] C. M. Wilson, T. Duty, F. Persson, M. Sandberg, G. Johansson, and P. Delsing, *Phys. Rev. Lett.* **98**, 257003 (2007).
- [20] A. Izmalkov, S. H. W. van der Ploeg, S. N. Shevchenko, M. Grajcar, E. Il'ichev, U. Hübner, A. N. Omelyanchouk, and H.-G. Meyer, *Phys. Rev. Lett.* **101**, 017003 (2008).
- [21] J. R. Petta, A. C. Johnson, J. M. Taylor, E. A. Laird, A. Yacoby, M. D. Lukin, C. M. Marcus, M. P. Hanson, and A. C. Gossard, *Science* **309**, 2180 (2005).
- [22] J. Petta, H. Lu, and A. Gossard, *Science* **327**, 669 (2010).
- [23] H. Ribeiro and G. Burkard, *Phys. Rev. Lett.* **102**, 216802 (2009).
- [24] Y. N. Demkov and V. Osherov, *JETP* **26**, 916 (1968).
- [25] C. Carroll and F. Hioe, *J. Phys. A: Math. Gen.* **19**, 2061 (1986).
- [26] Y. Kayanuma and S. Fukuchi, *J. Phys. B: At. Mol. Phys.* **18**, 4089 (1985).
- [27] V. L. Pokrovsky and N. A. Sinitsyn, *Phys. Rev. B* **65**, 153105 (2002).
- [28] Y. N. Demkov and V. Ostrovsky, *J. Phys. B* **34**, 2419 (2001).
- [29] B. Damski, *Phys. Rev. Lett.* **95**, 035701 (2005).
- [30] A. A. Rangelov, J. Piilo, and N. V. Vitanov, *Phys. Rev. A* **72**, 053404 (2005).
- [31] J. Oreg, F. T. Hioe, and J. H. Eberly, *Phys. Rev. A* **29**, 690 (1984).
- [32] B. Broers, H. B. van Linden van den Heuvell, and L. D. Noordam, *Phys. Rev. Lett.* **69**, 2062 (1992).
- [33] S. Chelkowski and G. N. Gibson, *Phys. Rev. A* **52**, R3417 (1995).
- [34] B. W. Shore, *Acta Phys. Slovaca* **63**, 361 (2013).
- [35] U. Gaubatz, P. Rudecki, S. Schiemann, and K. Bergmann, *J. Chem. Phys.* **92**, 5363 (1990).
- [36] N. V. Vitanov, T. Halfmann, B. W. Shore, and K. Bergmann, *Annu. Rev. Phys. Chem.* **52**, 763 (2001).
- [37] B. W. Shore, K. Bergmann, A. Kuhn, S. Schiemann, J. Oreg, and J. H. Eberly, *Phys. Rev. A* **45**, 5297 (1992).
- [38] D. A. Golter and H. Wang, *Phys. Rev. Lett.* **112**, 116403 (2014).
- [39] K. S. Kumar, A. Vepsäläinen, S. Danilin, and G. S. Paraoanu, *Nat. Commun.* **7**, 10628 (2016).
- [40] K. Bergmann, N. V. Vitanov, and B. W. Shore, *J. Chem. Phys.* **142**, 170901 (2015).
- [41] K. Bergmann, H. Theuer, and B. W. Shore, *Rev. Mod. Phys.* **70**, 1003 (1998).
- [42] J. Stehlik, M. Z. Maialle, M. H. Degani, and J. R. Petta, *Phys. Rev. B* **94**, 075307 (2016).
- [43] R. Kalra, A. Laucht, C. D. Hill, and A. Morello, *Phys. Rev. X* **4**, 021044 (2014).
- [44] P. Harvey-Collard, N. T. Jacobson, M. Rudolph, J. Dominguez, G. A. T. Eyck, J. R. Wendt, T. Pluym, J. K. Gamble, M. P. Lilly, M. Piore-Ladrière, and M. S. Carroll, [arXiv:1512.01606](https://arxiv.org/abs/1512.01606).
- [45] V. F. Maisi, A. Hofmann, M. Rössli, J. Basset, C. Reichl, W. Wegscheider, T. Ihn, and K. Ensslin, *Phys. Rev. Lett.* **116**, 136803 (2016).
- [46] F. R. Braakman, J. Danon, L. R. Schreiber, W. Wegscheider, and L. M. K. Vandersypen, *Phys. Rev. B* **89**, 075417 (2014).
- [47] See Supplemental Material at <http://link.aps.org/supplemental/10.1103/PhysRevB.94.241301> for adiabatic eigenfunctions and eigenvectors that are derived along with expressions for tunneling matrix elements.
- [48] T. Obata, M. Piore-Ladrière, Y. Tokura, Y.-S. Shin, T. Kubo, K. Yoshida, T. Taniyama, and S. Tarucha, *Phys. Rev. B* **81**, 085317 (2010).
- [49] M. D. Schroer, K. D. Petersson, M. Jung, and J. R. Petta, *Phys. Rev. Lett.* **107**, 176811 (2011).
- [50] G. Salis, Y. Kato, K. Ensslin, D. Driscoll, A. Gossard, and D. Awschalom, *Nature (London)* **414**, 619 (2001).
- [51] H. W. Jiang and E. Yablonovitch, *Phys. Rev. B* **64**, 041307 (2001).
- [52] J. H. Prechtel, F. Maier, J. Houel, A. V. Kuhlmann, A. Ludwig, A. D. Wieck, D. Loss, and R. J. Warburton, *Phys. Rev. B* **91**, 165304 (2015).
- [53] A. E. Hansen, M. T. Björk, C. Fasth, C. Thelander, and L. Samuelson, *Phys. Rev. B* **71**, 205328 (2005).
- [54] V. N. Golovach, A. Khaetskii, and D. Loss, *Phys. Rev. Lett.* **93**, 016601 (2004).
- [55] D. Stepanenko, M. Rudner, B. I. Halperin, and D. Loss, *Phys. Rev. B* **85**, 075416 (2012).
- [56] J. M. Nichol, S. P. Harvey, M. D. Shulman, A. Pal, V. Umansky, E. I. Rashba, B. I. Halperin, and A. Yacoby, *Nat. Commun.* **6**, 7682 (2015).
- [57] M. J. Rančić and G. Burkard, *Phys. Rev. B* **90**, 245305 (2014).
- [58] J. Nitta, T. Akazaki, H. Takayanagi, and T. Enoki, *Phys. Rev. Lett.* **78**, 1335 (1997).
- [59] D. Liang and X. P. Gao, *Nano Lett.* **12**, 3263 (2012).
- [60] J. Elzerman, R. Hanson, L. W. Van Beveren, B. Witkamp, L. Vandersypen, and L. P. Kouwenhoven, *Nature (London)* **430**, 431 (2004).
- [61] S. D. Barrett and T. M. Stace, *Phys. Rev. Lett.* **96**, 017405 (2006).
- [62] Y.-S. Shin, T. Obata, Y. Tokura, M. Piore-Ladrière, R. Brunner, T. Kubo, K. Yoshida, and S. Tarucha, *Phys. Rev. Lett.* **104**, 046802 (2010).
- [63] I. A. Merkulov, A. L. Efros, and M. Rosen, *Phys. Rev. B* **65**, 205309 (2002).

PAPER

Field-dependent superradiant quantum phase transition of molecular magnets in microwave cavities

To cite this article: Dimitrije Stepanenko *et al* 2016 *Semicond. Sci. Technol.* **31** 094003

View the [article online](#) for updates and enhancements.

Related content

- [Effective spin physics in two-dimensional cavity QED arrays](#)
Jií Miná, ebnem Güne Söyler, Pietro Rotondo *et al.*
- [Output field-quadrature measurements and squeezing in ultrastrong cavity-QED](#)
Roberto Stassi, Salvatore Savasta, Luigi Garziano *et al.*
- [Strongly interacting ultracold polar molecules](#)
Bryce Gadway and Bo Yan

Recent citations

- [First Demonstration of Magnetolectric Coupling in a Polynuclear Molecular Nanomagnet: Single-Crystal EPR Studies of \[Fe₃O\(O₂CPh\)₆\(py\)₃\]ClO₄·py under Static Electric Fields](#)
Athanasios K. Boudalis *et al*



IOP | ebooks™

Bringing you innovative digital publishing with leading voices to create your essential collection of books in STEM research.

Start exploring the collection - download the first chapter of every title for free.

Field-dependent superradiant quantum phase transition of molecular magnets in microwave cavities

Dimitrije Stepanenko¹, Mircea Trif², Oleksandr Tsypliyatsev^{3,4} and Daniel Loss⁵

¹Institute of Physics Belgrade, University of Belgrade, Pregrevica 118, 11080 Belgrade, Serbia

²Laboratoire de Physique des Solides, CNRS UMR-8502, Université Paris Sud, F-91405 Orsay Cedex, France

³School of Physics and Astronomy, The University of Birmingham, Birmingham, B15 2TT, UK

⁴Institut für Theoretische Physik, Universität Frankfurt, Max-von-Laue Strasse 1, D-60438 Frankfurt, Germany

⁵Department of Physics, University of Basel, Klingelbergstrasse 82, CH-4056 Basel, Switzerland

E-mail: Dimitrije.Stepanenko@ipb.ac.rs

Received 11 May 2016, revised 16 June 2016

Accepted for publication 12 July 2016

Published 25 August 2016



CrossMark

Abstract

We study a superradiant quantum phase transition in the model of triangular molecular magnets coupled to the electric component of a microwave cavity field. The transition occurs when the coupling strength exceeds a critical value, d_c , which, in sharp contrast to the standard two-level emitters, can be tuned by an external magnetic field. In addition to emitted radiation, the molecules develop an in-plane electric dipole moment at the transition. We estimate that the transition can be detected in state-of-the-art microwave cavities if their electric field couples to a crystal containing a sufficient number of oriented molecules.

Keywords: molecular magnets, quantum optics, quantum computing

(Some figures may appear in colour only in the online journal)

1. Introduction

The superradiant phase of a collection of emitters coupled to common electromagnetic field mode is characterized by a finite number of photons in the ground state of the combined system. In the model of two-level emitters coupled to a single cavity mode [1–4], the superradiant phase appears when the emitter-field coupling g exceeds some critical value g_c [5, 6]. Theoretical and experimental search for the superradiant phase transition has included atoms and molecules coupled to single- and multimode optical cavities, Josephson junction qubits in microwave resonators, as well as ultracold atoms in optical traps [7–11].

According to the no-go theorem [12–14], the ground state of any collection of two-level emitters with dipolar coupling to a mode of electromagnetic field does not contain cavity photons. This result seems to render the superradiant quantum phase transition impossible, and it was extended to

the case of many electromagnetic field modes and many levels in Josephson junctions [13, 14]. However, the superradiant phase transition was predicted to occur in the interacting emitters as well as in an ensemble of inhomogeneously coupled emitters and many modes [7, 15]. It was indeed observed in ultracold gases [9]. Here, we consider emission from an ensemble of interacting spins, and we are not aware of any extension of the no-go theorem that applies to our case.

Two-level emitters interacting with the quantized electromagnetic field of resonant cavity are described by the standard Dicke, Jaynes–Cummings, and Tavis–Cummings models of quantum optics [2]. Motivated by the spin-electric coupling of molecular magnets [16], we introduce a new model for the emitter in a cavity. The emitter degree of freedom represents the chirality of ground-state spin texture in a triangular molecular magnet, which interacts with the molecule's total spin. A crystal with oriented molecular

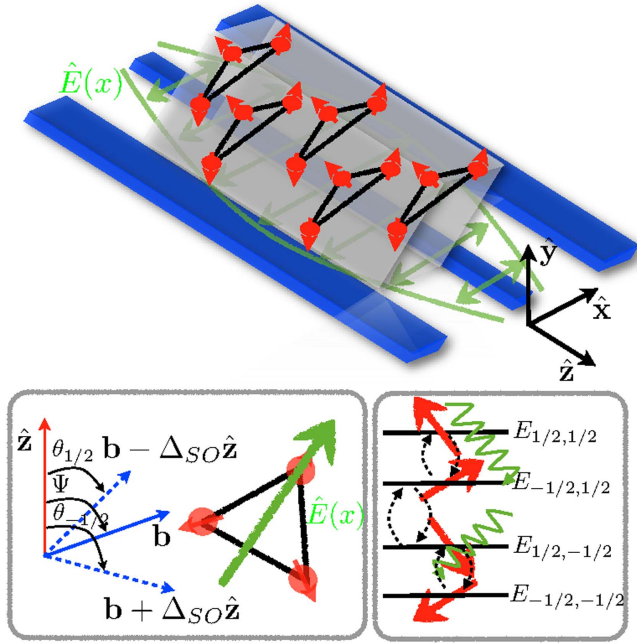


Figure 1. Geometry of a crystal of molecular magnets in a microwave cavity and external magnetic field. Electric field of the cavity mode is in the plane of the molecule (x - y), as shown on the top panel. External magnetic field \mathbf{B} produces the effective fields $\mathbf{b} = g_{\text{mol}}\mu_B\mathbf{B}$, which is tilted by the angle ψ from the normal \mathbf{e}_z to the plane of the molecules, and lies in the z - x plane. The fields $\hat{\mathbf{b}}(\pm 1/2)$ form angles $\theta_{\pm 1/2}$ with the z -axis, and define quantization axes of spin, as shown on the bottom left panel and described in the main text. On the bottom right panels, the effective quantization axes of the states with energies E_{C_z, S_z} are illustrated by arrows. The cavity field induces transitions between the states of equal spins and different chiralities, represented by the wavy lines. The angle $\delta = \theta_{-1/2} - \theta_{1/2}$ determines the coupling strength of different transitions.

magnets in a strip-line cavity is then described by a generalization of the Dicke model, see figure 1.

Molecular magnets are molecules with strong exchange interaction and pronounced spin anisotropy in the low-energy sector. At low energies they can be described as a set of interacting spins localized at positions of magnetic centers. The strong anisotropy governs the relaxation from spin-ordered states so that the transitions occur through quantum tunneling of magnetization over the anisotropy-induced barrier. In antiferromagnetic triangular molecules, the low energy states are two doublets of total spin $S = 1/2$, distinguished by the chirality of their spin textures $C_z = \pm 1/2$. Symmetry analysis then leads to the prediction that the transitions between the states of same spin and different chiralities are induced by external electric fields in the molecule's plane. This transition suggests that the spin order in these molecules can be manipulated by an external electric fields.

We find that the cavity and molecular magnets can be driven through the transition by modifying the direction or intensity of the external magnetic field. The critical coupling for the transition is magnetic field dependent, due to the interaction between the spins within the molecules. Spin interaction makes the ground- and low-energy excited states

coherent superpositions of entangled total spin and chirality of the spin texture. In molecular magnets [17], the quantum coherence was crucial for explaining the dynamics of magnetization: transitions between the spin states are coherent processes, and show the interference between transition paths [18–20] and the Berry phase [21–23]. The superradiant phase transition would therefore provide a way to study the spin coherence in the single-molecule magnets. In addition, observation of the magnetically controllable transition would prove the existence of spin-electric interaction.

Superradiance, the relaxation of an ensemble of emitters at a rate proportional to the square of their number, is another manifestation of coherent coupling of emitters to the quantized cavity field. It was predicted to occur in the molecular magnets, but the experimental results so far remain inconclusive [24–30]. As opposed to superradiance, the superradiant phase is a ground state property of the coupled emitter-cavity system. Therefore, the detection of the superradiant phase requires measurement of the static properties of the coupled emitter-cavity system, and not the following of the dynamics of relaxation from the excited state.

Control of our predicted superradiant phase transition is specific for the model of triangular spin-1/2 antiferromagnetic molecular magnets, since it depends on the form of spin-electric coupling. In addition to the specific form, the transition requires the interaction of sufficient strength. Experiments on molecular magnets, like charged Fe{4} clusters [31], and Mn ions in piezoelectric crystals [32] do show coupling of spins to electric fields. In these cases the electric fields modify the spin anisotropy. This interaction may allow for a similar analysis of electrically driven superradiant phase transition, once the details of the spin-electric interaction are known.

2. Model

At low energy, triangular molecular antiferromagnets are characterized by the total spin, $\mathbf{S} = \sum_{i=1}^3 \mathbf{s}_i$, where i counts the spins-1/2 on magnetic centers, and pseudospin-1/2 chirality \mathbf{C} , associated with the spin texture, see figure 1. The components of the chirality are defined in terms of spin operators as

$$C_x = -\frac{1}{3}(\mathbf{s}_1 \cdot \mathbf{s}_2 - 2\mathbf{s}_2 \cdot \mathbf{s}_3 + \mathbf{s}_3 \cdot \mathbf{s}_1), \quad (1)$$

$$C_y = \frac{1}{3}(\mathbf{s}_1 \cdot \mathbf{s}_2 - \mathbf{s}_3 \cdot \mathbf{s}_1), \quad (2)$$

$$C_z = \frac{1}{8\sqrt{2}}\mathbf{s}_1 \cdot (\mathbf{s}_2 \times \mathbf{s}_3). \quad (3)$$

The components C_x and C_y are two-spin operators that, in analogy with the Pauli spin operators, flip the chirality C_z , which is a three-spin operator [16]. The operators \mathbf{S} and \mathbf{C} are independent and satisfy spin commutation relations: $[S_i, S_j] = i\epsilon_{ijk}S_k$, $[C_i, C_j] = i\epsilon_{ijk}C_k$, and $[S_i, C_j] = 0$, where i, j, k count the Cartesian components of spin and chirality [16, 33]. Strong antiferromagnetic exchange between the

molecular spins constrains the total spin of the molecule to $S = 1/2$. This model is valid at the temperatures below the gap to excited $S = 3/2$ states, typically of the order of 10 K in spin triangles [34].

The two degrees of freedom, \mathbf{S} and \mathbf{C} , couple differently to external fields: while the spin couples to the magnetic field via Zeeman term, the chirality couples to \mathbf{E}_{\parallel} , the components of external electric field in the plane of the triangular molecule [16]. The Hamiltonian of the molecular magnet in external electric and magnetic fields is [16]

$$H_{\text{mol}} = 2\Delta_{\text{SO}}C_zS_z + \mathbf{b} \cdot \mathbf{S} + d_0\mathbf{E}_{\parallel} \cdot \mathbf{C}. \quad (4)$$

The Bohr magneton, μ_B , and the molecular gyromagnetic ratio, g_{mol} , are absorbed in the effective magnetic field $\mathbf{b} = g_{\text{mol}}\mu_B\mathbf{B}$, and we set $\hbar = 1$. The zero-field splitting, Δ_{SO} , caused by the spin-orbit interaction and with a typical strength $\Delta_{\text{SO}}/(g\mu_B) \sim 1$ T, produces an Ising coupling between S_z and C_z , with the spin z axis normal to the molecule's plane [17, 34]. The chirality interacts with the in-plane components of the electric field and, through the Ising coupling, with \mathbf{S} , the total spin [16, 33]. The selection rules for electrically driven transitions in equation (4) are set by the D_{3h} symmetry of the molecule, and read $\Delta C_z = \pm 1$. Therefore, it is possible to access the transitions that would be forbidden by the selection rules $\Delta S_z = \pm 1$ which are valid for the magnetic driving [33].

A crystal of N emitters interacting with a mode of the resonant cavity is described by

$$H = H_{\text{cav}} + \sum_j H_{0,j} + \sum_j V_j, \quad (5)$$

where $H_{\text{cav}} = \omega a^\dagger a$ describes the cavity photon, and each $H_{0,j} = 2\Delta_{\text{SO}}C_{j,z}S_{j,z} + \mathbf{b} \cdot \mathbf{S}_j$ describes a molecule interacting with an external classical magnetic field \mathbf{B} . The interaction terms

$$V_j = d(a + a^\dagger)C_{j,x}, \quad (6)$$

are couplings of molecules to the electric component of quantized cavity field. The operator a (a^\dagger) annihilates (creates) a cavity photon. The coupling constant $d = d_0E_x$ includes both the intrinsic single-molecule spin-electric coupling d_0 and the in-plane electric field amplitude E_x . The molecules in a crystal lie in parallel planes, so that their spin quantization axes all point in the same direction [35] that we label z , see figure 1. Any variation of molecular orientations, e.g., due to crystal defects, is equivalent to a change in the effective coupling between the molecular spins and the cavity photons. We assume that the Zeeman coupling of \mathbf{S} to the magnetic component of the cavity field is weak, as in the microwave cavities with molecules placed near the maximum of the electric field amplitude [36], and do not include it in equation (5).

The non-interacting Hamiltonian, $H_0 = H_{\text{cav}} + \sum_j H_{0,j}$, conserves the number of photons $\hat{n} = a^\dagger a$, as well as the z -components of chiralities, $C_{j,z}$. Within each simultaneous eigenspace of \hat{n} and $C_{j,z}$ it reduces to a spin Hamiltonian

$$H_{0,j,n,c} = n\omega + \mathbf{b} \cdot \mathbf{S}_j + 2c\Delta_{\text{SO}}S_{j,z}, \quad (7)$$

where n and c are the respective eigenvalues of the operators \hat{n} and $C_{j,z}$. This reduced Hamiltonian is readily diagonalized, and we find the energies

$$E_{n,c,s} = s|\tilde{\mathbf{b}}(c)| + n\omega \quad (8)$$

and the eigenstates

$$|n, c, s\rangle = |n, c\rangle \otimes |\mathbf{S} \cdot \mathbf{e}_c = s\rangle. \quad (9)$$

The effective magnetic fields are $\tilde{\mathbf{b}}(c) = \mathbf{b} + 2c\Delta_{\text{SO}}\mathbf{e}_z$, with $c = \pm 1/2$, and $s = \pm 1/2$ denotes the molecule's spin projection along \mathbf{e}_c , the direction of effective field $\tilde{\mathbf{b}}(c)$. Explicitly, the molecule's eigenstates in the $C_{j,z}, S_{j,z}$ basis are given by the unitary transformation $|n, c, s\rangle = |n\rangle \otimes U|c, s_z\rangle$, where $U = \sum_{c=\pm 1/2} P_c \exp(-i\theta_c S_y) P_c$ maps the state $|c, s_z\rangle$ of the molecule with chirality c and spin projection s_z to the z -axis into a state with the same chirality and the spin projection $s = s_z$ along the rotated spin axis (see figure 1). The angles $\theta_{\pm 1/2}$ are

$$\theta_c = \arccos \frac{2c\Delta_{\text{SO}} + b\cos\psi}{\sqrt{b^2\sin^2\psi + (2c\Delta_{\text{SO}} + b\cos\psi)^2}} \quad (10)$$

with ψ and b denoting the polar angle and intensity of the field \mathbf{b} . The operators $P_c = 2cC_z + 1/2$ are projectors to the states of a given chirality c .

3. Rotating wave approximation (RWA)

As opposed to the standard Jaynes-Cummings model in quantum optics [37], the RWA for a single-molecule magnet in a cavity cannot be obtained by simply neglecting the terms proportional to C_+a^\dagger and C_-a , since the chirality interacts with the spin, which in addition couples to an external magnetic field.

To derive the RWA of equation (5) we switch to the interaction picture, $V_j(t) = e^{iH_0 t} V_j e^{-iH_0 t}$, with respect to the terms $H_0 = \sum_j H_{0,j}$ that do not involve the interaction of the molecule with the cavity electric field. Using the known eigenvalues and eigenstates of H_0 , we find

$$V_j(t) = \frac{d}{2} \sum_{n,c,s,s'} e^{i(E_{n,c,s} - E_{n,-c,s'})t} M(c, s, s') \times |n, c, s\rangle \langle n, -c, s'| (e^{i\omega t} a^\dagger + e^{-i\omega t} a), \quad (11)$$

where $M(c, s, s') = \langle \mathbf{S}_j \cdot \mathbf{e}_c = s | \mathbf{S}_j \cdot \mathbf{e}_{-c} = s' \rangle$ is the scalar product of the spins with projections s and s' on the axes \mathbf{e}_c and \mathbf{e}_{-c} . Explicitly, $M(c, s, s) = \cos(\delta/2)$, $M(\pm 1/2, s, -s) = \mp i \sin(\delta/2)$, $\delta = \theta_{-1/2} - \theta_{1/2}$, and the angles $\theta_{\pm 1/2}$ are given in equation (10).

The RWA consists of neglecting the terms in the interaction-picture Hamiltonian, equation (11), that oscillate with frequencies close to molecular transitions $\omega_{ij} \sim |E_i - E_j|$, and keeping the terms that oscillate slowly, with frequencies close to the detuning between the transition and the cavity mode. In this case the fast-oscillating terms average out to zero, and we can neglect them. The resonant frequencies in our model are $\omega_r^\pm = (|\tilde{\mathbf{b}}(1/2)| \pm |\tilde{\mathbf{b}}(-1/2)|)/2$. We have set the direction of z axis so that $|\tilde{\mathbf{b}}(1/2)| \geq |\tilde{\mathbf{b}}(-1/2)|$.

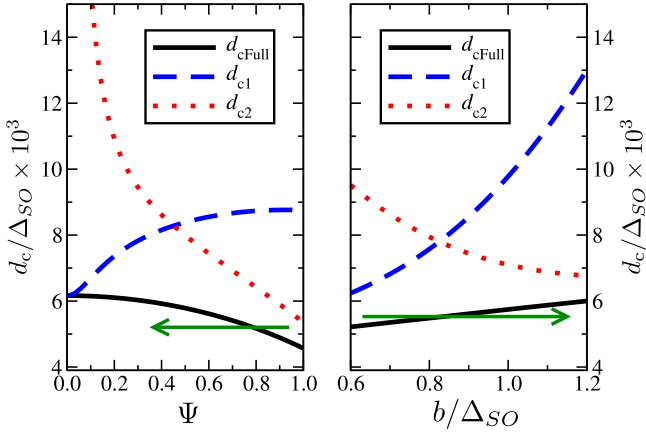


Figure 2. The critical couplings in the full RWA (d_{cFull}), in standard RWAs near ω_r^+ (d_{c1}), and near ω_r^- (d_{c2}), as a function of angle with respect to the normal to molecule's plane ψ , and the intensity b of the external magnetic field \mathbf{b} , respectively. Variations in either ψ or b lead the system through the superradiant quantum phase transition (motion along the arrows switches from $d > d_c$ to $d < d_c$). For this figure, the number of molecules is $N = 10^5$, and the cavity frequency is the mean of the two resonant frequencies $\omega = (\omega_r^+ + \omega_r^-)/2$ (see text). On the first panel $b = 0.9\Delta_{SO}$, and on the second $\psi = 0.6$ rad.

The condition for the validity of the RWA is that the molecule-cavity coupling constant d is much smaller than the resonant frequencies, $d \ll \omega_r^\pm$. In addition, the RWA can reproduce the standard model of a two-level emitter when the cavity frequency is tuned close to one of the transitions and far from the other, e.g., $|\omega - \omega^+| \gg |\omega - \omega^-|$. This tuning is possible only when

$$|\omega_r^+ - \omega_r^-| \gg d. \quad (12)$$

The condition in equation (12) can not be satisfied when $\mathbf{b} \approx \Delta_{SO}\mathbf{e}_z$, i.e., when the magnetic field axis is near the normal to the molecule, and the magnetic field intensity is comparable to spin-orbit splitting Δ_{SO} . We will focus on the case when both resonances have to be taken into account, either due to the deliberate tuning of the cavity frequency, or due to violation of equation (12). In this case, the amplitudes of the resonant transitions vary strongly with the magnetic field, and we will see that this leads to new effects. When equation (12) is satisfied, the cavity can be tuned so that the RWA leads to the Tavis–Cummings model [3, 4], and consequently to the familiar superradiant phase transition and a single transition resonant with the cavity, see figure 2. We will label the critical couplings in approximations that keep a single transitions as d_{c1} (d_{c2}).

After the removal of the counter-rotating terms and switching back to the Schrödinger picture, the molecule-cavity interaction is

$$V_{RWA} = d \sum_j (a + a^\dagger) \left(\frac{\cos\delta}{2} C_{j,x} - \sin\delta S_{j,y} C_{j,y} \right) + i(a - a^\dagger) \left(\sin\theta_{-\frac{1}{2}} S_{j,x} + \cos\theta_{-\frac{1}{2}} S_{j,z} \right) C_{j,y}. \quad (13)$$

The final Hamiltonian in RWA is $H_{RWA} = H_0 + V_{RWA}$, and it is analogous to the Tavis–Cummings model of two-level atoms in a resonant cavity. Similarly to the conservation of the number of excitations in the Tavis–Cummings model, H_{RWA} conserves the quantity

$$N_{exc} = \hat{n} + \sum_j (1 + \tilde{S}_{j,z} + 2C_{j,z}\tilde{S}_{j,z}), \quad (14)$$

where $\tilde{S}_j = US_jU^\dagger$, with U defined above equation (10). We interpret N_{exc} as the conserved number of excitations by counting molecules in the state $|c, s\rangle = |1/2, -1/2\rangle$ as zero excitations, molecules in the states $|-1/2, \pm 1/2\rangle$ as one excitation, molecules in the state $|1/2, 1/2\rangle$ as two excitations, and each cavity photon as one excitation. We choose an additive constant so that $N_{exc} = 0$ corresponds to all the molecules in the state $|1/2, -1/2\rangle$ and no photons in the cavity.

4. Superradiant quantum phase transition

We study the superradiant phase transition in the rotating wave and mean-field approximations. This amounts to substituting photon annihilation(creation) operator $a(a^\dagger)$ by their expectation value $\langle a \rangle (\langle a \rangle^*)$ in H_{RWA} , thus neglecting any quantum fluctuations. This approximation is valid for large photon numbers, $n \gg 1$. The mean-field energy, $E_{MF}(\langle a \rangle)$ is the ground state energy of

$$H_{RWA}^{MF}(\langle a \rangle) = \omega |\langle a \rangle|^2 + \sum_j H_{0,j} + V_{RWA}(\langle a \rangle). \quad (15)$$

We find that $E_{MF}(\langle a \rangle)$ is independent of the phase of $\langle a \rangle$, which we set to be real in further discussion. The mean-field value of the annihilation operator, $\langle a \rangle_{MF}$ is, by the self-consistency condition, the value of $\langle a \rangle$ for which $E_{MF}(\langle a \rangle)$ is at a minimum. Similarly, the mean field state of the molecules is the ground state of $H_{RWA}^{MF}(\langle a \rangle_{MF})$. Without RWA, the phase of $\langle a \rangle_{MF}$ is set by the minimization requirement so that the quantity is real [38].

When the cavity is decoupled from the molecules, $d = 0$, the system is in the normal state, and $\langle a \rangle_{MF} = 0$. The superradiant phase transition means the appearance of $\langle a \rangle_{MF} > 0$ for coupling strength larger than the critical value, $d > d_c$. We analytically determine the critical coupling d_c from the properties of $E_{MF}(\langle a \rangle)$. In the absence of photons, $E_{MF}(0)$ is a finite ground state energy of N molecules in the ground state. For large photon numbers, the energy is dominated by the free photon term, and therefore diverges, $\lim_{\langle a \rangle \rightarrow \infty} E_{MF} = \infty$. Furthermore, since $E_{MF}(\langle a \rangle)$ explicitly depends only on the square of its argument, $\partial_{\langle a \rangle} E_{MF}(\langle a \rangle)|_{\langle a \rangle=0} = 0$. We determine the critical coupling as the smallest value of d for which $\partial_{\langle a \rangle}^2 E_{MF}(\langle a \rangle)|_{\langle a \rangle=0} < 0$. Together with the limiting values and the zero derivative at zero, this condition guarantees the existence of a minimum for the mean-field energy that is lower than $E_{MF}(0)$ at some finite value of $\langle a \rangle$.

The procedure of minimization applied to H_{RWA}^{MF} , equation (15), and using the RWA potential with both

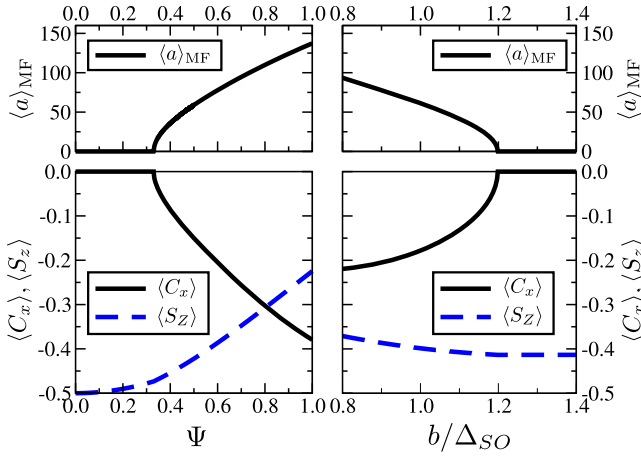


Figure 3. Response of molecules and cavity field to the changes in direction ψ (first panel) and intensity b (second panel) of the external magnetic field \mathbf{b} . At the superradiant transition, the mean-field value of the photon annihilation operator $\langle a \rangle_{\text{MF}}$ becomes nonzero (upper panels). At the same value of \mathbf{b} , an in-plane electric polarization $\propto \langle C_x \rangle$ appears, signaling the superradiant phase. The magnetization normal to the molecule's plane $\propto \langle S_z \rangle$ shows a more rapid change with \mathbf{b} then in the normal state. System parameters are the same as in figure 2, and $d = 6 \times 10^{-3} \Delta_{\text{SO}}$.

resonances, equation (13) gives the critical coupling

$$d_{\text{cFull}} = \sqrt{\frac{8\omega\Delta_{\text{SO}}b}{N\left[\tilde{b}\left(\frac{1}{2}\right) + \tilde{b}\left(-\frac{1}{2}\right)\cos\delta\right]}}. \quad (16)$$

This \mathbf{b} -dependent d_{cFull} is one of our main results, figure 2. The dependence is due to both the modification of the energy levels of H_0 , and to modification of the coupling constants for transitions through spin-overlap terms in equation (13). The result, equation (16) clearly can not be explained by the usual RWA at either of the resonant frequencies, as illustrated in figure 2. The value of $\langle a \rangle_{\text{MF}}$ grows as $\langle a \rangle_{\text{MF}} \propto \sqrt{d - d_c}$ for $d > d_c$, and $\langle a \rangle_{\text{MF}} \propto \sqrt{N}$. We note that the mean-field approximation can be applied to the Hamiltonian equation (5) without the RWA, predicting the superradiant phase transition with the critical coupling scaled by a factor of 2 from the value in equation (16). The dependence of d_c on \mathbf{b} allows for a controllable superradiant phase transition. Changes in d_c , given by equation (16), can lead the system into or out of the superradiant phase, see figure 2. The measurement of the escaping radiation as done, for example, by using input-output theory [39], would then serve as a signature of superradiant state [9, 40–42]. Turning the tables, identifying the superradiant phase transition would allow to extract the value of the spin-electric coupling constant.

The quantum properties of escaping light can not be determined in the mean-field theory, since we assume that the radiation is in a specific classical state described by the expectation value $\langle a \rangle_{\text{MF}}$. However, in the superradiant phase of the Dicke model, the emitted radiation is nonclassical in the sense that it cannot be described by a positive-definite probability distribution function [43]. We expect that there are

quantum correlations of emitted light from our system, but their evaluation is beyond the scope of this work.

In addition to the nonzero photon occupation of the cavity mode, see figure 3, the transition is characterized by a change in the expectation value of the chirality. For $d < d_c$, the molecules are in the state with $C_{j,x} = -1/2$, with zero expectation values of $C_{j,x(y)}$. After the transition, for $d > d_c$, the in-plane components of chirality have nonzero expectation value, i.e., $\langle C_{j,x} \rangle \neq 0$ in our model. The fact that only the x -components gets a finite expectation value comes from our phase convention for $\langle a \rangle$, and the form of the interaction with the electric fields [38]. The molecules develop electric dipole moments for $d > d_c$, and the transition can be detected by the electric response, for example by measuring the spin-electric susceptibility [33], as well as by the emitted radiation, lower panels of figure 3.

5. Experimental requirements

The detection of the controllable superradiant phase transition is possible in an experiment that would monitor the escaping radiation or the electric response of the molecular magnets coupled to a cavity, as they are driven through the transition by a change in external magnetic field. The transition occurs when $d_0 E_x > d_c$, see equation (16), and the controllable transition can be achieved for large electric field amplitude E_x and strong molecular spin-electric coupling d_0 . The critical coupling strength diminishes with the increasing number of molecules, $d_c \propto N^{-1/2}$. Other parameters that influence d_c are the strength of the magnetic field required for control and the cavity frequency. Both are set by the zero-field splitting of the molecular magnet, $\Delta_{\text{SO}} \approx g\mu_B B \approx \hbar\omega$. The typical value of zero-field splitting in triangular molecular antiferromagnets [34, 44] is $\Delta_{\text{SO}} \sim 1 \text{ K} \cdot k_B$. Therefore, the relevant resonant frequencies lie in the microwave range, $f = \omega/(2\pi) \sim 15 \text{ GHz}$, and the external magnetic fields needed for control are $B \sim 1 \text{ T}$.

We take the estimate for the value of the molecular spin-electric coupling constant, $d_0 \sim 10^{-4}|eR_0|$, where R_0 is the distance between the magnetic centers in the molecule from the *ab-initio* work [45, 46]. The corresponding numerical value of the dipole moment is $d_0 \sim 10^{-32} \text{ Cm}$. Assuming the electric field amplitude $E_x = \sqrt{\hbar\omega/c_1 V}$, where c_1 is the resonator capacitance per unit length, and V is the mode volume, we estimate that $E_x \sim 100 \text{ V/m}$ is achievable in narrow strip-line cavities [47], giving $d = d_0 E_x \sim 10^{-11} \text{ eV}$. Under these conditions, the controllable superradiant phase transition will occur if the crystal coupled to the cavity electric field contains $N > N_c \sim 10^{15}$ molecular magnets. Spin ensembles of comparable effective volume were coupled to microwaves by placing them on top of the resonators [48–50].

Coupling such a large number of molecules to a resonant cavity requires very dense crystals, with the intermolecular distances about 20 times shorter than typical 1 nm, i.e., the critical density n_c is four orders of magnitude too large. There are two molecular parameters that can be manipulated to relax

this requirement, the zero-field splitting, Δ_{SO} , and the intrinsic spin-electric coupling strength of a single molecule, d_0 . Estimating the cavity electric field from a single photon energy in the mode volume implies $E_x \propto \sqrt{\omega}$. Taking into account that the control magnetic field, b , the effective fields, $\tilde{b}(\pm 1/2)$, and the resonant frequency, ω , all scale with Δ_{SO} , equation (16) implies

$$n_c \propto \frac{\Delta_{\text{SO}}}{d_0^2}. \quad (17)$$

Triangular molecular magnets come in great variety, and the chemical alteration of their composition gives access to many spin Hamiltonians at low energies. The zero field splitting can be as low as $\Delta_{\text{SO}} \approx 3 \times 10^{-2}$ K, and potentially even lower [51], with the values in V_{15} , Fe_8 , and Cu_3 complexes in the range $10^{-2} - 1$ K [35, 51–55]. Modification of the intrinsic spin-electric coupling, d_0 , can reduce the critical density even more. Since $n_c \propto d_0^{-2}$, and increase in d_0 does not affect any other experimental parameter, searching for the molecules with large d_0 may be the right way to achieve the proposed controllable superradiant phase transition in a laboratory. An increase in d_0 by a factor of 100 from the numerically predicted value [45, 46] would bring the critical density to the value of 1 nm^{-3} .

The magnetic field dependent critical coupling, equation (16), is found in the model that assumes an ideal cavity, zero temperature, and validity of the mean-field approach. The constraints for the realistic experiments are less stringent. The superradiant phase appears in the system's ground state which is predominantly occupied at temperatures lower than the first molecule's excitation, $T \ll \Delta_{\text{SO}}/k_B \sim 1$ K. The time scale of relaxation to the superradiant ground state is given by the spin relaxation time of the molecular magnet, which can be as long as a microsecond [44]. This time should be longer than the Rabi time of the collective coupling between the molecules and the field mode, i.e. there should be many Rabi oscillations before the spins relax. For $N > N_c$, this requirement is satisfied due to scaling of the Rabi frequency. In addition, the cavity decay time should be longer than the spin decay time, which would require the cavity Q -factor of the order $Q \sim 10^5 - 10^6$ for long spin coherence times of $\tau_s \sim 1 \mu\text{s}$, and less stringent $Q \sim 10^3 - 10^4$ for $\tau_s \sim 10$ ns. In superconducting stripline cavities, the external magnetic field of the order of 1 T would reduce the Q -factor, unless the field lies in the plane of the strips. There is a geometry that allows for the variation of the angle ψ between the magnetic field \mathbf{b} and the normal to triangles while keeping \mathbf{b} in the plane of the superconductors. In this geometry, the triangles should lie in the plane normal to the axis of the strips. Further enhancement of Q -factor is possible by resonator engineering [56].

As a matter of principle, it is not necessary to use the stripline cavities, and any microwave resonator with large regions of significant electric field and sufficient Q -factor can support the superradiant phase transition. Manipulation of the electric field amplitude of the cavity mode and choosing a shape that can accommodate many molecules can be an

efficient way to reach the required coupling strength, since $N_c \propto E_x^{-2}$. Therefore, 3D cavities can also be used.

The disorder in the molecule's energies due to imperfections of the crystal may bring some of the molecules out of resonance and reduce the effective N below the total number of molecules. However, the superradiant effect also suppresses such inhomogeneous broadening [57–59]. When the collective coupling of many emitters exceeds the bandwidth of their ensemble, the broadening vanishes altogether so that even far off-resonant molecules interact strongly with the field mode. This allows one to increase the number of active emitters in the cavity in realistic devices.

6. Conclusions

We have introduced a model of a crystal of single-molecule triangular antiferromagnets interacting with an external classical homogeneous magnetic field and the electric component of a quantized cavity field. The model shows a superradiant quantum phase transition with the critical coupling tunable by applied magnetic field. The strong coupling regime is characterized by nonzero mean photon number and electric dipole moment in the triangle plane. With state-of-the-art cavities and current estimates of spin-electric coupling strength, the tunable transition is achievable for 10^{15} molecules coupled to the cavity. This value can be reduced by choosing the molecules with weak zero-field splitting Δ_{SO} and strong intrinsic spin-electric coupling d_0 . Observation of the predicted transition and its magnetic field dependence can serve as a probe of spin-electric interaction. While our models describes triangular single-molecule magnets, it can be extended in order to study of other emitters described by entangled discrete degrees of freedom.

Acknowledgments

We acknowledge discussions with Filippo Troiani. This work is funded from Serbian MPNTR grant OI171032, Swiss NF through NCCR QSIT and SCOPES IZ73Z0152500, public grant from the Laboratoire d'Excellence Physics Atom Light Matter (LabEx PALM, reference: ANR-10- LABX-0039), and EPSRC Grant No. EP/J016888/1.

References

- [1] Dicke R H 1954 *Phys. Rev.* **93** 99
- [2] Jaynes E and Cummings F 1963 *Proc. IEEE* **51** 89
- [3] Tavis M and Cummings F W 1968 *Phys. Rev.* **170** 379
- [4] Tavis M and Cummings F W 1969 *Phys. Rev.* **188** 692
- [5] Hepp K and Lieb E H 1973 *Ann. Phys., NY* **76** 360
- [6] Wang Y K and Hioe F T 1973 *Phys. Rev. A* **7** 831
- [7] Strack P and Sachdev S 2011 *Phys. Rev. Lett.* **107** 277202
- [8] Baumann K, Guerlin C, Brennecke F and Esslinger T 2009 *Nature* **464** 1301
- [9] Baumann K, Mottl R, Brennecke F and Esslinger T 2011 *Phys. Rev. Lett.* **107** 140402

- [10] Domokos P and Ritsch H 2002 *Phys. Rev. Lett.* **89** 253003
- [11] Larson J and Lewenstein M 2009 *New J. Phys.* **11** 063027
- [12] Knight J M, Aharonov Y and Hsieh G T C 1978 *Phys. Rev. A* **17** 1454
- [13] Bialynicki-Birula I and Kazimierz R 1979 *Phys. Rev. A* **19** 301
- [14] Viehmann O, von Delft J and Marquardt F 2011 *Phys. Rev. Lett.* **107** 113602
- [15] Zou L J, Marcos D, Diehl S, Putz S, Schmiedmayer J, Majer J and Rabl P 2014 *Phys. Rev. Lett.* **113** 023603
- [16] Trif M, Troiani F, Stepanenko D and Loss D 2008 *Phys. Rev. Lett.* **101** 217201
- [17] Gatteschi D, Sessoli R and Villain J 2006 *Molecular Nanomagnets* (Oxford: Oxford University Press)
- [18] Loss D, DiVincenzo D P and Grinstein G 1992 *Phys. Rev. Lett.* **69** 3232
- [19] Leuenberger M N and Loss D 2000 *Phys. Rev. B* **61** 1286
- [20] Leuenberger M N, Meier F and Loss D 2003 *Mon. hefte Chem.* **134** 217
- [21] Wernsdorfer W and Sessoli R 1999 *Science* **284** 133
- [22] González G and Leuenberger M N 2007 *Phys. Rev. Lett.* **98** 256804
- [23] González G, Leuenberger M N and Mucciolo E R 2008 *Phys. Rev. B* **78** 054445
- [24] Chudnovsky E M and Garanin D A 2002 *Phys. Rev. Lett.* **89** 157201
- [25] Tejada J, Amigo R, Hernandez J M and Chudnovsky E M 2003 *Phys. Rev. B* **68** 014431
- [26] Amigó R, Tejada J, Chudnovsky E, Hernandez J and Garca-Santiago A 2004 *J. Magn. Magn. Mater.* **272–276** 1106 Proc. Int. Conf. on Magnetism (ICM 2003), <http://sciencedirect.com/science/article/pii/S0304885303026325>
- [27] Bal M, Friedman J R, Mertes K, Chen W, Rumberger E M, Hendrickson D N, Avraham N, Myasoedov Y, Shtrikman H and Zeldov E 2004 *Phys. Rev. B* **70** 140403
- [28] Yukalov V I, Henner V K, Kharebov P V and Yukalova E P 2008 *Laser Phys. Lett.* **5** 887
- [29] Shafir O and Keren A 2009 *Phys. Rev. B* **79** 180404
- [30] Leviant T, Hanany S, Myasoedov Y and Keren A 2014 *Phys. Rev. B* **90** 054420
- [31] Nossa J F, Islam M F, Canali C M and Pederson M R 2013 *Phys. Rev. B* **88** 224423
- [32] George R E, Edwards J P and Ardavan A 2013 *Phys. Rev. Lett.* **110** 027601
- [33] Trif M, Troiani F, Stepanenko D and Loss D 2010 *Phys. Rev. B* **82** 045429
- [34] Choi K-Y, Matsuda Y H, Nojiri H, Kortz U, Hussain F, Stowe A C, Ramsey C and Dalal N S 2006 *Phys. Rev. Lett.* **96** 107202
- [35] Bertaina S, Chen L, Groll N, Van Tol J, Dalal N S and Chiorescu I 2009 *Phys. Rev. Lett.* **102** 050501
- [36] Imamoğlu A 2009 *Phys. Rev. Lett.* **102** 083602
- [37] Mandel L and Wolf E 1995 *Optical Coherence and Quantum Optics* (Cambridge: Cambridge University Press)
- [38] Baksic A and Ciuti C 2014 *Phys. Rev. Lett.* **112** 173601
- [39] Clerk A A, Devoret M H, Girvin S M, Marquardt F and Schoelkopf R J 2010 *Rev. Mod. Phys.* **82** 1155
- [40] Ciuti C, Bastard G and Carusotto I 2005 *Phys. Rev. B* **72** 115303
- [41] Auer A and Burkard G 2012 *Phys. Rev. B* **85** 235140
- [42] Kopylov W, Emary C and Brandes T 2013 *Phys. Rev. A* **87** 043840
- [43] Nataf P, Dogan M and Hur K Le 2012 *Phys. Rev. A* **86** 043807
- [44] Bertaina S, Gambarelli S, Mitra T, Tsukerblat B, Muller A and Barbara B 2008 *Nature* **453** 203
- [45] Islam M F, Nossa J F, Canali C M and Pederson M 2010 *Phys. Rev. B* **82** 155446
- [46] Nossa J F, Islam M F, Canali C M and Pederson M R 2012 *Phys. Rev. B* **85** 085427
- [47] Trif M, Golovach V N and Loss D 2008 *Phys. Rev. B* **77** 045434
- [48] Schuster D I *et al* 2010 *Phys. Rev. Lett.* **105** 140501
- [49] Kubo Y *et al* 2011 *Phys. Rev. Lett.* **107** 220501
- [50] Zhu X *et al* 2011 *Nature* **478** 221
- [51] Spielberg E T, Gilb A, Plaul D, Geibig D, Hornig D, Schuch D, Buchholz A, Ardavan A and Plass W 2015 *Inorg. Chem.* **54** 3432
- [52] Chiorescu I, Wernsdorfer W, Müller A, Bögge H and Barbara B 2000 *Phys. Rev. Lett.* **84** 3454
- [53] De Raedt H, Miyashita S, Michielsens K and Machida M 2004 *Phys. Rev. B* **70** 064401
- [54] Chaboussant G, Ochsenein S T, Sieber A, Gudel H-U, Mutka H, Muller A and Barbara B 2004 *Europhys. Lett.* **66** 423
- [55] Burzurí E, Luis F, Montero O, Barbara B, Ballou R and Maegawa S 2013 *Phys. Rev. Lett.* **111** 057201
- [56] de Graaf S E, Danilov A V, Adamyan A, Bauch T and Kubatkin S E 2012 *J. Appl. Phys.* **112** 123905
- [57] Tsypliyatsev O and Loss D 2009 *Phys. Rev. A* **80** 023803
- [58] Tsypliyatsev O and Loss D 2010 *Phys. Rev. B* **82** 024305
- [59] Sträter C, Tsypliyatsev O and Faribault A 2012 *Phys. Rev. B* **86** 195101

PAPER

Effective spin Hamiltonian of a gated triple quantum dot in the presence of spin–orbit interaction

To cite this article: Marko Milivojevi and Dimitrije Stepanenko 2017 *J. Phys.: Condens. Matter* **29** 405302

View the [article online](#) for updates and enhancements.

Related content

- [Three-electron spin qubits](#)
Maximilian Russ and Guido Burkard
- [Physics of lateral triple quantum-dot molecules with controlled electron numbers](#)
Chang-Yu Hsieh, Yun-Pil Shim, Marek Korkusinski et al.
- [Electron spins in artificial atoms and molecules for quantum computing](#)
Vitaly N Golovach and Daniel Loss

Recent citations

- [Symmetric spin–orbit interaction in triple quantum dot and minimisation of spin–orbit leakage in CNOT gate](#)
Marko Milivojevi



IOP | ebooks™

Bringing you innovative digital publishing with leading voices to create your essential collection of books in STEM research.

Start exploring the collection - download the first chapter of every title for free.

Effective spin Hamiltonian of a gated triple quantum dot in the presence of spin–orbit interaction

Marko Milivojević¹ and Dimitrije Stepanenko²

¹ Department of Physics, University of Belgrade, Studentski trg 12, 11158 Belgrade, Serbia

² Institute of Physics Belgrade, University of Belgrade, Pregrevica 118, 11080 Belgrade, Serbia

E-mail: milivojevic@rcub.bg.ac.rs

Received 7 June 2017, revised 12 July 2017

Accepted for publication 13 July 2017

Published 31 August 2017



Abstract

We derive and study the effective spin Hamiltonian of a gated triple quantum dot that includes the effects of spin–orbit interaction and an external magnetic field. In the analysis of the resulting spin interaction in linear and in general triangular geometry of the dots, we show that the pairwise spin interaction does depend on the position of the third dot. The spin–orbit induced anisotropy, in addition to changing its strength, also changes its symmetry with the motion of the third quantum dot outside the linear arrangement. Our results present a simplified model that may be used in the design of quantum computers based on three-spin qubits.

Keywords: spin–orbit coupling, quantum dots, exchange interactions

(Some figures may appear in colour only in the online journal)

1. Introduction

Spins of electrons confined to the single-electron quantum dots have been proposed as carriers of quantum information in solid-state quantum computers [1, 2]. They were the focus of intense theoretical and experimental investigation, leading to the understanding of the mechanisms of spin interactions with the surrounding semiconductor substrate through spin–orbit interaction and hyperfine coupling to the nuclei, as well as the interaction between the spins on neighboring quantum dots [3]. Spins in single-electron quantum dots coupled by the effective spin Hamiltonian are the basis for quantum computing schemes of ever simpler control and better coherence properties.

Encoding a qubit into states of few spins offers a trade-off between the number of used quantum dots and the complexity of required control mechanisms. With the original single-spin encoding [1], implementation of the quantum gates requires control of exchange interaction between the neighboring quantum dots, as well as of the rotations of individual spins about two, preferably orthogonal, axes. The requirement for two independent axes of rotation proved to be experimentally challenging. Encoding a qubit into states of a pair of spins

reduces the control requirement to the exchange interaction and rotations about a single axis. A rather useful technique for electrically controlled qubit rotations is the electric-dipole-induced spin resonance [4–7]. In this implementation, spin–orbit interaction [8–11] and nuclear spins [12–15] are typical sources of anisotropy, but they are also the main sources of spin decoherence. The control requirements are reduced even further by encoding the qubits into states of three spins. With the isotropic spin exchange interaction as the only resource, quantum computation is possible in three spin qubits encoded into states of equal total spin and equal projection of this total spin to the quantization axis [16–20]. Sequences of few tens of interaction pulses that produce a set of quantum gates sufficient for quantum computation have been found both numerically [16] and analytically [17–20].

A recently developed scheme for quantum computation, based on three-spin resonant exchange qubits, uses periodic modulation of the exchange interaction between the quantum dots to implement quantum gates [21–23]. In this and other three-spin qubits the strongest interaction, isotropic exchange $J_{ij}\mathbf{S}_i \cdot \mathbf{S}_j$ between the spins within a qubit, does not mix the logical qubit states with other states of the three spins [24].

The scheme relies on the isotropic exchange form of interaction between the spins, and on the independence of the interaction between two spins on the third one. This requirements should be well satisfied when the spin–orbit interaction is weak and when the dots that are not involved in the current spin operation are well separated from the ones that are.

The quantum dots are described in terms of interaction between their spins. Therefore, developing a simple prediction of the effective spin Hamiltonian for electrons bound to quantum dots is useful for predicting the behavior of spins in experiments. In this work, we find the effective interaction between the spins in a triplet of quantum dots that can represent either a single three-spin qubit or a pair of spins involved in a quantum gate in the presence of a third spin [25]. The model that we use includes a potential of a triple dot, Coulomb repulsion between the electrons, an external magnetic field [26] and spin–orbit interaction. As opposed to earlier work [27–29], we derive the full triple dot effective Hamiltonian suitable for description of experiments on multiple spin qubits, and do not rely on the approximation of decoupled double dot, while taking the spin–orbit interaction into account. The calculations are done at the level of Hund–Mulliken approximation, including one orbital state per quantum dot, leading to the effective Hubbard model and the low-energy effective spin Hamiltonian. We quantify the deviations of these resulting interactions from the ideal case of pairwise isotropic interactions independent from the third dot outside the pair. Spin–orbit interaction, to the lowest order, is described by the pairwise Dzyaloshinsky–Moriya interaction between the spins. The presence of the third dot leads to small changes in the interaction strength and its anisotropy. With the exception of the linear arrangement of the dots, the symmetry axis of the effective spin interaction depends on the position of the third dot. The magnetic field adds a small three-body term, in agreement with the earlier results [27–29].

In section 2 we introduce the model of triple quantum dot. In section 3 we derive the effective spin Hamiltonian for various geometries. In section 4, we discuss the isotropic interaction, and find the influence of the position of the third dot on the pairwise spin interaction. In section 5, we discuss the anisotropy in spin interaction and its variations as the geometric arrangement of the dots goes from linear to triangular. We present our conclusions in section 6.

2. Model

We consider a system of three coupled quantum dots (QDs) with three conduction band electrons bound to them. The dots are modeled by a potential with the minima at the position of the dots. Electrons in the potential minima interact through Coulomb interaction, feel the influence of the substrate through spin–orbit interaction, and move in an external magnetic field. The system Hamiltonian is

$$H = H_0 + C + H_{SO} + H_Z, \quad (1)$$

$$H_0 = \sum_{i=a,b,c} h_i, \quad (2)$$

$$h_i = \frac{1}{2m} (\mathbf{p}_i + q\mathbf{A}(\mathbf{r}_i))^2 + V(\mathbf{r}_i), \quad (3)$$

$$C = \sum_{i \neq j} \frac{1}{4\pi\epsilon_0\epsilon_r} \frac{e^2}{|\mathbf{r}_i - \mathbf{r}_j|}, \quad (4)$$

$$H_{SO} = \sum_{i=a,b,c} H_{D,i} + H_{R,i}, \quad (5)$$

$$H_Z = \sum_{i=a,b,c} g\mu_B \mathbf{B} \cdot \mathbf{S}_i. \quad (6)$$

The single-particle noninteracting Hamiltonians h_i describe an electron in the quantum dots potential $V(\mathbf{r}_i)$, and in the magnetic field derived from the vector potential $\mathbf{A}(\mathbf{r})$. We model the potential that binds the electrons to the triple dot as

$$V(\mathbf{r}) = \sum_{i=a,b,c} \frac{m\omega_0^2}{2} \left(1 - \frac{h}{\lambda^2}\right) \left((\mathbf{r} - \mathbf{R}_i)^2 e^{-\frac{m\omega_0^2}{2\lambda^2\hbar}(\mathbf{r} - \mathbf{R}_i)^2} \right) + \hbar\omega_0 h \left(1 - e^{-\frac{m\omega_0^2}{2\lambda^2\hbar}(\mathbf{r} - \mathbf{R}_i)^2}\right). \quad (7)$$

This potential separates into three harmonic wells of frequency ω_0 near the minima at $\mathbf{r} = \mathbf{R}_i$, $i = a, b, c$. The effective Bohr radius of a single isolated harmonic potential at the position of a dot is $a_B = \sqrt{\hbar/m\omega_0}$. We use $\hbar\omega_0 = 3$ meV [30], a typical value obtained in the experiments. The mass m is the conduction band electron effective mass, and for GaAs quantum dots it is $m = 0.067 m_e$, where m_e is the electron mass. The potential is parabolic in the vicinity of minima located at \mathbf{R}_i , and the parabolas are cut off by a Gaussian of width λa_B . The parameter h controls the depth of parabola. With parameter values $h = 3$ and $\lambda = 0.2$ the potential can host well localized and interacting spins.

Coulomb interaction of the electrons is described by C . We have used unscreened Coulomb potential with the effects of the host material described by the dielectric constant ϵ_r . For GaAs, $\epsilon_r = 13.1$.

Quantum dots are most often fabricated in two-dimensional electron gas (2DEG) within a III–V semiconductor. This typical host material for QDs shows both the Dresselhaus [31] and Rashba [32] SO interactions, and to a good approximation they are both linear in crystal momentum components. The form of SO coupling is constrained by the symmetry of the structure, and for GaAs 2DEG grown in [001] crystallographic direction it can be written as

$$H_{SO} = \boldsymbol{\Omega}(\mathbf{k}) \cdot \mathbf{S}, \quad (8)$$

where

$$\boldsymbol{\Omega}(\mathbf{k}) = (-f_D k_{[100]} + f_R k_{[010]}) \mathbf{e}_x + (-f_R k_{[100]} + f_D k_{[010]}) \mathbf{e}_y, \quad (9)$$

and f_R and f_D are Rashba and Dresselhaus parameters, respectively. The values of the parameters are fixed by the substrate composition and the shape of the potential well of the 2DEG. Components of wave vectors in the crystallographic frame are expressed in our coordinate system as

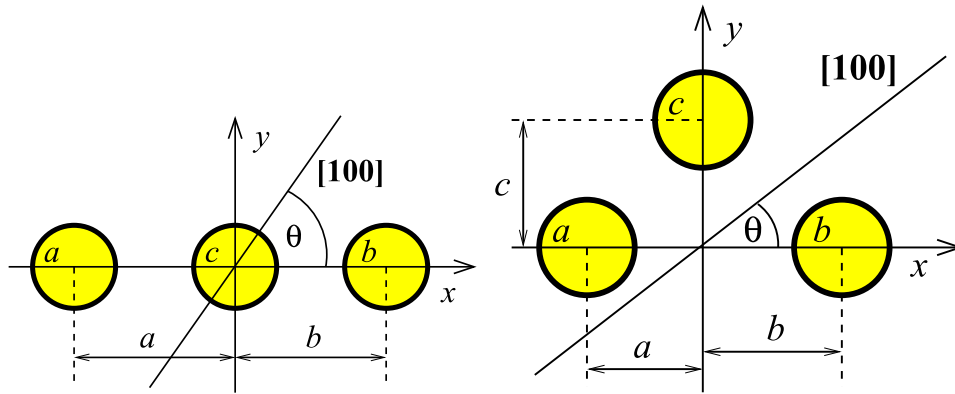


Figure 1. Geometry of the triple dot. Linear arrangement of the dots is shown in the left panel. Dots a , b and c lie on the x axis. Dot c is fixed at the origin, while the other two dots are allowed to move along the x axis. Triangular arrangement of the dots is illustrated on the right panel. Dots a and b are positioned on the x axis. The y coordinate of dot c can vary. In the magnetic field, we translate the coordinates so that the center of mass of the triple dot is at the origin. The orientation of the triple dot with respect to the crystalline axes of the substrate 2DEG in the (001) plane of a III–V semiconductor is set by the angle θ between the x axis and the $[100]$ crystalline axis.

$k_{[100]} = \cos\theta k_x + \sin\theta k_y$ and $k_{[010]} = -\sin\theta k_x + \cos\theta k_y$. The geometry of the dots is described by the angle θ that the x axis makes with $[100]$ crystallographic direction, see figure 1.

Orbital effects of the magnetic field are due to the field component in the direction normal to the quantum dots. This field couples with electric charge through the vector potential $\mathbf{A} = \frac{B_z}{2}(-y - Y_0, x - X_0, 0)$, where $(X_0, Y_0, 0) = \mathbf{R}_0 = (\mathbf{R}_a + \mathbf{R}_b + \mathbf{R}_c)/3$ is the position of the center of three dots. This choice of gauge preserves the symmetry of triangular arrangements in the presence of magnetic fields. Zeeman term, H_Z , couples magnetic field and electron spins

$$H_Z = \sum_{i=a,b,c} g\mu_B \mathbf{B} \cdot \mathbf{S}_i, \quad (10)$$

where g is the g -factor ($g \approx -0.44$ for GaAs), and μ_B is the Bohr magneton. Zeeman splitting is much smaller than the relevant orbital energies $g\mu_B B_z / \hbar\omega_0 \sim 0.03$ for magnetic field of interest in this system. We can neglect the Zeeman splitting when we deal with orbital degrees of freedom and include it later in the effective Hamiltonian.

3. Effective Hamiltonian

Experiments and quantum computing schemes that involve qubits in single-electron QDs are described in terms of effective spin Hamiltonians in which each electron spin is assigned to one of the QDs in the device [15, 16, 19, 20, 33–35]. This picture is appropriate in the limit of well localized electronic orbitals with small overlaps. Orbital excitations beyond the ground state within the quantum dots are separated by an energy of the order $\hbar\omega_0$, and can be safely neglected in a typical quantum dot potential. At the second step, the doubly occupied states of the Hubbard model with a pair of electrons in total spin $S = 0$ state sharing an orbital state are also removed from the model. In this final model, the orbital state is completely defined by the dot in which the electron resides, and the only remaining degrees of freedom are spins. The

effect of the virtual transitions to doubly occupied states are taken into account as an effective spin interaction. The electrons can be described by spins at the localized sites only if the Hubbard model states are localized to single dots.

An electron in the isolated QD is well described by the orbital ground state of a two-dimensional harmonic oscillator in external magnetic field. With the reduction of the dot size, the energy levels are split due to confinement. In the small dots and at low temperature, $k_B T \ll \hbar\omega_0$, the state of an electron in a quantum dot approaches the oscillator ground state in the presence of a magnetic field, i.e. the Fock–Darwin (FD) ground state [36]. Spin degrees of freedom give us two possible states which can be occupied by the electron in a FD state. That gives us 20 possible states of three electrons in three orbitals. We can divide these states in two groups according to their energies. The first group consist of eight states in which each QD is occupied by one electron, the second group is formed from 12 states where one QD is doubly occupied. We neglect the states in which all three electrons lie on a single dot, since their energy gap is larger by both the Coulomb repulsion U and an orbital excitation of the quantum dot.

Since the Coulomb repulsion between two electrons is much stronger when they occupy the same QD, the singly occupied state are low and the doubly occupied ones are high in energy. We are interested only in the eight-dimensional low-energy subspace of twenty-dimensional Hamiltonian H . These eight states encode the three-spin qubit.

The low- and high-energy space of the three-electron system are coupled by spin-independent terms of Coulomb repulsion and tunneling, as well as by the spin-dependent tunneling caused by the SO interaction. The effects of this coupling are seen as the effective interaction between the electrons in the low energy space. The states in the low-energy sector all have nominally the same orbital distribution with one spin-1/2 electron in each of the dots. Therefore, the effective low-energy Hamiltonian describes the interaction between localized spins. The Zeeman interaction does not affect the orbital states, and does not couple the low- and high-energy subspaces, so it appears in the effective Hamiltonian directly.

The Fock–Darwin ground state (FD) for harmonic confinement centered at the dot origin (x_0, y_0) is

$$\varphi(x, y) = \sqrt{\frac{m\omega}{\pi\hbar}} e^{-i\frac{eB_z}{2\hbar}(xy_0 - yx_0)} e^{-\frac{m\omega}{2\hbar}((x-x_0)^2 + (y-y_0)^2)}, \quad (11)$$

where $\omega = \sqrt{\omega_0^2 + \frac{1}{4}\omega_c^2}$, and the cyclotron frequency $\omega_c = \frac{eB_z}{m}$ measures the orbital’s magnetic compression. In the case of linear arrangement, see figure 1, we set the origin at the position of dot c , while dots a and b move along the x axis. We parameterize the triangular arrangement by putting the dots a and b along the x axis, and the dot c on the y axis. The FD states in a , b and c are φ_a , φ_b and φ_c , respectively. In a zero magnetic field, these wave functions are real.

The FD states are non orthogonal. Their overlaps, $S_{ij} = \langle \varphi_i | \varphi_j \rangle$ ($i, j \in \{a, b, c\}$), behave as

$$|S_{ij}| \propto \exp\left(-\frac{|r_{ij}|^2}{(2a_B)^2}\right), \quad (12)$$

quickly decaying once the interdot distance exceeds $2a_B$, twice the effective single dot Bohr radius. The magnetic field in z -direction makes the overlaps complex. Explicit expressions for the overlaps are given in appendix.

The calculation of matrix elements of the three-electron Hamiltonian is simplified if the basis single-electron orbitals are orthogonal. If $\varphi = (\varphi_a, \varphi_b, \varphi_c)^T$ represents three FD states, then the transformation $\Phi = S^{-1/2}\varphi$ gives orthogonal Wannier states $\Phi = (\Phi_a, \Phi_b, \Phi_c)^T$. The resulting orthogonal basis is not unique. We have used the direct square root of the overlap matrix. Another common choice is the transformation that, in addition to producing an orthogonal basis, minimizes the spread of the resulting orbitals [37]. We choose the phases in Φ so that the states become real in the limit of vanishing magnetic field.

The Hamiltonian H , (1), acts in the space spanned by placing three electrons in the states $c_{i,s}^\dagger|0\rangle$, where the index $i = a, b, c$ counts the Wannier orbitals, and $s = \pm 1/2$ labels the spin. The matrix elements of single-particle part of H between FD states, $\langle \text{FD1} | H_0 + H_{\text{SO}} | \text{FD2} \rangle$, and the matrix elements of Coulomb interaction between the pairs of FD states, $\langle \text{FD1}, \text{FD2} | C | \text{FD3}, \text{FD4} \rangle$ are calculated explicitly and presented in appendix. They are combined into matrix elements between the Wannier states. The effects of indistinguishability of the particles are accounted for by assigning the signs to the vacuum expectation value of the products of 8 creation and annihilation operators for spin-1/2 electrons in Wannier states when calculating the matrix elements of single particle operator $H_0 + H_{\text{SO}}$, and to the products of ten operators in two-particle operator C .

Resulting Hamiltonian is the Hubbard model for three electrons in three orbitals centered at the dots positions. The effective spin Hamiltonian is found by calculating the matrix elements of the Hamiltonian H between the states of three spin-1/2 electrons in Wannier orbitals, and projecting the result to the low-energy space, using the Schrieffer–Wolff (SW) transformation up to the fourth order [38, 39]. This perturbative

calculation is valid when the separation in energy between the singly- and doubly-occupied states, which is of the order of on-site repulsion U , is much larger than the matrix elements connecting the states, t . In our calculations $t/U < 0.25$.

The effective spin Hamiltonian of three localized spin-1/2 particles is

$$H = \sum_i H_i^{(1)}(\mathbf{S}_i) + \sum_{\langle i,j \rangle} H_{ij}^{(2)}(\mathbf{S}_i, \mathbf{S}_j) + H_{abc}^{(3)}(\mathbf{S}_a, \mathbf{S}_b, \mathbf{S}_c). \quad (13)$$

In the most general case, single-, two- and three-spin interactions ($H^{(1)}$, $H^{(2)}$, and $H^{(3)}$) appear in (13). The dominant terms, H_0 and C in the Hamiltonian (1) are spin-independent and the dominant spin interaction is two-electron isotropic exchange $H_{ex}(\mathbf{S}_i, \mathbf{S}_j) = J_{ij}\mathbf{S}_i \cdot \mathbf{S}_j$. The interactions are parameterized as

$$H_i^{(1)} = \mathbf{b}_i \cdot \mathbf{S}_i, \quad (14)$$

$$H_{ij}^{(2)} = J_{ij}\mathbf{S}_i \cdot \mathbf{S}_j + \mathbf{d}_{ij} \cdot (\mathbf{S}_i \times \mathbf{S}_j) + \mathbf{S}_i \cdot \Gamma_{ij} \cdot \mathbf{S}_j, \quad (15)$$

$$H_{abc}^{(3)} = \sum_{ijk} \gamma_{ijk} S_a^i S_b^j S_c^k, \quad (16)$$

where the isotropic exchange couplings J_{ij} , $i \neq j = a, b, c$ are scalars, effective magnetic fields \mathbf{b}_i , $i = a, b, c$, and antisymmetric anisotropies \mathbf{d}_{ij} , $i \neq j = a, b, c$ are vectors, symmetric anisotropies Γ_{ij} , $i \neq j = a, b, c$, are symmetric traceless rank-2 tensors, and γ_{ijk} , $i, j, k \in \{x, y, z\}$ are components of a direct product of three spin components that can combine into various rank-3 tensors. We will later use a scalar $\alpha = (1/6) \sum_{i,j,k} \varepsilon_{ijk} \gamma_{ijk}$ to parameterize the mixed product contribution to the three-spin interaction $H_\alpha^{(3)} = \alpha \mathbf{S}_a \cdot (\mathbf{S}_b \times \mathbf{S}_c)$.

Before we proceed, we expose our goals regarding the analysis of the effective spin Hamiltonian, since the coupled quantum dots system has already been exhaustively studied before. The simplest way to study this problem is to use tight-binding t - U model [27] for spin-independent terms, in which magnetic field is included through Peierls phases. The t - U model can not be used to study dependence of exchange parameters on the distance of the dots and/or the applied external magnetic field, which also affects the tunneling matrix elements. In a more detailed approach [26], magnetic field and distance dependence are incorporated in the parameters of Hubbard model. We expand on these results in two ways and focus on the case of three electrons in a triple dot that is relevant for quantum computing applications. We calculate the anisotropic exchange, parameterized by \mathbf{d}_{ij} , $i \neq j = a, b, c$ in the full triple-dot setup. In addition, we find that both this anisotropy and the dominant isotropic exchange parameterized by J_{ij} , $i \neq j = a, b, c$ depend on the full system geometry that includes the position of the third dot. These parameters are important in any implementation of a three-spin qubit. They quantify the deviations from the ideal case of pure isotropic exchange, and it is for this ideal form of interaction that the gate implementations were developed. Furthermore, even in the absence of accurate predictions of the intensity of resulting interactions, their symmetry may

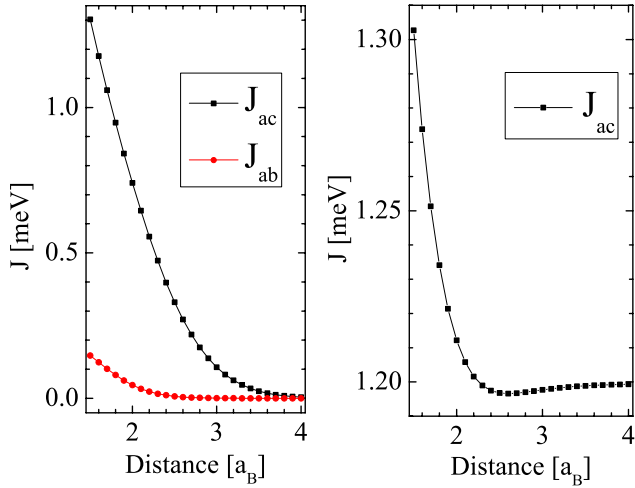


Figure 2. Exchange interaction in a linear triple quantum dot. In the left panel, exchange interaction parameters are plotted versus distance of the dots a and c in a symmetric arrangement. Dot c is fixed at the origin while the other two dots are able to move in such manner that $-a = b$. Dependence of the nearest neighbor interaction on the position of the third dot is illustrated in the right panel. For the linear arrangement of the dots with $a = -1.5a_B$ and $c = 0$, dependence of J_{ac} versus the distance of the dots bc (going from $1.5a_B$ to $4a_B$) is plotted. Parameters of the potential are $h = 3$ and $\lambda = 0.2$.

provide valuable information in designing the time-dependent spin Hamiltonians that are not affected by this deviation from the ideal. Having these goals in mind, we proceed with the analysis of the effective spin Hamiltonian.

4. Isotropic interaction

The dominant terms in our model Hamiltonian are kinetic energy, confinement and Coulomb repulsion. All of these terms are spin-independent, so they cause an effective spin interaction invariant to spin rotation. Isotropic Hamiltonian with pairwise interaction can be written in the form

$$H_{\text{iso}} = J_{ab} \mathbf{S}_a \cdot \mathbf{S}_b + J_{ac} \mathbf{S}_a \cdot \mathbf{S}_c + J_{bc} \mathbf{S}_b \cdot \mathbf{S}_c, \quad (17)$$

parameterized by the exchange interaction strengths J_{ab} , J_{ac} , and J_{bc} , as in (15). We analyze the dependence of these interactions on the geometry of the system. Raising (lowering) of the barrier height between the dots has the same effect as an increase (decrease) of the distance between them. This observation connects our results with experiments in control of the exchange strength. In the heart of the effective spin Hamiltonian approach is the requirement that orbitals of electrons are well localized at the centers of the quantum dots. Our results suggest that this condition is satisfied for $\ell > 1.5a_B$, and in this region $t/U < 0.23$. Exchange interactions in the linear arrangement, with equal nearest neighbor distances ($\ell_{ac} = \ell_{bc} = \ell$), are present in each pair of dots, as shown in figure 2. The distance dependence reveals the influence of third dot on two-spin interaction. In contrast to the standard approach in deriving the effective Hamiltonian using the Hubbard model of an isolated pair of dots, with only nearest neighbor interaction [40], our model also includes the

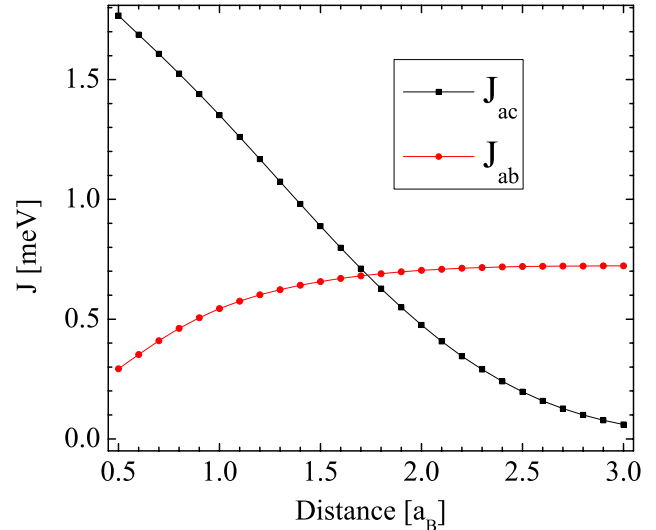


Figure 3. Exchange interaction parameters for the isosceles triangular arrangement. The plot shows the strength of exchange interaction as a function of deviation from the linear arrangement. Dot $a(b)$ is fixed at the $(-a_B, 0)(a_B, 0)$ and the c dot moves along the y axis from $0.5a_B$ to $3a_B$. In this case $J_{ac} = J_{bc}$, so only two different exchange parameters are plotted. When $c = \sqrt{3}a_B$, equilateral geometry is achieved with $J_{ac} = J_{bc} = J_{ab}$. Parameters of the potential are $h = 3$ and $\lambda = 0.2$.

matrix elements between the dots a and b , leading to a new term $J_{ab} \mathbf{S}_a \cdot \mathbf{S}_b$ in the Hamiltonian. This term is smaller, but comparable to J_{ac} for the $\ell < 2a_B$, see figure 2 (left). Since J_{ab} tends to zero much faster than J_{ac} , for $\ell > 2.5a_B$ it can be neglected.

In QD based quantum computing the control over spins is achieved through switching the pairwise exchange interactions on and off. It is assumed that while a gate is performed between the spins on neighboring QDs, all the other spins do not interact at all. In the effective Hamiltonian (17), H_{iso} , indirect coupling terms between the two dots are present due to the existence of the third dot. Second order contributions are smaller than the direct coupling, but observable.

Pairwise interaction between neighboring quantum dots depends on the position of the third one. In (figure 2 (right)), J_{ac} is plotted as a function of distance cb , while the distance ac is fixed at $1.5a_B$, explicitly showing the effect of the third dot. In the regime of totally decoupled third dot, exchange interaction for the double QD case is obtained. The variations of pairwise exchange coupling with the position of the third dot, show that the interaction J_{ac} can be controlled indirectly, by moving the dot b or by changing the barrier height between the dots c and b .

When the dots lie in a triangular arrangement, the relative strengths of isotropic exchange show a wider variety. We analyze these differences in an isosceles triangular arrangement (figure 3). The dots on x axis have the coordinates $(\pm a_B, 0)$, while y coordinate of the middle dot is moved along the y axis from $0.5a_B$ (t/U is then 0.17) to $3a_B$. Coupling is antiferromagnetic in this case, as in the case of double dot and in the linear arrangement of triple dot. Intensities of interactions $J_{ac} = J_{bc}$ decrease and tend to zero with the separation of the middle dot. On the other hand, J_{ab} has a slight increase due to

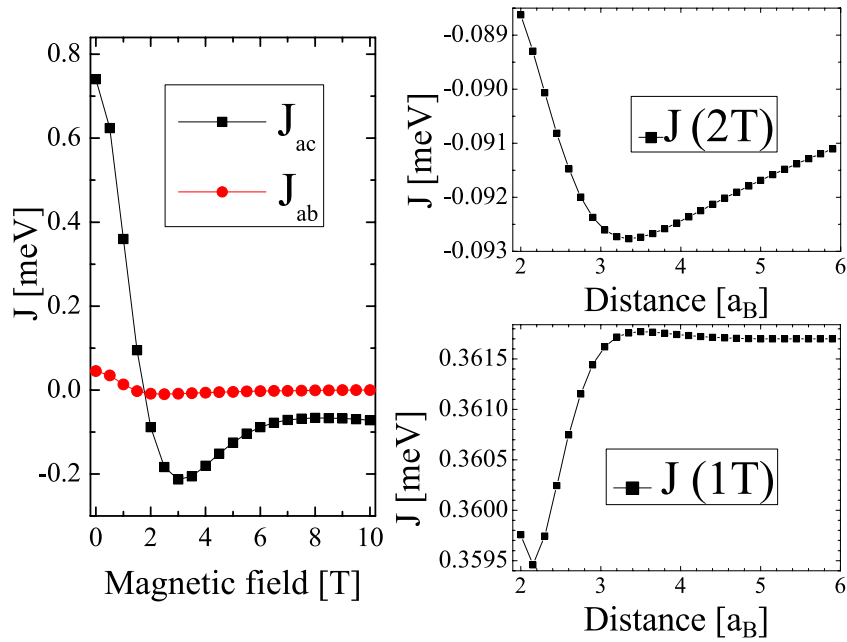


Figure 4. Exchange interaction in the magnetic field. In the linear arrangement of the dots with $ac = cb = 2a_B$, magnetic field alters the exchange interaction, and can even change its sign, as seen in the left panel. In the right panel, exchange parameter J_{ac} ($ac = 2a_B$) is plotted as function of the distance cb . The couplings are markedly different in external fields of 1 T and 2 T. Parameters of the potential are $h = 3$ and $\lambda = 0.2$.

the vanishing of negative hopping terms from a to b through c . Nonzero limit of J_{ab} and zero of J_{ac} suggest that we are in the regime of two dots decoupled from the third. For the equilateral arrangement ($c \approx 1.73a_B$), $J_{ab} = J_{ac}$, as expected. The main difference with respect to the linear setup is that all three dots can contribute to the full Hamiltonian. In the equilateral case, the symmetry requires that the eigenstates are fully delocalized across the three dots, and the eigenstates of three spins are correlated across the dots [41–43].

In the presence of magnetic fields, the orbitals of quantum dots shrink, and the overlaps become complex. In the linear arrangement, low-energy Hamiltonian has the same form as (17), but the intensities and the sign of these parameters are magnetic field dependent. In (figure 4 (left)), we illustrate the exchange coupling in a linear system with $ac = cb = 2a_B$ and the magnetic field strength going from 0 T to 10 T. In contrast to the nonmagnetic case, for magnetic field $1\text{ T} < B_z < 2\text{ T}$ we observe the transition from antiferromagnetic to ferromagnetic coupling constants due to the long-range Coulomb interaction. This transition was already observed in double quantum dots [44]. The antiferro-ferro transition can also be obtained by electrical means [45]. Magnetic field contributes to the FD states through the phase factor and magnetic squeezing, leading to a better localization of orbitals and weaker interaction. This is the reason for decline of isotropic exchange interaction strength, see (figure 4 (left)). In (figure 4 (right)) we illustrate the effect of the dot b on the exchange parameter J_{ac} . We start with the case where $ac = cb = 2a_B$, and move b so that cb goes from $2a_B$ to $6a_B$. Interactions in this setup depend on the magnetic field. In contrast to the case of linear geometry, the influence of dot b on J_{ac} is weak.

In the triangular arrangement, when magnetic field is introduced, a new term,

$$H_\alpha^{(3)} = \alpha \mathbf{S}_a (\mathbf{S}_b \times \mathbf{S}_c), \quad (18)$$

appears in the effective Hamiltonian [27–29]. This term depends on the flux enclosed by the three dots loop, and vanishes in the linear setup. Three-spin interaction in the Hubbard model is described by the three hopping matrix elements, making it weaker than the exchange interaction by an order of magnitude. In the triangles with large surface area, electrons show more delocalization across the dots in the low-energy states. In order to localize these electrons at the dots, and make their state more similar to perfectly localized spins of spin-based quantum dot qubits, the dot separation need to be larger than in the absence of magnetic field.

This condition further means that all the gate operations are much slower than in the linear setup since exchange parameters are weaker in this case. On the other hand, three-spin term can potentially be useful for preparation of the states with three-spin entanglement. The distance dependencies of the exchange parameters ($J_{ab} = J_{ac} = J_{bc} = J$) and the three-spin interaction in the equilateral geometry are illustrated in (figure 5). Spins are decoupled for magnetic fields stronger than 2 T. In weaker fields, $B_z < 2\text{ T}$ the exchange interaction and the three-spin term grow to the values that can affect the quantum computation.

5. Anisotropic interaction

The spin-orbit interaction, described by H_{SO} , introduces anisotropy into the effective spin Hamiltonian. The strongest interaction is rotationally invariant and given in (17). The weak terms describing tunneling caused by SO interaction, $|\Omega|/|t| \sim 0.1$ produce a second-order correction to the isotropic exchange parameters in the effective spin Hamiltonian.

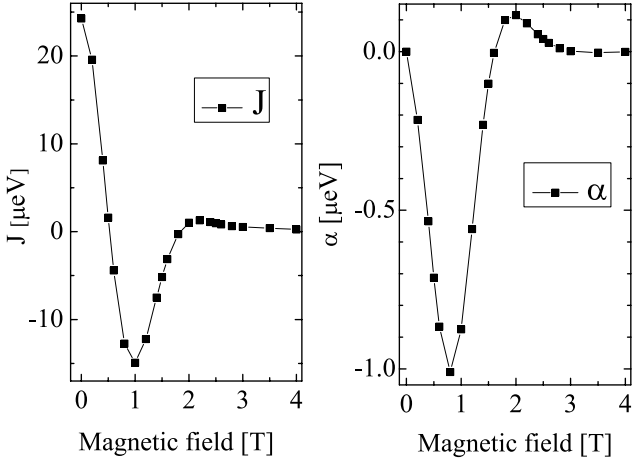


Figure 5. Exchange interaction parameter J and the three-spin term α for the equilateral triangular arrangement as a function of the magnetic field strength. Distance between the dots is $3.5a_B$. Parameters of the potential are $h = 3$ and $\lambda = 0.2$.

The dominant SO effect is the reduction of the symmetry of effective Hamiltonian, expressed as a sum of three antisymmetric Dzyaloshinsky–Moriya (DM) terms

$$H_{DM} = \mathbf{d}_{ab} \cdot (\mathbf{S}_a \times \mathbf{S}_b) + \mathbf{d}_{ac} \cdot (\mathbf{S}_a \times \mathbf{S}_c) + \mathbf{d}_{bc} \cdot (\mathbf{S}_b \times \mathbf{S}_c), \quad (19)$$

where the z components of all three \mathbf{d} vectors are equal to zero. Higher-order contributions of SO interaction give the Γ -terms of $H^{(2)}$ in (15), which are another factor $|\Omega|/t$ weaker than H_{DM} . We analyze only the DM terms, being the dominant correction to the isotropic interaction. Vectors \mathbf{d} originate from the orbital Hamiltonian written in a scalar product form (8). On hopping between the dots, these terms flips the component of spin \mathbf{S} along the quantization axis, with or without an additional phase. The hopping amplitude and the direction of spin after hopping depend on $\Omega(\mathbf{k})$. Matrix elements $\beta_{ij} = \langle \varphi_i | \Omega(\mathbf{k}) | \varphi_j \rangle$ of $\Omega(\mathbf{k})$ between FD states are calculated in appendix. Parameters β_{ij} depend on the geometry of the system (parameters a , b and c), overlap integrals S_{ij} between the FD states φ_i and φ_j , Rashba and Dresselhaus parameters f_R and f_D , as well as on the orientation of the triple dot with respect to the crystallographic axes, as described by θ . If we scale every β vector by the appropriate overlap integral, we obtain a simple relation

$$\frac{\beta_{ab}}{S_{ab}} + \frac{\beta_{bc}}{S_{bc}} + \frac{\beta_{ca}}{S_{ca}} = 0. \quad (20)$$

Additionally, the components of these vectors are constrained by the geometry of triple dot to satisfy relations

$$\frac{\beta_{ab}^y}{\beta_{ab}^x} = \frac{f_R \cos \theta + f_D \sin \theta}{f_D \cos \theta + f_R \sin \theta}, \quad (21)$$

$$\frac{\beta_{bc}^y}{\beta_{bc}^x} = \frac{(\ell f_R + c f_D) \cos \theta + (-c f_R + \ell f_D) \sin \theta}{(c f_R + \ell f_D) \cos \theta + (\ell f_R - c f_D) \sin \theta}, \quad (22)$$

where $\ell \in \{a, b\}$. Since every FD state centered at the observed point is the largest contributor to the Wannier state in the same dot, we expect that the relation between the components of β parameters in (21) is paralleled by the same relation between

the components of \mathbf{d} parameters scaled by the isotropic exchange interaction strengths J . We investigate this relation and find the \mathbf{d} vectors as a function of the system's geometry, SO parameters f_R , f_D and the orientation of the system with respect to the crystallographic axes, θ .

In the linear arrangement, the triple dot is an extension of the double quantum dot, and some of the properties of the double quantum dot [10], also hold true in this case. For example, when $f_D = f_R$ and $\theta = \frac{3\pi}{4}$, SO effects are equal to zero. The ratio d_{ij}^y/d_{ij}^x is independent of the dots positions,

$$\frac{d_{ij}^y}{d_{ij}^x} = \frac{f_R \cos \theta + f_D \sin \theta}{f_D \cos \theta + f_R \sin \theta}, \quad (23)$$

for every pair of dots. Our numerical analysis is performed for the Rashba and Dresselhaus parameters equal to $f_R = 5 \text{ meV \AA}$ and $f_D = 16.25 \text{ meV \AA}$ [46], respectively, and the angles $\theta = 0$ and $\pi/4$. For $\theta = 0$, ratio was $\frac{d^y}{d^x} = \frac{f_R}{f_D}$. For $\theta = \frac{\pi}{4}$, x and y component were equal, suggesting that SO vectors are along the crystallographic axis, independent on the f_R and f_D . The intensities of SO vectors for the cases discussed above are plotted as functions of the nearest neighbor distance in (figure 6 (left)). The condition analogous to (20), with β vectors replaced by \mathbf{d} vectors is never satisfied in the linear setup.

In three-spin qubits, anisotropy is an important source of deviations from the ideal behavior. We analyze the effect of the third dot on DM vector between the other two dots. In (figure 6 (right)) we show this effect for spin–orbit angles 0 and $\pi/4$ and Rashba and Dresselhaus parameters, $f_R = 5 \text{ meV \AA}$ and $f_D = 16.25 \text{ meV \AA}$, respectively. The direction of DM vector does not change, but its intensity does. Orientation of the dots within the plane, described by θ , does not change the nature of this dependence, but only the intensities of \mathbf{d}_{ij} .

Spin–orbit coupling always influences spins in the triangular arrangement, due to the fact that all three β vectors cannot be zero at the same time. The vector β_{ab} is zero when $f_R = f_D$ and $\theta = 3\pi/4$, while β_{ac} vanishes when $f_R = f_D$ and $\tan \theta = \frac{c+a}{c-a}$. Condition $\beta_{bc} = 0$ yields $f_R = f_D$ and $\tan \theta = \frac{c+b}{c-b}$. These requirements are compatible only when $c = 0$, i.e. with the dots in linear arrangement.

Apart from the fact that SO effects cannot be neglected, in this setup the directions of antisymmetric anisotropies \mathbf{d} can vary. To illustrate this feature, we analyze the isosceles right triangle geometry (figure 7) for different orientations of the triple dot with respect to crystalline axes ($\theta = 0$ and $\theta = \frac{\pi}{4}$). In this geometry, every dot is at the same distance from the origin, $-a = b = c$ and the values of f_R and f_D are unchanged from their values in the previously considered case of aligned dots. Using the relation (21) for this geometry we find

$$\frac{\beta_{ab}^y}{\beta_{ab}^x} = \frac{f_R}{f_D}, \quad \frac{\beta_{ac}^y}{\beta_{ac}^x} = 1, \quad \frac{\beta_{bc}^y}{\beta_{bc}^x} = -1 \quad (\theta = 0), \quad (24)$$

$$\frac{\beta_{ab}^y}{\beta_{ab}^x} = 1, \quad \frac{\beta_{ac}^y}{\beta_{ac}^x} = \frac{f_D}{f_R}, \quad \frac{\beta_{bc}^y}{\beta_{bc}^x} = \frac{f_R}{f_D} \quad (\theta = \frac{\pi}{4}). \quad (25)$$

Our numerical results suggest that the analogous ratios of the components of \mathbf{d} vectors are reached when the dots are more

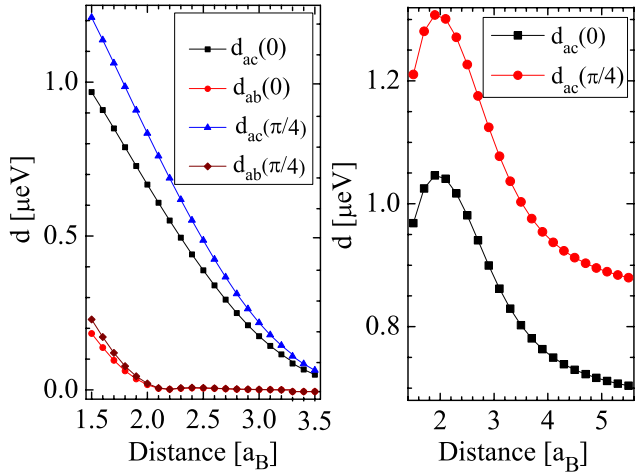


Figure 6. Dependence of anisotropy in two-spin interaction on geometry and on the orientation of linear triple quantum dot. (left) Intensity of SO parameters for the linear triple quantum dot in the cases of SO angles 0 and $\pi/4$. Dot c is fixed at the origin. Distances ac and bc are equal and vary from $1.5a_B$ to $3.5a_B$. (right) Dependence of the DM vector \mathbf{d}_{ac} on the position of the dot b for SO angles 0 and $\pi/4$. Distance ac is fixed at $1.5a_B$, while distance cb varies from $1.5a_B$ to $5.5a_B$. Potential parameters are $h = 3$ and $\lambda = 0.2$. Rashba coefficient is $f_R = 5 \text{ meV \AA}$ and Dresselhaus $f_D = 16.25 \text{ meV \AA}$.

than $2a_B$ apart from each other. The relation analogous to (20) is never satisfied.

Equilateral arrangement is the only setup in which equation analogous to (20) is satisfied. Due to the fact that $S_{ab} = S_{ac} = S_{bc}$, we can write it as $\beta_{ab} + \beta_{bc} + \beta_{ca} = 0$. We have numerically checked that condition $\mathbf{d}_{ab} + \mathbf{d}_{bc} + \mathbf{d}_{ca} \approx 0$ holds to numerical accuracy. While this symmetry seems promising for reducing the effects of anisotropy in spin interaction on the operation of the three-spin qubit, it is always associated with the simultaneous isotropic exchange interaction of all three spins, $J_{ab} = J_{bc} = J_{ca}$. Since this interaction conserves all the quantum numbers of encoded three spin qubits, it does not produce any quantum gate.

The magnetic field normal to the plane of triple dot adds to the anisotropy of effective spin interaction, in addition to squeezing of the orbitals and introduction of phases to the overlaps. The Dzyaloshinsky–Moriya vectors are magnetic field dependent since spin–orbit Hamiltonian depends on the momentum, acquiring the term $q\mathbf{A}$ in the magnetic field. We analyze the magnetic field dependence of anisotropy in the linear geometry of a triple dot. In contrast to the zero-field case, where β vectors were purely imaginary and ratio of their components was real number, in a magnetic field β has both real and imaginary component, so the connection with \mathbf{d} is less straightforward. Our numerical analysis shows that the ratios of antisymmetric anisotropy components are dependent on the magnetic field strength and the position of the third dot. In (figure 8 (left)) we plot the dependence of intensity of antisymmetric anisotropy vectors on magnetic field strength for distance $ac = cb = 2a_B$ between the dots. Intensity reaches a minimum for the fields around 1 T. In stronger fields, the intensity grows until $B_z = 3 \text{ T}$, and then declines towards zero. Dependence of antisymmetric anisotropy on the

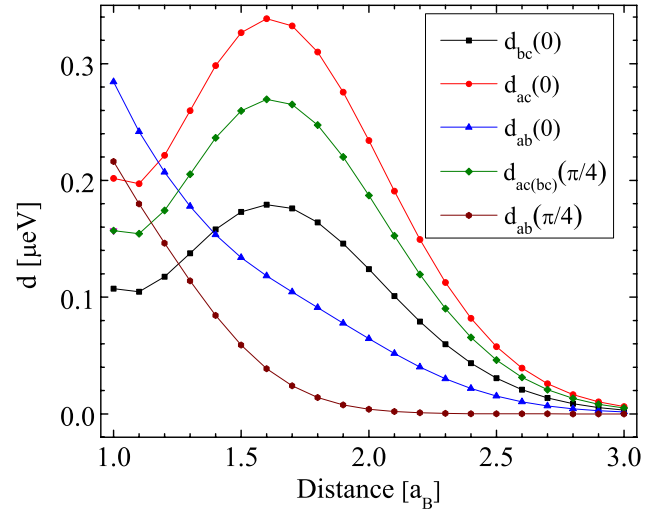


Figure 7. Intensity of SO parameters for the isosceles triple quantum dot for SO angles 0 and $\pi/4$ versus distance of each dot from the origin ($-a = b = c$). Potential parameters are $h = 3$ and $\lambda = 0.2$. Rashba coefficient is $f_R = 5 \text{ meV \AA}$ and Dresselhaus $f_D = 16.25 \text{ meV \AA}$.

position of the third dot is studied and presented in (figure 8 (right)) for magnetic fields of 2 T and 1 T.

For the triangular arrangement we were unable to make a parameterization of the dominant SO effects in terms of DM vectors. We believe that single-orbital model cannot describe the accumulated phase factor (different from 1) due to the magnetic field and SO field in the closed loop geometry. There is a way to overcome this problem by using a spin and position dependent transformation [47, 48] which is able to gauge away the linear SO terms. This was done in the case of double QD [49], in which SO effects needed to be studied in terms of eigenenergies due to the basis transformation. Since our study is done using the fixed basis and DM parameters, it is beyond the scope of this work.

The dependence of effective interaction between a pair of spins in a triple quantum dot on the position of the third one is a potential tool for experimental realization of quantum gates. In experiments on multiple dots, the gate is applied by time-dependent voltages on electrostatic gates that modify the confinement potential. As the quantum dots position coincides with the local minima of confinement potential, and the potential is locally parabolic, the small variations of gate voltages are equivalent to the motion of the dots. Therefore, a solution of time-dependent Schrödinger equation for our Hamiltonian with time dependent dot coordinates models the spin evolution driven by a time-dependent voltage.

As the spin–orbit interaction is seen as a nuisance in exchange-only quantum computing schemes, we wish to find if there is a way to remove the linear SO effects in triple QDs. It has been shown [8] that, by the proper local rotation of one spin, a double QD Hamiltonian, up to the linear SO contribution, can be written as $J(R_{\mathbf{u}}^{\theta}(\mathbf{S}_a)) \cdot \mathbf{S}_b$, where $R_{\mathbf{u}}^{\theta}$ represents a rotational matrix for an angle $\theta = |\mathbf{d}|/J$ around an axis $\mathbf{u} = (d_x, d_y, 0)/\theta J$. There is a simple prescription for removing DM terms in a linear array of QDs. Since in

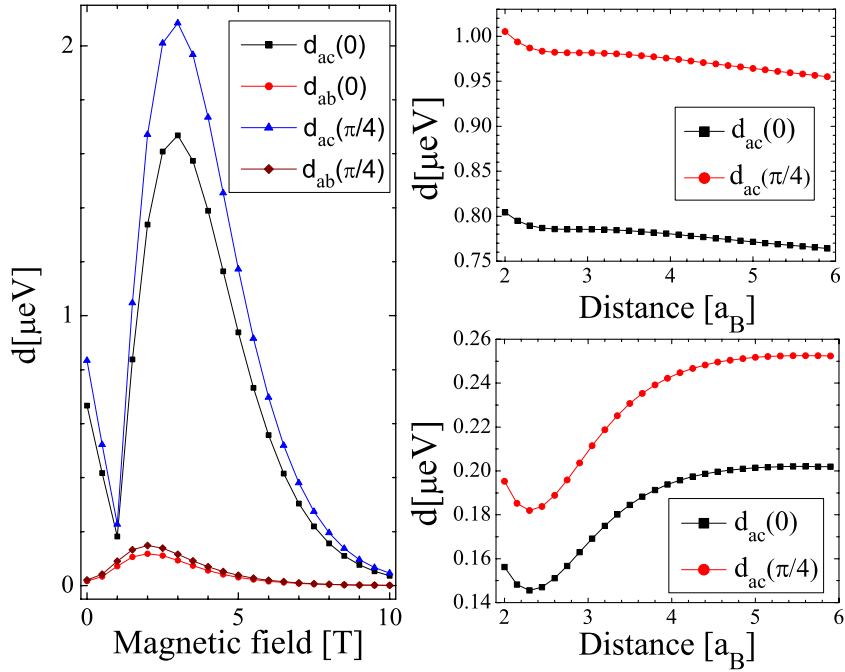


Figure 8. Dependence of two-spin interaction anisotropy on magnetic field and the position of third dot. (left) Intensity of SO parameters for the linear arrangement in the presence of perpendicular magnetic field. The geometry is set by $a(b) = -(+)2a_B$, $c = 0$. SO angles are 0 and $\pi/4$. (right) Intensity of SO parameter d_{ac} for the fixed distance $ac = 2a_B$ and magnetic field strengths 2 T (upper right) and 1 T (lower right) with respect to the distance cb going from $2a_B$ to $6a_B$. SO angles are 0 and $\pi/4$. Potential parameters are $\hbar = 3$ and $\lambda = 0.2$. Rashba coefficient is $f_R = 5 \text{ meV \AA}$ and Dresselhaus $f_D = 16.25 \text{ meV \AA}$.

that case nearest neighbor exchange is the dominant energy scale and the most quantum computation schemes use only this interaction [16, 18], it is enough to rotate two nearest neighbor spins in the same fashion as above. On the other hand, in triangular triple quantum dots, there is an additional freedom in the choice of time dependent interaction that implements a quantum gate. A different time-dependent Hamiltonian can be applied to each pair of spins, since now there is no clear distinction between nearest neighbor and next-nearest neighbor exchange. The question remains whether we can remove all three DM terms. We have a freedom of choice to rotate two spins in order to get rid of two DM terms: for instance, we are going to rotate spins \mathbf{S}_b and \mathbf{S}_c by the angles $\theta_{ab} = |\mathbf{d}_{ab}|/J_{ab}$ and $\theta_{bc} = |\mathbf{d}_{bc}|/J_{bc}$ around the vectors $\mathbf{u}_{ab} = (-d_{ab}^x, -d_{ab}^y, 0)/\theta_{ab}J_{ab}$ and $\mathbf{u}_{bc} = (-d_{bc}^x, -d_{bc}^y, 0)/\theta_{bc}J_{bc}$, respectively. Now that we have lost two DM terms, we are left with the double QD Hamiltonian of two rotated spins, $J_{bc}\mathbf{R}_{\mathbf{u}_{ab}}^{\theta_{ab}}(\mathbf{S}_b)\mathbf{R}_{\mathbf{u}_{bc}}^{\theta_{bc}}(\mathbf{S}_c)$. This Hamiltonian is equal to $J_{bc}\mathbf{S}_b \cdot \mathbf{S}_c + \mathbf{d}_{bc}(\mathbf{S}_b \times \mathbf{S}_c)$ if the condition

$$\frac{\mathbf{d}_{ab}}{J_{ab}} + \frac{\mathbf{d}_{bc}}{J_{bc}} + \frac{\mathbf{d}_{ca}}{J_{ca}} = 0 \quad (26)$$

holds. Our calculation shows that equilateral triple QD in zero magnetic field satisfies (26), but does not produce a useful gate. Therefore, architectures with the linear arrangements are the only ones where exchange-only quantum computation proceeds with a simple global redefinition of spin states. In other cases, spin-nonconserving transitions to noncomputational states has to be removed.

6. Conclusions

We have studied triple quantum dot system in linear and triangular arrangements. In the linear arrangement, antiferromagnetic exchange is present between all three pairs of dots. Exchange interaction between the outer dots is smaller than the nearest neighbor exchange but comparable to it when the distances of the neighboring dots is smaller than $2a_B$. The influence of the third dot on the exchange interaction between the other two dots is considerable for both the linear and triangular system in zero magnetic field. Magnetic field suppresses this dependence on the position of third dot. At the critical field strength in the range of 1 T, we observe a transition from antiferromagnetic to ferromagnetic exchange parameters in both linear and triangular setups.

In the linear arrangement, the Dzyaloshinsky–Moriya vectors between every pair of dots point in the same direction, and depend only on Rashba (f_R) and Dresselhaus (f_D) parameters, as well as on the angle θ between the crystallographic axis and the direction connecting the dots. We have shown that Dzyaloshinsky–Moriya vector intensity between two dots is highly dependent on the position of the third one. When $f_D = f_R$ and $\theta = 3\pi/4$ the effects of spin–orbit interaction vanishes, as in the case of double dot. In the magnetic field, dependence of Dzyaloshinsky–Moriya vectors direction on magnetic field as well as on the position of the third dot is observed while Dzyaloshinsky–Moriya vectors intensity is less sensitive to the third dot than in a nonmagnetic case. Anisotropy is always present in triangular arrangements. In this setup, Dzyaloshinsky–Moriya vectors directions are

additionally dependent on the third dot. For the equilateral arrangement, equation $\mathbf{d}_{ab} + \mathbf{d}_{bc} + \mathbf{d}_{ca} = \mathbf{0}$ is satisfied, helping us to remove dominant spin-orbit effects by the proper local spin rotation of two quantum dots.

Acknowledgments

This research is funded by the MPNTR grants ON171035 and ON171032, SNF SCOPES IZ73Z0152500, and DAAD grant 451-03-01858201309-3.

Appendix. Details of the Hamiltonian calculation

Matrix elements of S , \hat{x} , \hat{y} , \hat{p}_x and \hat{p}_y between two Fock–Darwin states $\varphi_i(x, y) = e^{i\frac{eB_z}{2\hbar}(x_i y - y_i x)} \sqrt{\frac{m\omega}{\pi\hbar}} e^{-\frac{m\omega}{2\hbar}((x-x_i)^2 + (y-y_i)^2)}$ and $\varphi_j(x, y) = e^{i\frac{eB_z}{2\hbar}(x_j y - y_j x)} \sqrt{\frac{m\omega}{\pi\hbar}} e^{-\frac{m\omega}{2\hbar}((x-x_j)^2 + (y-y_j)^2)}$, centered at (x_i, y_i) and (x_j, y_j) are equal to

$$S_{ij} = \langle \varphi_i | \varphi_j \rangle = \exp \left[-\frac{4m^2\omega^2 + e^2 B_z^2}{16m\omega\hbar} ((x_i - x_j)^2 + (y_i - y_j)^2) \right] \exp \left[i\frac{eB_z}{2\hbar} (y_i x_j - x_i y_j) \right], \quad (\text{A.1})$$

$$\hat{x}^{ij} = \langle \varphi_i | \hat{x} | \varphi_j \rangle = S_{ij} \left(\frac{1}{2}(x_i + x_j) + i\frac{eB_z}{4m\omega} (y_i - y_j) \right), \quad (\text{A.2})$$

$$\hat{y}^{ij} = \langle \varphi_i | \hat{y} | \varphi_j \rangle = S_{ij} \left(\frac{1}{2}(y_i + y_j) - i\frac{eB_z}{4m\omega} (x_i - x_j) \right), \quad (\text{A.3})$$

$$\hat{p}_x^{ij} = \langle \varphi_i | \hat{p}_x | \varphi_j \rangle = S_{ij} \left(\frac{im\omega}{2} (x_i - x_j) - \frac{eB_z}{4} (y_i + y_j) \right), \quad (\text{A.4})$$

$$\hat{p}_y^{ij} = \langle \varphi_i | \hat{p}_y | \varphi_j \rangle = S_{ij} \left(\frac{im\omega}{2} (y_i - y_j) + \frac{eB_z}{4} (x_i + x_j) \right). \quad (\text{A.5})$$

Matrix element of H_0 (1)

$$\begin{aligned} \langle \varphi_i | H_0 | \varphi_j \rangle &= \hbar\omega_0 S_{ij} - \frac{m^2\omega_0^2\omega}{2\pi\hbar} (I^p(x_i, x_j) I^s(y_i, y_j) + I^s(x_i, x_j) I^p(y_i, y_j)) \\ &+ \frac{m\omega}{\pi\hbar} \left[\frac{1}{2} m\omega_0^2 \left(1 - \frac{\hbar}{\lambda^2} \right) \sum_{k=a,b,c} (F^s(x_k, x_i, x_j) F^p(y_k, y_i, y_j) \right. \\ &+ F^p(x_k, x_i, x_j) F^s(y_k, y_i, y_j)) \\ &+ \left. \hbar\omega_0 h \left(3\frac{\pi\hbar}{m\omega} S_{ij} - \sum_{k=a,b,c} F^p(x_k, x_i, x_j) F^p(y_k, y_i, y_j) \right) \right], \end{aligned} \quad (\text{A.6})$$

where

$$\begin{aligned} F^p(x_k, x_i, x_j) &= \sqrt{\frac{\pi}{A}} \exp \left[-\frac{m}{2\hbar} \left(\omega(x_i^2 + x_j^2) + \omega_0 \frac{x_k^2}{\lambda^2} \right) + \frac{(B + iE_x)^2}{4A} \right], \\ F^s(x_k, x_i, x_j) &= \frac{1}{4A^2} [(B + iE_x)^2 + 2A(1 - 2(B + iE_x)x_k + 2Ax_k^2)] \\ &F^p(x_i, x_j, x_k), \\ I^p(x_i, x_j) &= \sqrt{\frac{\pi}{C}} \exp \left[-\frac{m\omega}{2\hbar} (x_i^2 + x_j^2) + \frac{(D + iE_x)^2}{4C} \right], \\ I^s(x_i, x_j) &= \frac{1}{4C^2} [(D + iE_x)^2 + 2C(1 - 2(D + iE_x)x_j + 2Cx_j^2)] I^p(x_i, x_j), \end{aligned} \quad (\text{A.7})$$

with $A = \frac{m}{\hbar}(\omega + \frac{\omega_0}{2\lambda^2})$, $B = \frac{m}{\hbar}(\omega(x_i + x_j) + \omega_0 \frac{x_k}{2\lambda^2})$, $C = \frac{m\omega}{\hbar}$, $D = (x_i + x_j)C$, $E_x = \frac{1}{2\hbar}(y_i - y_j)eB_z$.

Expressions $F^p(y_k, y_i, y_j)$ and $F^s(y_k, y_i, y_j)$, $I^p(y_i, y_j)$ and $I^s(y_i, y_j)$ have the same form, only the set of numbers $\{x_k, x_i, x_j\}$ is changed with the set $\{y_k, y_i, y_j\}$ and E_x is changed with $E_y = \frac{1}{2\hbar}(x_j - x_i)eB_z$.

Matrix elements of $\Omega(\mathbf{k})$ (9)

$$\begin{aligned} \beta_{ij} &= \langle \varphi_i | \Omega(\mathbf{k}) | \varphi_j \rangle \\ &= \left[-\frac{\hat{p}_x^{ij} + \frac{1}{2}eB_z \hat{y}^{ij}}{\hbar} (f_D \cos \theta + f_R \sin \theta) \right. \\ &+ \left. \frac{\hat{p}_y^{ij} - \frac{1}{2}eB_z \hat{x}^{ij}}{\hbar} (f_R \cos \theta - f_D \sin \theta) \right] e_x \\ &+ \left[-\frac{\hat{p}_x^{ij} + \frac{1}{2}eB_z \hat{y}^{ij}}{\hbar} (f_D \sin \theta \right. \\ &+ \left. f_R \cos \theta) + \frac{\hat{p}_y^{ij} - \frac{1}{2}eB_z \hat{x}^{ij}}{\hbar} (f_D \cos \theta - f_R \sin \theta) \right] e_y. \end{aligned} \quad (\text{A.8})$$

H_{SO} (1) matrix element between the Fock–Darwin states φ_i and φ_j with spin components included is

$$\begin{aligned} \langle \varphi_i \pm | H_{SO} | \varphi_j \mp \rangle &= \left[-\frac{\hat{p}_x^{ij} + \frac{1}{2}eB_z \hat{y}^{ij}}{\hbar} (f_D \cos \theta + f_R \sin \theta) \right. \\ &+ \left. \frac{\hat{p}_y^{ij} - \frac{1}{2}eB_z \hat{x}^{ij}}{\hbar} (f_R \cos \theta - f_D \sin \theta) \right] \\ &+ \left[\pm i \frac{\hat{p}_x^{ij} + \frac{1}{2}eB_z \hat{y}^{ij}}{\hbar} (f_D \sin \theta + f_R \cos \theta) \right. \\ &\mp \left. i \frac{\hat{p}_y^{ij} - \frac{1}{2}eB_z \hat{x}^{ij}}{\hbar} (f_D \cos \theta - f_R \sin \theta) \right]. \end{aligned} \quad (\text{A.9})$$

Coulomb interaction Hamiltonian C (1) is two-particle operator whose matrix elements between four different Fock–Darwin states positioned at $\mathbf{a} = (a_1, a_2)$, $\mathbf{b} = (b_1, b_2)$, $\mathbf{c} = (c_1, c_2)$ and $\mathbf{d} = (d_1, d_2)$ ($\varphi_t(x, y) = e^{i\frac{eB_z}{2\hbar}(t_1 y - t_2 x)} \sqrt{\frac{m\omega}{\pi\hbar}} e^{-\frac{m\omega}{2\hbar}((x-t_1)^2 + (y-t_2)^2)}$ for $t \in \{a, b, c, d\}$) is equal to

$$\begin{aligned} C_{abcd} &= \sqrt{\frac{m\omega\pi}{2\hbar}} \exp \left[i\frac{eB_z}{8\hbar} [z_1(a_2 + b_2 - c_2 - d_2) \right. \\ &+ \left. z_2(-a_1 - b_1 + c_1 + d_1)] \right] \exp \left[\frac{e^2 B_z^2}{32m\omega\hbar} (\alpha_1^2 + \alpha_2^2) \right] \\ &\times \exp \left[\frac{\hbar}{16m\omega} (\zeta_1^2 + \zeta_2^2) \right] I_0 \left(\frac{\hbar}{16m\omega} (\zeta_1^2 + \zeta_2^2) \right) \\ &\times \exp \left[\frac{m\omega}{8\hbar} (|\mathbf{z}|^2 - 4[|\mathbf{a}|^2 + |\mathbf{b}|^2 + |\mathbf{c}|^2 + |\mathbf{d}|^2]) \right], \end{aligned} \quad (\text{A.10})$$

where $\mathbf{z} = \mathbf{a} + \mathbf{b} + \mathbf{c} + \mathbf{d}$, $\alpha_1 = a_2 + b_2 - c_2 - d_2$, $\alpha_2 = -a_1 - b_1 + c_1 + d_1$, $\zeta_1 = -\frac{m\omega}{\hbar}(b_1 + d_1 - a_1 - c_1) + i\frac{eB_z}{2\hbar}(a_2 + d_2 - b_2 - c_2)$, $\zeta_2 = -\frac{m\omega}{\hbar}(b_2 + d_2 - a_2 - c_2) - i\frac{eB_z}{2\hbar}(a_1 + d_1 - b_1 - c_1)$.

References

- [1] Loss D and DiVincenzo D P 1998 *Phys. Rev. A* **57** 120
- [2] Imamoglu A, Awschalom D D, Burkard G, DiVincenzo D P, Loss D, Sherwin M and Small A 1999 *Phys. Rev. Lett.* **83** 4204

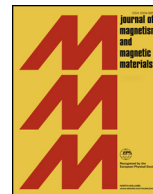
- [3] Kloeffel C and Loss D 2013 *Annu. Rev. Condens. Matter Phys.* **4** 51
- [4] Nadj-Perge S, Frolov S M, Bakkers E P A M and Kouwenhoven L P 2010 *Nature* **468** 1084
- [5] Schroer M D, Petersson K D, Jung M and Petta J R 2011 *Phys. Rev. Lett.* **107** 176811
- [6] Nadj-Perge S, Pribrig V S, Van Den Berg J W G, Zuo K, Plissard S R, Bakkers E P A M, Frolov S M and Kouwenhoven L P 2012 *Phys. Rev. Lett.* **108** 166801
- [7] Golovach V N, Borhani M and Loss D 2006 *Phys. Rev. B* **74** 165319
- [8] Bonesteel N E, Stepanenko D and DiVincenzo D P 2001 *Phys. Rev. Lett.* **87** 207901
- [9] Burkard G and Loss D 2002 *Phys. Rev. Lett.* **88** 047903
- [10] Stepanenko D, Bonesteel N E, DiVincenzo D P, Burkard G and Loss D 2003 *Phys. Rev. B* **68** 115306
- [11] Stepanenko D and Bonesteel N E 2004 *Phys. Rev. Lett.* **93** 140501
- [12] Coish W A and Loss D 2005 *Phys. Rev. B* **72** 125337
- [13] Khaetskii A V, Loss D and Glazman L 2002 *Phys. Rev. Lett.* **88** 186802
- [14] Chekhovich E A, Makhonin M N, Tartakovskii A I, Yacoby A, Bluhm H, Nowack K C and Vandersypen L M K 2013 *Nat. Mater.* **12** 494
- [15] Hanson R, Kouwenhoven L P, Petta J R, Tarucha S and Vandersypen L M K 2007 *Rev. Mod. Phys.* **79** 1217
- [16] DiVincenzo D P, Bacon D, Kempe J, Burkard G and Whaley K B 2000 *Nature* **408** 339
- [17] Fong B H and Wandzura S M 2011 *Quantum Inf. Comput.* **11** 1003
- [18] Setiawan F, Hui H-Y, Kestner J P, Wang X and Das Sarma S 2014 *Phys. Rev. B* **89** 085314
- [19] Zeuch D, Cipri R and Bonesteel N E 2014 *Phys. Rev. B* **90** 045306
- [20] Zeuch D and Bonesteel N E 2016 *Phys. Rev. A* **93** 010303
- [21] Taylor J M, Srinivasa V and Medford J 2013 *Phys. Rev. Lett.* **111** 050502
- [22] Medford J, Beil J, Taylor J M, Rashba E I, Lu H, Gossard A C and Marcus C M 2013 *Phys. Rev. Lett.* **111** 050501
- [23] Doherty A C and Wardrop M P 2013 *Phys. Rev. Lett.* **111** 050503
- [24] Hawrylak P and Korkusinski M 2005 *Solid State Commun.* **136** 508
- [25] Baart T A, Fujita T, Reichl C, Wegscheider W and Vandersypen L M K 2017 *Nat. Nanotechnol.* **12** 26
- [26] Delgado F, Shim Y-P, Korkusinski M and Hawrylak P 2007 *Phys. Rev. B* **76** 115332
- [27] Scarola V W, Park K and Das Sarma S 2004 *Phys. Rev. Lett.* **93** 120503
- [28] Hsieh C-Y, Rene A and Hawrylak P 2012 *Phys. Rev. B* **86** 115312
- [29] Hsieh C-Y, Shim Y-P, Korkusinski M and Hawrylak P 2012 *Rep. Prog. Phys.* **75** 114501
- [30] Tarucha S, Austing D G, Honda T, Van Der Hage R J and Kouwenhoven L P 1996 *Phys. Rev. Lett.* **77** 3613
- [31] Dresselhaus G 1955 *Phys. Rev.* **100** 580
- [32] Rashba E I 1960 *Fiz. Tv. Tela* **2** 1224
- [33] Rashba E I 1960 *Sov. Phys. Solid State* **2** 1109
- [34] Petta J R, Johnson A C, Taylor J M, Laird E A, Yacoby A, Lukin M D, Marcus C M, Hanson M P and Gossard A C 2005 *Science* **309** 2180
- [35] Johnson A C, Petta J R, Taylor J M, Yacoby A, Lukin M D, Marcus C M, Hanson M P and Gossard A C 2005 *Nature* **435** 925
- [36] Koppens F H L, Buizert C, Tielrooij K J, Vink I T, Nowack K C, Meunier T, Kouwenhoven L P and Vandersypen L M K 2006 *Nature* **442** 766
- [37] Gaudreau L, Studenikin S A, Sachrajda A S, Zawadzki P, Kam A, Lapointe J, Korkusinski M and Hawrylak P 2006 *Phys. Rev. Lett.* **97** 036807
- [38] Fock V 1928 *Z. Phys.* **47** 446
- [39] Darwin C 1930 *Math. Proc. Camb. Phil. Soc.* **27** 86
- [40] Marzari N, Mostofi A A, Yates J R, Souza I and Vanderbilt D 2012 *Rev. Mod. Phys.* **84** 1419
- [41] Bravyi S, DiVincenzo D P and Loss D 2011 *Ann. Phys.* **10** 2793
- [42] Winkler R 2003 *Spin-Orbit Coupling Effects in Two-Dimensional Electron and Hole Systems*, Springer Tracts in Modern Physics vol 191 (Berlin: Springer)
- [43] Russ M and Burkard G 2015 *Phys. Rev. B* **91** 235411
- [44] Weinstein Y S and Hellberg C S 2005 *Phys. Rev. A* **72** 022319
- [45] Georgeot B and Mila F 2010 *Phys. Rev. Lett.* **104** 200502
- [46] Trif M, Troiani F, Stepanenko D and Loss D 2008 *Phys. Rev. Lett.* **101** 217201
- [47] Burkard G, Loss D and DiVincenzo D P 1999 *Phys. Rev. B* **59** 2070
- [48] Shim Y-P and Hawrylak P 2008 *Phys. Rev. B* **78** 165317
- [49] Dickman S and Hawrylak P 2003 *JETP* **77** 34
- [50] Levitov L S and Rashba E I 2003 *Phys. Rev. B* **67** 115324
- [51] Aleiner I L and Fal'ko V I 2001 *Phys. Rev. Lett.* **87** 256801
- [52] Baruffa F, Stano P and Fabian J 2010 *Phys. Rev. Lett.* **104** 126401
- [53] Baruffa F, Stano P and Fabian J 2010 *Phys. Rev. B* **82** 045311



ELSEVIER

Contents lists available at ScienceDirect

Journal of Magnetism and Magnetic Materials

journal homepage: www.elsevier.com/locate/jmmm

Research articles

Extreme conduction electron spin resonance: $A/B \rightarrow (5 + 3\sqrt{3})/4$, the universal limit of lineshape asymmetry ratioDejan M. Djokić^{a,b,*}, Dimitrije Stepanenko^a, Zorana Dohčević-Mitrović^a^a Nanostructured Matter Laboratory, Institute of Physics Belgrade, University of Belgrade, Pregrevica 118, 11 080 Belgrade, Serbia^b Laboratory of Physics of Complex Matter, Ecole Polytechnique Fédérale de Lausanne, Station 3, CH-1015 Lausanne, Switzerland

ARTICLE INFO

Keywords:

Magnetic resonance
Spin relaxation
Microwave absorption
Microcrystalline conductors
Skin depth

ABSTRACT

We derive the Electron Spin Resonance (ESR) lineshape in conducting crystals, relying on the density matrix description. In our approach, lineshape is determined as linear combination of absorptive and dispersive signals with non-negatively real coefficients, corresponding to the NMR limit. The significant points and segments of the total signal at resonance have been systematically quantified, and along that line, we have formulated an alternative fitting strategy consisting of few straightforward steps to obtain the relevant ESR parameters in metallic systems. Finally, by examining different crystal geometries, the universal value, $A/B \rightarrow (5 + 3\sqrt{3})/4$, of the lineshape asymmetry ratio has been derived in the case of metallic particles with extreme conductivity.

1. Introduction

1.1. Past progress in conduction electron spin resonance

Conduction Electron Spin Resonance (CESR) in bulk and micro-sized conducting crystalline materials has captured much scientific attention for its capacity to probe the electric conductivity of materials in a noninvasive way. This makes CESR particularly informative, as there are hardly few experimental techniques able to compete with it in probing conducting systems, where the motion of free carriers has a profound eddy current effect upon the asymmetry of the signal at resonance. The pioneering attempts to tackle the effects of eddy currents in conducting systems, set up by AC field used to excite resonance, date back to the 1950's. As evidenced by Feher and Kip [1], Dyson [2] proposed that asymmetric CESR lines observed in bulk metals arise from a combination of the following two effects. First, the AC field becomes attenuated within a characteristic skin depth. Secondly, the free electrons are capable of diffusing in and out of the skin depth many times between subsequent spin reversals at resonance. The latter fact is particularly important in CESR based on the transmission technique. In this case the magnetization penetrates much farther into the metal as compared to the AC magnetic field, which additionally contributes to asymmetry in resonance signals [3,4]. Chapman et al. [5] soon afterwards developed a theoretical treatment to understand both on- and off-resonance signal for specimens in the shape of flat plates, long cylinders, and spheres, in order to predict the asymmetric nature of the

CESR absorption depending on the sample geometry. Dyson was the very first to fully derive such characteristic CESR profiles; thus, these asymmetric lines are referred to as Dysonians. It is often the case that the asymmetry is quantified by the A/B ratio which serves as a reliable indicator of metallicity in experiments. Platzman and Wolf [6] studied spin waves excitations in non-ferromagnetic metals at resonance using the Fermi-liquid theory. The results of their generalized approach in the limit of short momentum relaxation times are equivalent to those of Dyson's. In the meantime, Dyson's theory was further extended to encompass various shapes of crystals and particular resonant field orientations [7–9].

In the early 1980's, however, Kaplan perceived a material discrepancy between the application of Dyson's theory and experiments operating in the reflection mode [10]. This was explained by the fact that CESR signals originate from paramagnetic species on the crystal surface which imposes the inclusion of a dispersion component coming from surface polaritons, unlike CESR signals obtained in the transmission mode. Namely, Kaplan suggested that the resonance in conducting systems is excited rather with electric than with magnetic component of the AC field. The electric field is coupled with the free carrier momentum on the crystal surface through the relativistic spin-orbit interaction that, with application of purely quantum mechanical density matrix method, ultimately leads to the following most general form of the CESR signal: $S(\omega) = \alpha\chi''(\omega) + \beta\chi'(\omega)$ as studied in [11]. Components χ'' and χ' stand for the absorptive and the dispersive part of the signal, while α and β are the sizes of their respective contributions,

* Corresponding author at: Nanostructured Matter Laboratory, Institute of Physics Belgrade, University of Belgrade, Pregrevica 118, 11 080 Belgrade, Serbia.

E-mail address: djokic@ipb.ac.rs (D.M. Djokić).

<https://doi.org/10.1016/j.jmmm.2019.165616>

Received 27 March 2019; Received in revised form 16 June 2019; Accepted 18 July 2019

Available online 19 July 2019

0304-8853/© 2019 Elsevier B.V. All rights reserved.

which both vanish in the limit of extremely conductive samples and/or short skin depths relative to the size of samples. The notion of complex spin susceptibilities is further elaborated by Siegman [12] who links χ'' to amplifying and χ' to reactive magnetic response near resonance. It is interesting to note that the form $\alpha\chi'' + \beta\chi'$ is indeed a particular form of Dysonian, corresponding to the so-called “NMR limit” [13,14], when electrons diffusion rate is much smaller than the rate of spin relaxation. Kaplan put forward that no other limit is necessary to consider in order to properly understand CESR spectra of ordinary metals. Furthermore, in this case, no particular spin dynamics can lead to Gaussian-profiled absorptions (χ'') due to the dimensionality or motionally narrowed signals [15,16], so that only Lorentzian profiles of the pure absorption are considered.

Over recent years, use of CESR has proven increasingly efficient in studying micrometer-sized crystals in the shape of metallic clusters and/or metallic colloids [17,18]. Baudron et al. [19] employed this probe in order to acquire the resistivity data in a contactless way when working with fragile organic compounds. At nanoscopic scales, CESR finds its practical usefulness in both understanding spin relaxation dynamics and determining the nature of electron transport in fullerenes, carbon nanotubes, and nano-diamond particles [20–22]. Sensitivity of ESR signal shape to the relative length scales of high frequency skin effect, characteristic electron diffusion length, and the spin diffusion lengths make altogether it a useful probe for effects that happen in a thin layer on the surface of conducting sample. Therefore, the lineshape indicates size of particles in micro-structured samples.

1.2. Problem description and structure details

Dyson [2] originally put forward the theory capable to directly associate the onset of asymmetry with the dynamics of charge carriers in metallic samples of different sizes. However, this theory has not proven universally applicable for two reasons. First, ESR techniques may be operating at either transmission or reflection mode, and only former was originally described by Dyson’s theory. Second, there are polariton surface modes emerging from the coupling between the electromagnetic wave and electric dipole excitations. These were studied by Kaplan [10] who focused on Dyson’s CESR signals that decompose only into a non-negative linear combination of absorption and dispersion. We will rely in this account on this approach in order (i) to analyze the CESR signal, (ii) to quantitatively describe its important lengths and points necessary for simplification of a fitting procedure of CESR lineshape which we establish in this work, as well as, (iii) to explain and derive the geometry independent asymmetry ratio limit ($A/B \rightarrow (5 + 3\sqrt{3})/4$) in the case of extreme CESR carried out on highly conducting samples. This limiting value is quite often encountered in literature as 2.55 limit, and yet, to the best of our knowledge, it has never been extracted analytically. The A/B ratio also tends to this universal value once nano- or micro-sized metallic samples start to agglomerate into larger ones. Such a feature makes CESR particularly useful in controlling the degree to which the clustering takes place [23,24].

The present study delves into the theoretical account of the field-dependent CESR signal and its derivative starting with retarded Green’s function formalism in angular quasi-frequency space. A method has been set out for properly analyzing the CESR curves, together with their links to geometry and conductivity dependences in terms of sample-dimension-to-skin-depth variable. Our major analytical finding represents the closed-form solution of A/B in the high-conduction limit. Most critically for experimentalists affiliated to the ESR community, this work discusses a scheme to unambiguously resolve the phase emerging in magnetic resonance – an issue particularly essential for CESR measurements at modern-day spectrometers. Owing to the prevalence of paramagnetic measurements, the phases are habitually zeroed out.

2. Theoretical aspects and results

Following the approach by Kaplan [25,10,26], we focus on ESR whose absorption spectral lines are fairly represented by the spectral function $S(q, \omega)$ of a carrier electron spin, which is determined by retarded Green’s function $G^R(q, \omega)$, where $\Sigma(q, \omega)$ is retarded self energy [27,28]. In Fourier space, $G^R(q, \omega)$ is specified as follows

$$G^R(q, \omega) = \frac{1}{\omega - \Sigma(q, \omega) - i\eta}, \quad \eta \rightarrow 0^+, \quad (1)$$

where $\Sigma(q, \omega) \equiv \Re\Sigma(q, \omega) + i\Im\Sigma(q, \omega)$ is a complex-valued function. In a CESR experiment, $q \approx 0$, since the microwave wavelength is much longer than the crystal lattice spacing. This approximation does not take into account dynamics of the environment which influences the electron spin. Generally, one has to pay attention to spin diffusion effects in CESR that might drive the physics well beyond long wavelength scales [29–31]. We therefore assume that the spectral function describes local effects by setting $\Re\Sigma(q, \omega) \simeq \Re\Sigma(\omega) = \omega_0$ (ω_0 the resonant field H_0) and that $\Im\Sigma(q, \omega) \simeq \Im\Sigma(\omega) = -\Delta\omega$ ($\Delta\omega$ the line-width ΔH). The physical meaning of $\Re\Sigma(q, \omega)$ and $\Im\Sigma(q, \omega)$ is grasped at a microscopic level. The resonant condition is translated into $H_0 = \kappa\omega_0$, where ω_0 stands for the resonant angular frequency and $\kappa \equiv \hbar/(g\mu_B\mu_0 S)$. g represents electron Landé factor in the material, \hbar is reduced Planck constant, μ_B is Bohr magneton, μ_0 is vacuum permeability, and electron spin $S = 1/2$. Similarly, $\Delta H = \kappa\Delta\omega$. In SI units, $g \cdot \kappa = 1.809792 \times 10^{-5}$ A/(mHz), while in cgs units, $g \cdot \kappa = 2.274252 \times 10^{-7}$ Ørsted’s.

For convenience of notation we stick to the quasi-frequency formalism in which ω is a quasi-frequency, since the externally applied magnetic field H (directly proportional to ω by κ) is actually being swept. In that way, the normalized spectral function (in the case of pure absorption) looks like

$$S(\omega) \equiv -\frac{1}{\pi} \Im G^R(\omega) = \frac{\Delta\omega/\pi}{(\omega - \omega_0)^2 + \Delta\omega^2} \equiv \chi''(\omega). \quad (2)$$

It is necessary to say that $G^R(\omega)$ routinely goes out of phase with the microwave AC stimulus. Root cause of this phase slip is in the effects not taken into account by the bare response function (2). Most prominently, the cavity and electronics of the ESR spectrometer, as well as the dynamics of electron spins in the sample, introduce a correction to the ESR response. For that reason, the ESR signal is derived from Green’s function multiplied by a complex function $\rho(\varphi)e^{-i\varphi}$, with real both $\rho(\varphi)$ and φ . Consequently, $G^R(\omega) \rightarrow G^R(\omega)\rho(\varphi)e^{-i\varphi}$, where φ is a free variable and $\rho(\varphi \rightarrow 0) \rightarrow 1$. Function $\rho(\varphi)$ describes instrumental artifacts arising from phase-mismatched ESR cavities, as well as the effects exerted by intrinsic crystal properties, such as dynamical screening of the AC field at skin depth scales [32]. The analysis of former is often avoided by matching the cavity so that the so-called tangent of loss angle, $\tan\varphi$, becomes minimal. In that case, the quality factor $Q_\varphi \equiv 1/\tan\varphi$ reaches its maximum, especially once $\varphi \rightarrow 0$. However, in ESR performed on conducting crystals the aforementioned matching is undesirable because valuable information about the crystal physics could be lost. Therefore, following the line of reasoning from (2), the CESR output now becomes proportional to

$$S(\omega, \varphi) \propto \mathcal{N}\rho(\varphi)\chi''(\omega)\cos\varphi + \chi'(\omega)\sin\varphi, \quad (3)$$

where term $\chi'(\omega) \equiv \frac{(\omega - \omega_0)/\pi}{(\omega - \omega_0)^2 + \Delta\omega^2}$ stands for dispersive part of the signal, while \mathcal{N} is appended as the number of active spins probed at resonance. \mathcal{N} also reflects on how dynamically susceptible a paramagnetic system is, which will be normalized to 1 for simplicity. Here, we emphasize again that the essence of ω is encapsulated in the scanned magnetic field ($\omega \equiv H/\kappa$). That is why ω is rather a quasi- than a true frequency, except for the case of the true microwave angular frequency $\omega_0 = 2\pi\nu_0$ which is fixed in standard ESR setups [33]. The proportionality factor in (3) is related to ESR spectrometer configuration, not to crystal properties. Moreover, the genuine ESR signal represents the first

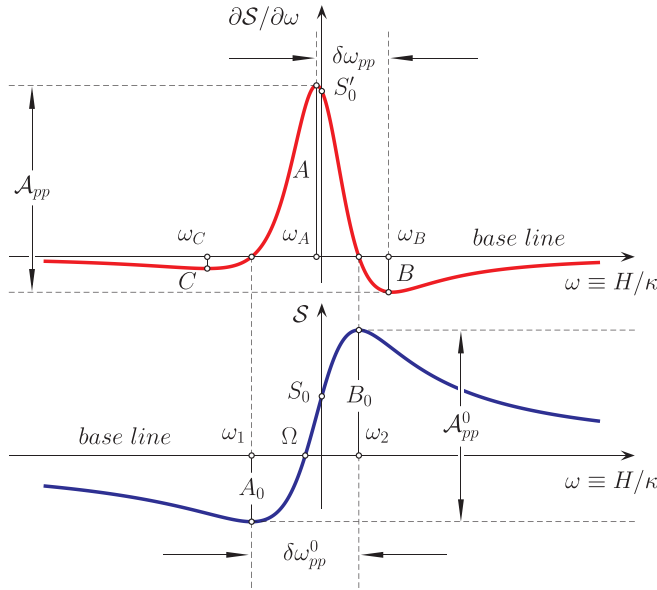


Fig. 1. Lorentzian absorption profile admixed with the associated dispersion (lower in blue) and the related first derivative of the signal with respect to the quasi-frequency (upper in red). The coordinates and lengths of all the relevant points and segments are also given. (For interpretation of the references to colour in this figure legend, the reader is referred to the web version of this article.)

derivative of $S(\omega, \varphi)$, that is $\partial_\omega S(\omega, \varphi)$ or $S'(\omega, \varphi)$, as a result of the deployed lock-in technique. The double integral of $S'(\omega, \varphi)$ is $\mathcal{N}\rho(\varphi)\cos\varphi$. It does include the φ dependent contribution, which becomes pure \mathcal{N} only when $\varphi \rightarrow 0$.

2.1. Significant points of the spectral lineshape functions

This subsection is devoted to a full description of the characteristic points and segments of CESR signal, both differentiated ($\partial S/\partial\omega$) and non-differentiated (S). Their values depend upon two types of variables. The first type includes φ and $\rho(\varphi)$ that originate from the effects of microwave loss in conducting systems and geometry, whereas the remaining variables come from the spin relaxation processes ($\Delta\omega$), g -factor or H_0 position being identified as $\kappa\omega_0$, and the number of susceptible spins \mathcal{N} . For simplicity, we have normalized \mathcal{N} to 1 and shifted ω_0 to 0, without loss of generality.

The significant values of ω are shown in Fig. 1 which features Lorentzian absorption profile admixed with its dispersion $S(\omega)$ (lower, in blue) and the signal first derivative $S'(\omega)$ (upper, in red). Points ω_1 and ω_2 are ω -positions of the two extremal lobes, while Ω stands for the single node of $S(\omega)$. Points ω_A , ω_B , and ω_C are ω -positions of the three extremal lobes of $S'(\omega)$, while there are the two nodes which must coincide with ω_1 and ω_2 . In the convention we use, factor of ω_0 needs to be added to all the points of $S(\omega)$ and $S'(\omega)$ lineshape functions. Segments A_0 and B_0 correspond to the depth and height of the two extremal lobes of $S(\omega)$, respectively, while S_0 represents its value at zero ω . Segments A , B , and C are lengths (depths or heights) of the three extremal lobes in $S'(\omega)$, whereas S'_0 measures its height at zero. The lengths of all the segments in both cases, $S(\omega)$ and $S'(\omega)$, should be multiplied with \mathcal{N} for generalization purposes. Table 1 provides a detailed overview of the significant points and lengths whose values are given as functions expressed in a $\mathcal{F}(\varphi, \rho(\varphi), \Delta\omega)$ form for both $S(\omega)$ (left double-column) and $S'(\omega)$ (right double-column). Other relevant values, such as peak-to-peak positions, will be discussed later in the text.

Walmsley and co-workers [13,14] have demonstrated that a Dysonian line exactly coincides with the sum of positively contributed

absorptive and dispersive curves in the so-called "NMR-limit", when $0 \leq \varphi < \pi/2$. This limit implies that electron diffusion processes are much slower than spin relaxation processes in ordinary metals. On the other hand, it is of practical interest to consider the case when the spectrum is phased not due to the intrinsic physics of the system, but rather owing to the limitations of experimental means. Thus, the real and imaginary part of the measured ESR spectrum do not essentially emerge as the real and imaginary part of the field-differentiated inherent spin susceptibility. In high magnetic field ESR experiments of a few-hundred GHz resonant frequency, such as in a quasi optical high field ESR setup operating in a submillimeter frequency range [34,35], data are usually fitted to an arbitrary combination of absorption and dispersion Lorentzian lines. Even in the case of non-conducting, purely ESR absorptive, crystals which have no intrinsic phase, the combination is present as a sole uncontrollable instrumental consequence to even allow $0 \leq \varphi < 2\pi$. The phase with such a range will be henceforth named as ϕ which must not be mistaken for φ that falls into the first quadrant (+, +) only. Therefore, in ESR systems with no tunable cavities, the ESR signal fractions coming from χ'' and χ' can even assume negative values. As a consequence, physically valuable information on the phase inherent to the conducting systems may irreversibly be lost by the inescapable instrumental arrangement. However, it is often the case that samples probed at high frequency ESR contain several ESR active species among which one can be a set of localized defects detected due to the high sensitivity of the probe. One such example is semi-metallic crystalline kagomé compound based on organic tetrathiafulvalene which contains a very low concentration of magnetic defects [19]. Being insulating, these defects may serve as a reference in a high field ESR experiment since they are intrinsically phaseless unlike the major CESR active line. If a spectral component coming from such localized species is present, then the real part is itself purely absorptive and this piece of information can be exploited to (de) phase the spectrum. For that reason, it is of the utmost importance to know the phase difference between the signals of CESR and of localized ESR species, in order to impart the valuable information on the sample conductivity. The two lines are presumably weighted by their instrumental phases which are the same up to the phase period or phase anti-period. Namely, if one has a closer look at $S'(\omega, \phi)$ one notices that there are features of this function which are anti-periodic (and therefore also periodic) in ϕ . For that reason, one has to come up with an irreducible working range of ϕ which is sufficient to reduce the high field ESR signal to a form that is as simple as possible. It turns out that a combination of absorption and dispersion Lorentzian lines with phase $0 \leq \phi < 2\pi$, emerging in ESR spectrometers with no controllable cavity, has its unique counterpart in the first quadrant of $0 \leq \varphi < \pi/2$. One can notice that $\chi''(\omega)$ and $\chi'(\omega)$ are the even and odd function of ω , respectively. However, the parities of $\partial_\omega \chi''(\omega)$ and $\partial_\omega \chi'(\omega)$ go reverse. Relying on these (anti) symmetry properties of $S'(\omega, \phi)$ each quadrant is covered by the following procedure which makes mapping onto the first quadrant:

$$\begin{aligned} \phi \in (+, +) &\Rightarrow S'(\omega, \phi) = +S'(+\omega, \varphi), \text{ for } \varphi \in (+, +), \\ \phi \in (-, +) &\Rightarrow S'(\omega, \phi) = +S'(-\omega, \varphi), \text{ for } \varphi \in (+, +), \\ \phi \in (-, -) &\Rightarrow S'(\omega, \phi) = -S'(+\omega, \varphi), \text{ for } \varphi \in (+, +), \\ \phi \in (+, -) &\Rightarrow S'(\omega, \phi) = -S'(-\omega, \varphi), \text{ for } \varphi \in (+, +). \end{aligned} \quad (4)$$

For simplicity, we have carried out the transformation $\mathcal{H}(\phi)$, which formally translates variable ϕ into $\varphi = \mathcal{H}(\phi)$ in the following manner:

$$\begin{aligned} \mathcal{H}(\phi) &= (-1)^{\text{floor}[2\phi/\pi - 2\text{sgn}[\phi]]} \\ &\times (\pi + \phi - \pi(\text{quot}[3 + \text{floor}[2\phi/\pi - 2\text{sgn}[\phi]], 2] + \text{sgn}[\phi])), \end{aligned} \quad (5)$$

where $\text{floor}[\phi]$, $\text{sgn}[\phi]$, and $\text{quot}[\phi]$ stand for floor, signum, and quotient function in that order. Thus, if there are more than one ESR active species coming from the same sample probed at high frequency ESR

Table 1

Values of the relevant points and segments of the two lineshape functions: S (left) and $\delta S/\delta\omega$ (right) expressed as $\mathcal{F}(\varphi, \rho(\varphi), \Delta\omega)$ dependences.

Points/Segments (S)	$\mathcal{F}(\varphi, \rho(\varphi), \Delta\omega)$	Points/Segments ($\delta S/\delta\omega$)	$\mathcal{F}(\varphi, \rho(\varphi), \Delta\omega)$
ω_1	$\Delta\omega \cot \frac{\varphi}{2}$	ω_A	$\Delta\omega (2\cos \frac{\varphi+\pi}{3} - \cos\varphi)/\sin\varphi$
Ω	$-\Delta\omega \cot\varphi$	ω_B	$\Delta\omega (2\cos \frac{\varphi-\pi}{3} - \cos\varphi)/\sin\varphi$
ω_2	$\Delta\omega \tan \frac{\varphi}{2}$	ω_C	$\Delta\omega (-2\cos \frac{\varphi}{3} - \cos\varphi)/\sin\varphi$
$\delta\omega_{pp}^0 \equiv \omega_2 - \omega_1 $	$2\Delta\omega/\sin\varphi$	$\delta\omega_{pp} \equiv \omega_B - \omega_A $	$2\sqrt{3}\Delta\omega \sin \frac{\varphi}{3}/\sin\varphi$
$S_0 \equiv S(0, \varphi)$	$\rho(\varphi) \cos\varphi/(\pi\Delta\omega)$	$S'_0 \equiv S'(0, \varphi)$	$\rho(\varphi) \sin\varphi/(\pi\Delta\omega^2)$
$A_0 \equiv S(\omega_1, \varphi) $	$\rho(\varphi) \cos^2 \frac{\varphi}{2}/(\pi\Delta\omega)$	$C \equiv S'(\omega_C, \varphi) $	$\rho(\varphi) \sin^3 \frac{\varphi}{3}/(\pi\Delta\omega^2)$
$B_0 \equiv S(\omega_2, \varphi) $	$\rho(\varphi) \sin^2 \frac{\varphi}{2}/(\pi\Delta\omega)$	$B \equiv S'(\omega_B, \varphi) $	$\rho(\varphi) \sin^3 \varphi (1 - 2\sin(\frac{\pi}{6} - \frac{2\varphi}{3})) / ((-3 + 4\sin(\frac{\pi}{6} - \frac{2\varphi}{3}) + 2\sin(\frac{\pi}{6} + \frac{4\varphi}{3}))^2 \pi\Delta\omega^2)$
$\mathcal{A}_{pp}^0 \equiv A_0 + B_0$	$\rho(\varphi)/(\pi\Delta\omega)$	$\mathcal{A}_{pp} \equiv A + B$	$3\sqrt{3}\rho(\varphi) \cos \frac{\varphi}{3}/(4\pi\Delta\omega^2)$

systems (let's say two like in the mentioned kagomé compound), we first find their intrinsic phases by employing function $\mathcal{H}(\phi)$ to each, and then subtract their φ values afterwards. In the case when one of the two lines is in fact a CESR line, their phase difference computed in this way reveals the conduction properties of the material.

The antisymmetry of $\omega_A(\phi)$, $\omega_B(\phi)$, and $\omega_C(\phi)$ is outlined in Fig. 2(a). The figure evidently demonstrates the odd parity of the three dependences with respect to $\phi = 180^\circ$. This entails a possibility of halving the entire ϕ domain whereby no property of $S'(\phi)$ is affected. Moreover, this domain can be further dimidiated (cut in half and glued together) on the basis of characteristics of A and B delineated in Fig. 2(b). Namely, it turns out that B and C interchange beyond $\phi = 90^\circ$ so that it is sufficient to map the $S'(\omega, \phi)$ function onto the first quadrant in accordance with the procedure given in (4) and (5). Consequently, all the desired curve features presented in Table 1 can be deduced completely from the dependence on φ . One such parameter is

$A/B \equiv f(\varphi)$, the so-called asymmetry parameter, which measures the ratio between the highest peak height and the lowest dip depth:

$$A/B = \frac{(1 + 2\cos \frac{2\varphi}{3})(3\cos(\frac{\pi}{6} - \frac{\varphi}{3}) + \sin\varphi)}{4\cos(\frac{\pi}{6} - \frac{\varphi}{3})(1 + \sin(\frac{\pi}{6} - \frac{2\varphi}{3}))^2}, \quad (6)$$

which varies only in the range from 1 to 8, as shown in Fig. 2(c). This property is maintained in the extensions beyond $\phi = \pi/2$, unlike $A_0/B_0 = \cot^2 \frac{\varphi}{2}$ in the case of $S(\omega, \phi)$, which may take arbitrary positive values.

2.2. Fitting shortcuts

It is of practical use to experimentalists to have an instructive procedure for fitting CESR spectra in a rather expeditious way. Though exact, algorithms based on the nonlinear least square method, used to refine the fitting parameters by successive iterations, represent slow solution-focused approaches. Here we offer a fitting strategy consisting of few shortcuts towards extracting the relevant CESR parameters, such as phase, microwave loss function, spin relaxation time, and g-factor, immediately from a given lineshape. In Fig. 2(d), the red line represents a single CESR line as recorded in a standard ESR measurement. The first step in interpretation includes tracing the base line (dashed line in Fig. 2) and the three significant points: (i) the point with the greatest height ($H_0 + H_A, A$), (ii) the point with the greatest depth ($H_0 + H_B, -B$), and (iii) the spectral node as the crossing point between the spectra and base line ($H_0 + H_2, 0$). By measuring the ratio A/B one finds the phase parameter φ from Eq. (6) as $\varphi = f^{-1}(A/B)$, or alternatively, one can carefully read off the A/B vs φ data from Fig. 2(c). The next steps comprise of measuring the peak-to-peak distances, both horizontal ($\delta H_{pp} = \kappa\delta\omega_{pp}$) and vertical ($\mathcal{A}_{pp} \equiv A + B$). Following Table 1, the ESR linewidth $\Delta H \equiv \kappa\Delta\omega$, which is in direct relationship with spin relaxation time, is obtained as $\Delta H = \frac{\sqrt{3}\sin\varphi}{6\sin(\varphi/3)}\delta H_{pp}$, where $\delta H_{pp} \equiv \kappa\delta\omega_{pp}$. Microwave loss function $\rho(\varphi)$ can be expressed as

$$\rho(\varphi) = \frac{\pi\sqrt{3}\sin^2\varphi}{27\cos(\varphi/3)\sin^2(\varphi/3)}\delta H_{pp}^2\mathcal{A}_{pp},$$

which is based on the results from Table 1 too. Nevertheless, the derivation of \mathcal{A}_{pp} has been made on the assumption that the spin susceptibility is normalized to unity. Consequently, \mathcal{A}_{pp} must be multiplied by factor \mathcal{N} . It is therefore necessary to properly calibrate the spectrometer in order to relate the digits displayed on the screen with the actual intensity values related to the authentic number of the active spins (\mathcal{N}). ESR reference materials, such as conventionally adopted DPPH solvent complexes [36,37] are frequently used for that point requiring the phase to be set to zero. In conducting systems, however, $\rho(\varphi)$ may well be smaller than 1. This makes such calibrations quite convoluted because they must be cautiously carried out under the strictly same phase-less resonant conditions. Still, in conducting systems φ can purposefully be adjusted to zero which automatically leads to the maximum of microwave loss function

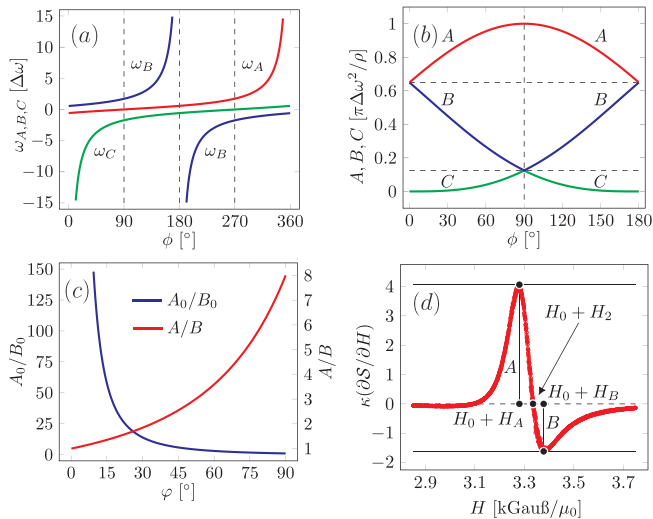


Fig. 2. The odd parity of $\omega_A(\phi)$, $\omega_B(\phi)$, and $\omega_C(\phi)$ over $\phi \in [0, 2\pi)$ (a) and the symmetric behaviour of the angular dependent A , B , and C with respect to $\phi = 90^\circ$ (b). The φ dependence of asymmetry parameters A/B and A_0/B_0 are given in (c), while (d) delineates arbitrarily simulated CESR data at nearly $\nu_0 = 9.4$ GHz with the representative points meant for fitting shortcuts. First magnetic field derivative of the absorbed power near resonance, $\delta S/\delta H$, must be multiplied by factor κ in order for the spectra to coincide with $\delta S/\delta\omega$ in Fig. 1 (upper in red). External magnetic field strengths H_i are jointly equal to $\kappa\omega_i$ for each $i \in \{1, 2, A, B, C\}$, where ω_i are given in Table 1. External H field is expressed in kGauß/ μ_0 , which in cgs metric converts to the same numbers of kØrstedts ($\mu_0 = 1$ and 1 Gauß = 1 Ørsted), whereas in SI metric the external H field must be expressed in A/m ($\mu_0 = 4\pi \times 10^{-7}$ H/m and 1 T = 10^4 Gauß). (For interpretation of the references to colour in this figure legend, the reader is referred to the web version of this article.)

($\rho(\varphi) = 1$). To this effect, we resort to (i) extra ESR measurements at different crystal orientations with respect to the AC field configuration for which the CESR lineshape asymmetry ratio is drastically moderated down to 1 [19], or simply, (ii) extra measurements can be carried out with the sample crushed to a form of powder with ultra-micro-sized crystallites [17,18]. In either way, (i) or (ii), $\varphi = 0$ so that the microwave loss function obtained at finite phase reads

$$\rho(\varphi) = \frac{\sin^2 \varphi}{9 \cos(\varphi/3) \sin^2(\varphi/3)} \frac{\delta H_{(\varphi)pp}^2 \mathcal{A}_{(\varphi)pp}}{\delta H_{(0)pp}^2 \mathcal{A}_{(0)pp}}, \quad (7)$$

where subscripts (0) and (φ) correspond to the peak-to-peak distances measured at $A/B = 1$ or $\rho(0) = 1$ and $A/B > 1$ or $\rho(\varphi) < 1$, respectively.

Particularly interesting is narrowly locating the resonant magnetic field H_0 , as an imperative for a rigorous g -factor determination. Ideally, in isotropic highly conducting systems, the g -factor attains the free electron value of 2.0023 which is accurate even to five significant figures. Common CESR experiments deal with g -factors of rapidly moving electrons scattered by lattice vibrations which deviate only little from this number. This leads to the motional narrowing phenomenon because the CESR linewidth is oftentimes $\propto (g - 2.0023)^2$ [21]. Therefore, requirements for both high precision and reasonable accuracy in finding g -factor values are essential in order to trace the origin of the active spins. A cost-effective solution consists of measuring the position of the third significant point, the so-called spectral node $H_0 + H_2$. Value $H_2 = \frac{\sqrt{3} \tan(\varphi/2) \sin \varphi}{6 \sin(\varphi/3)} \delta H_{pp}$ must be subtracted from this position to come up with the proper H_0 value. Given that ESR is a highly sensitive probe, omitting this subtraction would have misleading consequences on the interpretation of what the ESR active species are in the system. The most trivial case boils down to $\varphi = 0$ when $H_2 = 0$ so that the subtraction is naturally left out. This common wisdom, nonetheless, cannot be extended to the general $\varphi \neq 0$ case that would otherwise provide an erroneous g -factor explanation.

2.3. Geometry independent universality

Following [10] CESR function profile can safely be written down as $x\chi''(\omega) + y\chi'(\omega)$, where x and y are the non-negative absorption and dispersion fractions respectively. Microwave loss function, $\rho(\varphi)$, is thus identified as $\sqrt{x^2 + y^2}$, while φ takes on $\arctan(y/x)$. Along this line, for all absorptions $\chi''(\omega)$ of Lorentzian nature, $A/B \leq 8$ must always be fulfilled no matter what the values of $x \geq 0$ and $y \geq 0$ are in general. This is a restriction imposed on A/B , as there is no limitation on φ within the interval $[0, \pi/2]$. However, concrete response functions in CESR seems not to be as general, and may have further restrictions to φ and thence A/B , which are closely related to crystal properties. In this section we survey three relevant geometries of metallic crystals: infinite plate of thickness d , long cylinder of diameter d , and sphere of diameter d . Using properly defined boundary conditions in Maxwell equations, Chapman et al. [5] explicitly derived the *on-resonance* signal expressions for $x(\eta)$ and $y(\eta)$, where $\eta \equiv d/\delta$ and δ represents the skin depth. AC field acting perpendicularly to the crystal face is screened within this depth which falls off with increasing resonant frequency and, if not anomalous [38], depends on the crystal conductivity explicitly.

Microwave loss function $\rho(\varphi)$ and the asymmetry ratio $A/B \equiv f(\varphi)$ are explicit functions of φ . Moreover, as $\varphi = \arctan(y(\eta)/x(\eta))$, it is rather practical to express the two dependences in terms of η on the log scale for the three considered geometries, as given in Figs. 3 and 4. We observe three local maxima in A/B for the three different geometries: for plate ($\varphi \approx 72.12^\circ$, $A/B \approx 4.86$), for cylinder ($\varphi \approx 55.86^\circ$, $A/B \approx 3.26$), and for sphere ($\varphi \approx 42.18^\circ$, $A/B \approx 2.40$). When $\eta \rightarrow 1/2$ the AC field fully penetrates into the crystal, and then $\rho \rightarrow 100\%$ and $A/B \rightarrow 1$, while $\varphi \rightarrow 0$ for all the three geometries. This corresponds to the case of insulators or very small metallic particles with the pure absorption and no dispersion for $d/2 \leq \delta$. The other limit concerns large or extremely conductive metallic samples when $\eta \rightarrow \infty$. The limit leads to

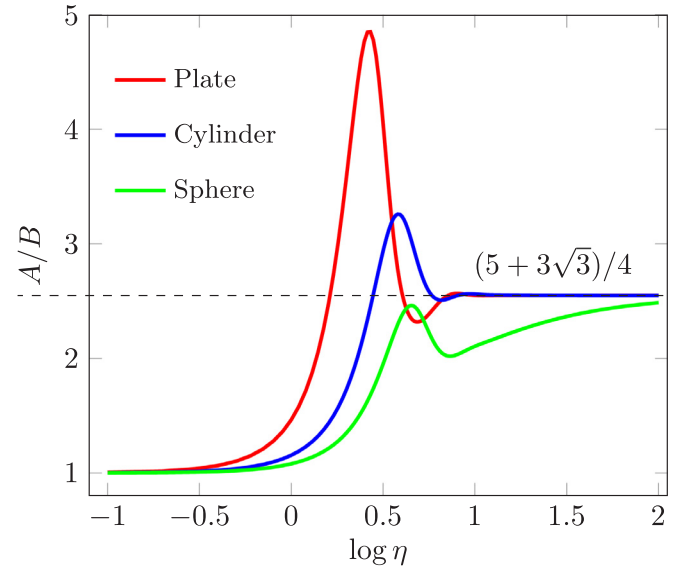


Fig. 3. Evolution of the asymmetry ratio A/B with respect to η for the three geometries considered: infinite plate (red), long cylinder (blue), and sphere (green).

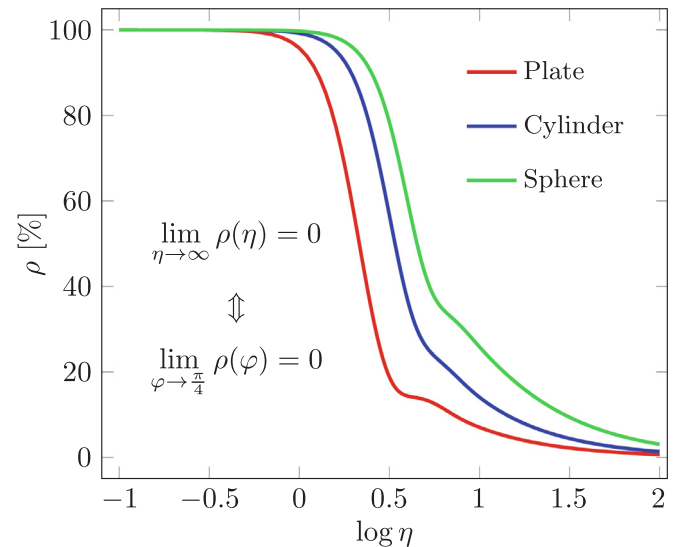


Fig. 4. Evolution of the microwave loss function $\rho(\eta)$ with respect to η for the three geometries considered: infinite plate (red), long cylinder (blue), and sphere (green). (For interpretation of the references to colour in this figure legend, the reader is referred to the web version of this article.)

$\rho \rightarrow 0$, $\varphi \rightarrow \pi/4$, and $A/B \rightarrow f(\pi/4) = (5 + 3\sqrt{3})/4 \approx 2.54904\dots$, irrespective of geometry. Both fractions $x(\eta \rightarrow \infty)$ and $y(\eta \rightarrow \infty)$ are in this case infinitesimally small and the total signal is practically lost. It is crucial to note that at $\eta \rightarrow \infty$ limit, or alternatively $\varphi \rightarrow \pi/4$, each $x(\eta)$ and $y(\eta)$ tends to vanish [10], so that this limit can be treated universally, independent of the assumed geometries. Whatever the analyzed geometry is, both $x(\eta \rightarrow \infty)$ and $y(\eta \rightarrow \infty)$ tend toward zero at equal asymptotic rates, giving $x/y \rightarrow 1$. For this reason $A/B = (5 + 3\sqrt{3})/4$ can safely be considered as the universal value at equal absorption and dispersion contributions to the vanishing CESR spectra. This value can be very often found in literature, yet poorly termed as the 2.55 asymmetry limit without particular analytical derivation. To the extent of our knowledge, this limiting value has not previously been reported in an analytic form.

3. Concluding remarks

In conclusion, we have surveyed the preceding progress in CESR to concentrate on a particular limit of Dyson's theory following a purely quantum mechanical treatment after Kaplan. Known as NMR's, this limit implies that the CESR lineshape is a mixture of absorption and dispersion with non-negative contributions. We have quantitatively analyzed the related CESR profiles by attaching the importance to the applicable points and segments. These have been further implemented in a proposed fitting procedure consisting of few quick shortcuts. Being particularly expeditious and able to keep the relevant information about the sample properties at the same time, the procedure has an advantage over standard ways to fit CESR spectra. At last, it has been demonstrated that the asymmetry ratio limit in the case of highly conducting particles, the so-called extreme CESR, has the universal geometry independent value of $A/B \rightarrow (5 + 3\sqrt{3})/4$, which is consistent with a familiar numeric value often seen in literature and nearly equal to 2.55.

Acknowledgments


The authors are profoundly indebted to Professor László Forró for fruitful discussions in the field. Support by the Serbian Ministry of Education, Science, and Technological Development through project OI 171032 is greatly acknowledged.

References

- [1] G. Feher, A.F. Kip, Electron spin resonance absorption in metals. I Experimental, *Phys. Rev.* 98 (1955) 337–348 doi:10.1103/PhysRev.98.337.
- [2] F.J. Dyson, Electron spin resonance absorption in metals. II. Theory of electron diffusion and the skin effect, *Phys. Rev.* 98 (1955) 349–359 doi:10.1103/PhysRev.98.349.
- [3] M.I. Azbel, V.I. Gerasimenko, I.M. Lifshitz, Paramagnetic resonance and polarization of nuclei in metals, *Sov. Phys. JETP* 5 (1957) 986–996.
- [4] M.I. Azbel, V.I. Gerasimenko, I.M. Lifshitz, On the theory of paramagnetic resonance in metals, *Sov. Phys. JETP* 8 (1959) 480–487.
- [5] A.C. Chapman, P. Rhodes, E.F.W. Seymour, The effect of eddy currents on nuclear magnetic resonance in metals, *Proc. Phys. Soc. B* 70 (1957) 345–360, <https://doi.org/10.1088/0370-1301/70/4/301>.
- [6] P.M. Platzman, P.A. Wolff, Spin-wave excitation in nonferromagnetic metals, *Phys. Rev. Lett.* 18 (1967) 280–283, <https://doi.org/10.1103/PhysRevLett.18.280>.
- [7] H.R. Webb, Electron-spin-resonance line shape in spherical metal particles, *Phys. Rev.* 158 (1967) 225–233, <https://doi.org/10.1103/PhysRev.158.225>.
- [8] J.H. Pifer, R. Magno, Conduction-electron spin resonance in a lithium film, *Phys. Rev. B* 3 (1971) 663–673, <https://doi.org/10.1103/PhysRevB.3.663>.
- [9] A.H. Kahn, Theory of microwave eddy currents and paramagnetic resonance in materials of intermediate conductivity, *Phys. Rev. B* 16 (1977) 64–72, <https://doi.org/10.1103/PhysRevB.16.64>.
- [10] J.I. Kaplan, J. Reuben, Electron spin resonance line shapes of paramagnetic species on surfaces, *J. Phys. Chem.* 86 (1982) 4465–4466, <https://doi.org/10.1021/j100220a001>.
- [11] A.G. Marshall, D.C. Roe, Dispersion versus absorption: spectral line shape analysis for radiofrequency and microwave spectrometry, *Analyt. Chem.* 50 (1978) 756–763, <https://doi.org/10.1021/ac50027a023>.
- [12] A.E. Siegman, *Lasers*, University Science Books, Mill Valley, California, USA, 1986.
- [13] L. Walmsley, G. Ceotto, J.H. Castilho, C. Rettori, Magnetic field modulation frequency, sample size and electromagnetic configuration effects on the spin resonance spectra of graphite intercalation compounds, *Synth. Met.* 30 (1989) 97–107, [https://doi.org/10.1016/0379-6779\(89\)90645-0](https://doi.org/10.1016/0379-6779(89)90645-0).
- [14] L. Walmsley, Translating conduction-electron spin-resonance lines into lorentzian lines, *J. Magn. Reson. A* 122 (1996) 209–213, <https://doi.org/10.1006/jmra.1996.0196>.
- [15] M. Oshikawa, I. Affleck, Electron spin resonance in $s = \frac{1}{2}$ antiferromagnetic chains, *Phys. Rev. B* 65 (2002) 134410–134437, <https://doi.org/10.1103/PhysRevB.65.134410>.
- [16] J.P. Joshi, S.V. Bhat, On the analysis of broad Dysonian electron paramagnetic resonance spectra, *J. Magn. Res.* 168 (2004) 284–287, <https://doi.org/10.1016/j.jmr.2004.03.018>.
- [17] F. Beuneu, P. Vajda, Spectroscopic evidence for large ($>1\mu\text{m}$) lithium-colloid creation in electron-irradiated Li_2O single crystals, *Phys. Rev. Lett.* 76 (1996) 4544–4547, <https://doi.org/10.1103/PhysRevLett.76.4544>.
- [18] F. Beuneu, P. Vajda, O.J. Zogal, Magnetic resonance of micrometer size Li-metal colloids in electron-irradiated Li_2O crystals, *Colloids Surfaces A: Physicochem. Eng. Aspects* 158 (1999) 83–87, [https://doi.org/10.1016/S0927-7757\(99\)00134-X](https://doi.org/10.1016/S0927-7757(99)00134-X).
- [19] S.A. Baudron, P. Batail, C. Coulon, R. Clérac, E. Canadell, V. Laukhin, R. Melzi, P. Wzietek, D. Jérôme, P. Auban-Senzier, S. Ravy, (EDT-TTF- CONH_2) $_6$ [$\text{Re}_6\text{Se}_6(\text{CN})_{2005}$], a metallic kagome-type organic-inorganic hybrid compound: Electronic instability, molecular motion, and charge localization, *J. Am. Chem. Soc.* 127 (2005) 11785–11797, <https://doi.org/10.1021/ja0523385>.
- [20] A. Janossy, O. Chauvet, S. Pekker, J.R. Cooper, L. Forró, Conduction electron spin resonance in rb_3c_{60} , *Phys. Rev. Lett.* 71 (1993) 1091–1094, <https://doi.org/10.1103/PhysRevLett.71.1091>.
- [21] W.D. Rice, R.T. Weber, P. Nikolaev, S. Arepalli, V. Berka, A.L. Tsai, J. Kono, Spin relaxation times of single-wall carbon nanotubes, *Phys. Rev. B* 88 (2013) 041401–041405, <https://doi.org/10.1103/PhysRevB.88.041401>.
- [22] P. Szirmai, G. Fábrián, J. Koltai, B. Náfrádi, L. Forró, T. Pichler, O.A. Williams, S. Mandal, C. Bäuerle, F. Simon, Observation of conduction electron spin resonance in boron-doped diamond, *Phys. Rev. B* 87 (2013) 195132, <https://doi.org/10.1103/PhysRevB.87.195132>.
- [23] K.W. Blazey, K.A. Müller, F. Blatter, E. Schumacher, Conduction electron spin resonance of caesium metallic clusters in zeolite x, *Europhys. Lett.* 4 (1987) 857–861, <https://doi.org/10.1209/0295-5075/4/7/017>.
- [24] J.J. van der Klink, H.B. Brom, Nmr in metals, metal particles and metal cluster compounds, *Prog. Nucl. Magn. Reson. Spectr.* 36 (2) (2000) 89–201, [https://doi.org/10.1016/S0079-6565\(99\)00020-5](https://doi.org/10.1016/S0079-6565(99)00020-5).
- [25] J.I. Kaplan, G. Fraenkel, *NMR of Chemically Exchanging Systems*, Academic Press, 1980.
- [26] J.I. Kaplan, Absorption lineshapes modified by an experimentally undetected absorption, *J. Magn. Reson.* 80 (1988) 340–343, [https://doi.org/10.1016/0022-2364\(88\)90306-X](https://doi.org/10.1016/0022-2364(88)90306-X).
- [27] D. ter Haar, *Fluctuation, Relaxation, and Resonance in Magnetic Systems*, Oliver and Boyd, Edinburgh, Schotland, 1962.
- [28] T.-K. Ng, *Introduction to Classical and Quantum Field Theory*, Wiley, Weinheim, Germany, 2009.
- [29] P.M. Richards, *Proceedings of the International School of Physics, Enrico Fermi, North-Holland, Amsterdam LIX, 1976*, p. 539.
- [30] T.T.P. Cheung, Z.G. Soos, Theory of exchange narrowing in low-dimensional correlated spin systems, *J. Chem. Phys.* 69 (8) (1978) 3845–3853, <https://doi.org/10.1063/1.437050>.
- [31] D.L. Huber, Spin diffusion in geometrically frustrated heisenberg nterferromagnets, *J. Phys.: Condens. Matter* 15 (2003) L579–L583, <https://doi.org/10.1088/0953-8984/15/37/L04>.
- [32] P. Wölfle, E. Abrahams, Phenomenology of ESR in heavy-fermion systems: Fermi-liquid and non-Fermi-liquid regimes, *Phys. Rev. B* 80 (2009) 235112–235119, <https://doi.org/10.1103/PhysRevB.80.235112>.
- [33] B. Cowan, *Nuclear Magnetic Resonance and Relaxation*, Cambridge University Press, Cambridge, UK, 1997 doi: 10.1017/CBO9780511524226.
- [34] B. Náfrádi, R. Gaál, T. Fehér, L. Forró, Microwave frequency modulation in continuous-wave far-infrared ESR.
- [35] B. Náfrádi, R. Gaál, A. Sienkiewicz, T. Fehér, L. Forró, Continuous-wave far-infrared ESR spectrometer for high-pressure measurements, *J. Magn. Res.* 195 (2008) 206–210, <https://doi.org/10.1016/j.jmr.2008.09.014>.
- [36] A.M. Prokhorov, V.B. Fedorov, Aniferromagnetism of free radicals, *Soviet Phys. JETP* 16 (1963) 1489.
- [37] F. Teruaki, Magnetic interaction in solvent-free DPPH and DPPH solvent complexes, *Bull. Chem. Soc. Jpn.* 54 (1981) 3110–3116, <https://doi.org/10.1246/bcsj.54.3110>.
- [38] A.A. Abrikosov, *Introduction to the Theory of Normal Metals Solid State Supplement 12*, Academic Press, New York, USA, 1972.

FULL ARTICLE

Naturally safe: Cellular noise for document security

Danica Pavlović¹ | Mihailo D. Rabasović¹ | Aleksandar J. Krmpot¹ | Vladimir Lazović¹ | Srećko Čurčić² | Dejan V. Stojanović³ | Branislav Jelenković¹ | Wang Zhang⁴ | Di Zhang⁴ | Nenad Vukmirović¹ | Dimitrije Stepanenko¹ | Branko Kolarić^{1,5}  | Dejan V. Pantelić^{1*}

¹Institute of Physics, University of Belgrade, Belgrade, Serbia

²Institute of Zoology, University of Belgrade—Faculty of Biology, Belgrade, Serbia

³Institute of Lowland Forestry and Environment, University of Novi Sad, Novi Sad, Serbia

⁴State Key Lab of Metal Matrix Composite, Shanghai Jiao Tong University, Shanghai, China

⁵MNM Group, Department of Physics, UMONS, Mons, Belgium

*Correspondence

Dejan V. Pantelić, Institute of Physics, University of Belgrade, Photonics Center, Pregrevica 118, 11080 Zemun, Belgrade, Serbia.

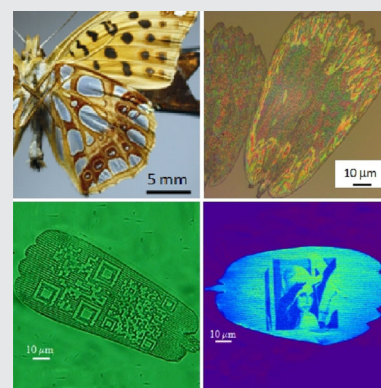
Email: pantelic@ipb.ac.rs

Funding information

Joint Funding of Development and Research Projects of the Republic of Serbia 407 and the People's Republic of China; Ministry of Education, Science and Technological 404 Development of the Republic of Serbia, Grant/Award Numbers: III45016, III43002, ON171038, ON173038, ON171017, ON171032; Institute of Physics; Innovation Fund; German Academic Exchange Service; Ministry of Education, Science and Technological Development of the Republic of Serbia

Abstract

Modern document protection relies on the simultaneous combination of many optical features with micron and submicron structures, whose complexity is the main obstacle for unauthorized copying. In that sense, documents are best protected by the diffractive optical elements generated lithographically and mass-produced by embossing. The problem is that the resulting security elements are identical, facilitating mass-production of both original and counterfeited documents. Here, we prove that each butterfly wing-scale is structurally and optically unique and can be used as an inimitable optical memory tag and applied for document security. Wing-scales, exhibiting angular variability of their color, were laser-cut and bleached to imprint cryptographic information of an authorized issuer. The resulting optical memory tag is extremely durable, as verified by several century-old insect specimens still retaining their coloration. The described technique is simple, amenable to mass-production, low cost and easy to integrate within the existing security infrastructure.



KEYWORDS

biophotonics, complexity, iridescence, optical document security, variability

1 | INTRODUCTION

Insects have been used more than any other living creatures as a blueprint for design of novel devices. Butterflies and moths (order: Lepidoptera) are particularly inspiring, due to vast number of species (nearly 180 000) [1] and peculiar

optical properties of their wings covered with large number (500–1000/mm²) of tiny, overlapping scales [2] (see section 1 of Appendix S1 for a short description of their properties). Some of them are structurally colored [3] that is, produce colors by interference, diffraction and scattering, rather than pigments. This is due to complex, regular or

irregular, micro/nanostructures, which can be classified in several groups according to their morphology [4]. Most frequently, iridescence (characterized by directionally dependent coloration [3]) can be observed.

Back into the XVIII century, Benjamin Franklin came up with an idea to reproduce the complexity of natural structures for document protection. He printed venation patterns of plant leaves on dollar bills to prevent counterfeiting [5]. Nowadays, his method was superseded by artificial security components, such as optically variable devices (OVDs) [6]. Diffractive optical elements (DOEs) are commonly exploited for the purpose, due to their, inherently complex microstructures, recognizable optical pattern and capability for mass-production by embossing. There is a significant drawback: for the specific type of document, all embossed copies of DOEs are identical. If a fake DOE is manufactured, counterfeited document can be made in large quantities, too. For that reason, an important goal is to invent a device which will provide unique and individual protection for each document. Protective elements should be highly complex, unique, difficult to reverse engineer and imitate. In the relevant literature, such objects are called physical one-way functions and can be realized by embedding randomly dispersed plastic, micron-sized spheres in a transparent medium and observing mesoscopic light scattering [7]. As another example, we mention using a randomized pattern of scattering from paper-based substrates [8].

Imprints of naturally occurring structures were proposed as security elements by Hamm-Dubischar [9], Biermann and Rauhe [10], and Rauhe [11], who presented the idea of document protection using biomineralized shells of radiolarians and diatoms. The protection is based on the structural complexity of their shells. The main problem is that optical effects are not particularly conspicuous, and the complexity can be assessed only at the morphological level, using scanning electron microscopy (SEM). Another problem is that structural variations among individuals of the same species seem to be small.

Whichever security element is used, it must be integrated in a security system relying on three inspection lines [6]: the first line is overt and can be visually inspected by anyone; the second is semi-covert and uses machine inspection; while the third one is covert and relies on forensic inspection with highly specialized equipment.

Here, we analyze the structural complexity, randomness, variability and uniqueness of the optical pattern of iridescent butterfly wing scales. We aim to establish their usefulness as inimitable OVDs for individualized, covert and overt, optical document security. Additionally, we investigate wing-scales as a memory medium for inscription of additional cryptographic information.

2 | STRUCTURE AND IRIDESCENCE OF *ISSORIA LATHONIA* BUTTERFLY WING-SCALES

In this section, we analyze morphological and optical features of scales belonging to the underside silver wing-patches of the Queen of Spain Fritillary, *Issoria lathonia* (Linnaeus, 1758), (see Figure 1A and section 2 of Appendix S1 for a short description of the butterfly's life history). This particular species was studied for the characteristic coloration of individual wing-scales, consisting of red, green and bluish spots randomly dispersed along a grating-like structure (see reflection microscope image in Figure 1B,C). The resulting silver color is produced by the local, additive spectral mixing [12].

Field-emission gun scanning electron microscope (FEGSEM) images reveal detailed structure of the scale's upper lamina (UL in Figure 1D). It consists of lamellar longitudinal ridges (R) regularly separated by a distance of 1.5 μm . There is, also, a fish-bone-shaped sub-wavelength grating (SW) with period of 150 nm, radiating from ridges. The interior of the scale is hollow, filled only with nano-pillars, separating UL and lower lamina (LL).

Nonlinear optical microscopy was used to analyze three-dimensional (3D) structure of wing-scales using two-photon excited fluorescence (TPEF) of chitin. Nonlinear microscope was constructed in-house [13] (see Appendix S1 for details) and used to reveal that the wing scales have irregular, wavy shape (see Figure 1E). This significantly contributes to variability of the resulting optical pattern, together with variation of the thicknesses of upper and lower laminae and their mutual distance.

We have found that the individual wing scales are iridescent, that is, the color pattern strongly depends on illumination and observation directions. The pattern has maximum brightness and sharpness for orthogonal illumination, directly through the microscope objective (resulting in an image like in Figure 1C).

3 | VARIABILITY OF OPTICAL PATTERN AND UNIQUENESS OF BUTTERFLY WING-SCALES

In this section, we will establish a connection between the wing scale morphology and the resulting reflection spectrum. To do that, we have to make a numerical model, enabling us to calculate the reflection spectrum of a single wing scale, removed from the wing and attached to a transparent substrate (as in Figure 1C). For simplicity, each scale is represented by two, wavy thin plates, separated by the layer of air. To approximate waviness each scale is divided into a number of vertical sections with different positions

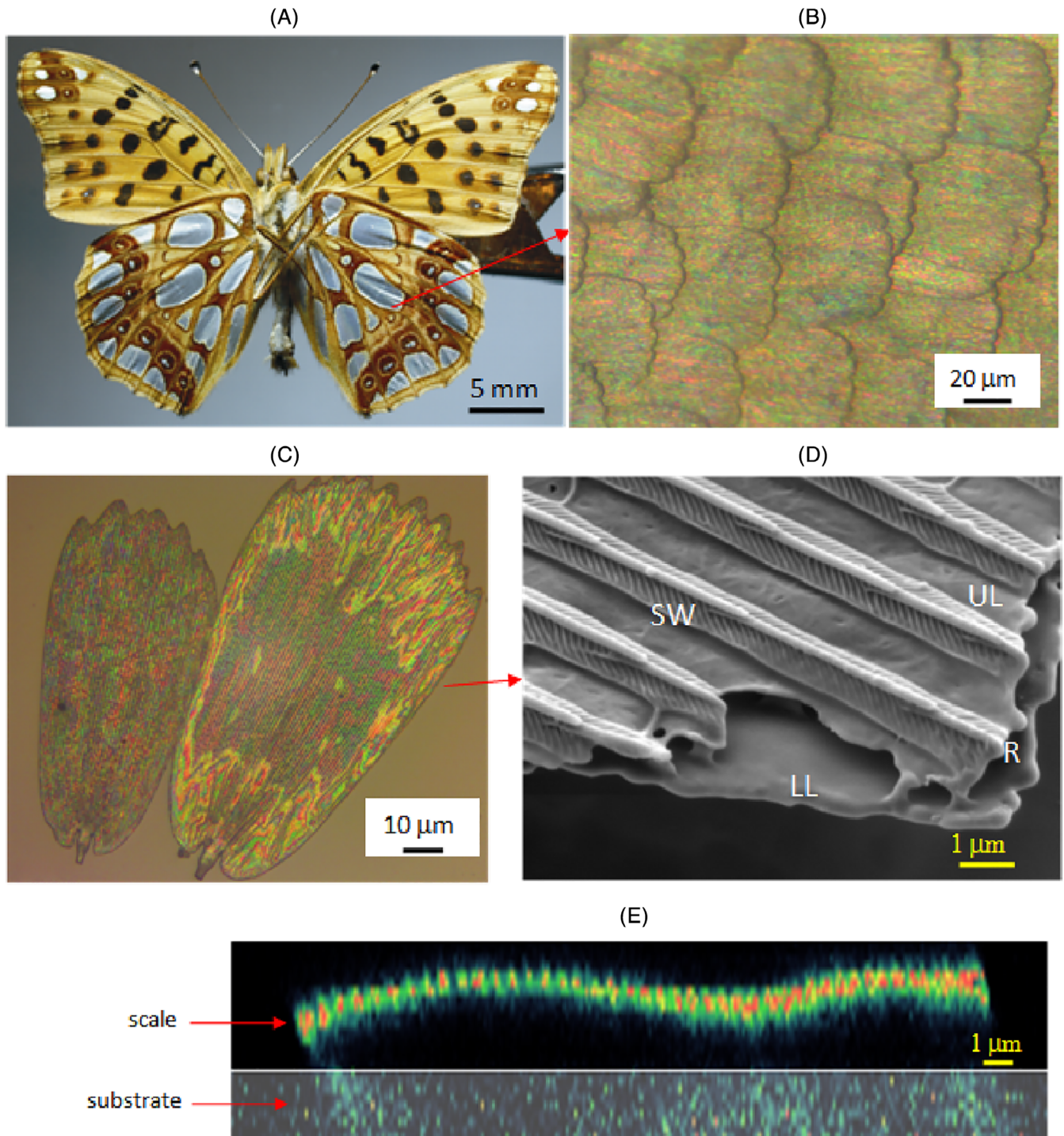


FIGURE 1 A, Ventral side of *Issoria lathonia* butterfly. B, Reflection microscope (10 \times , 0.25 NA) image of wing scales from the silver patch. C, Reflection microscope image (20 \times , 0.4 NA) image of two isolated wing-scales, removed from the wing of *I. lathonia*. D Scanning electron microscope image of the *I. lathonia* wing scale. LL and UL are lower and upper lamina, respectively, R is a ridge, while SW is a, fishbone-shaped, sub-wavelength grating. E, Wavy cross-section of butterfly wing scale (as recorded on a nonlinear optical scanning microscope)

and thicknesses of layers (Figure 2A). Each section contains two layers of chitin, the first of which was regarded as a sub-wavelength scattering surface, due to its irregularity and presence of the subwavelength grating (Figure 1D). Both

layers are separated from the glass substrate by an additional air layer.

Reflection spectrum of each section was calculated using a transfer matrix method, modified to include the effects of

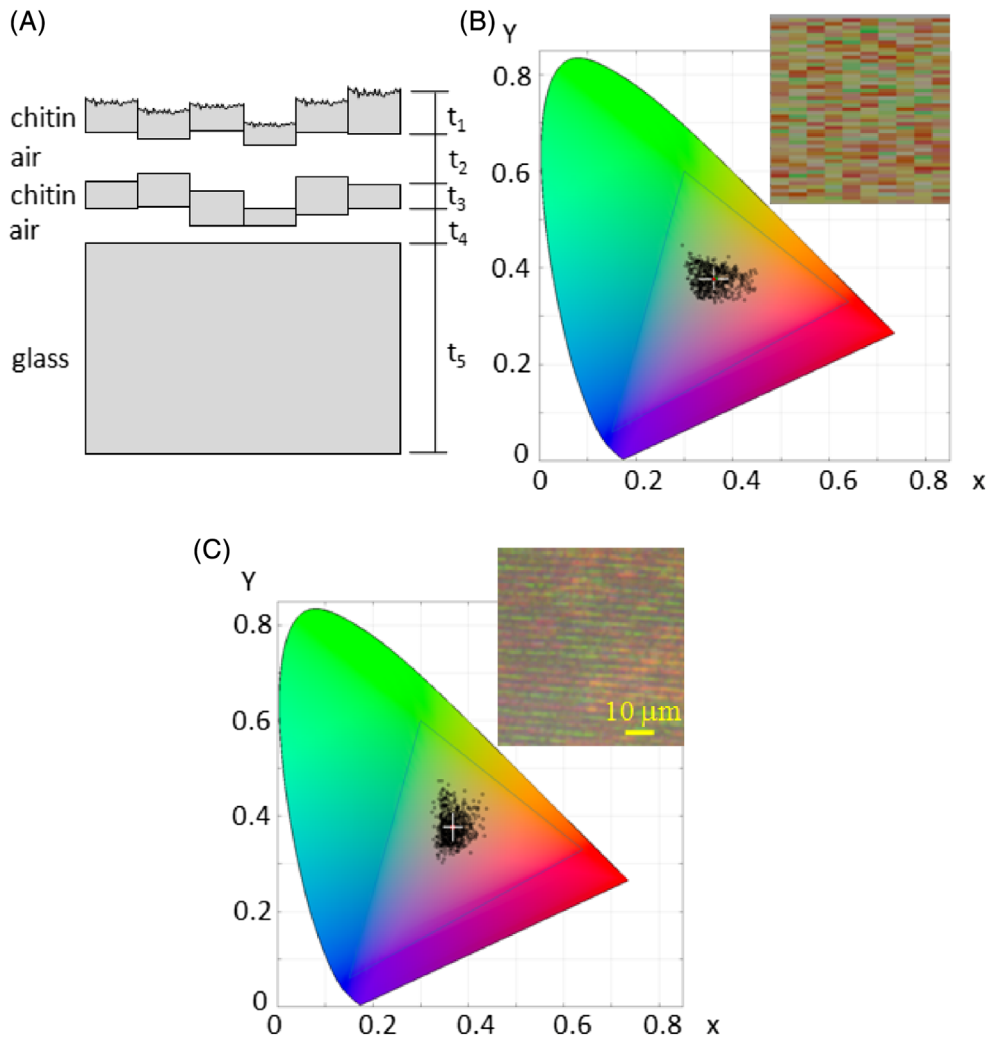


FIGURE 2 A, A theoretical model of a wing scale on the glass substrate. B, Color coordinates of a modeled pattern are presented in a CIE 1931 diagram, together with the color pattern in the inset. C, Color coordinates of *Issoria lathonia* pattern are presented in a CIE 1931 diagram. A section of a *I. lathonia* wing scale pattern, used to calculate color coordinates, is presented in the inset. Crosses in B and C represent average color value and their lengths indicate SDs in x - and y -directions

scattering [14]. Layer thicknesses (t_1, t_2, \dots, t_5 in Figure 2A) and their corresponding refractive indices were the parameters of the model, as well as the root mean square roughness (RMS) of the surfaces.

To simulate the wing scale as a whole, the same calculation was performed for each section. The starting point of our simulation was the layer thicknesses estimated from Figures 1D,E (~ 100 nm chitin, ~ 1000 nm air layer thickness—see section 3 of Appendix S1 for the complete list of parameter values). Layer thicknesses were stochastically varied (according to normal distribution) with pre-defined SD $\sigma = 15$ nm. Following the calculation of spectrum for each section, xyY color coordinates were calculated. They were presented in a CIE 1931 diagram (black dots in Figure 2B), which was designed to closely match human color perception (through three color-matching functions) [15]. It is, also, a useful tool to represent RGB values of color-camera images recorded through this research.

Calculated colors are, also, represented as a pattern of rectangular colored patches (see inset in Figure 2B). For

comparison, color coordinates of experimentally recorded pattern (inset in Figure 2C) were also computed and presented in CIE 1931 diagram (Figure 2C).

We were not able to obtain perfect match in CIE diagrams (Figures 2B,C), for the same reason which prevents a counterfeit to forge a wing scale—complexity of the problem. However, we were able to match the position of the mean color coordinate (small white crosses in CIE diagrams) of theoretical and experimental image. The shape of the color scattering distribution is different, but the SDs are similar.

The most important result is that the variation of layer thicknesses by only ± 15 nm leads to experimentally recorded variability of coloration. This means that one trying to copy the exact coloration pattern of the wing scale, has to maintain an extreme precision of manufacturing—at least one-tenth of the layer thickness variability (~ 1.5 nm). The task is well beyond practical limits of modern technology, and cellular noise precludes replication of identical wing-scales by natural means.

Wing-scales described above have a sufficient number of degrees of freedom (in terms of layer thicknesses and waveness) to enable significant variability. Here, we want to find how difficult would be to find two identical scales.

We first analyze the statistical properties of the wing-scales color patterns by decomposing an image into its RGB components and calculating two-dimensional (2D) autocorrelation function for each color channel separately—see details in section 4 of Appendix S1. It can be seen (Figure S1) that autocorrelation peak is asymmetrical, that is, its width along the wing-scale grating was estimated at 30 μm , while in the orthogonal direction it is 1.5 μm .

By taking into account that average dimensions of the scales are 50 \times 100 μm , we can easily calculate that there are $[50/1.5] \times [100/30] = 33 \times 3 = 99$ (numbers were rounded to the nearest integer) statistically independent, colored patches. We can discriminate intensity of a single color channel in, at least, 10 discrete levels—easily achievable for any low-cost or mobile phone camera. In that case, we may estimate that there are, at least theoretically, 10^{99} wing-scales with different patterns per every channel. Thus, finding a scale exactly the same as another, previously chosen, one is impossible from any practical point of view.

Each wing-scale is a dead remnant of an individual cell and thus reflects intrinsic randomness of cellular development. This is a natural consequence of cellular noise [16], which is a well-established fact in biology, resulting in non-deterministic relation between genotype and phenotype. The important thing about butterfly wing scales is that they “freeze” the cellular noise, by leaving it in a state just before the cell died. Cellular noise cannot be switched-off and it is expected to be similar in all other butterfly species. In that sense, the similar level of randomness is expected on all wing-scales of all butterflies [17] including those of the *Issoria lathonia* species.

4 | OPTICAL DOCUMENT PROTECTION WITH WING SCALES

The main idea of this research is to use butterfly wing-scales as a natural, hologram-like, OVDs, permanently attached to a document (eg, a plastic credit card). In contrast to artificial OVDs, natural ones are unique (guaranteed by the cellular noise) and difficult to copy (due to their layered, micro- and nano-scale patterns).

We decided to use a near-field color pattern as a security feature of a document protection system and read it under the optical microscope. Practical inability to place a document at exactly the same position and orientation within the reading system requires shift- and rotation-invariant pattern recognition algorithm. We decided to use algorithm based

on Fourier-Mellin transform (FMT) [18] which fulfills the above requirements.

Nine *I. lathonia* wing-scales were attached to a glass substrate and their reflection microscope images were recorded at several positions and orientations (55 images in all). The recorded images were first decomposed into RGB components and the green one (G) was transformed using FMT. Correlations between corresponding FMT pairs were calculated and the corresponding statistical distribution is shown in Figure 3. The correlation coefficient, corresponding to the same wing-scale at displaced positions, had typical values around 0.4, while it never had values below 0.1. The most frequent values of correlation coefficient for two different wing-scales were around 0.02, and were never larger than 0.06. By placing validity threshold at 0.08, correct discrimination between wing scales is guaranteed.

To correct for accidental tilt or defocusing of the wing scale image, we have recorded images at 3 to 4, closely spaced, focal positions. Consequently, focus stacking algorithm was used (using Picolay free software) to extract well-focused parts in each recorded image and combine them in a single, sharp image.

In order to build a strong security system, malicious party has to be prevented from picking any butterfly wing-scale and attaching it to a document. This can be performed by making a document self-verifying by using a digital signature of the document issuer, within the public key infrastructure (PKI) system [19]. Here, we show that the necessary authentication information can be written on the wing-scale itself.

We used femtosecond laser-processing to additionally modify butterfly wing scales and exploit them as a write-

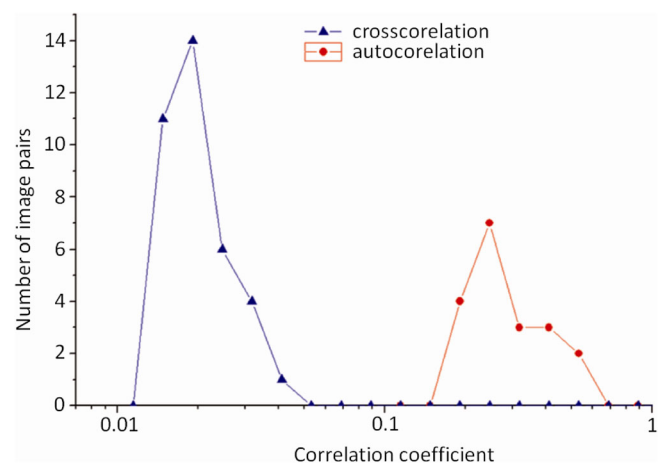
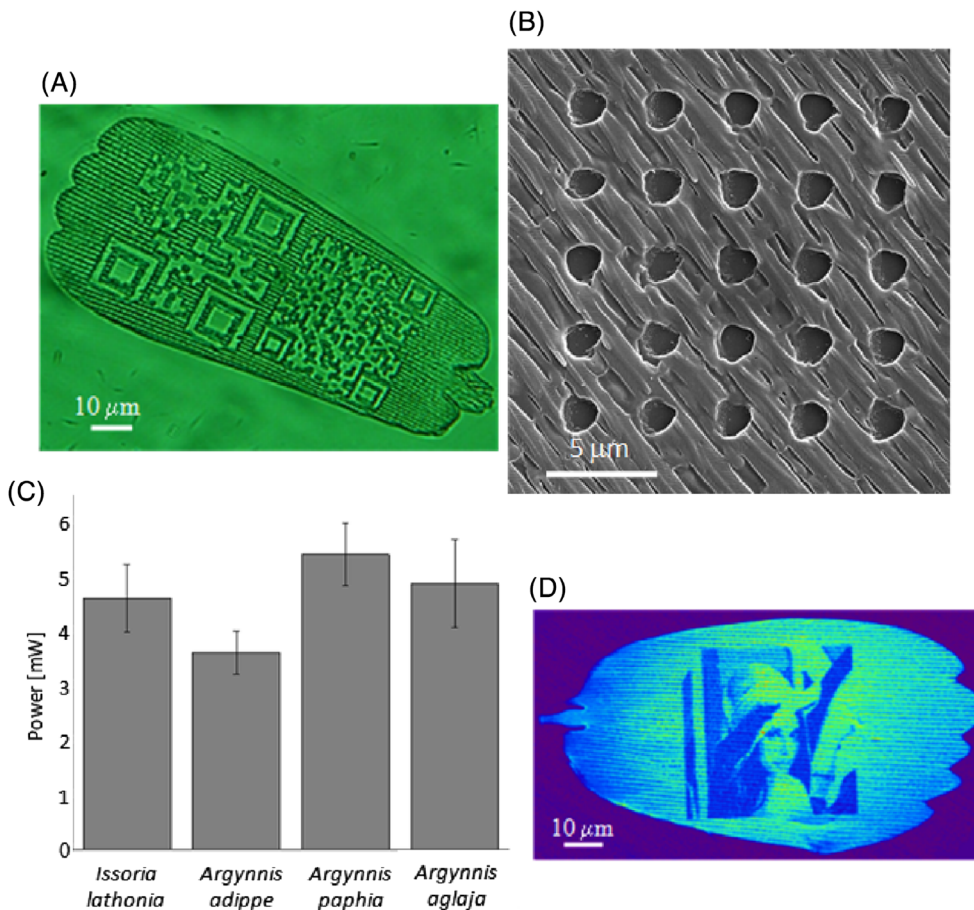


FIGURE 3 Cross- and auto-correlations of ensemble of 55 pairs of wing-scale images. Graph shows a number of image pairs vs the corresponding correlation coefficient. Maximum cross-correlation coefficient is at 0.02, while autocorrelation coefficient is always above 0.2

**FIGURE 4**

(A) Transmission microscope image of a femtosecond-laser-cut wing scale (QR-codes). (B) Array of holes on a *Issoria lathonia* wing-scale showing the minimum achievable diameter of a laser cut. (C) Thresholds for laser cutting of four butterfly species used throughout this research. (D) Selectively bleached wing scale with a Lena image observed by fluorescence modality of a nonlinear microscope

only memory. The software of a home-made nonlinear-microscope [13] was modified to enable vector and raster drawing of an arbitrary image (see section 5 of Appendix S1 for additional details). Depending on the average laser power, repetition rate and dwell time, wing scale can be cut (as in Figure 4A)). Minimal diameter of a laser cut achieved throughout this research is $1.7 \mu\text{m}$, as shown in Figure 4B. Damage threshold is 4.5 mW (using $40 \times 1.3 \text{ NA}$ microscope objective) and 8.0 mW (with $20 \times 0.8 \text{ NA}$ microscope objective). Three more butterfly species were analyzed in that respect, with similar damage thresholds (Figure 4C). In practice, we operated above threshold to enable reliable and repeatable laser-drawing. That is why we achieved the minimum cut width which is considerably above the lateral resolution of our femtosecond system [13]. Based on that and the average size of the wing-scale ($\sim 50 \times 100 \mu\text{m}^2$), we estimated the information capacity of a single scale at about 3000 bits, providing that the damaged spot is treated as binary 1, and undamaged as binary 0.

Here, we point out that each bit, written on the wing-scale, reduces the number of statistically independent patches. We will assume that one half of the wing-scale surface is laser processed (reducing the original wing-scale area of $50 \times 100 = 5000 \mu\text{m}^2$ to approximately $35 \times 70 = 2450 \mu\text{m}^2$). That leaves approximately $[35/1.5] \times [70/30] = 23 \times 2 = 46$ colored patches

(numbers are, again, rounded to the nearest integer). Thus, as in the previous section, we may estimate the number of different wing scales at 10^{46} (per every RGB channel), each one being protected by 1500 bits of additional information.

By reducing the laser power below the damage threshold, we were able to bleach the autofluorescence of the wing-scale and use it to inscribe covert information (Figures 4D) as a gray level image.

5 | DISCUSSION AND CONCLUSIONS

While speaking of document protection, an important question immediately comes to mind: how difficult it is to counterfeit wing-scale? Forgeries can be produced by either (a) imitating the structure or (b) imitating the corresponding optical effect with another, possibly simpler, structure. The first approach is based on “reverse-engineering” and manufacturing of identical protective element structure, while the second one is based on imitating the optical effect.

Reverse engineering of butterfly wing-scales implies analysis of the 3D morphology and material properties (refractive index and absorption) followed by some-kind of lithographic copying of both the morphology and material properties. Even with the most advanced technologies

(microtomography, electron or X-ray holography), this approach will be extremely limited in terms of available resolution of 3D analytic and lithographic methods (of the order of 10 nm), duration and cost [20].

Imitating the optical effect requires careful analysis of iridescence across the whole visible spectrum and angular range, followed by finding a method to faithfully reproduce the optical wavefront. This also poses a fundamental question: is it possible to have identical wave-fields generated by different structures? The question goes into scattering theory, with a plethora of papers dealing with the uniqueness of the direct and inverse problems. There is no general answer to the question, because it depends on the nature of the scatterer (penetrable or non-penetrable), boundary conditions (conductive, dielectric, amplifying), wavelength and angular range of probing radiation [21]. There are more or less exotic situations where uniqueness is not guaranteed, such as amplifying medium or medium with optical cloaks [22]. But, for the range of problems relevant to this work, the answer is no—there are no two different scatterers producing the same scattered field (far or near) [23].

The wing-scales are best protected by their uniqueness implying necessity to counterfeit every single document time and again. Another point is that, both the material composition and morphology are unique, producing a plethora of optical effects: overall shape, iridescence, absorption, polarization, fluorescence, moiré, defects, far and near-field diffraction pattern, local spectra, etc. In addition, scales possess different optical properties on their upper and under side, which may be used to produce security features which can be read from both sides in perfect alignment (so-called see-through register). Simultaneous use of all or some of the mentioned effects vastly increases the capabilities of wing scale as a protective element.

An important question is whether wing scales can be copied by some of holographic methods. Up to now, volume and surface relief holograms have been copied using contact [24], non-contact [25] or scanning [26] methods. However, these techniques are not useful for copying step-index, layered structure of wing scales, because of the sinusoidal nature of holographic gratings. Additionally, subwavelength gratings of wing-scales (S in Figure 3) cannot be copied, due to evanescent fields obtained by diffraction. These tiny structures are essential for the final coloration of the wing scale, because they produce uniformly scattered radiation in the blue part of the spectrum (see blue component of the wing scale pattern in Figure 8A).

It should be emphasized that Lepidoptera species are not equally suitable for document protection. As already mentioned, these structures must have complex nanometer to micron-size features, with significant variability and must be difficult to analyze and reverse engineer. We preferred

nymphalid species, possessing silver patches on their wings. Other Lepidoptera species, with structurally colored scales have been tested. However, the scales of these species were not so easy to process and manipulate, with the equipment at our disposal.

There is a number of ways how insect scales can be manipulated and attached to documents, as described in the following patent applications [27–29]. Generally speaking, they have to be, either embedded within the transparent medium with large refractive index difference (compared to that of the scale), or placed in a recess with a transparent, protective, covering. The procedure can be performed by micromanipulation or by standard printing techniques (silk-screen, flexo-printing).

Once embedded, scale contents have to be read by some means, which depends on the insect species, type of the scales and the optical effect sought for. In addition to iridescence pattern detection described above, there are other choices: overall shape of the scale, near field color pattern, far-field diffraction pattern, moiré pattern, or pattern of defects (looking like minutia in a fingerprint), with many variations (such as phase and amplitude) and combinations (by recording simultaneously several effects). Reading devices can be based on far- or near-field detection, holography or scanning techniques using CD/DVD readout heads. In the context of document protection, strong variability of patterns with angular position of illumination and observation, as well as the polarization sensitivity are very important. This is what prevents malicious attacks by simple color laser-printing.

The document protection described here is limited to machine reading level. It can be extended to the forensic level, by reading electron microscope image (Figure 1D)), with, for example, cross-rib distances serving as a random feature. If visual protection is desired, a large number of scales can be transferred to another substrate, so to cover large area, visible with the naked eye. One of the scales can be chosen for machine and forensic protection, as described in Reference [28].

Practical implications of the proposed document protection method are numerous. There are thousands of wing scales on a single butterfly specimen suitable for document protection (we have estimated 40 000 iridescent wing scales on *I. lathonia* silver spots). With appropriate choice of butterfly species (eg, *Morpho* spp.) this number can be much larger. If commercially available dry butterfly specimens are used, we have estimated the cost of a single wing scale at $85 \cdot 10^{-6}$ \$. Alternatively, butterfly species can be reared using well-established techniques of sericulture (silkworm raising). Wing-scales can be collected cheaply and applied using any of standard printing techniques (silk-screen, offset, ink-jet). Range of applications is huge: banknotes, credit-

cards, CD/DVDs, bonds, valuable goods. It is not even hard to imagine using wing-scales as a hardware lock for digital information security.

The base material of wing-scales is chitin, which is extremely and verifiably durable. Natural history museums have century-old butterfly specimens retaining their structural coloration and we have more than 30 years old specimens of *I. lathonia* with silver patches as shiny as in live insects. Even more, fossilized insects retain their iridescence after petrification and last for millions of years [30]. This should be compared to, recently described, five-dimensional optical memory [31], claiming “seemingly unlimited lifetime.”

Wing scales may reversibly change their dimensions in response to temperature variation [32], humidity and vapors [33]. As a consequence, there is a slight spectral shift, but it is too small to affect application of wing scales in document security, under normal atmospheric conditions. Systematic changes during extended periods of time are not expected due to hydrophobicity, insolubility and biological inertness of wing-scales [34]. However, we have not measured the long-term stability of wing scale patterns, we plan to perform accelerated aging tests in the near future and reveal details regarding the effect of aging on pattern stability.

Anyway, the validity period of most documents is less than 10 years, a period during which wing scales are expected to remain unaffected. Furthermore, taking into account the chemical and physical stability of chitin and the fact that optical response of the insects a hundred and more centuries-old (from museum) and from fossil samples exhibit extraordinary similarity with visual response measured from “the fresh” samples, suggest that corresponding patterns are very stable and could have long-term cryptographic applications.

ACKNOWLEDGMENTS

We express our gratitude to the Ministry of Education, Science and Technological Development of the Republic of Serbia for supporting this research through the projects Nos. III45016, III43002, ON171038, ON173038, ON171017, ON171032 and by the Science and Technology Development Programme—Joint Funding of Development and Research Projects of the Republic of Serbia and the People's Republic of China: Mimetics of insects for sensing and security, No. I-2. This work was also partially supported by the projects: No 451-03-01038/2015-09/1 of bilateral collaboration program between Ministry of Education, Science and Technological Development of the Republic of Serbia and German Academic Exchange Service (DAAD); by the project: “Upscaling Teslagram technology based on variable and complex biological structures for security printing,” funded by the Innovation Fund of the Republic of Serbia.

B.K. warmly acknowledges the assistance of Ms. Bojana Bokic, Institute of Physics, University of Belgrade in design of graphical abstract for this publication.

CONFLICT OF INTEREST

Institute of Physics Belgrade is the applicant and the owner of three pending patent applications given in a list of references [27–29] whose contents is partially described in this paper. Five authors (D.V.P., D.P., M.D.R., V.L. and A.J.K.) are also authors of abovementioned patent applications. Specific aspects of manuscript covered in patent applications are: laser cutting and bleaching of wing scales, as well as a partial list of butterfly species usable for this purpose.

AUTHOR CONTRIBUTIONS

D.V.P. conceived the idea; M.D.R., A.J.K. and D.V.P. have constructed the nonlinear microscope used in this research. D.P., A.J.K., M.D.R. and V.L. performed experiments and measurements. D.V.P. designed an optical model of wing-scales, while N.V. and D.S. performed the theoretical analysis of uniqueness of butterfly wing-scales. B.J. D. Z., W. Z. and B. K were included in data analysis and supervised the research. D.S., S.Ć and D.P. made adequate choice of appropriate butterfly species used in this research, while D.V.P., D.P. and M.D.R. prepared the manuscript, based on comments of other authors. This work is performed in partial fulfillment of the requirements for the PhD degree of Vladimir Lazović at the University of Belgrade, Faculty of Physics. All authors gave final approval for publication and agree to be held accountable for the work performed therein.

ETHICAL STANDARDS

Insects used in this research are NOT on the list of strictly protected and protected species defined in: By-law on proclamation and protection of strictly protected and protected wild species of plants, animals and fungi, Official gazette of the Republic of Serbia Nos. 5/2010 and 47/2011. All experiments were performed on dry specimens from the collection of Dejan Stojanović. The research did not include live insects.

ORCID

Branko Kolarić  <https://orcid.org/0000-0003-0203-7897>

REFERENCES

- [1] G. F. Robert, P. H. Adler, *Insect Biodiversity, Science and Society*, Chichester, UK: Willey-Blackwell, 2009.

- [2] X. Zhou, S. W. Applebaum, M. Coll, *Environ. Entomol.* **2000**, 29, 1289.
- [3] S. M. Doucet, M. G. Meadows, *J. R. Soc. Interface* **2009**, 6, S115.
- [4] W. Zhang, J. Gu, Q. Liu, H. Su, T. Fan, D. Zhang, *Phys. Chem. Chem. Phys.* **2014**, 16, 19767.
- [5] E. P. Newman, *Proc. Am. Philos. Soc.* **1971**, 115, 341.
- [6] R. L. Van Renesse, *Optical document security*, 3rd ed. Norwood, MA: Artech House, **2004**.
- [7] R. Pappu, B. T. J. Recht, N. Gershenfeld, *Science* **2002**, 297, 2026.
- [8] J. D. R. Buchanan et al., *Science* **2005**, 436, 475.
- [9] Hamm-Dubischar, C. Patent No. WO 2007031077 (A1), Inorganic marking particles for characterizing products for proof of authenticity method for production and use thereof (**2007**).
- [10] Biermann, N. & Rauhe, H., Method for Producing Security Markings. WO2004070667 A2 (**2004**).
- [11] Rauhe, H., Verfahren zur Herstellung von informationstragenden mikropartikelgemischen. Patent DE10238506 A1 (**2004**).
- [12] P. Vukusic, R. Kelly, I. Hooper, *J. Roy. Soc. Interface* **2009**, 6, S193.
- [13] D. M. Rabasović et al., *J. Biomed. Opt.* **2015**, 20(016010), 1.
- [14] D. Pantelić, S. Savić-Šević, D. V. Stojanović, S. Čurčić, A. J. Krmpot, M. Rabasović, D. Pavlović, V. Lazović, V. Milošević, *Phys. Rev. E* **2017**, 95, 032405.
- [15] J. e. Schanda, *Colorimetry: Understanding the CIE System*. Hoboken, NJ: John Wiley & Sons, **2007**.
- [16] I. G. Johnston et al., *PLoS Comput. Biol.* **2012**, 8, e1002416:1.
- [17] A. Dinwiddie, R. Null, M. Pizzano, L. Chuong, A. Leigh Krup, H. Ee Tan, N. H. Patel, *Dev. Biol.* **2014**, 392, 404.
- [18] J. Wood, *Pattern Recog.* **1996**, 29, 1.
- [19] L. O'Gorman, I. Rabinovich, *IEEE Trans. Pattern Anal. Mach. Intell.* **1998**, 20, 1097.
- [20] K. Watanabe, T. Hoshino, K. Kanda, Y. Haruyama, T. Kaito, S. Matsui, *J. Vac. Sci. Technol. B* **2005**, 23, 570.
- [21] D. Colton, R. Kress, *Inverse Acoustic and Electromagnetic Scattering Theory*, 2nd ed. New York, NY: Springer, **1998**.
- [22] F. Monticone, A. Alu, *Phys. Rev. X* **2013**, 3(041005), 1.
- [23] G. Bao, P. Li, J. Lin, F. Triki, *Inverse Probl* **2015**, 31, 093001.
- [24] S. Toxqui-López, A. Olivares-Pérez, I. Fuentes-Tapia, A. Quintero-Romo, *Opt. Mater.* **2007**, 29, 1604.
- [25] B. D. Chrysler, R. K. Kostuk, *Appl. Optics* **2018**, 57, 8887.
- [26] M. Okui, K. Wakunami, R. Oi, Y. Ichihashi, B. J. Jackin, K. Yamamoto, *Appl. Optics* **2018**, 57, 4117.
- [27] Pantelic, D., Rabasovic, M., Krmpot, A., Lazovic, V. & Pavlovic, D., Security device individualized with biological particles. PCT/EP2015/081398 (**2015**).
- [28] Pantelic, D., Rabasovic, M., Krmpot, A., Lazovic, V. & Pavlovic, D., Security tag containing a pattern of biological particles. PCT/EPO2015/081400 (**2015**).
- [29] Pantelic, D., Rabasovic, M., Krmpot, A., Lazovic, V. & Pavlovic, D., Security tag with laser-cut particles of biological origin. PCT/EP2015/081407 (**2015**).
- [30] M. E. McNamara et al., *PLoS Biol.* **2011**, 9, e1001200:1.
- [31] J. Zhang, M. Gecevičius, M. Beresna, P. G. Kazansky, *Phys. Rev. Lett.* **2014**, 112, 033901.
- [32] A. D. Pris, Y. Utturkar, C. Surman, W. G. Morris, A. Vert, S. Zalyubovskiy, T. Deng, H. T. Ghiradella, R. A. Potyrailo, *Nat Photon* **2012**, 6, 195.
- [33] R. A. Potyrailo, H. Ghiradella, A. Vertiatichikh, K. Dovidenko, J. R. Cournoyer, E. Olson, *Nat photonics* **2007**, 1, 123.
- [34] H.-M. Hu, J. A. Watson, B. W. Cribb, G. S. Watson, *Biofouling* **2011**, 27, 1125.

SUPPORTING INFORMATION

Additional supporting information may be found online in the Supporting Information section at the end of this article.

How to cite this article: Pavlović D, Rabasović MD, Krmpot AJ, et al. Naturally safe: Cellular noise for document security. *J. Biophotonics*. 2019;12: e201900218. <https://doi.org/10.1002/jbio.201900218>



Nitrogen plasma surface treatment for improving polar ink adhesion on micro/nanofibrillated cellulose films

Katarina Dimic-Misic · Mirjana Kostić · Bratislav Obradović · Ana Kramar · Stevan Jovanović · Dimitrije Stepanenko · Marija Mitrović-Dankulov · Saša Lazović · Leena-Sisko Johansson · Thad Maloney · Patrick Gane

Received: 26 October 2018 / Accepted: 14 January 2019 / Published online: 26 February 2019
© The Author(s) 2019

Abstract We find that nitrogen plasma treatment of micro/nanofibrillated cellulose films increases wettability of the surface by both liquid polar water and nonpolar hexadecane. The increased wetting effect is more pronounced in the case of polar liquid, favouring the use of plasma treated micro/nanofibrillated cellulose films as substrates for a range of inkjet printing including organic-based polar-solvent inks. The films were formed from aqueous suspensions of progressively enzymatic pretreated wood-free cellulose fibres, resulting in increased removal of amorphous species producing novel nanocellulose surfaces displaying increasing crystallinity. The mechanical properties of each film are shown to be highly dependent on

the enzymatic pretreatment time. The change in surface chemistry arising from exposure to nitrogen plasma is revealed using X-ray photoelectron spectroscopy. That both polar and dispersive surface energy components become increased, as measured by contact angle, is also linked to an increase in surface roughness. The change in surface free energy is exemplified to favour the trapping of photovoltaic inks.

Keywords DBD plasma · Nitrogen plasma surface treatment · Nanocellulose films · Enzymatic nanocellulose · Printing of organic-based polar inks

K. Dimic-Misic (✉) · L.-S. Johansson · T. Maloney · P. Gane
Department of Bioproducts and Biosystems, School of Chemical Engineering, Aalto University, 00076 Aalto, Helsinki, Finland
e-mail: katarina.dimic.misic@aalto.fi

M. Kostić · A. Kramar
Faculty of Technology and Metallurgy, University of Belgrade, Karnegijeva 4, Belgrade 11000, Serbia

B. Obradović
Faculty of Physics, University of Belgrade, Studentski trg 12, Belgrade 11001, Serbia

S. Jovanović · D. Stepanenko · M. Mitrović-Dankulov · S. Lazović
Institute of Physics Belgrade, University of Belgrade, Pregrevica 118, Belgrade 11080, Serbia

Introduction and background

Sustainability is one of the key targets for industrial practice today. The related research aimed at new biobased materials derived from renewable sources, is relevant for the sustainable economy. In the bioproducts industry, micro/nanofibrillated cellulose (MNFC) has attracted attention in a number of potential applications (Hubbe et al. 2017a). It can be used in standard wood products, such as paper and boards. However, most of the benefits derived from MNFC stem from its wider uptake in a range of industrial value chains, such as biodegradable packaging films and laminates. MNFC has interesting intrinsic properties derived from large specific surface area and its

alternate regions of crystallinity. The hydroxylated surface chemistry is readily suitable for chemical modification. Films formed from MNFC are considered smart materials and studied for functional materials applications. Enzyme-treated fibres used to produce cellulose nanofibrils provide higher crystallinity in the resulting nanocellulose, as enzymes digest amorphous cellulose, which acts as the glue between crystalline cellulose regions. Direct hydrogen bonding of crystalline cellulose, therefore, gives a stronger material film. An example of an important application of MNFC is as a substrate for printed solar cells based on organic inks (Zhu et al. 2014). The surface properties of MNFC films, such as wettability by liquid, topography, chemistry, surface charge, the presence of hydrophobic and hydrophilic domains, density and conformation of functional groups, all play a crucial role in printability and barrier properties. Their ability to support controlled migration of solvent ink vehicle and chromatographic differentiation of ink components is important in the printing of inkjet printable (IP) inks, and especially for production of bio-based printed functionality in a wide range of applications, such as printed electronics and printed diagnostics (Hoeng et al. 2016; Jutila et al. 2018).

Solar panel IP photovoltaic (PV) inks contain a complex mix of materials, including the organic electron acceptor (p-type) and negative electron donor (n-type) suspended in solvent together with specific surfactant(s) intended to keep the p-type and n-type components de-mixed (Kumar and Chand 2012). Although drop-on-demand (DoD) inkjet printing is a very competitive candidate for printing PV inks on film substrates, there are limitations in respect to mutual compatibility between the surface of MNFC films and mixed polar-dispersive solvents constituting the PV ink (Singh et al. 2010; Yinhua et al. 2013). Electrolyte is highly polar, for example, and so sufficient wettability is needed by providing a polar surface, despite the parallel requirement for wettability by organic species (Schultz et al. 1977; Özkan et al. 2016). This complex polar-dispersive surface energy balance is, therefore, critical (Hansson et al. 2011).

Exposure to plasma is a convenient method to modify the surface properties of polymeric materials, while keeping their bulk properties intact, making a material better adapted for printing (Möller et al. 2010; Kramer et al. 2006; Catia et al. 2015). Furthermore, as we demonstrate, it is a convenient way to introduce

desired groups onto the surface of materials (Mi-hailovic et al. 2011). Surface properties depend on parameters of plasma treatment such as applied electrical field energy, type of feed gas, pressure, exposure time, and reactor geometry (van de Vyver et al. 2011; Jun et al. 2008).

In this work, we modify enzyme pretreated fibre-derived MNFC film surfaces using nitrogen plasma to enhance their amphiphilic surface affinity to polar and non-polar IP PV inks. Measurements of the surface free energy, surface roughness (atomic force microscopy (AFM)) and material composition [X-ray photoelectron spectroscopy (XPS)] were used to characterise the MNFC film surface before and after plasma treatment. The affinity for IP PV ink was assessed visually after inkjet printing. We also identify a correlation between the observed change in free surface energy of the MNFC film, arising from the plasma treatment, with the effect of the enzymatic pretreatment. This is related to the level of residual crystallinity increasing as a function of progressive enzymatic pretreatment (Galagan et al. 2011; Cernakova et al. 2006; Pertile et al. 2010; Vanneste et al. 2017).

To meet the requirement of sufficient tensile strength of MNFC films for the application exemplified, the rheological properties of enzymatically pretreated MNFC fibrillar suspensions were compared with the mechanical properties of corresponding obtained films, so that rheology can be used as a predictor of film strength (Maloney 2015; Zhu et al. 2014).

Materials and methods

Preparation of MNFC

For the manufacture of short MNFC fibrils, the pulp was first washed to create the sodium form by adding sodium hydroxide to a 2 w/w% fibre suspension until the pH reached 10, and then re-washed with deionised water to a conductivity of 8.2 μS . The enzymatic treatment was performed with a commercial enzyme ECOPULP[®] R (Ecopulp Finland Oy), produced by a genetically modified strain of *Trichoderma reesei* fungus (Rantanen et al. 2015). The activity properties of the enzyme are reported to be 17,700 nkat cm^{-3} cellulase with a protein level of 93 mg cm^{-3}

(Willberg-Keyriläinen et al. 2019). An amount of 3 mg of enzyme per gram of pulp fibre was added to a 2.5 w/w% suspension and the temperature was increased to 57 °C at pH 5.5 during hydrolysis, whilst keeping under constant agitation. The period of digestion was increased for each subsequent sample in 30 min steps, Table 1. The enzymatic activity was terminated by adjusting the pH to 9–10 by sodium carbonate and increasing the temperature to 90 °C. After cooling the suspension overnight in cold storage, the samples were refined using an homogeniser (model M-110P, Microfluidics, USA), passing the material under a pressure of 2000 bar through a 100 µm flow gap. The solids content of the MNFC suspension after the fluidisation was 1.65 w/w%.

The enzymatic pretreatment of pulp as a route for producing low-charged MNFC resulted in the production of short fibrils, which, in the case studied here, have much lower aspect ratio than MFC and NFC produced via chemical oxidative pretreatment or mechanical refining alone, as illustrated in Fig. 1 comparing MNFC/300/and MNFC/0/suspensions (Table 1), revealing much shorter fibrils obtained upon 300 min of enzymatic hydrolysis.

MNFC film preparation

With increasing enzymatic treatment time, the resulting MNFC suspension viscosity decreased significantly, and the solid content for preparation of the respective films ranged from 0.6 to 1.9 w/w% to meet the target film grammage of 60 g m⁻² produced under conditions of 23 °C and relative humidity (RH) 50%.

Films were made on a sheet-former according to ISO standard 5269-1, with some modification of the screen to aid fines retention. Due to the very strong water retention of MNFC, and its fine size, a polyamide monofilament open mesh fabric SEFAR NITEX® 03-1/1 with a pore size of 1 µm was placed

on top of a 125 µm metal screen. The pulp suspension was poured at high viscosity onto the former without adding water or stirring the slurry. The system was pressurised to 0.3 bar and the sealing lid was used on the sheet-former. Double-sided adhesive tape, of 5 mm width, was attached to the edges of the drying plate between plate and formed film, with purpose of fixing the edge of the film to prevent it shrinking during drying (Fig. 2).

Material treatment and characterisation

Optical microscopy was used to study the fibrillar sample suspensions and films using an Olympus BX 61 microscope equipped with a DP12 camera.

Water retention the water retention value (WRV) of the MNFC was determined in accordance to the standard SCAN-C 102XE with a slight modification in that 10 w/w% suspension of the MNFC was added in various ratios to a suspension of bleached unrefined pulp. The pulp matrix helps the MNFC dewater and remain retained on the screen. The WRV of neat MNFC can be evaluated by extrapolating to zero pulp, not including the swelling of the pulp fibres (Möller et al. 2010). The experiment was performed in triplicate for each sample.

Dielectric barrier discharge (DBD) plasma operates in a thermodynamically non-equilibrium condition (so-called cold plasma) in which the ion and molecular translational temperature is much lower than the electron temperature, such that excessive gas heating can be suppressed (Kostic et al. 2009; Prysiazny et al. 2013). The advantage is that the plasma can be generated at atmospheric pressure, either in open or closed environment. In an open atmosphere, the plasma discharges can be produced with a gas flow between the electrodes (Mihailovic et al. 2011; Chu et al. 2002; Jens et al. 2017).

Table 1 Materials used in this study: bleached hardwood Kraft pulp treated with enzymes under controlled conditions, with progressive increase in enzymatic digestion time by 30 min steps for each subsequent sample

Enzymatic treatment time/ min	0 (reference)	30	60	90	120	150	180	210	240	270	300
Sample label	MNFC/0/	MNFC/ 30/	MNFC/ 60/	MNFC/ 90/	MNFC/ 120/	MNFC/ 150/	MNFC/ 180/	MNFC/ 210/	MNFC/ 240/	MNFC/ 270/	MNFC/ 300/

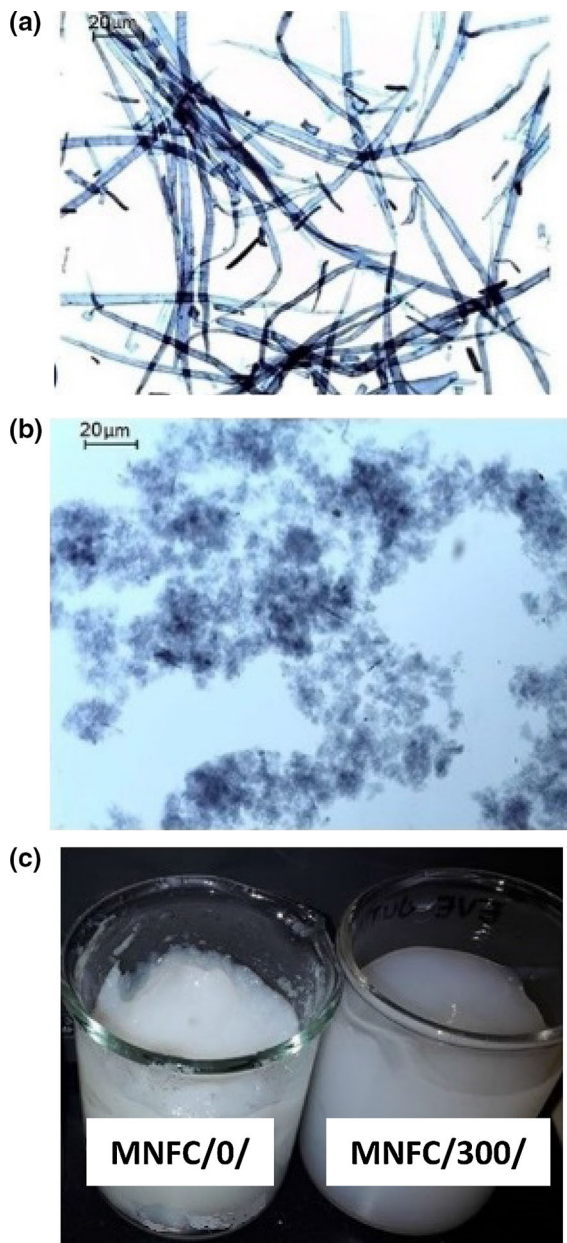


Fig. 1 Images of fibrils sample suspensions obtained with optical microscopy revealing the effect of processing conditions on the fibril size and aspect ratio: **a** without enzymatic treatment produced MNFC/0/ yielding long fibrils, **b** MNFC/300/ short, low aspect ratio fibrils, and **c** displaying the corresponding 2 w/w % MNFC suspensions of MFC/0/ and MNFC/300/. The difference in gelation strength is due to the different size of fibrils and corresponding amount of water dispersed within the fibrillar matrix

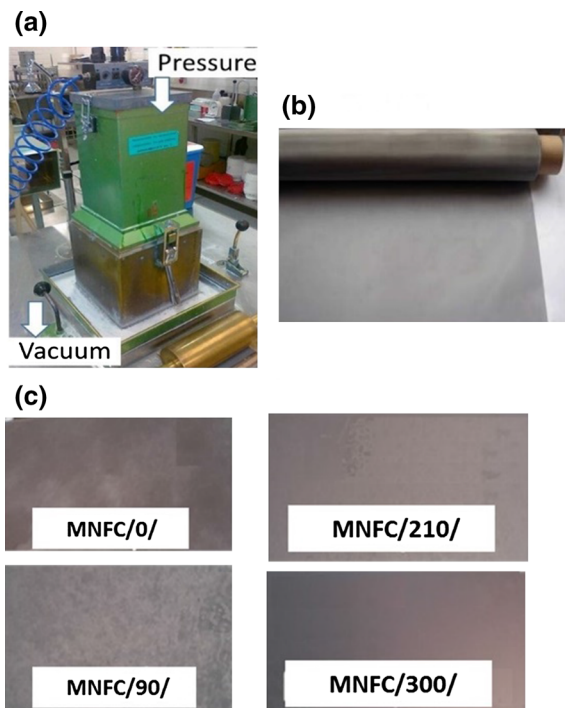
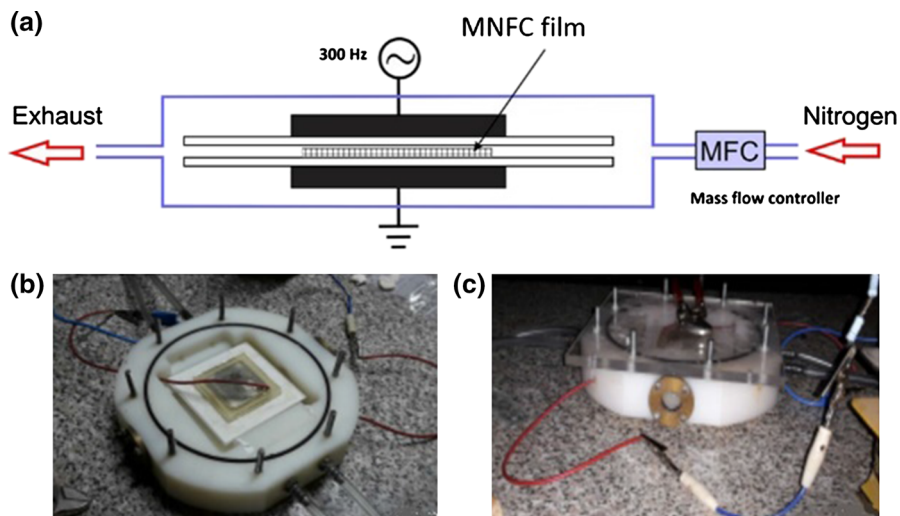


Fig. 2 MNFC film preparation: **a** sheet forming device with **b** 10 μm mesh supplemented nylon screen, and **c** samples of cut-offs ($60 \times 15 \text{ mm}^2$) from MNFC films produced from pulp refined with different enzymatic pretreatment time (Table 1). Transparency and uniformity of films increases with hydrolysis time

A further attractive characteristic of the DBD plasma at atmospheric pressure is that it can be used to modify or activate surfaces of a wide range of materials, from polymers, textile fibres to biological tissues, without damaging them (Kostic et al. 2009; Pertile et al. 2010; Mihailovic et al. 2011). To generate the DBD plasma we used a home-made device built at the Faculty of Physics, University Belgrade, Fig. 3. The DBD is assembled in a chamber with nitrogen gas injected into the discharge volume ($6 \text{ dm}^3 \text{ min}^{-1}$) through ten equidistant holes to ensure homogeneous gas flow. MNFC films were treated for 0 s, 30 s and 60 s, respectively. The device was operated at 6 kV DC and 300 electric field pulses per second (Hz) for the prescribed durations of time, for all the films, as a higher voltage resulted in burning of the thin MNFC films, especially for those made from pulp exposed to long enzymatic pretreatment time.

Fig. 3 DBD device with two electrodes and sample placed between them: **a** schematic illustration of DBD plasma device, **b** plasma chamber housing the sample placed 1 mm from the upper electrode, and **c** closed plasma set up with glass lid placed above the top of the upper electrode



Determination of free surface energy (FSE) components

For the evaluation of any change in free surface energy of MNFC films arising from nitrogen plasma treatment, the contact angle (CA) is determined.

Most liquids are rapidly spreading on a high energy surface, and so a representative contact angle (CA) cannot be readily measured, Schultz et al. (1977) developed a method where CA can be measured by submerging the surface in one liquid and using a second liquid to measure the contact angle. In this case a hydrocarbon *n*-hexadecane is used as the submerging liquid having the purely dispersive liquid–vapour surface tension of $\gamma_{LV}^h = 27.4 \text{ mJ m}^{-2}$, much lower than the expected surface free energy of the MNFC samples, and water as the contact angle liquid with the highly polar liquid–vapour surface tension $\gamma_{LV}^w = 72.8 \text{ mJ m}^{-2}$ (Hansson et al. 2011). A sessile drop of water is lowered into contact with the horizontal film immersed under hexadecane using a precise pipette delivering 70 μl of liquid and the progressive change in drop shape due to the change in CA recorded with a Nikon camera (D5000) in time steps of 1 ms. The CA of water is also recorded separately to represent the print challenge of a highly polar ink (Özkan et al. 2016; Dimic-Misic et al. 2015). For each given MNFC sample and given liquid data variation is within 10%. The identification of contact line geometry and evaluation of CA uses numeric software tools, as presented visually in Fig. 4. For a parallel optimal method for polar FSE determination

with water alone, the Girifalco and Good approach (1957), combined with the Neumann equation of state was used. This latter allowed the polar contribution to FSE be estimated and thus can be added to the formerly measured dispersive component. Each measurement was conducted five times. For each given MNFC sample, the relative error of measured FSE was shown to be $\sim 10\%$.

Surface topography

Plasma action on the film surface can lead to a degree of debonding of fibrils as well as electrostatic charging and potential for subsequent additional moisture adsorption. Such changes can lead to re-conformation of the surface, even though no mechanical forces have been applied (Kostic et al. 2009; Chu et al. 2002). The change in topography of the MNFC films was investigated by Atomic Force Microscopy (AFM) (Veeco Instruments, model Dimension V). Using a MultiMode 8 with Bruker NanoScope V controller. Each MNFC film sample was dry-cast onto a Mica support for AFM imaging. Micrographs were obtained in trapping mode under ambient conditions, using TAP 300 tips (resonant frequency 300 kHz, line force being kept constant at 40 Nm^{-1}) and the AFM images were processed and analysed with the Bruker NanoScope Analysis 1.5 software.

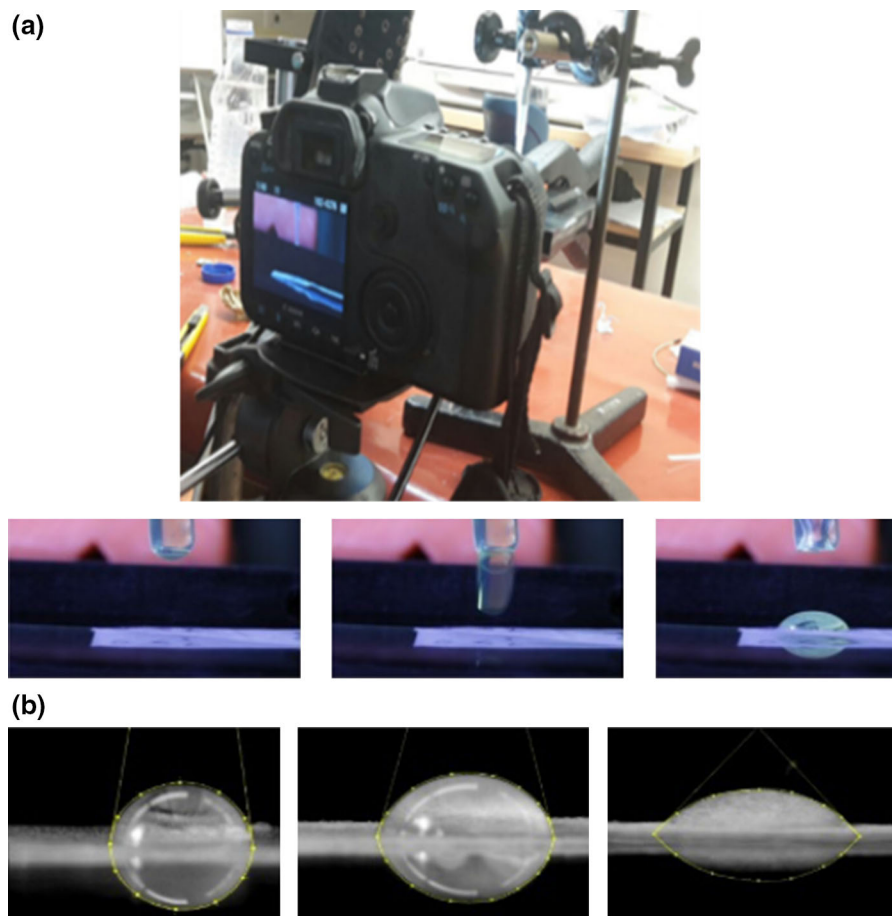


Fig. 4 Set-up for evaluating water CA under *n*-hexadecane with high speed camera (Nikon D5000): **a** images of films on camera viewfinder and **b** image processing of drop spreading (see also Fig. 8)

Mechanical properties

Mechanical properties of the MNFC films were measured by an MTS 400/M vertical tensile tester equipped with a 20 N load cell. The instrument was controlled by a TestWorks 4.02 program. Specimen strips with dimensions of $60 \times 15 \text{ mm}^2$ were clipped from the MNFC films with a lab paper cutter (Afsahi et al. 2018). The thickness of the strips was separately measured with an L&W micrometer SE 250. The gauge length was 40 mm and the testing velocity was 0.5 mm min^{-1} . The results are presented as an average value obtained from five parallel specimens.

Surface chemical composition

Surface composition of the MNFC films was evaluated with X-ray photoelectron spectroscopy (XPS), using a

Kratos AXIS Ultra electron spectrometer, with monochromatic Al K α irradiation at 100 W and under charge neutralisation. Both the untreated MNFC films and plasma treated specimens were analysed. For the preparation, samples were pre-evacuated for at least 12 h, after which wide area survey spectra (for elemental analysis) as well as high resolution regions of C1s and O1s were recorded from several locations, and an in situ reference of pure cellulose was recorded for each sample batch (Johansson and Campbell 2004). With the parameters used, XPS analysis was recorded on an area of 1 mm^2 and the analysis depth is less than 10 nm. Carbon high resolution data were fitted using CasaXPS and a four component Gaussian fit tailored for celluloses.

MNFC suspension rheology

The rheological properties of MNFC suspensions were analysed at 2 w/w% concentration at 23 °C with an Anton Paar MCR 300 shear rheometer. The dynamic viscosity (η) was determined by steady shear-flow measurements, using the bob-in-cup geometry (Motaschemi et al. 2014). Due to the potential for wall depletion (apparent slip) and thixotropic behaviour of MNFC suspensions, the “bob” was a four-bladed vane spindle with a diameter of 10 mm and a length of 8.8 mm, while the metal cup had a diameter of 17 mm. A pre-shear protocol was applied using constant shear at a shear rate $\dot{\gamma} = 100 \text{ s}^{-1}$ for 5 min, followed by a rest time of 10 min prior to recording the flow curves. Flow curves of MNFC suspensions were constructed under decreasing shear rate of $\dot{\gamma} = 1000\text{--}0.01 \text{ s}^{-1}$, with a logarithmic spread of data points (Dimic-Misic et al. 2013). To distinguish the MNFC suspensions in terms of their colloidal interactions as an effect of hydrolysis time, aspect ratio, crystallinity and friction between nanofibrils during the flow (Pääkkönen et al. 2016; Dimic-Misic et al. 2018), the log–log plot flow curves were fitted to a power law according to the Oswald–de Waele empirical model, as shown in Eq. (1)

$$\eta = k\dot{\gamma}^{1-n} \quad (1)$$

where k and n are the flow index and the power-law exponent, respectively: $n = 1$ indicates a Newtonian fluid and $n > 1$ indicates pseudo-plastic (shear thinning) behaviour.

The Herschel–Bulkley equation describes the dynamic yield stress τ_d^0 as

$$\tau = \tau_d^0 + k\dot{\gamma}^n \quad (2)$$

where τ is the shear stress.

Printing

The photovoltaic (PV) inkjet printing inks (IP) contain a complex mix of materials, solvent and surfactants that keep the p-type and n-type components de-mixed (Hashmi et al. 2015; Özkan et al. 2016). A piezoelectric laboratory scale drop-on-demand (DoD) materials inkjet printer (Dimatix 2831-DMP) was used to test the printability of the plasma treated MNFC films (Dimic-Misic et al. 2015). The solvent of the IP ink is

3-methoxypropionitrile, which is highly polar and non-volatile (boiling point 164 °C), viscosity 1.2 mPa s and density 0.937 g cm⁻³, as stated by the supplier, Sigma Aldrich. The surface tension measurement was performed on the ink with an optical tensiometer (CAM 200 from KSV instruments) in pendant drop mode, giving a value of 29.2 mN m⁻¹ (mJ m⁻²).

Results and discussion

The *rheological properties* of the MNFC suspensions are given in Table 2, showing the change in dewatering, dynamic yield point and flocculation/water trapping gel-like structure (consistency coefficient, k) and shear thinning properties (index, n , expressed as the positive difference $n - 1$) and change in fibre morphology expressed as the fines content using the dynamic drainage jar (DDJ).

It is clear to see that with increase in enzymatic hydrolysis time, dewatering decreases as fibrils become thinner and smaller, and suspensions become more gel-like rheologically (Rantanen et al. 2015). At the same time, crystallinity of fibrils increases and water trapping structure/flocculation within the matrix with contrasting increased mobility in the flow regime once the structure is broken (Pääkkönen et al. 2016). The dynamic yield point, the minimum stress needed to be induced to set the suspension into flow increases as the suspensions become more gel like, but, also, breakage of that suspension induces greater shear thinning as fibrils are smaller and more crystalline, orienting easily in the flow direction (Pääkkönen et al. 2016; Hubbe et al. 2017b).

The *mechanical and optical properties* of MNFC films are presented in Table 3, where it is evident that the sheet density of the films increases with increase in hydrolysis time, while the packing density of the smaller crystalline particles increases. The permeability of those films created with the finer nanofibrils obtained after 120 min hydrolysis in turn falls rapidly, and it was not possible to measure using air flow techniques. The light scattering coefficient decreases also as the packing density is increased and the amorphous parts of the cellulose fibres were reduced, while, due also to higher packing density, the elasticity modulus increases, showing that films had improved strength.

Table 2 Properties of MNFC suspensions

Enzymatic treatment time (min)	WRV (cm ³ g ⁻¹)	Yield point, τ_d^0 (Pa)	Consistency coefficient, k (Pa s ⁻ⁿ)	Shear thinning coefficient, $ 1 - n $	DDJ fines value (%)
<i>MNFC suspension properties</i>					
0	1.25	34.12	431.23	0.82	93.8
30	1.61	47.34	241.3	0.81	88.8
60	1.83	54.23	139.65	0.81	79.5
90	2.19	68.45	89.67	0.81	62.4
120	2.55	91.45	69.45	0.84	27.0
150	2.85	438.34	57.23	0.84	21.0
180	2.98	29.82	35.15	0.86	11.8
210	3.33	19.64	19.67	0.86	9.6
240	3.37	12.67	14.34	0.87	6.5
270	3.32	8.99	9.97	0.89	1.5
300	3.34	4.74	5.45	0.91	0.2

Table 3 Mechanical and optical properties of MNFC films

Enzymatic treatment time (min)	Film weight (g m ⁻²)	Density (g cm ⁻³)	Permeability [$\mu\text{m}(\text{Pa s})^{-1}$]	Light scattering coefficient (m ² kg ⁻¹)	E-Modulus (GPa)
<i>Film properties</i>					
0	73.91	0.637	69.86	37.43	2.53
30	76.12	0.794	9.96	22.83	4.16
60	71.35	0.910	1.06	16.12	5.12
90	72.31	1.016	NA	9.94	7.02
120	70.53	1.090	NA	6.93	8.59
150	70.81	1.127	NA	5.81	9.13
180	69.57	1.145	NA	4.48	8.95
210	71.08	1.178	NA	3.74	11.26
240	70.10	1.179	NA	3.08	9.17
270	71.18	1.226	NA	3.11	9.76
300	65.27	1.187	NA	3.31	10.03

Roughness colour contour and profile plots of the surface of MNFC/30/150/300 films before and after plasma treatment are presented in Fig. 5. Before plasma treatment, the roughness of the films is directional, being different in the two measured directions (red and blue profile lines). The map for MFC/30/ indicates that there are voids present between 1 and 2 μm wide, while in the case of MFC/300/ the surface is flatter with less voids and of much smaller size. This means that the degree of enzyme hydrolysis directly increases the resulting smoothness due to the

ever finer fibrillar elements produced, as the crystalline parts are separated due to breakdown of the amorphous constituent. After plasma treatment, the amorphous material containing surfaces, e.g. MNFC/30/, are also seen to become relatively rougher than the highly hydrolysed crystalline films, e.g. MNFC/300/. The action of the plasma is to increase voyage in the courser particulate systems, as previously described, due to effects of charge, fibril debonding etc. (Jun et al. 2008). In MNFC/30/, it is possible to identify irregular both small and large voids appearing after plasma

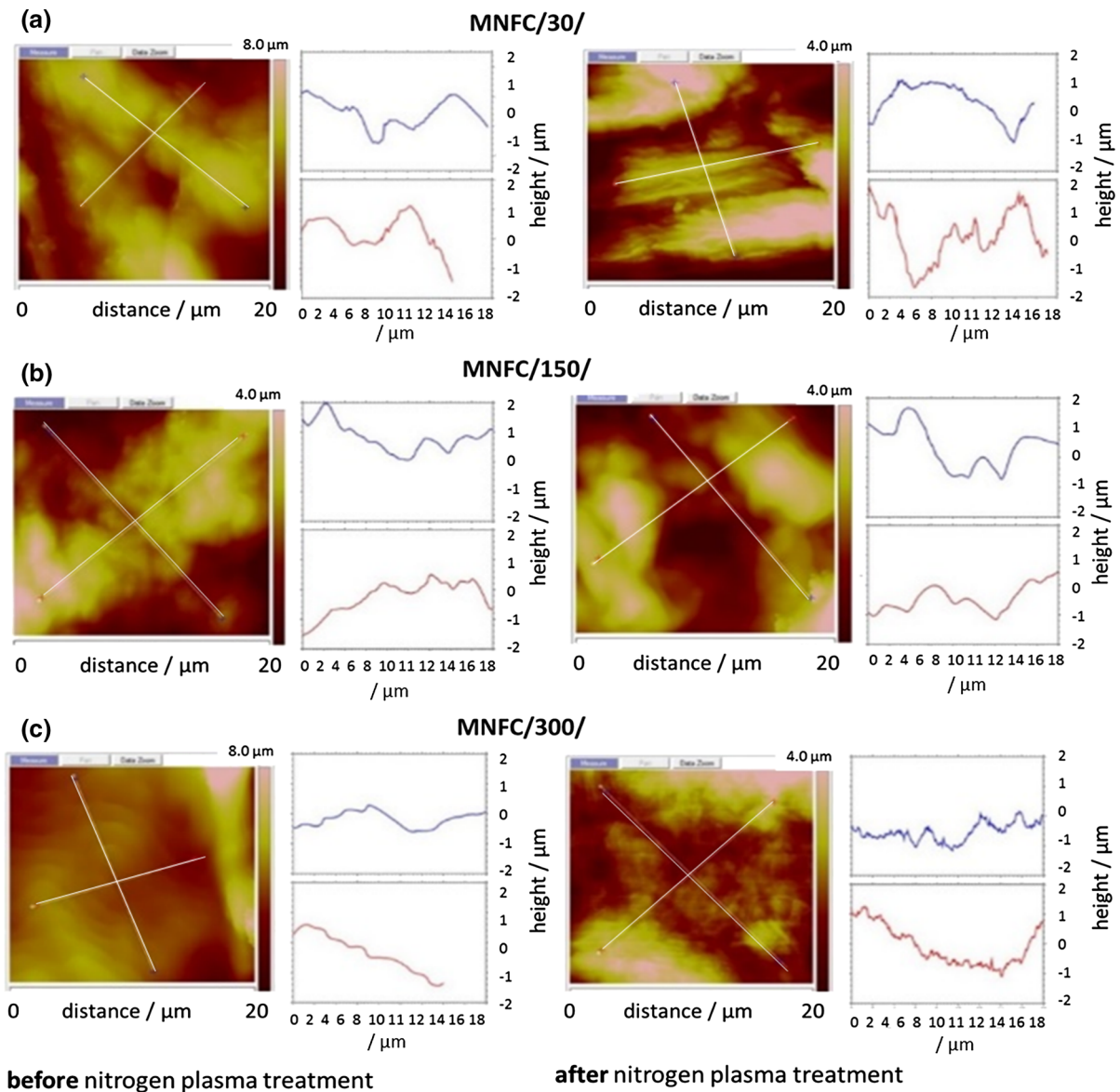
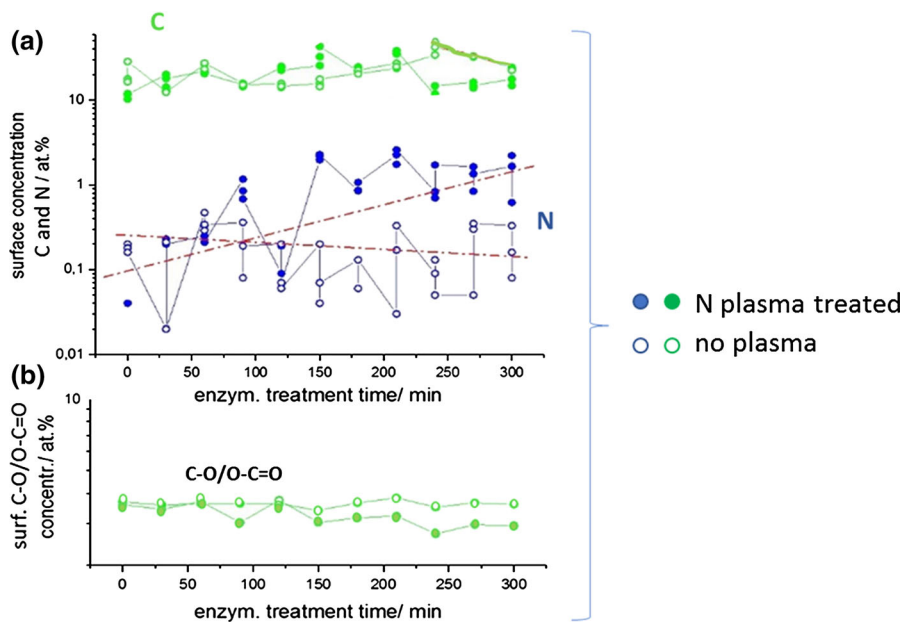


Fig. 5 Surface morphology and roughness of **a** MNFC/30/, **b** MNFC/150/ and **c** MNFC/300/ before and after DBD nitrogen plasma treatment

treatment, while in MNFC/300/, the surface of the film has almost no such jagged appearance with voids only smaller than 1 μm . Nitrogen plasma treatment, thus, obviously changes the morphology of the films, on both the micro (nano) and macro level, which is likely also to have an influence on the wetting behaviour and decrease in CA due to the increased meniscus liquid–solid wetting line length (Prysiashnyi et al. 2013; Pertile et al. 2010).

The *surface chemical species* are revealed by the XPS spectra, from which the atomic % of C–C, C–O, O=C=O and N can be derived, Fig. 6. The effect of surface modification after nitrogen plasma can be clearly seen as the level of N attachment increasing as a function of the enzymatic removal of amorphous content (Johansson and Campbell 2004). The samples with increased crystalline proportion after longer enzymatic treatment nonetheless show similar C–C bond content. Similarly, with reduction of the

Fig. 6 Surface modification obtained through XPS data showing **a** increase in N atoms at constant carbon content, and **b** change in ratio of C–O/O–C=O groups

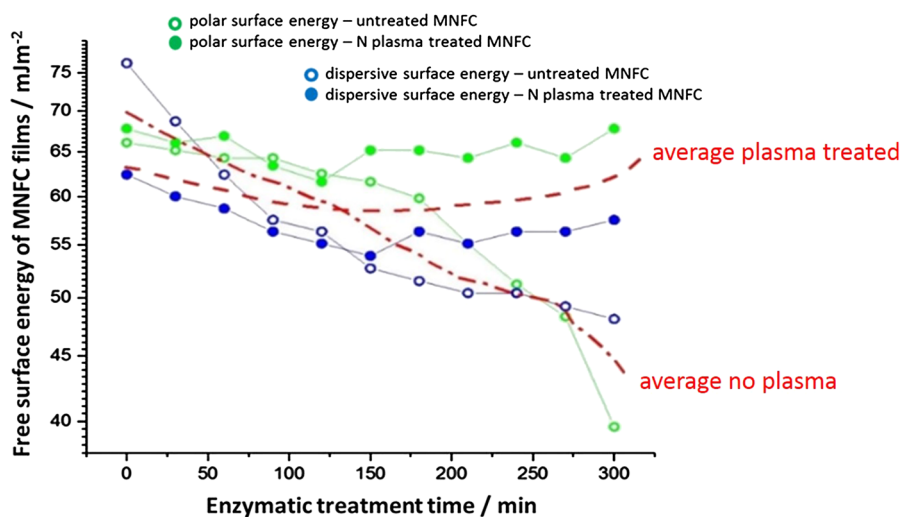


amorphous part with increased hydrolysis, the number of C–O groups decreases while C=O groups and other C and N containing groups are formed.

The results shown in Fig. 7 reveal that with the increase in enzymatic treatment of the raw material pulp there is a reduction of total FSE in the corresponding MNFC films in both polar and dispersive energy (green and blue unfilled symbols, respectively). A reversal of the decline in FSE as a function of enzymatic treatment can be observed resulting from nitrogen plasma treatment, showing compensating increases in both polar and dispersive measured

components (green and blue filled symbols, respectively). Thus, an increase in wettability for water and n-hexadecane is reflected by a decrease in CA as the plasma treatment acts on the more crystalline samples (Johansson and Campbell 2004). However, as the roughness is also seen to increase as a function of plasma treatment for the lower crystalline samples (less exposure to enzymatic breakdown), one would expect from the Wenzel model that the wettability would increase. That we see a recorded increase in n-hexadecane CA, and thus decrease in dispersive FSE, we can conclude that the action of the plasma

Fig. 7 Surface free energy (SFE) of MNFC films as a function of the treatment time (Table 1)



discharge on the amorphous part is initially to reduce the dispersive energy component, and so likely act, at least partially, to breakdown first the amorphous content resulting in debonding and hence roughening (Hansson et al. 2011). This effective etching of amorphous parts of fibrils is then replaced by the action of nitrogen attachment, such that the higher average FSE values regained in the more crystalline samples after plasma treatment are significantly higher than the theoretical FSE 59.4 mJ m^{-2} of cellulose, and this is achieved via the major contribution of the plasma-induced increase in polar component.

The increased contribution of the polar component in the FSE donated by the cationic N adsorption under plasma exposure is, therefore, expected to enhance the compatibility with the application of highly polar inks, especially if their components are anionic (Vanneste et al. 2017; Ma et al. 2010; Hoth et al. 2008). The images in Fig. 8 confirm this expectation, where the improved wetting of the surface by water as a function of plasma exposure time is paralleled by the greater pick-up (trapping) of ink colorant (Hoeng et al. 2016).

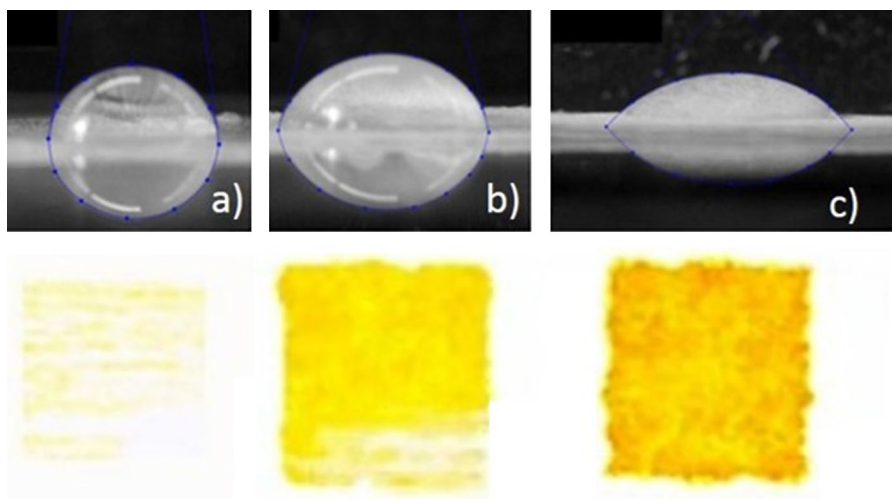
Summary and conclusions

Micro nanofibrillated cellulose films formed from aqueous suspension can be made stronger by pretreatment of the raw fibre using enzymatic hydrolysis. However, the wettability by ionic liquids, including functional inkjet printing inks, such as are suitably used for printed electronics, solar cells etc., decreases

as a result, limiting the use of such films in practice. Nitrogen plasma treatment, however, enables wettability by such formulations to be improved. The mechanism by which this occurs has been studied in this work presented in this paper and the following conclusions can be drawn:

- Total free surface energy increases with nitrogen plasma treatment of highly enzymatically hydrolysed fibrillar films (contact angle decreases), with a major increase in the polar component.
- Nitrogen is also included into the surface.
- Upon exposure to nitrogen plasma, dispersive surface energy initially decreases on those films made of pulp that was not treated or undergone short enzymatic treatment time, whereas the polar surface energy component remains relatively unchanged on such films.
- This effect is related to the interaction of the nitrogen plasma with the amorphous cellulose component in the non-hydrolysed fibrils.
- The dispersive energy component can once again be increased by exposure to nitrogen plasma in the case of the more crystalline fibrillar material derived from increased hydrolysis via enzymatic pretreatment.
- The surface area per unit mass was increased by the plasma treatment, apparently due to increased roughness on a nanometre scale.
- Highly ionic liquids, water and solvents typically used to disperse surfactant-containing organic-

Fig. 8 IP ink printed on MNFC/300/film showing the dependence on wettability of the surface after nitrogen plasma treatment (see also Fig. 4); lower water droplet CA on the film corresponds with a significant increase in print colour density: **a** untreated film, **b** plasma treated for 30 s and **c** plasma treated for 60 s



based inks, wet MNFC film better as hydrolysing pretreatment of fibres is increased and subsequent nitrogen plasma is applied.

Perspectives and future work arising from these findings include the need to study the origins of the surface roughening effect. Is this a random generation of surface disruption or is there a material transfer mechanism at play, involving perhaps vaporisation and redistribution? The impact on the amorphous component by plasma treatment could offer a means to induce a phase change at the material surface. Similarly, other gas plasma treatments should be investigated in the longer term to understand whether the role of atomic substitution versus the application of energy discharge has the greater treatment potential.

Acknowledgments Open access funding provided by Aalto University. The authors from the Institute of Physics Belgrade gratefully acknowledge financial help from the Ministry of Education, Science and Technological Development of the Republic of Serbia. The authors wish to thank to Prof. Milorad M. Kuraica from the Faculty of Physics, Laboratory for Plasma Physics, University of Belgrade, for his patience and skill in assisting with plasma experiments. Open access funding provided by Aalto University.

Open Access This article is distributed under the terms of the Creative Commons Attribution 4.0 International License (<http://creativecommons.org/licenses/by/4.0/>), which permits unrestricted use, distribution, and reproduction in any medium, provided you give appropriate credit to the original author(s) and the source, provide a link to the Creative Commons license, and indicate if changes were made.

References

- Afsahi G, Dimic-Misic K, Gane P, Budtova T, Maloney T, Vuorinen T (2018) The investigation of rheological and strength properties of NFC hydrogels and aerogels from hardwood pulp by short catalytic bleaching (H cat). *Cellulose* 25:1637–1655
- Catia R, Castro G, Rana S, Fangueiro R (2015) Characterization of physical, mechanical and chemical properties of quiscal fibres: the influence of atmospheric DBD plasma treatment. *Plasma Chem Plasma Process* 35:863–878
- Cernakova L, Stahel P, Kovacik C, Johansson K, Cernak M (2006) Low-cost high-speed plasma treatment of paper surfaces. In: 9th TAPPI advanced coating fundamentals symposium, Turku, Finland, pp 8–10
- Chu PK, Chen JY, Wang LP, Huang N (2002) Plasma-surface modification of biomaterials. *Mater Sci Eng R Rep* 36:143–206
- Dimic-Misic K, Puisto A, Gane P, Nieminen K, Alava M, Paltakari J, Maloney T (2013) The role of MFC/NFC swelling in the rheological behaviour and dewatering of high consistency furnishes. *Cellulose* 20:2847–2861
- Dimic-Misic K, Karakoc A, Özkan M, Ghufran HS, Maloney T, Paltakari J (2015) Flow characteristics of ink-jet inks used for functional printing. *J Appl Eng Sci* 13:207–212
- Dimic-Misic K, Maloney T, Gane P (2018) Effect of fibril length, aspect ratio and surface charge on ultralow shear-induced structuring in micro and nanofibrillated cellulose aqueous suspensions. *Cellulose* 25:117–136
- Galagan Y, Rubingh JEJ, Andriessen R, Fan CC, Blom PW, Veenstra SC, Kroon JM (2011) ITO-free flexible organic solar cells with printed current collecting grids. *Solar Energy Mater Solar Cells* 95:1339–1343
- Girifalco LA, Good RJ (1957) A theory for the estimation of surface and interfacial energies. I. Derivation and application to interfacial tension. *J Phys Chem* 61:904–909
- Hansson PM, Skedung L, Claesson PM, Swerin A, Schoelkopf J, Gane PAC, Rutland MW, Thormann E (2011) Robust hydrophobic surfaces displaying different surface roughness scales while maintaining the same wettability. *Langmuir* 27:8153–8159
- Hashmi SG, Özkan M, Halme J, Dimic-Misic K, Zakeeruddin SM PJ, Grätzel M, Lund PD (2015) High performance dye-sensitized solar cells with inkjet printed ionic liquid electrolyte. *Nano Energy* 17:206–215
- Hoeng F, Denneulin A, Bras J (2016) Use of nanocellulose in printed electronics: a review. *Nanoscale* 8:13131–13154
- Hoth CN, Schilinsky P, Choulis SA, Brabec CJ (2008) Printing highly efficient organic solar cells. *Nano Lett* 8(2008):2806–2813
- Hubbe MA, Ferrer A, Tyagi P, Yin Y, Salas C, Pal L, Rojas OJ (2017a) Nanocellulose in thin films, coatings, and plies for packaging applications: a review. *BioResources* 12:2143–2233
- Hubbe MA, Tayeb P, Joyce M, Tyagi P, Kehoe M, Dimic-Misic K, Pal L (2017b) Rheology of nanocellulose-rich aqueous suspensions: a review. *BioResources* 12:9556–9661
- Jens V, Ennaert T, Vanhulsel A, Sels B (2017) Unconventional pretreatment of lignocellulose with low-temperature plasma. *Chemsuschem* 10:14–31
- Johansson LS, Campbell JM (2004) Reproducible XPS on biopolymers: cellulose studies. *Surf Interface Anal* 36:1018–1022
- Jun W, Fengcai Z, Bingqiang C (2008) The solubility of natural cellulose after DBD plasma treatment. *Plasma Sci Technol* 10:743
- Jutila E, Koivunen R, Kiiski I, Bollström R, Sikanen T, Gane PAC (2018) Microfluidic lateral flow cytochrome P450 assay on a novel printed functionalized calcium carbonate-based platform for rapid screening of human xenobiotic metabolism. *Adv Funct Mater* 28(31):1802793–1802803
- Kostić M, Radić N, Obradović BM, Dimitrijević S, Kuraica MM, Škundrić P (2009) Silver-loaded cotton/polyester fabric modified by dielectric barrier discharge treatment. *Plasma Process Polym* 6(1):58–67
- Kramer F, Klemm D, Schumann D, Heßler N, Wesarg F, Fried W, Stadermann D (2006) Nanocellulose polymer composites as innovative pool for (bio) material development.

- In: *Macromolecular symposia*, WILEY-VCH Verlag, vol 244, pp 136–148
- Kumar P, Chand S (2012) Recent progress and future aspects of organic solar cells. *Prog Photovolt Res Appl* 20:377–415
- Ma H, Yip HL, Huang F, Jen AKY (2010) Interface engineering for organic electronics. *Adv Funct Mater* 20:1371–1388
- Maloney TC (2015) Network swelling of TEMPO-oxidized nanocellulose. *Holzforschung* 69:207–213
- Mihailović D, Šaponjić Z, Radoičić M, Lazović S, Baily CJ, Jovančić P, Nedeljković J, Radetić M (2011) Functionalization of cotton fabrics with corona/air RF plasma and colloidal TiO₂ nanoparticles. *Cellulose* 18:811–825
- Mohtaschemi M, Dimic-Misic K, Puisto A, Korhonen M, Maloney T, Paltakari J, Alava MJ (2014) Rheological characterization of fibrillated cellulose suspensions via bucket vane viscometer. *Cellulose* 21:1305–1312
- Möller M, Leyland N, Copeland G, Cassidy M (2010) Self-powered electrochromic display as an example for integrated modules in printed electronics applications. *Eur Phys J Appl Phys* 5:33205
- Özkan M, Dimic-Misic K, Karakoc A, Hashm SG, Lund P, Maloney T, Paltakari J (2016) Rheological characterization of liquid electrolytes for drop-on-demand inkjet printing. *Organ Electron* 38:307–315
- Pääkkönen T, Dimic-Misic K, Orelma H, Pönni R, Vuorinen T, Maloney T (2016) Effect of xylan in hardwood pulp on the reaction rate of TEMPO-mediated oxidation and the rheology of the final nanofibrillated cellulose gel. *Cellulose* 23(1):277–293
- Pertile RA, Andrade FK, Alves JC, Gama M (2010) Surface modification of bacterial cellulose by nitrogen-containing plasma for improved interaction with cells. *Carbohydr Polym* 82:692–698
- Prsyazhnyi V, Kramar A, Dojcinovic B, Zekic A, Obradovic BM, Kuraica MM, Kostic M (2013) Silver incorporation on viscose and cotton fibers after air, nitrogen and oxygen DBD plasma pretreatment. *Cellulose* 20:315–325
- Rantanen J, Dimic-Misic K, Kuusisto J, Maloney TC (2015) The effect of micro and nanofibrillated cellulose water uptake on high filler content composite paper properties and furnish dewatering. *Cellulose* 22:4003–4015
- Schultz J, Tsutsumi K, Donnet JB (1977) Surface properties of high-energy solids: II. Determination of the nondispersive component of the surface free energy of mica and its energy of adhesion to polar liquids. *J Colloid Interface Sci* 59:277–282
- Singh M, Haverinen HM, Dhagat P, Jabbour GE (2010) Inkjet printing-process and its applications. *Adv Mater* 22:673–685
- van de Vyver S, Geboers J, Jacobs PA, Sels BF (2011) Recent advances in the catalytic conversion of cellulose. *Chem-CatChem* 3:82–94
- Vanneste J, Ennaert T, Vanhulsel A, Sels B (2017) Unconventional pretreatment of lignocellulose with low-temperature plasma. *ChemSusChem* 10(1):14–31
- Willberg-Keyriläinen P, Ropponen J, Lahtinen M, Pere J (2019) Improved reactivity and derivitization of cellulose after pre-hydrolysis with commercial enzymes. *BioResources* 14(1):561–574
- Yinhua Z, Fuentes-Hernandez C, Khan TM, Liu JC, Hsu J, Shim JW, Dindar A, Youngblood JP, Moon RJ, Kippelen B (2013) Recyclable organic solar cells on cellulose nanocrystal substrates. *Sci Rep* 3:1536
- Zhu H, Narakathu BB, Fang Z, Aijazi AT, Joyce M, Atashbar M, Hu L (2014) A gravure printed antenna on shape-stable transparent nanopaper. *Nanoscale* 6(15):9110–9115

Publisher's Note Springer Nature remains neutral with regard to jurisdictional claims in published maps and institutional affiliations.



Probing charge carrier transport regimes in BiFeO₃ nanoparticles by Raman spectroscopy

Dejan M. Djokić*, Bojan Stojadinović, Dimitrije Stepanenko, Zorana Dohčević-Mitrović

Nanostructured Matter Laboratory, Institute of Physics Belgrade, University of Belgrade, Pregrevica 118, Belgrade 11 080, Republic of Serbia

ARTICLE INFO

Article history:

Received 18 October 2019

Revised 29 January 2020

Accepted 4 February 2020

Keywords:

Raman spectroscopy
Electronic background
BiFeO₃ nanoparticles
Variable range hopping

ABSTRACT

We report a finding of two transport regimes in multiferroic BiFeO₃ nanoparticles, which correspond to variable range hopping (VRH) mechanisms. Switch between the two regimes coincides with the transition between antiferromagnetic (AF) and paramagnetic (PM) phase. At low temperatures, it was found that temperature dependence of indirectly extracted resistivity is consistent with Efros-Shklovskii mechanism. As with high temperatures, data fit favourably to Mott VRH theory. Estimated resistivity value of $\sim 350\text{m}\Omega\text{cm}$ violates the Mott-Ioffe-Regel criterion, corroborating that the transport does not proceed through conduction bands. Conductivity was probed noninvasively via Raman contactless setup and studied as a function of temperature.

© 2020 Acta Materialia Inc. Published by Elsevier Ltd. All rights reserved.

Introduction. Multiferroic BiFeO₃ has recently attracted much attention due to its desirably high ferroelectric Curie temperature of ca 1100K and AF Néel temperature T_N of around 640K, both decreasing only slightly with decreasing crystallite size [1,2]. At nanoscales, BiFeO₃ turns out to be rather prospective for industrial applications in photovoltaics, satellite communications, electrically accessed magnetic memory, and novel sensing technologies [3]. Electric resistance of BiFeO₃ is one of the crucial parameters that must meet the relevant industrial requirements. In order to avoid leakage of electric charge, achieving high resistivity is one of the main concerns, and using nano-powders is seen as a promising development route.

As a highly informative experimental tool, Raman scattering spectroscopy stands for a local probe also being able to assess the nature and dynamics of charge carriers in conductive systems in a contactless way. On the other hand, it is exceedingly hard to identify the transport mechanism responsible for charge conduction using exclusively the contact probes [4,5]. Raman spectral response of the scattered light in metals with disorder and doped semiconductors is typically composed of several peaks due to the Raman active phonon excitations and a smooth frequency continuum which reflects direct electronic response [6]. This letter focuses on the temperature evolution of this continuous spectral background which is formed by low-energy electronic excitations, and referred to in the literature as the Raman electronic background [7–11]. The charge carrier scattering rate is intimately linked to the electronic

background in Raman spectra. This enables us to follow the character of charge transport in BiFeO₃ nanoparticles undergoing the AF/PM phase transition at the temperature around 640K.

As the particle size decreases into nanoscale domain, two crucial changes affect the charge transport in semiconductors. Band structures become distorted with decreasing particle size and, eventually, the states change their nature to get localized. Beyond certain scale, there is no conduction band and the commonly adopted picture of the intrinsic semiconductor transport due to the thermal activation via conduction band states breaks down. As the structure becomes more and more disordered, localization centers that can trap carriers appear more prominent with the decreasing particle size. Therefore, hopping varied with distance between the localization centers can be safely hypothesized to be the dominant transport mechanism even at high temperatures due to the evanescence of the conduction band.

Our measurements of temperature dependent electronic Raman background on the multiferroic BiFeO₃ nanoparticles of high purity, synthesized via sol-gel method [12], have been interpreted in terms of the VRH transport mechanism, which appears leading even at quite high temperatures. The role of localization centers is played by the surface states localized within particles, and with energies in the vicinity of Fermi level. An exceptionally high value of resistivity has been evidenced which rules out a metallic type of conductivity to make VRH a viable transport mechanism in the BiFeO₃ nanoparticles. We communicate a detection of the two different 3D VRH charge carrier transport mechanisms in the nanoscaled BiFeO₃, as probed by Raman spectroscopy. They correspond to different impact of electron correlations upon the

* Corresponding author.

E-mail address: djokic@ipb.ac.rs (D.M. Djokić).

transport on the opposite sides of the AF/PM phase transition. In the AF phase, the transport can well be described by the Efros-Shklovskii VRH theory [13], while in the PM phase, the transport follows the original Mott VRH theory [14].

Raman Scattering Spectra. μ -Raman scattering measurements were performed using a Linkam THMSG600 microscope heating-cooling stage in the temperature range from 80K up to 723K. Raman spectra were collected in backscattering configuration on TriVista 557 Raman system equipped with a nitrogen cooled CCD detector. The $\lambda = 532\text{nm}$ line of solid state Nd:YAG laser was used as an excitation source with sub-mW laser powers on the sample in order to eliminate heating effects. In the μ -Raman spectra of BiFeO₃ nanoparticles measured over 80 – 723K, more than thirteen optical phonon modes of A₁ and E symmetry have been observed. These spectra, deconvoluted using Lorentzian absorption profiles, are shown in Fig. 1 for four representative temperatures.

The total number and frequencies of the observed Raman active phonon modes of BiFeO₃ nanoparticles are identical to those detected in temperature dependent Raman scattering spectra carried out on bulk BiFeO₃ single crystals [15], apart from the splittings of some of the polar LO+TO phonon modes in the BiFeO₃ nanoparticles [16,17]. In bulk, factor group analysis predicts exactly thirteen ($4A_1 + 9E$) Raman active phonon modes [18]. Unlike the bulk BiFeO₃, the Raman active optical modes of the BiFeO₃ nanoparticles are seated on a distinctively broad spectroscopic feature (Fig. 1 shaded in light gray), which markedly varies with temperature. A similar spectroscopic background consisting of a non-resonant continuous profile was encountered in metal-oxide thin films [19], but with nearly structureless and of a rather enhanced intensity. This background is associated with a purely electronic Raman response, i.e. electronic scattering contribution independent of phonon bands, as a result of the atomic scale surface roughness. Furthermore, inelastic Raman scattering by particle-hole pair excitations was evidenced to lead to the emergence of electronic background in both metal-island films with adsorbants [20] and in very small metallic particles [21], which was interpreted in terms of the momentum conservation breakdown in the presence of the surface states. In hole-doped manganese perovskites, Liu et al. [22] found out that the broad electronic Raman response, accompanied with the scattering by conduction electrons, exhibits a distinctive change through the phase transition which could be followed quantitatively by the evolution of electron correlation effects.

A theory that describes and quantifies the profiles of Raman electronic background in "dirty" conductors was first developed by Falkovsky [7]. The author observed the effects of electronic excitations at low energies via scattering by impurities or phonons to include a finite momentum transfer ($q \neq 0$) caused by the finite penetration depth. Soon afterwards, Zawadowski and Cardona [8] employed a Feynman diagrammatic approach to evaluate the Kubo response function in the ladder approximation [23] for $q = 0$, establishing a close connection with the charge carrier transport lifetime. Feynman diagrams for nonresonant Raman scattering are given in Fig. 2(a). The wavy lines denote photon propagators with initial and final (momentum, energy): (\vec{k}_i, ω_i) and (\vec{k}_f, ω_f) up to the reduced Planck's constant. The incoming photon generates an electron-hole pair scattered by a phonon or impurity excitation ($\vec{q} = \vec{k}_i - \vec{k}_f, \omega = \omega_i - \omega_f$). In the ladder approximation, a phonon or impurity (dashed line in Fig. 2(a)), excited by the electron within the pair, is caught by the counterpart hole and vice versa. Finally, due to the dominating ladder-like diagrams, the approximation leads to the electronic Raman differential cross section [9,11], which can be written down as

$$\frac{d^2\sigma}{d\omega d\Omega} = \mathcal{A}_\tau \times \frac{1}{1 - \exp(-\hbar\omega/k_B T)} \times \frac{\omega\tau}{1 + (\omega\tau)^2}. \quad (1)$$

The constant \mathcal{A}_τ depends on several factors varying from one experiment to another [10], which we attach no importance to in the present study. Bose-Einstein thermal correction factor and Drude-like expression are given by the second and third term in the product, respectively. The effective scattering rate, $1/\tau$, includes two terms,

$$1/\tau = \underbrace{1/\tau_0}_{\text{bulk}} + \underbrace{Dq^2}_{\text{nano}}, \quad (2)$$

where $1/\tau_0$ denotes the scattering rate of the charge carrier by impurities in the $q = 0$ limit coming from the bulk channel, and the second term describes the effects of momentum non-conserving processes. The bulk term will be safely disregarded in the present case.

Actually, there is no evidence of the electronic Raman background in bulk semiconductor BiFeO₃ crystals [15], as opposed to the present case of BiFeO₃ nanocrystals (Fig. 1). The second term in Eq. (2), which originates from the nanoscopic nature of the crystalline BiFeO₃ particles is due to the momentum conservation breakdown. Thus, $q = 2\pi/\langle\ell\rangle$, where $\langle\ell\rangle$ represents the characteristic length of the expected nanoparticle size. We can automatically assume that the second term dominantly contributes to the effective scattering rate $1/\tau$. Prefactor D represents the diffusion constant and is intimately related to the electric resistivity ρ by the Einstein relation: $D^{-1} = e^2 g(\epsilon_F) \rho$, where $e = 1.6 \times 10^{-19}$ C, with $g(\epsilon_F)$ as the average value of the density of electronic states that give rise to the conduction in the vicinity of Fermi level [9]. The temperature evolution of the effective scattering rate $1/\tau$ can be followed from Fig. 2(b) delineating a temperature set of the normalized Drude-like $\hbar\omega$ -dependences extracted from the measured Raman temperature dependent spectra of the BiFeO₃ nanoparticles.

Charge Carrier Transport. Temperature variation of the logarithm of conductivity, $\ln(1/\rho)$, is oftentimes plotted as a function of $(1/T)^n$ in disordered materials, such as nano BiFeO₃, and "badly" conducting ceramics [25]. Exponent n imparts information on the DC conduction mechanism. When it is close to 1/4, n bears a signature of 3D Mott VRH transport mechanism [14], whereas an n value close to 1/2 indicates the presence of strong Coulomb correlations in 3D VRH [13]. Both VRH conduction mechanisms are supposed to prevail at low temperatures owing to the localized states around Fermi level in bulk semiconductors with disorder (blue arrow in Fig. 2(c) left). At rather high temperatures, the conduction runs by thermal activation via conduction band of the intrinsic semiconductor (red arrow in Fig. 2(c) left). However, once the particle size reaches nanoscales, the overlaps among the orbitals decrease. As a result, the bands become too sparse to cause splittings by opening up rather large gaps. The bands high in energy, such as conduction band, therefore tend to disappear as often encountered in disordered nanoscale samples, contrary to the corresponding bulk matter. For that reason, it is reasonable to assume that VRH mechanisms are applicable over temperature ranges that may extend up to higher temperatures in disordered nanostructures like BiFeO₃, and surely far outweigh the intrinsic thermally activated transport via conduction band which can be ignored, as is given in the right part of Fig. 2(c).

Crystalline BiFeO₃ nanoparticles exhibit the phase transition around 640K. At temperatures below it, the Coulomb correlations become sufficiently strong to form the AF phase, while above it the absence of the correlations is manifested through the weakly metallic-like PM state. We postulate the presence of localized surface states with energies close to the Fermi level that mediate the VRH transport over an extended temperature range. Temperature variations of $\ln(1/\tau)$, which is $\propto \ln(1/\rho)$ by Einstein relation, do differ on two sides of the AF/PM phase transition. The n values, which straighten out the $\ln(1/\tau) \propto T^{-n}$ curves are essentially different in the two phases.

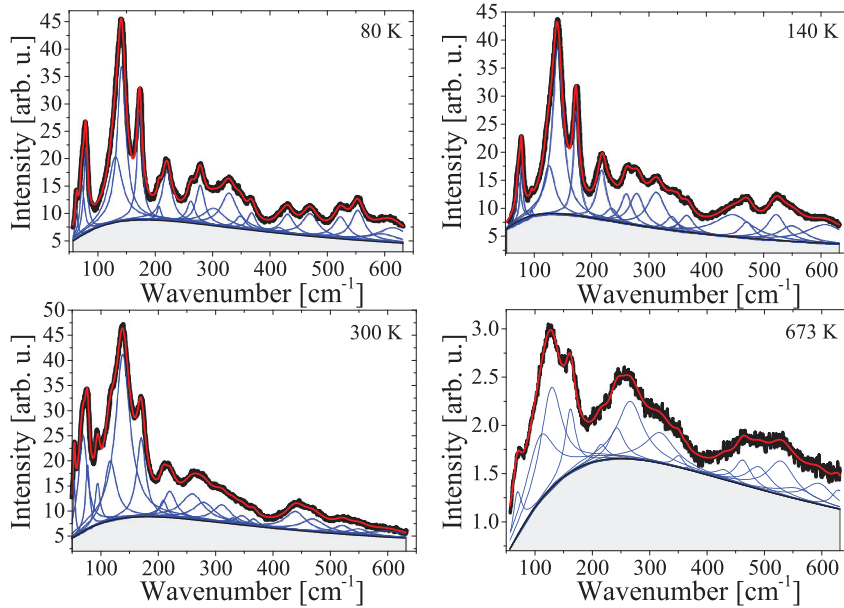


Fig. 1. Raman scattering spectra at four representative temperatures comprising of a smooth electronic background (area shaded in light gray) and more than thirteen phonon peaks (blue lines). The total fitting line is drawn in red, whereas the data points are given in black. (For interpretation of the references to colour in this figure legend, the reader is referred to the web version of this article.)

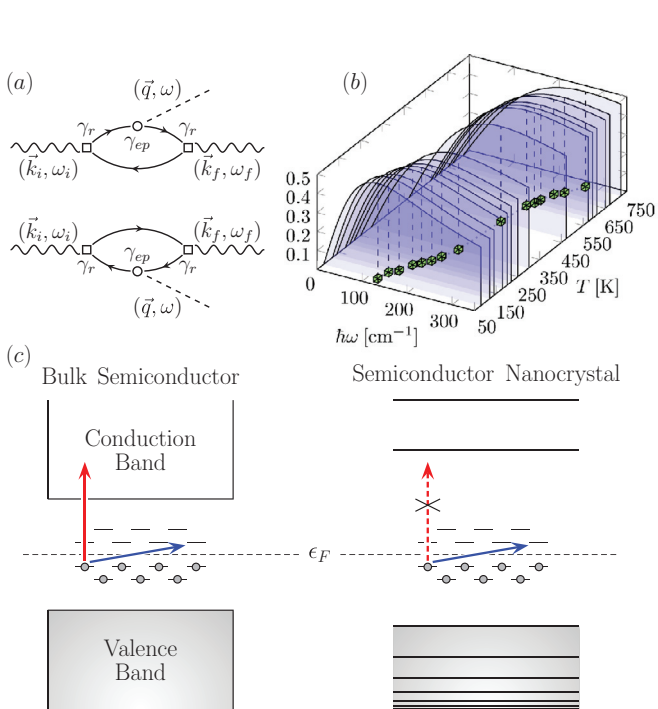


Fig. 2. (a) The Feynman diagrams describing the Raman scattering of light (wavy lines) processes by phonons or impurities (dashed lines) with electron-hole formations (solid lines). The processes are of third order in electron or hole scattering by phonons and impurities. Electron and hole contributions are represented by upper and lower diagrams, respectively. γ_r stands for electron-photon interaction (\square vertex), while γ_{ep} stands for electron-phonon interaction (\circ vertex) [24]. (b) Temperature dependent Raman electronic Drude-like background of BiFeO₃ nanoparticles (Fig. 1) normalized by both Bose-Einstein thermal correction factor and \mathcal{A}_T (Eq. (1)). Cubes in green follow the temperature evolution of effective scattering rate $1/\tau$, in temperature (T)-Raman shift ($\hbar\omega$) plane. (c) Conduction mechanisms due to the intrinsic activation from valence to conduction band (red arrow) and VRH promoted by localized states around Fermi level (blue arrow) in bulk (left) and nanocrystal (right) semiconductor. (For interpretation of the references to colour in this figure legend, the reader is referred to the web version of this article.)

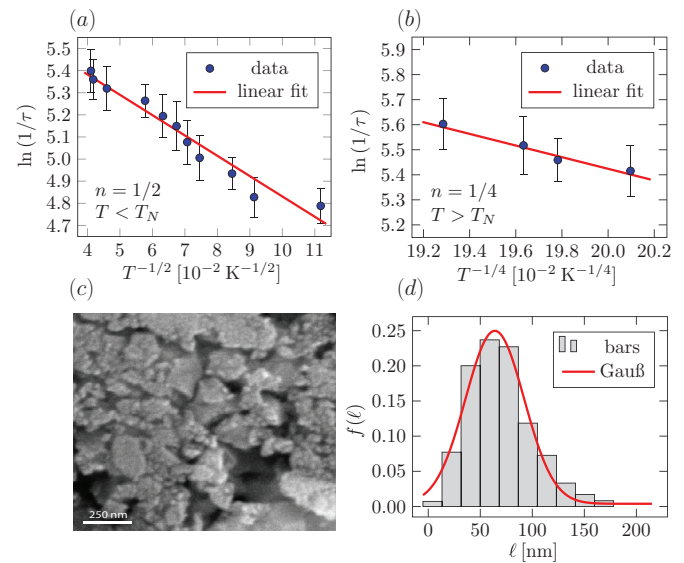


Fig. 3. Temperature (T^{-n}) dependence of the logarithm of the effective scattering rate ($\ln(1/\tau)$) for $T < T_N$ in figure (a) with $n = 1/2$ and for $T > T_N$ in figure (b) with $n = 1/4$. Linear fits are given in red lines. (c) Tescan SM-300 image of the surface morphology of the BiFeO₃ nanoparticle batch and (d) the related histogram of the particle diameter distribution (bars in gray) fitted by the normal distribution function (Gauß) given in red line with (64 ± 2) nm as the mean value and (28 ± 2) nm as the standard deviation. $f(\ell)$ stands for the frequency of appearance with respect to the nanoparticle size ℓ . (For interpretation of the references to colour in this figure legend, the reader is referred to the web version of this article.)

The temperature dependences of $\ln(1/\tau)$ are linearized against T^{-n} , with $n = 1/2$ (Fig. 3(a)) and $n = 1/4$ (Fig. 3(b)) in the strongly correlated AF ($T < T_N$) and PM phase ($T > T_N$), respectively, which is in accordance with the predictions for the applicability of the two VRH mechanisms [13,14]. To be precise, the temperature evolution of $\ln(1/\tau)$ is proportional to $(T_n/T)^n$, with $k_B T_{1/2} \approx e^2 / (4\pi\epsilon_0\epsilon_r\xi)$ for $n = 1/2$ [13] and $k_B T_{1/4} \approx 18.1 / (g(\epsilon_F)\xi^3)$ for $n = 1/4$ [26], where $k_B = 1.38 \times 10^{-23}$ J/K and $\epsilon_0 = 8.85 \times 10^{-12}$ F/m. Parameter ξ is the localization length of wave function

of the electronic surface states, while ϵ_r represents the relative permittivity constant, calculated as $\epsilon_r \approx 28$ using the impedance dielectric spectroscopy of nanocrystalline BiFeO₃ [27].

Relying on the extracted slopes from the two linear fits in Fig. 3(a) & (b), we have come up with $\xi \approx 7$ nm. This finding proves quite meaningful as a localization length of wave function of the electronic surface states since $\xi < \langle \ell \rangle$, where the average particle size $\langle \ell \rangle$ reaches up nearly to 66 nm. This value has been computed as the mean value from the Gaussian particle size distribution obtained from Scanning Electron Microscopy (SEM) image of BiFeO₃ nanoparticles at room temperature and using the Scanning Probe Image Processor software (Fig. 3(c) & (d)). Furthermore, the density of localized states, $g(\epsilon_F)$, can also be determined by manipulating the fitting parameters extracted from Fig. 3(a) & (b). Namely, $g(\epsilon_F) \approx 2.1 \times 10^{18}$ localized states per (eV \times cm³) in the high temperature PM phase. This allows us to estimate the resistivity value ρ from Eq. (1) and the Einstein relation. Thus, following Fig. 2(b), at high temperatures $h/\tau \approx 250$ cm⁻¹, where $h = 6.626 \times 10^{-34}$ Js. Accordingly, $\rho \approx 4\pi^2\tau/(\langle \ell \rangle^2 e^2 g(\epsilon_F)) \approx 350$ m Ω cm at lowest. Its extraordinarily high value is not possible in conventional metals and exceeds the maximum resistivity value allowed by the Mott-Ioffe-Regel limit of at most ~ 1 m Ω cm [28,29], which classifies nanocrystalline BiFeO₃ as a bad conductor. This finding strongly suggests that the conduction band energy sector is likely to fade away to ultimately acquire markedly low electronic density of states, leaving no room for the fixed thermally activated transport to take over 3D VRH. Nevertheless, other reliable experimental tools, such as AC/DC transport measurements, infrared and electron spin resonance spectroscopy on somewhat larger particles, might be a good proposal to uphold the validity of the VRH mechanisms we have put forward.

Conclusions. In summary, here is reported an indirect finding of the two different VRH transport regimes through the analysis of the temperature dependent electronic Raman background of BiFeO₃ nanoparticles. The switch between the two strikingly different VRH transport regimes coincides with AF/PM phase transition. The VRH exponent of $n = 1/2$ is associated with the AF strongly correlated phase below T_N implying the presence of correlations, whereas the exponent $n = 1/4$ neatly linearizes the temperature dependence of the logarithm of effective scattering rate in the PM state above T_N . It has been also deduced that the nanoscaled BiFeO₃ falls into the family of bad conductors due to its exceptionally high resistivity value. At last, it is worth mentioning that, to the extent of our knowledge, the existence of different conduction VRH regimes in AF and PM phases has never been previously recognized in BiFeO₃ nanocrystals.

Declaration of Competing Interest

The authors declare that they have no known competing financial interests or personal relationships that could have appeared to influence the work reported in this paper.

Acknowledgments

We are grateful to Professor László Forró for valuable discussions on the topics of VRH transport mechanism. This work is

supported by the Serbian Ministry of Education, Science, and Technological Development through project OI 171032.

References

- [1] J. Wang, J.B. Neaton, H. Zheng, V. Nagarajan, B.S.B. Ogale, Liu, D. Viehland, V. Vaithyanathan, D.G. Schlom, U.V. Waghmare, N.A. Spaldin, K.M. Rabe, M. Wuttig, R. Ramesh, *Science* 299 (2003) 1719–1722, doi:10.1126/science.1080615.
- [2] T.J. Park, G.C. Papaefthymiou, A.J. Viescas, A.R. Moodenbaugh, S.S. Wong, *Nano Lett.* 7 (2007) 766–772, doi:10.1021/nl063039w.
- [3] G. Catalan, J.F. Scott, *Adv. Mater.* 21 (2009) 2463–2485, doi:10.1002/adma.200802849.
- [4] A. Mukherjee, M. Banerjee, S. Basu, N.T.K. Thanh, L.A.W. Green, M. Pal, *Physica B: Cond. Matt.* 448 (2014) 199–203, doi:10.1016/j.physb.2014.03.082.
- [5] S. Ruby, S.S.R. Inbanathan, *Appl. Surf. Sci.* 449 (2018) 10–14, doi:10.1016/j.apsusc.2017.11.231.
- [6] L.A. Falkovsky, *Phys. Usp.* 47 (2004) 249–272, doi:10.1070/pu2004v047n03abeh001735.
- [7] L.A. Falkovsky, *Sov. Phys. JETP* 68 (1989) 661–663.
- [8] A. Zawadowski, M. Cardona, *Phys. Rev. B* 42 (1990) 10732–10734, doi:10.1103/PhysRevB.42.10732.
- [9] T.P. Devereaux, *Phys. Rev. B* 45 (1992) 12965–12975, doi:10.1103/PhysRevB.45.12965.
- [10] E.Y. Sherman, O.V. Misochko, *J. Phys. Condens. Matter* 15 (2003) 3751–3758, doi:10.1088/0953-8984/15/22/309.
- [11] T.P. Devereaux, R. Hackl, *Rev. Mod. Phys.* 79 (2007) 175–233, doi:10.1103/RevModPhys.79.175.
- [12] B. Stojadinović, Z. Dohčević-Mitrović, D. Stepanenko, M. Rosić, I. Petronijević, N. Tasić, N. Ilić, B. Matović, B. Stojanović, *Ceram. Int.* 43 (2017) 16531–16538, doi:10.1016/j.ceramint.2017.09.038.
- [13] A.L. Efros, B.I. Shklovskii, *J. Phys. C Solid State Phys.* 8 (1975) L49–L51, doi:10.1088/0022-3719/8/4/003.
- [14] N.F. Mott, E.A. Davis, *Electronic Processes in Non-Crystalline Materials*, Oxford University Press, 1979.
- [15] H. Fukumura, H. Harima, K. Kisoda, M. Tamada, Y. Noguchi, M. Miyayama, *J. Magn. and Magn. Mat.* 310 (2007) e367–e369, doi:10.1016/j.jmmm.2006.10.282.
- [16] J. Hlinka, J. Pokorný, S. Karimi, I.M. Reaney, *Phys. Rev. B* 83 (2011) 020101–020104, doi:10.1103/PhysRevB.83.020101.
- [17] J. Bielecki, P. Svedlindh, D.T. Tibebe, S. Cai, S.-G. Eriksson, L. Börjesson, C.S. Knee, *Phys. Rev. B* 86 (2012) 184422–184437, doi:10.1103/PhysRevB.86.184422.
- [18] D.L. Rousseau, R.P. Bauman, S.P.S. Porto, *J. Raman Spectrosc.* 10 (1981) 253–290, doi:10.1002/jrs.1250100152.
- [19] A. Otto, J. Timper, J. Billmann, G. Kovacs, I. Pockrand, *Surf. Sci.* 92 (1980) L55–L57, doi:10.1016/0039-6028(80)90237-X.
- [20] C.Y. Chen, E. Burstein, S. Lundquist, *Solid State Commun.* 32 (1979) 63–66, doi:10.1016/0038-1098(79)90998-0.
- [21] R. Monreal, F. Flores, Y. Gao, T. López-Ríos, *Europhys. Lett.* 4 (1987) 115–120, doi:10.1209/0295-5075/4/1/019.
- [22] H.L. Liu, S. Yoon, S.L. Cooper, S.-W. Cheong, P.D. Han, D.A. Payne, *Phys. Rev. B* 58 (1998) R10115–R10118, doi:10.1103/PhysRevB.58.R10115.
- [23] A.A. Abrikosov, L.P. Gorkov, I.E. Dzyaloshinsky, *Quantum Field Theoretical Methods in Statistical Physics*, Pergamon Press (Oxford), 1965.
- [24] M. Cardona, *Light Scattering in Solids I - Introductory Concepts*, Springer-Verlag (Berlin), 1983.
- [25] L. Zuppiroli, L. Forró, *Phys. Lett. A* 141 (1989) 181–185, doi:10.1016/0375-9601(89)90785-8.
- [26] W.D. Rice, R.T. Weber, P. Nikolaev, S. Arepalli, V. Berka, A.L. Tsai, J. Kono, *Phys. Rev. B* 88 (2013) 041401–041405, doi:10.1103/PhysRevB.88.041401.
- [27] B. Stojadinović, University of Belgrade, 2018 Ph.D. thesis. Faculty of Physics,
- [28] O. Gunnarsson, M. Calandra, J.E. Han, *Rev. Mod. Phys.* 75 (2003) 1085–1099, doi:10.1103/RevModPhys.75.1085.
- [29] N.E. Hussey, K. Takenaka, H. Takagi, *Philos. Mag.* 84 (2004) 2847–2864, doi:10.1080/14786430410001716944.

NanoScience and Technology

Juan Bartolomé
Fernando Luis
Julio F. Fernández *Editors*

Molecular Magnets

Physics and Applications

 Springer

Editors

Juan Bartolomé
Institute of Material Science of Aragón and
Department of Condensed Matter Physics
CSIC–University of Zaragoza
Zaragoza, Spain

Julio F. Fernández
Institute of Material Science of Aragón and
Department of Condensed Matter Physics
CSIC–University of Zaragoza
Zaragoza, Spain

Fernando Luis
Institute of Material Science of Aragón and
Department of Condensed Matter Physics
CSIC–University of Zaragoza
Zaragoza, Spain

ISSN 1434-4904
NanoScience and Technology
ISBN 978-3-642-40608-9
DOI 10.1007/978-3-642-40609-6
Springer Heidelberg New York Dordrecht London

ISSN 2197-7127 (electronic)
ISBN 978-3-642-40609-6 (eBook)

© Springer-Verlag Berlin Heidelberg 2014

This work is subject to copyright. All rights are reserved by the Publisher, whether the whole or part of the material is concerned, specifically the rights of translation, reprinting, reuse of illustrations, recitation, broadcasting, reproduction on microfilms or in any other physical way, and transmission or information storage and retrieval, electronic adaptation, computer software, or by similar or dissimilar methodology now known or hereafter developed. Exempted from this legal reservation are brief excerpts in connection with reviews or scholarly analysis or material supplied specifically for the purpose of being entered and executed on a computer system, for exclusive use by the purchaser of the work. Duplication of this publication or parts thereof is permitted only under the provisions of the Copyright Law of the Publisher's location, in its current version, and permission for use must always be obtained from Springer. Permissions for use may be obtained through RightsLink at the Copyright Clearance Center. Violations are liable to prosecution under the respective Copyright Law.

The use of general descriptive names, registered names, trademarks, service marks, etc. in this publication does not imply, even in the absence of a specific statement, that such names are exempt from the relevant protective laws and regulations and therefore free for general use.

While the advice and information in this book are believed to be true and accurate at the date of publication, neither the authors nor the editors nor the publisher can accept any legal responsibility for any errors or omissions that may be made. The publisher makes no warranty, express or implied, with respect to the material contained herein.

Printed on acid-free paper

Springer is part of Springer Science+Business Media (www.springer.com)

Contents

Part I Tunneling of Single Molecule Magnets

1 From Quantum Relaxation to Resonant Spin Tunneling	3
Javier Tejada	
1.1 Historic Notes	3
1.2 Early Experiments on Magnetic Tunneling at the University of Barcelona	5
1.3 Experiments on Mn-12	8
1.4 Conclusion	12
References	13
2 Quantum Tunneling of the Collective Spins of Single-Molecule Magnets: From Early Studies to Quantum Coherence	17
Bernard Barbara	
2.1 Introduction	17
2.2 Prehistory and History	18
2.2.1 Micro-SQUID Measurements	22
2.2.2 Mn ₁₂ -ac, The First Single Molecular Magnet	22
2.3 Quantum Tunneling in Single Molecule Magnets	24
2.3.1 Single Molecule Magnets: Basic Properties	24
2.3.2 First Evidences	26
2.3.3 Main Evidences	28
2.4 Theory and Comparisons with Experiments	33
2.4.1 Resonance Conditions	33
2.4.2 Quantum Fluctuations and Barrier Erasing	34
2.4.3 Tunnel Splittings, Spin-Parity and Observation of MQTM	34
2.4.4 Quantum Tunneling and Spin-Bath	36
2.5 Quantum Tunneling and Coherence in Single Ion Magnets	44
2.5.1 First Evidence of MQTM in SIMs and Comparison with SMMs	44
2.5.2 First Evidence of MQCM in SIMs, Paving the Way for SMMs	47

2.6	Quantum Coherence in Single Molecule Magnets	50
2.7	Conclusion and Perspectives	54
	References	55
3	Spin Tunneling in Magnetic Molecules That Have Full or Partial Mechanical Freedom	61
	Eugene M. Chudnovsky	
3.1	Introduction	61
3.2	Nanomechanics of a Two-State Spin System Rotating About a Fixed Axis	64
3.2.1	Quantum Mechanics of a Two-State Spin System	64
3.2.2	Renormalization of the Spin Tunnel Splitting in a Nano-oscillator	65
3.3	Free Quantum Rotator with a Two-State Macrospin	67
3.3.1	Anomalous Commutation Relations	67
3.3.2	Rotating Two-State Spin System	70
3.3.3	Ground State	72
3.4	Conclusions	74
	References	75
4	A Microscopic and Spectroscopic View of Quantum Tunneling of Magnetization	77
	Junjie Liu, Enrique del Barco, and Stephen Hill	
4.1	Spin Hamiltonian	77
4.1.1	Giant-Spin Approximation Hamiltonian	78
4.1.2	Multi-Spin Hamiltonian	82
4.2	Quantum Tunneling of Magnetization in High-Symmetry Mn ₃ Single-Molecule Magnets	83
4.2.1	The Mn ₃ Single-Molecule Magnet	84
4.2.2	QTM Selection Rules in Mn ₃	85
4.2.3	The Influence of Disorder on QTM	88
4.2.4	Berry Phase Interference in Trigonal Symmetry	92
4.3	Quantum Tunneling of Magnetization in the High-Symmetry Ni ₄ Single-Molecule Magnet	93
4.3.1	The Ni ₄ Single-Molecule Magnet	93
4.3.2	Quantum Tunneling of Magnetization in the Ni ₄ SMM	96
4.3.3	Disorder	98
4.4	Quantum Tunneling of Magnetization in Low-Symmetry Mn ₄ Single-Molecule Magnets	99
4.4.1	The Mn ₄ Single-Molecule Magnets	99
4.4.2	EPR and QTM Spectroscopy in Mn ₄ SMMs with and Without Solvent	100
4.4.3	Berry Phase Interference in Mn ₄ -Bet	103
4.5	Summary and Outlook	106
	References	108

Part II Beyond Single Molecules

5	Magnetic Avalanches in Molecular Magnets	113
	Myriam P. Sarachik	
5.1	Background	113
5.2	Temperature-Driven Magnetic Deflagration	116
5.2.1	Avalanche Ignition	117
5.2.2	Avalanche Speed	120
5.3	Cold Deflagration	123
5.4	Summary and Outlook for the Future	124
	References	125
6	Theory of Deflagration and Fronts of Tunneling in Molecular Magnets	129
	D.A. Garanin	
6.1	Introduction	129
6.2	Magnetic Deflagration	132
6.2.1	Ignition of Deflagration	134
6.2.2	Deflagration Fronts	135
6.3	Fronts of Tunneling	139
6.3.1	Tunneling Effects in the Relaxation Rate	139
6.3.2	Dipolar Field in Molecular Magnets	143
6.3.3	Fronts of Tunneling at $T = 0$	147
6.3.4	1d Theory of Quantum Deflagration	151
6.3.5	3d Theory of Quantum Deflagration	154
6.4	Discussion	156
	References	157
7	Dipolar Magnetic Order in Crystals of Molecular Nanomagnets	161
	Fernando Luis	
7.1	Introduction	161
7.2	Theoretical Background	165
7.2.1	Spin Hamiltonian	165
7.2.2	Mean-Field Approximations	166
7.3	Dipolar Order vs. Single-Molecule Magnet Behavior	168
7.3.1	Magnetic Order and Relaxation Towards Thermal Equilibrium	168
7.3.2	Influence of Dipolar Interactions on Magnetic Relaxation and Spin Tunneling	169
7.3.3	Experimental Determination of the Average Interaction Fields	170
7.4	Dipolar Order of Molecular Nanomagnets with Low Magnetic Anisotropy. Ferromagnetism in Mn_6	172
7.5	Dipolar Order in a Transverse Magnetic Field. Ferromagnetism in Mn_{12} Acetate	175
7.5.1	Magnetic Ordering Via Pure Quantum Tunneling	175

7.5.2	Quantum Annealing	175
7.5.3	The Quantum Ising Model	176
7.5.4	Magnetic Order in Mn_{12} Acetate	177
7.6	Magnetic Order and Quantum Phase Transition in Fe_8	181
7.7	Conclusions and Outlook	186
	References	187
8	Single-Chain Magnets	191
	Dante Gatteschi and Alessandro Vindigni	
8.1	Introduction	191
8.2	Thermal Equilibrium and Slow Dynamics in Ideal SCMs	194
8.3	Tailoring SCMs by Building-Block Approach	198
8.4	Realistic Spin Hamiltonians for Single-Chain Magnets	201
8.5	Glauber Model and Single-Chain Magnets	206
8.6	Glauber Model for Finite Chains	211
8.7	Beyond the Glauber Model	215
8.8	Conclusion and Perspectives	217
	References	218
9	Magnetism of Metal Phthalocyanines	221
	Juan Bartolomé, Carlos Monton, and Ivan K. Schuller	
9.1	Introduction	221
9.2	Solid State MPcs	222
9.3	MPc Thin Films	229
9.4	MPc Molecules Adsorbed on Substrates	234
9.5	Perspectives of MPcs	239
	References	242
Part III Applications		
10	Potentialities of Molecular Nanomagnets for Information Technologies	249
	Marco Affronte and Filippo Troiani	
10.1	Introduction	249
10.2	Classical and Quantum Bits	251
10.3	Issues, Trends and Benchmarks of Information Technologies	257
10.4	Quantum Computation	262
10.5	Conclusions and Future Directions	270
	References	270
11	Molecular Magnets for Quantum Information Processing	275
	Kevin van Hoogdalem, Dimitrije Stepanenko, and Daniel Loss	
11.1	Introduction	275
11.2	Encoding of Qubits in Molecular Magnets	278
11.3	Single-Qubit Rotations and the Spin-Electric Effect	280
11.4	Two-Qubit Gates	286
11.5	Decoherence in Molecular Magnets	288
11.6	Initialization and Read-out	291

11.7 Grover's Algorithm Using Molecular Magnets	292
References	294
12 Single-Molecule Spintronics	297
Enrique Burzurí and Herre S.J. van der Zant	
12.1 Introduction	297
12.1.1 How to Detect Spin in Magnetic Molecules?	298
12.2 Coulomb Blockade	299
12.3 Spectroscopy of Magnetic Spin States	301
12.3.1 Weak Coupling: SET Excitations	302
12.3.2 Intermediate Coupling: Inelastic Spin-Flip Co-tunneling Process	303
12.3.3 Kondo Correlations	304
12.3.4 Ground State to Ground State: Gate Spectroscopy	305
12.3.5 Summary	307
12.4 Fabrication of a Spin Transistor	307
12.4.1 Electron-Beam Lithography	307
12.4.2 Electromigration	309
12.4.3 Preliminary Characterization	310
12.5 A Practical Example. The Fe ₄ Single-Molecule Magnet	310
12.5.1 Why the Fe ₄ Single-Molecule Magnet?	310
12.5.2 Spin Excitations: Inelastic Spin Flip Spectroscopy	312
12.5.3 Gate-Voltage Spectroscopy	313
12.5.4 Kondo Excitations and High-Spin State	314
12.6 Future Directions	315
12.6.1 Quantum Tunneling of the Magnetization and Berry Phase	315
12.6.2 Ferromagnetic Electrodes	316
12.6.3 Spin Crossover Molecules	316
References	317
13 Molecular Quantum Spintronics Using Single-Molecule Magnets	319
Marc Ganzhorn and Wolfgang Wernsdorfer	
13.1 Introduction	319
13.2 Molecular Nanomagnets for Molecular Spintronics	320
13.3 Introduction to Molecular Spintronics	321
13.3.1 Direct Coupling Scheme	322
13.3.2 Indirect Coupling Scheme	324
13.3.3 Magnetic Torque Detector or Probing Via Mechanical Motion	325
13.3.4 NanoSQUID or Probing Via Magnetic Flux	327
13.4 Magnetism of the TbPc ₂ Molecular Nanomagnet	328
13.4.1 Molecular Structure	329
13.4.2 Spin Hamiltonian	329
13.4.3 Quantum Tunneling of Magnetization and Landau-Zener Model	332
13.4.4 Spin-Lattice Relaxation	333

13.5 Molecular Quantum Spintronics with a Single TbPc ₂	335
13.5.1 Read-out of the Electronic Spin	336
13.5.2 Read-out of the Nuclear Spin	344
13.5.3 Coupling of a Single TbPc ₂ SMM to a Carbon Nanotube's Mechanical Motion	354
13.5.4 Coupling of a Single TbPc ₂ SMM to a Quantum Dot	358
13.6 Conclusion	360
References	361
14 Molecule-Based Magnetic Coolers: Measurement, Design and Application	365
Marco Evangelisti	
14.1 Introduction	365
14.2 Theoretical Framework	367
14.3 Experimental Evaluation of the MCE	368
14.3.1 Indirect Methods	368
14.3.2 Direct Measurements	370
14.4 Designing the Ideal Refrigerant	373
14.4.1 Magnetic Anisotropy	374
14.4.2 Magnetic Interactions	375
14.4.3 Magnetic Density and Choice of Units	378
14.5 Towards Applications: On-Chip Refrigeration	382
14.6 Concluding Remarks	385
References	385
Index	389

Chapter 11

Molecular Magnets for Quantum Information Processing

Kevin van Hoogdalem, Dimitrije Stepanenko, and Daniel Loss

Abstract In this chapter we will examine the possibility of utilizing molecular magnets for quantum information processing purposes. We start by giving a brief introduction into quantum computing, and highlight the fundamental differences between classical- and quantum computing. We will introduce the five DiVincenzo criteria for successful physical implementation of a quantum computer, and will use these criteria as a guideline for the remainder of the chapter. We will discuss how one can utilize the spin degrees of freedom in molecular magnets for quantum computation, and introduce the associated ways of controlling the state of the qubit. In this part we will focus mainly on the spin-electric effect, which makes it possible to control the quantum states of spin in molecular magnets by electric means. We will discuss ways to couple the quantum state of two molecular magnets. Next, we will identify and discuss the different decoherence mechanisms that play a role in molecular magnets. We will show that one of the advantages of using molecular magnets as qubits is that it is possible to use degrees of freedom that are more robust against decoherence than those in more traditional qubits. We briefly discuss preparation and read-out of qubit states. Finally, we discuss a proposal to implement Grover's algorithm using molecular magnets.

11.1 Introduction

Conceptually, a computer is a device that takes an input and manipulates it using a predetermined set of deterministic rules to compute a certain output. Both input and output are defined in terms of bits, classical physical systems which can be in one of two different states. These states are typically denoted 0 and 1. The set of rules that a computer uses for a computation, also named the algorithm, can be described by a set of gates. A simple example of a gate is the one-bit NOT-gate, which gives a 1 as output when the input is 0, and vice versa. An example of a two-bit

K. van Hoogdalem · D. Stepanenko · D. Loss (✉)
Department of Physics, University of Basel, Klingelbergstrasse 82, 4056 Basel, Switzerland
e-mail: daniel.loss@unibas.ch

K. van Hoogdalem
e-mail: kevin.vanhoogdalem@unibas.ch

J. Bartolomé et al. (eds.), *Molecular Magnets*, NanoScience and Technology,
DOI [10.1007/978-3-642-40609-6_11](https://doi.org/10.1007/978-3-642-40609-6_11), © Springer-Verlag Berlin Heidelberg 2014

275

gate is the NAND-gate, which gives a 0 as output only if both the input bits are 1, and yields a 1 otherwise. Interestingly, it can be shown that any classical algorithm can be implemented using a combination of NAND-gates only. However, this completeness theorem does not state anything about the time in which a certain problem can be solved. Instead, such questions belong to the field of computational complexity theory [1]. A large class of problems, called NP, contains all the problems for which a candidate solution can be checked in polynomial time. In contrast, the class of problems that can be solved in polynomial time is called P. Whether P is a strict subset of NP is one of the great open problems in mathematics. It is widely believed that there are problems in the difference between P and NP. Some of the candidates were shown to be solvable using a quantum computer, but an efficient solution on a classical computer is unknown. This inability of a classical computer to solve certain problems efficiently is one of the main driving forces behind the study of quantum computation. Heuristically one might argue that, since classical computers are governed by Newtonian mechanics—which is only valid in certain limits of the underlying quantum theory—a quantum computer must have computational power which is at least the same as, and hopefully greater than, that of a classical computer [2]. Different algorithms exist that support the claim that a quantum computer is inherently more powerful than a classical computer. Among these are Deutsch-Jozsa's [3, 4], Grover's [5], and Shor's algorithm [6].

Besides being interesting from this pragmatic point of view, quantum computing is also of fundamental importance in the fields of information theory and computer science. The fact that quantum mechanics plays a role in information theory becomes clear when one realizes that abstract information is always embedded in a physical system, and is therefore governed by physical laws. This was made explicit by Deutsch [7], when he proposed a stricter version of the Church-Turing hypothesis, emphasizing its 'underlying physical assertion'. The original Church-Turing hypothesis loosely states that every function which would naturally be regarded as computable can be computed by the universal Turing machine [8, 9], and this statement can be seen as the basis underlying computer science. In a sense, a universal Turing machine is a theoretical formalization of a computer (with an infinite memory) as we described it previously. Deutsch replaces this hypothesis by his more physical Church-Turing principle: 'Every finitely realizable physical system can be perfectly simulated by a universal model computing machine operating by finite means'. He then went on to show that the universal Turing machine does not fulfill the requirements for a universal model computing machine, while the universal quantum computer, proposed in the same work, is compatible with the principle. In this way, the universal quantum computer takes the role of the universal Turing machine.

The basic unit of information in a quantum computer is a qubit [10]. Like a classical bit, a qubit is a physical two-level system, with basis states denoted by $|0\rangle$ and $|1\rangle$. Unlike a classical bit, however, a qubit is a quantum system. This makes the information stored in a qubit ultimately analog, since a qubit can be in any state $|\psi\rangle = \alpha|0\rangle + \beta|1\rangle$, with α and β complex numbers such that $|\alpha|^2 + |\beta|^2 = 1$. In a quantum computer, a gate will act linearly on a state $|\psi\rangle$, and hence in a sense on

$|0\rangle$ and $|1\rangle$ simultaneously. This quantum parallelism is one of the advantages of a quantum computer. Of course, one must keep in mind that reading out the qubit (measuring the state) collapses the quantum state into one of the basis states $|0\rangle$ or $|1\rangle$, so this parallelism cannot be used trivially. The other key advantage of using quantum computing is the fact that two qubits can be entangled, i.e. there can exist non-classical correlations between two qubits. The final important property of qubits is captured by the no-cloning theorem [11], which states that it is impossible to copy an unknown quantum state. This theorem invalidates the use of classical error-correction methods -which are typically based on redundancy, and therefore require copying of bits- for quantum computation. Instead, one has to resort to quantum error-correction codes that rely upon entanglement and measurement, but do not require an ability to copy an unknown quantum state.

Quantum mechanics dictates that the time evolution of an isolated quantum state is described by a unitary operator. This means that the action of any valid quantum gate must also be described by a unitary operator. In fact, it turns out that this is the only requirement on a valid quantum gate. Consequently, there exists a rich variety of quantum gates: Where the only non-trivial classical one-bit gate is the NOT-gate, any rotation in the one-qubit Hilbert space is a quantum gate. As an important example of a one-qubit gate that has no classical analog we mention the Hademard-gate, which transforms $|0\rangle$ into $(|0\rangle + |1\rangle)/\sqrt{2}$ and $|1\rangle$ into $(|0\rangle - |1\rangle)/\sqrt{2}$. An example of a two-qubit gate is the CNOT-gate, which acts as a NOT-gate on the second qubit when the first qubit is in the state $|1\rangle$, and does nothing otherwise. It can be shown that arbitrary single qubit rotations together with the CNOT-gate are sufficient to implement any two-qubit unitary evolution exactly [12].

After all these theoretical considerations, one might wonder what is actually required to build a physical quantum computer. The requirements have been succinctly summarized by DiVincenzo, in terms of his five DiVincenzo criteria for successful implementation of a quantum computer [2]. In order to have a functional quantum computer we need

- a collection of well-defined physical quantum two-level systems (qubits), which should be well-isolated and scalable, i.e. it should be possible to add qubits at will.
- a procedure to initialize the system in an initial state, for instance $|00\dots 0\rangle$.
- the ability to perform logic operations on the qubits, i.e. one- and two-qubit gates.
- long enough decoherence times compared to the ‘clock time’ of the quantum computer for quantum error correction to be efficient.
- the ability to read out the final state of the qubit.

Satisfying these criteria in a single system simultaneously has turned out to be quite a tour de force. Although tremendous progress -both theoretical and experimental- towards completion of this goal has been made in a wide variety of different areas of solid state physics, it is at this point not clear which system will turn out to be most suitable. Of all the systems that have been proposed as a basis for qubit, we mention here quantum dots [13, 14], cold trapped ions [15], cavity quantum electrodynamics [14, 16], bulk nuclear magnetic resonance [17], low-capacitance

Josephson junctions [18], donor atoms [19, 20], linear optics [21], color centers in diamond [22–24], carbon nanotubes [25], nanowires [26], and lastly the topic of this chapter: Molecular magnets [27–32].

11.2 Encoding of Qubits in Molecular Magnets

We have seen that information in a quantum computer must be encoded in qubits, i.e. well-defined physical quantum two-level systems. Probably the first candidate for a qubit that comes to mind is a single spin in for example an atom. However, experimentally it would be very challenging to control this single spin, since the length scale on which this control would have to take place is prohibitively small. On the other side of the spectrum, solid state implementations of qubits such as Ref. [13] require fields on the scale of several tens to hundreds of nanometers only, making control of the state easier (though still very hard). However, with the increased size we pay the price of additional sources of decoherence, and a huge effort has been made in recent years to combat these sources. For molecular magnets, the requirements on the spatial scale on which control has to be possible are loosened with respect to those for a single spin, because the typical size of such systems is relatively large. However, molecular magnets are still small as compared to other solid states implementations of qubits. This fact, as well as the possibility of chemically engineering molecular magnets with a wide variety of properties, may make one hopeful that sources of decoherence in molecular magnets can be suppressed. Indeed, we will show later that such suppression is possible by choosing the degree of freedom that encodes the qubit wisely.

On the other hand, since molecular magnets have a complex chemical structure containing many interacting magnetic atoms, it is not a priori clear that it will be possible to identify a well-separated, stable, and easily controllable two-level subspace in the spectrum. As we will show next, the fact that this does in fact turn out to be possible is due to the high symmetry of the molecule and the existence of well-separated energy scales. We have seen in previous chapters that molecular magnets can—to a very good approximation—be described by a collection of coupled spins. The low-energy multiplet of the system is then described by a spin-multiplet with fixed total spin, separated from excited states on an energy scale set by the exchange interaction. This low-energy multiplet has either maximal total spin for ferromagnetically coupled individual spins, or minimal total spin for antiferromagnetically coupled spins. In the latter case, the details of the ground state are then determined by the symmetry of the molecule, and frustration can play an important role.

The first requirement which has to be fulfilled by any qubit-candidate is that the physical system has to show genuine quantum behavior. Quantum behavior of the spin state in molecular magnets has been shown in experiments on quantum tunneling of magnetization [33–40], and shows up in hysteresis curves of ferromagnetic (although similar effects are predicted to occur in antiferromagnetic systems [41, 42]) molecular magnets with large spin and high anisotropy barrier [36, 37, 43–45]. In the absence of external fields, the barrier due to the anisotropy lifts the de-

generacy between states with different magnetization, and leads to the existence of long-lived spin states. Transitions between different spin states can be driven in a coherent manner, and manifest themselves as stepwise changes in the magnetization. The fact that the transitions show interference between transition paths and Berry phase effects are a signature of their coherent nature [46–52].

Quantum computing in antiferromagnetically coupled spin clusters was studied in Ref. [29]. In the simplest cases of a spin chain or a bipartite lattice with an odd number of spins the degenerate ground state is a spin doublet with effective total spin $1/2$. The total spin can be controlled by an applied magnetic field just as a single spin can, and exchange interaction between two clusters can be introduced by coupling single spins in the two different clusters. A downside of using a collection of spins is that generally decoherence increases with number of spins, unless one manages to encode the qubit in a state which is protected due to symmetry, something we will come back to later. In Ref. [30], Cr-based AFM molecular rings, and specifically Cr_7Ni , were proposed as suitable qubit candidates.

An interesting way of encoding a qubit is offered by geometrically frustrated molecules [32, 53]. Exemplary molecules that display geometric frustration are antiferromagnetic spin rings with an odd number of spins. The simplest example of such a system is given by an equilateral triangular molecule with a spin- $1/2$ particle at each vertex, such as is for instance realized to a good approximation in Cu_3 (we will use Cu_3 as an abbreviation for the molecule $\text{Na}_9[\text{Cu}_3\text{Na}_3(\text{H}_2\text{O})_9(\alpha\text{-AsW}_9\text{O}_{33})_2] \cdot 26\text{H}_2\text{O}$) (see Ref. [54]). Spin rings (of which the spin triangle is the simplest non-trivial example) in general are described by the Heisenberg Hamiltonian with Dzyaloshinskii-Moriya interaction

$$H_0 = \sum_{i=1}^N J_{i,i+1} \mathbf{S}_i \cdot \mathbf{S}_{i+1} + \mathbf{D}_{i,i+1} \cdot (\mathbf{S}_i \times \mathbf{S}_{i+1}). \quad (11.1)$$

Here, N is the number of spins in the ring, and $\mathbf{S}_{N+1} = \mathbf{S}_1$. For the triangular molecular magnet $N = 3$. Furthermore, the fact that the point group symmetry of the triangular molecule is D_{3h} imposes the constraints $J_{i,i+1} = J$ and $\mathbf{D}_{i,i+1} = D\hat{\mathbf{z}}$ on the parameters of the Hamiltonian of an planar molecule. Since we are considering antiferromagnetic systems, J is positive. In a Cu_3 molecule, $|J|/k_B \sim 5$ K and $|D|/k_B \sim 0.5$ K. Due to this separation of energy scales, and in the absence of strong magnetic- or electric fields, the Hilbert space containing the 8 eigenstates of the triangular molecule can be split up in a high-energy quadruplet with total spin $\mathbf{S} = 3/2$ and a low-energy quadruplet with total spin $\mathbf{S} = 1/2$. The splitting between the two subspaces is $3J/2$.

In the absence of Dzyaloshinskii-Moriya interaction the low-energy subspace is fourfold degenerate. The eigenstates are given by

$$|1/2, \pm 1\rangle = \frac{1}{\sqrt{3}} \sum_{j=0}^2 e^{\pm i2\pi j/3} C_3^j |\uparrow\downarrow\downarrow\rangle, \quad (11.2)$$

and $|-1/2, \pm 1\rangle$. The latter states are also given by (11.2) but with all the spins flipped. These states are thusly labeled as $|m_S, m_C\rangle$, with m_S the quantum number

belonging to the z projection of the total spin of the triangle, and m_C the z projection of the chirality of the molecular magnet. The chirality operator \mathbf{C} has components

$$\begin{aligned} C_x &= -\frac{2}{3}[\mathbf{S}_1 \cdot \mathbf{S}_2 - 2\mathbf{S}_2 \cdot \mathbf{S}_3 + \mathbf{S}_3 \cdot \mathbf{S}_1], \\ C_y &= \frac{2}{\sqrt{3}}[\mathbf{S}_1 \cdot \mathbf{S}_2 - \mathbf{S}_3 \cdot \mathbf{S}_1], \\ C_z &= \frac{4}{\sqrt{3}}\mathbf{S}_1 \cdot [\mathbf{S}_2 \times \mathbf{S}_3]. \end{aligned} \quad (11.3)$$

The chirality contains information about the relative orientation of the spins that make up the molecule. Like the components of the total spin operator, the components of the chirality operator obey angular momentum commutation relations. It is straightforward to show that the total spin and chirality commute. We will show later that states with opposite chirality are split by an energy gap which is determined by the magnitude of the Dzyaloshinskii-Moriya interaction. Furthermore, we can separate states with opposite total spin by applying a magnetic field. This allows us to choose which doublet makes up the ground state, chirality or total spin. In this way it is possible to either encode the qubit in the total spin of the molecule or in the chirality. Furthermore, even though the commutation relations of the chirality components are the same as those of the spin components, the transformation properties of spin and chirality under rotations, reflections, and time-reversal do differ. Therefore, interactions of chirality with external fields can not be inferred from the analogy with spins. We will discuss later how using the chirality offers certain benefits with regards to the possibility to control the qubit and with regards to increasing the decoherence time of the qubit.

11.3 Single-Qubit Rotations and the Spin-Electric Effect

If one chooses to encode a qubit in a spin state -be it the spin of an electron in a quantum dot, or the total spin of a molecular magnet- the most intuitive way to implement a one-qubit gate is by utilizing the Zeeman coupling $\mu_B \mathbf{B} \cdot \bar{g} \cdot \mathbf{S}$, where \bar{g} is the g -tensor. This coupling in principle allows one to perform rotations around an arbitrary axis by applying ESR (electron spin resonance) pulses. Indeed, it has been shown to be possible to implement single spin rotations on a sub-microsecond time scale using ESR techniques in quantum dots [55]. Furthermore, Rabi-oscillations of the magnetic cluster V_{15} have been shown to be possible, also on a sub-microsecond time scale [56]. At the moment, however, it appears experimentally very challenging to increase the temporal- and spatial resolution with which one can control magnetic fields to the point that is required for quantum computation in molecular magnets (i.e. nanosecond time scale and nanometer length scale).

For this reason, a large effort has been made to find alternative ways to control the spin state of molecular magnets. One natural candidate to replace magnetic manipulation is electric control. Strong, local electric fields can be created near a STM

tip, and these fields can be rapidly turned on and off by applying an electric voltage to electrodes that are placed close to the molecules that are to be controlled.

Electric manipulation requires a mechanism that gives a sizable spin-electric coupling. In quantum dots, the mechanism behind this coupling is the relativistic spin-orbit interaction (SOI), and experiments that show that it is possible to perform single spin rotations by means of electric dipole spin resonance (EDSR) have been proposed [57] and performed [58]. Unfortunately, the fact that this effect scale with the system size L as L^3 makes them unsuitable for molecular magnets, which are much smaller.

Instead, in Ref. [32], Trif et al. proposed a mechanism that leads to spin-electric coupling in triangular magnetic molecules with spin-orbit interaction and broken inversion symmetry. The mechanism relies on the fact that in such systems an electric field can alter the exchange interaction between a pair of spins within a molecule due to the field's coupling to the dipole moment of the connecting bond.

The lowest order coupling between electric field and the spin state of the triangular molecule is given by the electric-dipole coupling, through the Hamiltonian $H_{e-d} = -e \sum_i \mathbf{E} \cdot \mathbf{r}_i \equiv -e \mathbf{E} \cdot \mathbf{R}$. Here, e is the electron charge and \mathbf{r}_i is the position of the i -th electron. The total dipole moment of the molecule is given by $-e \sum_i \mathbf{r}_i = -e \mathbf{R}$. Because of the D_{3h} symmetry of the molecule, the diagonal elements of total dipole moment operator must vanish in the proper symmetry-adapted basis. However, the electric-dipole coupling can mix states with different chirality. The nonzero matrix elements are the ones that are invariant under the symmetry-transformations of the triangular magnet. Since the $|m_S, \pm 1\rangle$ states and the operators $\pm X + iY$ both transform as the irreducible representation E' of the group D_{3h} , it follows that the only nonzero components in the low-energy subspace of the triangular molecules are

$$\langle m_S, \pm 1 | -eX | m'_S, \mp 1 \rangle = i \langle m_S, \pm 1 | -eY | m'_S, \mp 1 \rangle \equiv d \delta_{m_S, m'_S}. \quad (11.4)$$

Coupling to the $S = 3/2$ subspace is suppressed by the finite gap between the two subspaces. By its very nature, this symmetry analysis cannot yield any information on the magnitude of the effective electric dipole parameter d . This information will have to be extracted using other methods, such as ab initio modeling, Hubbard modeling, or experiments, something we will come back to later. We do note that a finite amount of asymmetry of the wave functions centered around each vertex of the triangle is required for the matrix elements in (11.4) to be nonzero. This asymmetry is caused by the small amount of delocalization of the electron states due to the exchange interaction with the states on the other vertices and creates the finite dipole moment of individual bonds. The dipole moment of the bonds, furthermore, must depend on the relative orientation of the two spins which are connected by that bond (i.e. whether they are parallel or anti-parallel) in order for the matrix elements in (11.4) to be nonzero.

Since the electric-dipole coupling connects states with different chirality, we can rewrite it in terms of the vector $\mathbf{C}_{\parallel} = (C_x, C_y, 0)$ as $H_{e-d}^{\text{eff}} = d \mathbf{E}' \cdot \mathbf{C}_{\parallel}$. The vector \mathbf{E}' is given by $\mathbf{E}' = \mathcal{R}(7\pi/6 - 2\theta) \mathbf{E}$, where $\mathcal{R}(\phi)$ describes a rotation by an angle ϕ

around the z axis, and θ is the angle between $\mathbf{r}_1 - \mathbf{r}_2$ and $\mathbf{E}_{\parallel} = (E_x, E_y, 0)$. With the definition of the chirality operator as given in (11.4), we can rephrase the effective electric-dipole Hamiltonian in terms of exchange coupling between the individual spins

$$H_{\text{e-d}}^{\text{eff}} = \frac{4dE}{3} \sum_{i=1}^3 \sin \left[\frac{2\pi}{3}(1-i) + \theta \right] \mathbf{S}_i \cdot \mathbf{S}_{i+1}, \quad (11.5)$$

where E is the magnitude of the in plane components of the electric field. Since the change in the exchange interaction $J_{i,i+1}$ is proportional to $|\mathbf{E}_{\parallel} \times (\mathbf{r}_{i+1} - \mathbf{r}_i)|$, only the component of the electric field that is perpendicular to the bond $\mathbf{r}_{i+1} - \mathbf{r}_i$ affects the exchange interaction $J_{i,i+1}$. This is consistent with the picture that the finite dipole moment of the bond between two vertices is caused by the deformation of the wave function due to exchange interaction. Otherwise, the strength of the coupling is completely determined by the parameter d . The fact that the change in $J_{i,i+1}$ is not uniform is crucial here, since therefore $[H_0, H_{\text{e-d}}^{\text{eff}}] \neq 0$ even in the absence of DM interaction, which allows the electric-dipole interaction to induce transitions between states with different chirality.

We have seen then that the electric-dipole coupling allows one to perform rotations of the chirality state about the x - and y axis, but not around the z axis (assuming a diagonal g -tensor). This is sufficient to perform arbitrary rotations in chirality space. However, so far the total spin does not couple to the electric field. This situation is remedied when we include spin-orbit interaction.

As with the electric-dipole coupling, one can deduct the form of the spin-orbit interaction from general symmetry considerations. Given the D_{3h} symmetry of the molecule, the most general form of the spin-orbit interaction is

$$H_{\text{SO}} = \lambda_{\text{SO}}^{\parallel} T_{A_2} S_z + \lambda_{\text{SO}}^{\parallel} (T_{E_+''} S_- + T_{E_-''} S_+). \quad (11.6)$$

Here, T_{Γ} denotes a tensor which acts on the orbital space and transforms according to the irreducible representation Γ . The nonzero elements in the low-energy subspace are then given by $\langle m_S, \pm 1 | H_{\text{SO}} | m'_S, \pm 1 \rangle = m_S \lambda_{\text{SO}}^{\perp} \delta_{m_S, m'_S}$, which leads to the spin-orbit Hamiltonian $H_{\text{SO}} = \Delta_{\text{SO}} C_z S_z$, where $\Delta_{\text{SO}} = \lambda_{\text{SO}}^{\parallel}$. Alternatively, one can use the fact that the spin-orbit interaction can be described by the Dzyaloshinskii-Moriya term in (11.1). Because of the symmetry of the molecule, the only nonzero component of the DM vector $\mathbf{D}_{i,i+1}$ is the out-of-plane component, so that it takes the form $\mathbf{D}_{i,i+1} = (0, 0, D_z)$. This gives the same form for H_{SO} as the previous considerations, provided one identifies $\lambda_{\text{SO}}^{\parallel} = D_z$.

Combining the results from this section, it follows that the Hamiltonian describing a triangular magnet in the presence of a magnetic- and electric field can be written in terms of the chirality and total spin of the molecule as

$$H = \Delta_{\text{SO}} C_z S_z + \mu_B \mathbf{B} \cdot \bar{\mathbf{g}} \cdot \mathbf{S} + d\mathbf{E} \cdot \mathbf{C}_{\parallel}. \quad (11.7)$$

Hence, for a magnetic field in the z direction, the eigenstates are $|\pm 1/2, \pm 1\rangle$, and an electric field causes rotations of the chirality state, but does not couple states

with opposite total spin. When \mathbf{B} is not parallel to $\hat{\mathbf{z}}$, S_z is no longer a good quantum number, and hence an applied electric field can cause rotations in the total spin subspace through the electric-dipole and spin-orbit coupling. In this way it becomes possible to perform arbitrary rotations of the total spin state.

In Ref. [53], the authors were able to identify the parameters of the effective spin Hamiltonian with the parameters of the underlying Hubbard model. On the one hand, this has opened up the possibility to determine the parameters of the effective spin Hamiltonian by means of ab initio calculations [59, 60]. On the other hand, the description of the spin-electric effect in the language of the Hubbard model is useful because it gives an intuitive interpretation of the phenomena that we discussed so far. The Hubbard model description of a molecular magnet including spin-orbit interaction is given by

$$H_H = \sum_{i,j} \sum_{\alpha,\beta} \left[c_{i\alpha}^\dagger \left(t\delta_{\alpha\beta} + \frac{i\mathbf{P}_{ij}}{2} \cdot \sigma_{\alpha\beta} \right) c_{j\beta} + \text{H.c.} \right] + \sum_j U_j (n_{j\uparrow}, n_{j\downarrow}). \quad (11.8)$$

Here, $c_{i\alpha}^\dagger$ creates an electron with spin α whose wave function $|\phi_{i\sigma}\rangle$ is given by a Wannier function located around atom i . Furthermore, t describes spin-independent hopping. The vector \mathbf{P}_{ij} describes spin-dependent hopping due to spin-orbit interaction and hence is proportional to the matrix element $\nabla V \times \mathbf{p}$ between Wannier states centered around atom i and j . The vector σ contains the Pauli matrices. Lastly, U describes the on-site repulsion. Typically, one considers a single-orbital model, and assumes that U is the largest energy scale. A perturbative expansion of (11.8) in $(|t|, |\mathbf{P}_{ij}|)/U$ allows one then to map the Hubbard model on a Heisenberg Hamiltonian with DM interaction [61, 62].

Equation (11.8) describes two scenarios. First, if the index i runs over the three magnetic atoms of the triangle only, it describes coupling between the magnetic atoms through direct exchange. Alternatively, (11.8) can describe the situation in which the coupling between two magnetic atoms is mediated by a non-magnetic bridge by adding a doubly-occupied non-magnetic atom on every line connecting two vertices. The former choice allows for a simpler description, whereas the latter choice is anticipated to be the more realistic one for molecular magnets. We will shortly discuss how either can be used to obtain more insight into the spin-electric effect.

The first thing one can show is that in the case of direct-exchange interaction the basis functions of the Hubbard model to first order in t and $\lambda_{\text{SO}} \equiv \mathbf{P}_{ij} \cdot \mathbf{e}_z$ (due to symmetry $\mathbf{P}_{ij} = \lambda_{\text{SO}} \mathbf{e}_z$) are

$$|\Phi_{A'_2}^{1\sigma}\rangle = |\psi_{A'_2}^{1\sigma}\rangle \quad (11.9)$$

$$\begin{aligned} |\Phi_{E'_\pm}^{1\sigma}\rangle &= |\psi_{E'_\pm}^{1\sigma}\rangle + \frac{(e^{-2\pi i/3} - 1)(t \pm \sigma \lambda_{\text{SO}})}{\sqrt{2}U} |\psi_{E'_\pm}^{2\sigma}\rangle \\ &\quad + \frac{3e^{2\pi i/3}(t \pm \sigma \lambda_{\text{SO}})}{\sqrt{2}U} |\psi_{E'_\pm}^{2\sigma}\rangle, \end{aligned} \quad (11.10)$$

where $|\psi_\Gamma^{n\sigma}\rangle$ denotes the symmetry-adapted eigenstate of the Hubbard model with three electrons, total spin σ , and either single- ($n = 1$) or double ($n = 2$) occupancy that transforms according to the irreducible representation Γ . Specifically, the spin part of $|\psi_{E'_\pm}^{1\sigma}\rangle$ is given by the states $|\sigma, \pm 1\rangle$ in (11.2). It follows that in the limit of $t, \lambda_{\text{SO}} \ll U$ (the limit in which the spin model gives an accurate description) the eigenstates of the Hubbard model are indeed the chirality states. At finite t, λ_{SO} , the eigenstates contain small contributions from doubly-occupied states.

Within the direct-exchange model, the electric field couples to the state of the molecule via two different mechanisms. The first term that has to be added to the Hubbard Hamiltonian comes from the fact that the electric potential takes different values at the positions of the magnetic centers in a molecule, which affects the on-site energy of the electrons as

$$H_{\text{e-d}}^0 = -e \sum_{\sigma} \frac{E_y a}{\sqrt{3}} c_{1\sigma}^\dagger c_{1\sigma} - \frac{a}{2} \left(\frac{E_y}{\sqrt{3}} + E_x \right) c_{2\sigma}^\dagger c_{2\sigma} + \frac{a}{2} \left(\frac{E_x}{\sqrt{3}} - E_y \right) c_{3\sigma}^\dagger c_{3\sigma}. \quad (11.11)$$

Here, a is the distance between two magnetic atoms. The second contribution is given by

$$H_{\text{e-d}}^1 = \sum_{i,\sigma} t_{ii+1}^{\mathbf{E}} c_{i\sigma}^\dagger c_{i+1\sigma} + \text{H.c.}, \quad (11.12)$$

which describes the modification of the hopping strength due to the electric field. The electric field-dependent hopping is given by $t_{ii+1}^{\mathbf{E}} = -\langle \phi_{i\sigma} | e\mathbf{r} \cdot \mathbf{E} | \phi_{i+1\sigma} \rangle$, and is hence related to the matrix elements of the electric dipole moment which mix the different Wannier functions. As before, a symmetry analysis tells us that the only nonzero matrix elements within the total spin-1/2 subspace are those proportional to

$$\langle \phi_{E'_+}^{\sigma} | ex | \phi_{E'_-}^{\sigma} \rangle = -i \langle \phi_{E'_+}^{\sigma} | ey | \phi_{E'_-}^{\sigma} \rangle \equiv d_{EE}. \quad (11.13)$$

Here, $|\phi_\Gamma^\sigma\rangle$ describes the linear combination of Wannier states with total spin σ which transforms according to the irreducible representation Γ . One can then calculate the matrix elements of both the electric-dipole coupling as well as the spin-orbit Hamiltonian perturbatively in $(t, eaE, d_{EE}E)/U$. Furthermore, since the electrons are localized, the off-diagonal elements of the dipole moment, d_{EE} , satisfy $d_{EE} \ll ea$. To lowest order the results are

$$|\langle \Phi_{E'_-}^{1\sigma} | H_{\text{e-d}}^0 | \Phi_{E'_+}^{1\sigma} \rangle| \propto \left| \frac{t^3}{U^3} eEa \right|, \quad (11.14)$$

$$|\langle \Phi_{E'_-}^{1\sigma} | H_{\text{e-d}}^1 | \Phi_{E'_+}^{1\sigma} \rangle| \approx \left| \frac{4t}{U} Ed_{EE} \right|, \quad (11.15)$$

$$|\langle \Phi_{E'_-}^{1\sigma} | H_{\text{SO}} | \Phi_{E'_+}^{1\sigma} \rangle| = \pm \frac{5\sqrt{3}\lambda_{\text{SO}}t}{2U} \text{sgn}(\sigma). \quad (11.16)$$

These first two matrix elements can be identified with the matrix elements in (11.7) that mix the states with different chirality, and hence determine the parameter d . The last matrix element determines D_z . Therefore, all parameters of the effective spin model in (11.7) can be determined from the underlying microscopic model. In Ref. [60], Nossa et al. utilized the presented analysis to determine the value of D_z and J in the molecular magnet Cu_3 using spin-density functional theory.

It is known that in molecular magnets the direct exchange mechanism is often suppressed due to the localized nature of the electrons that determine the magnetic properties (which are typically of a d -wave nature) combined with the fact that the magnetic atoms are typically separated by non-magnetic bridge atoms. In Cu_3 , for instance, exchange interaction between two Cu atoms follows a superexchange path along a Cu-O-W-O-W-O-Cu bond, which makes the Cu atoms third nearest neighbors [54]. A more accurate description on a microscopic basis of the spin-electric effect in a triangular magnet is therefore given by a model which includes a doubly-occupied non-magnetic atom on every line connecting two vertices, so that the mechanism behind the exchange interaction is superexchange. This is further strengthened by the expectation that the orbitals of the magnetic atoms do not deform easily in an electric field, whereas the bridge orbitals are expected to change their shape more easily.

In Ref. [53], the authors analyzed the behavior of a single Cu-Cu bond, including the non-magnetic bridge atom that connects the two Cu atoms, under the application of an electric field. By performing a fourth-order Schrieffer-Wolf transformation [63] on the Hamiltonian (11.8) for such a bond (using $(|t|, |\mathbf{P}_{ij}|)/U$ as small parameter) one can map the Hubbard model on the spin model

$$H_{12} = J\mathbf{S}_1 \cdot \mathbf{S}_2 + \mathbf{D} \cdot (\mathbf{S}_1 \times \mathbf{S}_2) + \mathbf{S}_1 \cdot \mathbf{\Gamma} \cdot \mathbf{S}_2. \quad (11.17)$$

Here, $\mathbf{\Gamma}$ is a traceless- and symmetric matrix. Equation (11.17) describes the most general quadratic spin Hamiltonian possible. The parameters $J, \mathbf{D}, \mathbf{\Gamma}$ can be determined from the parameters of the Hubbard model. Assuming that the bond angle between the Cu atom and the bridge atom is finite, the largest possible symmetry of a single bond with bridge atom is C_{2v} . This determines which spin parameters can be nonzero. If the electric field breaks the C_{2v} symmetry, extra terms can be generated. However, from the C_{2v} symmetry it follows that the strongest spin-electric coupling will be in the plane spanned by the Cu atoms and the bridge atom, and perpendicular to the Cu-Cu bond. This is due to the fact that this is the only direction in which the bond can have a finite dipole moment in the absence of an electric field (due to the molecular field), which gives rise to linear electric-dipole coupling. Indeed, it is this coupling that causes the effective Hamiltonian in (11.5), with effective electric-dipole moment given by

$$d = \frac{4}{U^3} [(48t^3 - 20tp_z^2)\kappa_t + (-20t^2p_z + 3p_z^3)\kappa_{p_z}]. \quad (11.18)$$

Here, t is the hopping parameter, p_z is the z component of the spin-orbit hopping, and $\kappa_t = \delta t/E$ and $\kappa_{p_z} = \delta p_z/E$ relate the changes in t and p_z to the electric field E .

Using ab initio methods, the authors in Ref. [59] calculated the effective electric-dipole moment d in Cu_3 . They found the value $d = 3.38 \times 10^{-33}$ C m. This corresponds to $d \approx 10^{-4}ea$, where a is the length of the Cu-Cu bond, and leads to Rabi oscillation times $\tau \approx 1$ ns for electric field $E \approx 10^8$ Vm^{-1} .

So far, we have only discussed single-qubit rotations. However, for a complete set of quantum gates, we also need a two-qubit gate. In the next section, we will discuss different proposals that have been made on how to implement such a two-qubit gate.

11.4 Two-Qubit Gates

Suppose we chose to encode our qubit states in the spin degrees of freedom of a system. Two-qubit gates such as the CNOT- or the $\sqrt{\text{SWAP}}$ -gate can then be implemented by turning on the Heisenberg exchange interaction between two spins for a certain time [64]. For spins in quantum dots, this is relatively simply done by applying appropriate voltage pulses to the gate that controls the tunneling between two quantum dots. In contrast, in molecular magnets the exchange interaction between two molecules is typically determined by the chemistry of the molecule, and one has to search for more sophisticated ways to implement two-qubit gates.

The first method to couple the state of two qubits that we will discuss is based on coupling of two triangular molecular magnets through a quantum mechanical electric field in a cavity or stripline [32]. Such electric fields offer long-range and switchable coherent interaction between two qubits. The electric field of a photon with frequency ω in a cavity of volume V is given by $\mathbf{E}_0(b_\omega^\dagger + b_\omega)$, where b_ω^\dagger creates a photon with frequency ω and the amplitude of the field is $|\mathbf{E}_0| \propto \sqrt{\hbar\omega/V}$. The coupling of such a photon to the in plane component of the chirality \mathbf{C}_\parallel of a triangular molecule is then given by $\delta H_E = d\mathbf{E}'_0 \cdot \mathbf{C}_\parallel(b_\omega^\dagger + b_\omega)$. In the rotating wave approximation, the Hamiltonian that describes the low-energy subspace of N triangular molecular magnets which interact with the photon field is given by $H_{\text{s-ph}} = \sum_j H^{(j)} + \hbar\omega b_\omega^\dagger b_\omega$, with

$$H^{(j)} = \Delta_{\text{SO}} C_z^{(j)} S_z^{(j)} + \mathbf{B} \cdot \bar{\mathbf{g}} \cdot \mathbf{S}^{(j)} + d|\mathbf{E}_0| [e^{i\phi_j} b_\omega^\dagger C_-^{(j)} + \text{H.c.}]. \quad (11.19)$$

Here, $\phi_j = 7\pi/6 + \theta_j$. Application of a magnetic field \mathbf{B} with an in plane component allows one to couple both the chirality as well as the total spin degrees of freedom of spatially separated molecules. This coupling can be turned on and off by bringing the molecules in resonance with the photon mode, by applying an additional local electric field. One difficulty in using cavities is that the electric fields are weaker than those at an STM tip. A typical value is $|\mathbf{E}_0| \approx 10^3$ V m^{-1} , which leads to Rabi times $\tau \approx 0.01$ – 100 μs .

For the discussion of another proposed implementation of an electrically controlled two-qubit gate (in this case the $\sqrt{\text{SWAP}}$ -gate), we turn our attention to the polyoxometalate $[\text{PMo}_{12}\text{O}_{40}(\text{VO})_2]^{q-}$. This molecule consists of a central mixed-valence core based on the $[\text{PMo}_{12}\text{O}_{40}]$ Keggin unit, capped by two vanadyl groups

containing one localized spin each [31]. In such a molecule, one can encode a two-qubit state in the spins of the vanadyl groups. The spins of the two vanadyl groups are weakly exchange coupled via indirect exchange interaction mediated by the core. The crucial property of the core is that one can tune the number of electrons it contains, since the exchange interaction between the vanadyl spins depends on the number of electrons on the core. Namely, if the core contains an odd number of electrons, the spin of the unpaired electron on the core couples to those of the vanadyl groups, and the effective interaction between the two qubits is relatively strong. In contrast, for an even number of spins on the core, the spins on the core pair up to yield a ground state with total spin 0. In this case, the exchange interaction between the pair of vanadyl spins is strongly reduced as compared to the situation with an odd number of electrons on the core. Since the redox flexibility of such polyoxometalates is typically rather high, the number of electrons n_C on the core can be tuned by electric means, by bringing the molecule near the tip of an STM. The system is then described by the Hamiltonian

$$H = -J(n_C)\mathbf{S}_L \cdot \mathbf{S}_R - J_C(\mathbf{S}_L + \mathbf{S}_R) \cdot \mathbf{S}_C + (\epsilon_0 - eV)n_C + Un_C(n_C - 1)/2. \quad (11.20)$$

Here, $\mathbf{S}_{L/R}$ are the spin operators of the two vanadyl groups, and \mathbf{S}_C is the spin of the core. $J(n_C)$ denotes the exchange interaction between the two vanadyl spins. Given the previous discussion, $J(0) \approx 0$. The orbital energy of the electron on the core is given by ϵ_0 , and V is the electric potential at the core. Lastly, U is the charging energy of the molecule, which defines the largest energy scale in the problem. We consider the subspace of only $n_C = 0$ or $n_C = 1$ electrons on the core.

The two-qubit $\sqrt{\text{SWAP}}$ is now implemented as follows: One starts out with an electric potential such that the stable configuration has $n_C = 0$ electrons on the core. That way, the two qubits are decoupled. By applying a voltage pulse V_g to the STM tip, one can switch to the state with $n_C = 1$ electrons. The Hamiltonian that describes the spin-state of the molecule is then given by [31]

$$H_1 = -[J(1) - J_C]\mathbf{S}_L \cdot \mathbf{S}_R - \frac{J_C}{2}\mathbf{S}^2. \quad (11.21)$$

Here, $\mathbf{S} = \mathbf{S}_L + \mathbf{S}_R + \mathbf{S}_C$ is the total spin of the molecule. The time-evolution of the system is determined by (11.21) for the duration τ_g of the pulse, afterwards the two vanadyl spins will be decoupled again. The first part of this Hamiltonian contains the wanted exchange coupling, and one can implement different two-qubit gates depending on the pulse length τ_g . For the $\sqrt{\text{SWAP}}$ -gate, this time is given by the condition

$$[J(1) - J_C]\frac{\tau_g}{\hbar} = \frac{\pi}{2} + 2\pi n, \quad (11.22)$$

where n is an integer. The second term in (11.21) depends on the spin-state of the core, and is unwanted. However, we can get rid of it by choosing the pulse-length

such that the unitary evolution associated with the second term is equal to the unit operator. This condition turns out to be satisfied for times

$$\tau_g = \frac{4\pi}{3} \frac{\hbar}{|J_C|} m, \quad (11.23)$$

where m is an integer. Together, these last two equations give a requirement on $J(1)$ and J_C , namely

$$\frac{J(1)}{|J_C|} = \text{sgn}(J_C) + \frac{3}{8} \frac{1-4n}{m}. \quad (11.24)$$

So far, we have assumed that switching between states with $n_C = 0$ and $n_C = 1$ can be perfectly controlled and is instantaneous. In reality, however, this transition is governed by quantum processes, and is a probabilistic process governed by the tunneling rate Γ between STM tip and molecule. Therefore, τ_g is inherently a stochastic quantity. To analyze these quantum effects, the authors in Ref. [31] numerically calculated the averaged fidelity $\mathcal{F} = \sqrt{\rho_{\text{real}} \rho_{\text{ideal}}}$ between the idealized $\sqrt{\text{SWAP}}$ -gate with instantaneous switching and the real $\sqrt{\text{SWAP}}$ -gate with the stochastic tunneling ($\rho_{\text{real}}/\rho_{\text{ideal}}$ denote the obvious density matrices at the end of the $\sqrt{\text{SWAP}}$ -gate operation here). They found that the fidelity can be as high as $\mathcal{F} = 0.99$.

11.5 Decoherence in Molecular Magnets

Up to this point, we have assumed that the evolution of the quantum state of any qubit is unitary, and hence the information content of the qubit is infinitely long-lived. This assumption is only valid for a perfectly isolated system. In reality, however, any qubit will be coupled to its environment. Fluctuations in the environment can then lead to decoherence: The process whereby information about a quantum state is lost due to interaction with an environment. Decoherence of a single qubit typically takes place on two different time scales. The longitudinal decoherence time, or T_1 -time, describes the average time it takes the environment to induce random transitions from $|0\rangle$ to $|1\rangle$, and vice versa. The transverse decoherence time, the T_2 -time, describes the time it takes a systems to lose its information about the coherence between the $|0\rangle$ and $|1\rangle$ state. In other words, the T_2 -time is the time it takes for a system initially in the pure quantum state described by the density matrix $\hat{\rho}_0 = |\psi_0\rangle\langle\psi_0|$, where $|\psi_0\rangle = \alpha|0\rangle + \beta|1\rangle$, to transform into the classical state $\hat{\rho}(t) = |\alpha|^2|0\rangle\langle 0| + |\beta|^2|1\rangle\langle 1|$. In this sense, decoherence is the cause of the transition from the quantum- into the classical regime. The T_1 -time sets an upper limit on the time a system can be used as a classical bit, whereas a system can only be used as a qubit for times $T \ll T_1, T_2$. The T_1 - and T_2 -time of a system are not unrelated, and can indeed become of comparable magnitude in certain systems. For molecular magnets at low temperatures, however, typically $T_2 \ll T_1$.

The first measurement of the T_2 -time of a system consisting of molecular magnets was performed by Ardavan et al. in 2007 (Ref. [65]). The measurements were performed on Cr_7M heterometallic wheels (M denotes Ni or Mn), and the authors found T_2 -times of $3.8 \mu\text{s}$ for perdeuterated diluted Cr_7Ni solutions. The typical way to measure relaxation times is to use standard spin-echo techniques [66]. The T_2 -time can be obtained from the decay with τ of a 2-pulse Hahn-echo measurement, consisting of the sequence: $\pi/2 - \tau - \pi - \tau - \text{echo}$. In a similar manner, the T_1 -time can be determined using the sequence $\pi - T - \pi/2 - \tau - \pi - \tau - \text{echo}$. Here, T is varied, and τ is constant and short. One of the difficulties in measuring the T_2 -times in magnetic clusters is the fact that, in a crystal, the different molecules are coupled by dipole-dipole interactions. This limits the T_2 -time. The natural approach to avoid this problem is to consider molecules in solution. However, here the problem is that many magnetic clusters with high spin display strong axial anisotropy, with relatively large zero-field splitting. In a solution, these clusters will orient in a random matter. This problem is circumvented by using Cr_7Ni -clusters, which have a $S = 1/2$ ground state (and hence no zero-field splitting), and small anisotropy of the g -factor.

It was found that the main mechanism limiting the T_2 -time of the Cr_7Ni -clusters was coupling to protons. To increase the decoherence time, the authors therefore considered the perdeuterated analogue compound. Indeed, according to expectations (^2D has a gyromagnetic ratio which is about $1/6$ of that of ^1H), this increased the coherence time roughly by a factor of 6, leading to a T_2 -time of $3.8 \mu\text{s}$ at 1.8 K.

Our remaining discussion of decoherence in molecular magnets follows that of Ref. [67]. In spin systems, the two most common sources of decoherence are fluctuations in the electric environment (which couple to the spin state via spin-orbit interaction) and fluctuations of the spin state of the N nuclear spins \mathbf{I}_p in the host material of the qubit, which are coupled to the system spins \mathbf{S}_i due to hyperfine interaction. We will mainly focus on the latter mechanism, since it typically limits the decoherence time [56, 65]. The hyperfine interaction between nuclear spins and system spins is due to dipole-dipole interaction as well as contact interaction

$$H_{\text{HF}} = D_{\text{HF}} \sum_i \sum_p \frac{\mathbf{S}_i \cdot \mathbf{I}_p - 3(\mathbf{S}_i \cdot \hat{\mathbf{r}}_{ip})(\mathbf{I}_p \cdot \hat{\mathbf{r}}_{ip})}{r_{ip}^3} + \sum_i a_i \mathbf{S}_i \cdot \mathbf{I}_{q(i)}. \quad (11.25)$$

Here, $D_{\text{HF}} = (\mu_0/4\pi)g_I\mu_I g_S\mu_S$, and $\mathbf{r}_{ip} = \mathbf{r}_i - \mathbf{r}_p$. The contact interaction strength a_i is due to the finite overlap of the wave functions of the system spin and nuclear spins located at the same magnetic center. For small clusters, the latter term only leads to oscillations of the coherence, and hence we can neglect it [67]. To see how the hyperfine interaction leads to decoherence, let us consider a system in which the state of the qubit and that of the bath are initially uncorrelated. Furthermore, let the initial state of the qubit be given by $|\psi(0)\rangle = \frac{1}{\sqrt{2}}(|0\rangle + |1\rangle)$, and let the bath be prepared in the (mixed or pure) state described by the density operator $\hat{\rho}_n(0) = \sum_{\mathcal{I}} p_{\mathcal{I}} |\mathcal{I}\rangle \langle \mathcal{I}|$. Here, $|\mathcal{I}\rangle = |m_1^{\mathcal{I}}, \dots, m_N^{\mathcal{I}}\rangle$ with $m_i^{\mathcal{I}}$ the projection of the nuclear spin operator \mathbf{I}_i along the magnetic field. Two examples of possible

states the bath may be prepared in are the spin-polarized (pure) state with polarization P , and the equal superposition (mixed) state. In the first case, $p_{\mathcal{I}} = \delta_{\mathcal{I},n}$, where $|n\rangle$ is the state such that $\sum_p I_p^z |n\rangle = \frac{P}{2} |n\rangle$. In the latter case, $p_{\mathcal{I}} = 1/2^N$. This is the initial state of the bath in the absence of an external magnetic field, ignoring interactions between the nuclear spins. Over time, interactions between the bath and the qubit will introduce correlations between the two subsystems, evolving the state $|\Psi_{\mathcal{I}}(0)\rangle = |\psi(0)\rangle \otimes |\mathcal{I}\rangle$ into the state $|\Psi_{\mathcal{I}}(t)\rangle = \frac{1}{\sqrt{2}}(|0, \mathcal{I}_0\rangle + |1, \mathcal{I}_1\rangle)$ (if we consider only loss of phase coherence). In general, the states $|\mathcal{I}_0\rangle$ and $|\mathcal{I}_1\rangle$ will not be the same. Therefore, the reduced density matrix of the qubit, given by $\hat{\rho}_S(t) = \text{Tr}_n[\sum_{\mathcal{I}} P_{\mathcal{I}} |\Psi_{\mathcal{I}}(t)\rangle \langle \Psi_{\mathcal{I}}(t)|]$, may have a decreased degree of coherence (i.e. smaller off-diagonal elements), since the nuclear spins are correlated with the spins of magnetic centers that encode the qubit. The degree of coherence can be quantified by $r(t) = \sum_{\mathcal{I}} P_{\mathcal{I}} r_{\mathcal{I}}(t)$, where $r_{\mathcal{I}}(t) = \langle \mathcal{I}_1(t) | \mathcal{I}_0(t) \rangle$, and $\langle 0 | \hat{\rho}_S(0) | 1 \rangle = r_{\mathcal{I}}/2$. It is known that the decoherence rate depends on the initial state of the nuclear spin bath. For example, it has been shown that techniques such as narrowing of the nuclear state can drastically increase the decoherence times in quantum dot systems [68].

Next, we want to show in what way (11.25) leads to decoherence in a spin-cluster qubit (such as is realized in the triangular magnet in Sect. 11.2) in more detail. We have shown before that in spin clusters the qubit state is typically not encoded in the \mathbf{S}_i 's themselves, but instead in quantities like the total spin \mathbf{S} or the chirality \mathbf{C} . However, we can always denote the basis states of the qubit by $|0\rangle$ and $|1\rangle$. Quite generally then, by projecting the spin operators \mathbf{S}_i on the space spanned by $|0\rangle, |1\rangle$, and performing a second order Schrieffer-Wolff transformation on the resulting Hamiltonian, one can transform (11.25) into the Hamiltonian $H = \sum_{k=0,1} |k\rangle \langle k| \otimes H_k$, with

$$H_k = \sum_{p=1}^N \omega_p^k I_p^{z'} + \sum_{p \neq q} (A_{pq}^k I_p^{z'} I_q^{z'} + B_{pq}^k I_p^+ I_q^-), \quad (11.26)$$

where $\hat{\mathbf{z}}' = \mathbf{B}/|\mathbf{B}|$. In the derivation of (11.26), we ignored terms that do not conserve energy. $\omega_p^0 - \omega_p^1$ is linear in H_{HF} , and the quantities $A_{pq}^0 - A_{pq}^1$ and $B_{pq}^0 - B_{pq}^1$ are quadratic in H_{HF} . The fastest contribution to decoherence is due to inhomogeneous broadening due to the terms $\propto I_p^{z'}$ in (11.26). These terms describes the magnetic field due to the nuclear spins, which is called the Overhauser field. The Overhauser field depends on the specific realization of the nuclear spin state (for times $t \ll \tau_n$, where τ_n is the typical evolution time of the nuclear spin state, the magnetic field is static). Therefore, if the nuclear spins are in a mixture of states, the coherence of the state $|\psi(0)\rangle$ is washed out due interference of the states that undergo time-evolution under different effective magnetic fields. This can be seen from the decoherence factor $r(t)$, which for $t \ll \tau_n$ evolves as $r(t) \approx e^{i(E_0 - E_1)t} \sum_{\mathcal{I}} P_{\mathcal{I}} e^{i\delta_{\mathcal{I}}t}$, where

$$\delta_{\mathcal{I}} \approx g_S \mu_S \sum_i \mathbf{B}_{\text{HF}}^{\mathcal{I}}(\mathbf{r}_i) \cdot [\langle 0 | \mathbf{S}_i | 0 \rangle - \langle 1 | \mathbf{S}_i | 1 \rangle]. \quad (11.27)$$

The sum is over the spins in the spin cluster. Furthermore, $\mathbf{B}_{\text{HF}}^{\mathcal{I}}(\mathbf{r}_i) = D_{\text{HF}} \sum_p m_p^{\mathcal{I}} [\hat{\mathbf{z}}' - 3(\hat{\mathbf{z}}' \cdot \hat{\mathbf{r}}_{ip})\hat{\mathbf{r}}_{ip}]/r_{ip}^3$ is the Overhauser field. It has been shown, that decoherence of a qubit encoded in the total spin $\mathbf{S} = \sum_{i=1}^3 \mathbf{S}_i$ of a triangular cluster due to the distribution of the Overhauser field for the equal superposition mixed state typically takes place on time scales of 100 ns. The second order terms in (11.26) give contributions to the decoherence times that are several orders of magnitude smaller.

We have seen that due to hyperfine interaction, both the qubit state as well as the nuclear spin state evolve in time. Furthermore, even in the absence of hyperfine interaction the nuclear spin state itself evolves in time, according to the Hamiltonian $H_n = \hat{\mathbf{B}} \cdot \sum_p \omega_p \mathbf{I}_p + D_n \sum_{p < q} [\mathbf{I}_p \cdot \mathbf{I}_q = 3(\mathbf{I}_p \cdot \hat{\mathbf{e}}_{pq})(\mathbf{I}_q \cdot \hat{\mathbf{e}}_{pq})]/r_{pq}^3$. This dynamics of the nuclear bath can lead to additional broadening of the Overhauser field, and has been shown to lead to decoherence on the μs -time scale for a qubit state encoded in the total spin.

An interesting possibility to increase the decoherence time of a qubit is a triangular spin cluster was put forward in Ref. [67]. The idea is to use the chirality of cluster as qubit, instead of the total spin. In that case, the states $|0\rangle$ and $|1\rangle$ of this section become $|0\rangle_{C_z} = |-1/2, 1\rangle$, $|0\rangle_{C_z} = |-1/2, -1\rangle$. The crucial property of these state that causes the increased decoherence time is that since

$$\langle 1 | S_{z,i} | 1 \rangle = \langle 0 | S_{z,i} | 0 \rangle = -1/6, \quad (11.28)$$

the Overhauser field from (11.27) does not couple to the qubit. Therefore, decoherence processes in (11.26) are second order only. This can lead to decoherence times approaching milliseconds.

11.6 Initialization and Read-out

Initialization of a qubit in its ground state is arguably the DiVincenzo criterion that is most routinely realized. Therefore, we will not spend a lot of time discussing it here. The way to prepare a qubit in its ground state is by cooling it down to temperatures that are much smaller than the gap between the ground state in which one wants to prepare the system and the first excited state. This gap, which could for instance be due to magnetic anisotropy, is typically of the order of a few Kelvin, and may be controlled by external means, such as placing the molecular magnet in a magnetic field. This limits the temperature at which experiments can be done to several mK to K.

The read-out of the spin state is a topic on itself, and we refer the reader to the literature for an overview of the different techniques that are used [69].

11.7 Grover's Algorithm Using Molecular Magnets

One special topic that we wish to discuss in this chapter is the implementation of Grover's algorithm using molecular magnets [27]. Grover's algorithm can be used to find an entry in an unsorted database with N entries. A typical situation in which this would be required is if we were given a phone number, and wanted to find the associated name in a phone book. Classically, we would have to start with the first entry, and work our way down the list. Finding the name in this manner requires on average $N/2$ queries. If we had encoded the information in the phone book in a quantum state, we would have been able to find the correct entry with high probability in $O(N^{1/2})$ queries using Grover's algorithm. A crucial requirement for this algorithm is the possibility to generate arbitrary superpositions of eigenstates (and in particular the superposition where all eigenstates have approximately the same weight).

In large-spin magnetic molecules, the eigenstates are labeled by the quantum number m_S , the z projection of the total spin $S \gg 1/2$. The Hamiltonian describing a single spin S with easy-axis along the z direction is given by

$$H = -AS_z^2 - BS_z^4 + V, \quad (11.29)$$

where $V = g\mu_B \mathbf{H} \cdot \mathbf{S}$. This gives rise to the typical double-well spectrum with non-equidistant level spacing. Such level spacing is crucial for the proposal in Ref. [27], as will become clear shortly. Suppose one starts out by preparing the system in the ground state $|\psi_0\rangle = |s\rangle$, and wishes to create an equal superposition of all the states $|m_0\rangle, |m_0 + 1\rangle, \dots, |s - 1\rangle$, where $m_0 = 1, 2, \dots, s - 1$. This corresponds to using $n - 1$ states for Grover's algorithm, where $n = s - m_0$. In principle, one can create superpositions by applying a weak transverse magnetic field \mathbf{H}_\perp (whose effect can be described using perturbation theory) which drives multiphoton transitions via virtual states through its coupling to S^+, S^- . However, to create the equal superposition that is required for Grover's algorithm, the amplitudes of all k -photon processes (here $k = 1, 2, \dots, s - m_0$) must be equal. Clearly, perturbation theory is not valid in this regime. Therefore, a more sophisticated scheme is required.

The scheme that is proposed in Ref. [27] to create an equal superposition uses a single coherent magnetic pulse of duration T with a discrete frequency spectrum $\{\omega_m\}$. It contains n high-frequency components and a single low-frequency component ω_0 , chosen such that $\hbar\omega_0 \ll \epsilon_{m_0} - \epsilon_{m_0+1}$. Here, ϵ_m is the energy of the eigenstate $|m\rangle$. The frequencies of the n high-frequency components are given by $\hbar\omega_{s-1} = \epsilon_{s-1} - \epsilon_s - \hbar(n-1)\omega_0$ and $\omega_m = \epsilon_m - \epsilon_{m+1} + \hbar\omega_0$ for $m = m_0, \dots, s-2$. For the molecular magnet Mn_{12} , the high-frequency components have frequencies between 20-120 GHz, and ω_0 is around 100 MHz. Because of the non-equidistant splitting of the energy levels, all frequencies are different. The low-frequency component is applied along the easy axis, the high frequency components are in plane, so that the coupling is given by

$$V_{\text{low}}(t) = g\mu_B H_0(t) \cos(\omega_0 t) S_z, \quad (11.30)$$

$$\begin{aligned}
V_{\text{high}}(t) &= \sum_{m=m_0}^{s-1} g\mu_B H_m(t) [\cos(\omega_m t + \Phi_m) S_x - \sin(\omega_m t + \Phi_m) S_y] \\
&= \sum_{m=m_0}^{s-1} \frac{g\mu_B H_m(t)}{2} [e^{i(\omega_m t + \Phi_m)} S^+ + e^{-i(\omega_m t + \Phi_m)} S^-]. \quad (11.31)
\end{aligned}$$

Hence, absorption (emission) of a high-frequency σ^- -photon induces a transition with $\Delta m = -1$ (1); the low-frequency π -photons do not change m , instead they supply the energy required to fulfill the resonance condition for allowed transitions. The phases Φ_m can be chosen freely, we will come back to this point later. With this setup, the lowest order transition between the ground state $|s\rangle$ and all states $|m\rangle$ (for $m_0 \leq m < s$) is n 'th order in $V(t) = V_{\text{low}}(t) + V_{\text{high}}(t)$.

To see this, let us consider an explicit example where $s = 10$, $m_0 = 5$, and hence $n = 5$. The lowest order transition from $|s\rangle$ to $|s-1\rangle$ uses 4 π -photons of energy $\hbar\omega_0$ and 1 σ^- -photon with energy $\hbar\omega_{s-1}$. The transition from $|s\rangle$ to $|s-2\rangle$ uses 3 π -photons of energy $\hbar\omega_0$, 1 σ^- -photon with energy $\hbar\omega_{s-1}$, and 1 σ^- -photon with energy $\hbar\omega_{s-2}$; and so on for the other transitions. ω_0 can be chosen such that lower order transitions are forbidden due to the requirement of energy conservation. The amplitude of higher order transitions is small in the perturbative regime.

Since all transition amplitudes are the same order in $V(t)$, they are all approximately equal. To make them exactly equal requires some fine-tuning. For rectangular pulses with $H_k(t) = H_k$ for $T/2 < t < T/2$, the n 'th order contribution to the S -matrix for the transition between $|s\rangle$ and $|m\rangle$, denoted by $S_{m,s}^{(n)}$, is given by

$$\begin{aligned}
S_{m,s}^{(n)} &= \sum_F \Omega_m \frac{2\pi}{i} \left(\frac{g\mu_B}{2\hbar} \right)^n \frac{\prod_{k=m}^{s-1} H_k e^{i\Phi_k} H_0^{m-m_0} p_{m,s}(F)}{(-1)^{q_F} q_F! r_s(F)! \omega_0^{n-1}} \\
&\quad \times \delta^{(T)} \left(\omega_{m,s} - \sum_{k=m}^{s-1} \omega_k - (m - m_0)\omega_0 \right). \quad (11.32)
\end{aligned}$$

The sum runs over all Feynman diagrams F . $\Omega_m = (m - m_0)!$, $q_F = m - m - r_s(F)$, $p_{m,s}(F) = \prod_{k=m}^s \langle k | S_z | k \rangle^{r_k(F)} \prod_{k=m}^{s-1} \langle k | S^- | k+1 \rangle$, with $r_k(F) = 0, 1, 2, \dots \leq m - m_0$ the number of π -transitions in the transition belonging to the Feynman diagram F . $\delta^{(T)}(\omega) = 1/(2\pi) \int_{-T/2}^{T/2} dt e^{i\omega t}$ is the delta-function of width T . It ensures energy conservation. For the example above, the requirement $|S_{m,s}^{(n)}| \approx |S_{-1,s}^{(n)}|$ for all $m \geq m_0$ (which corresponds to the equal superposition) is satisfied for parameters

$$H_8/H_0 = 0.04, \quad H_7/H_0 = -0.25, \quad H_6/H_0 = -0.61, \quad H_5/H_0 = -1.12. \quad (11.33)$$

H_9 can be chosen independently. For numerical estimates, we refer to the original paper, Ref. [27]. This concludes the discussion of generating the equal superposition required for Grover's algorithm.

With some adaptations, a single step in Grover's algorithm can be used to read-in and decode quantum information. This opens up the possibility to use molecular

magnets as dense and efficient memory devices. The phases Φ_m in (11.30)–(11.31) play a crucial role here. We denote $\Phi_m = \sum_{k=s-1}^{m+1} \Phi_k + \phi_m$. As we have seen before, we can irradiate the system with a coherent magnetic pulse of duration T such that all $S_{m,s}^{(n)} = \pm\eta$. In other words, the state after the pulse is $|\psi\rangle = \sum_{m=m_0}^s a_m |m\rangle$, where the amplitudes $a_1 = 1$ and $a_m = \pm\eta$. By identifying the amplitude $\pm\eta$ with the logical-1, respectively logical-0, we see that this state encodes a n -bit state. Because of the Φ_m dependence of the S -matrix (see (11.32)), we can switch between the $\pm\eta$ amplitude by choosing $\phi_m = 0, \pi$. This allows us to encode a general state between 0 and $2^n - 1$ in the quantum state of the molecular magnet. The set $\{\phi_m\}$ that one uses depends on the number that has to be encoded. For instance, encoding $12_{10} = 1101_2$ requires $\phi_9 = \phi_8 = \phi_7 = 0$ and $\phi_6 = \phi_5 = \pi$. Here, the states with $m = 9, 8, 7, 6, 5$ represent respectively the binary digits $2^0, 2^1, 2^2, 2^3, 2^4$.

To decode the state of the molecule, one applies a pulse for which $S_{m_0,s}^{(n)} = S_{m_0+1,s}^{(n)} = \dots = S_{s-1,s}^{(n)} = -\eta$. This pulse amplifies the bits which have amplitude $-\eta$, and suppresses those with amplitude η . The accumulated error in this procedure is approximately $n\eta^2$. Read-out of this decoded state can be done by measuring the occupation of the different levels by standard spectroscopy, for instance using pulsed ESR. Irradiation with a pulse which contains the frequency $\hbar\omega_{m-1,m} = \epsilon_{m-1} - \epsilon_m$ drives transitions that are given by $S_{m-1,m}^{(1)}$. If the state $|m\rangle$ is occupied (meaning that its amplitude was $-\eta$), we would observe stimulated absorption when irradiating with frequency $\omega_{6,7}$ and stimulated emission when irradiating with frequency $\omega_{7,8}$. Since the energy levels are non-equidistant, this uniquely identifies the level.

Acknowledgements The authors would like to acknowledge financial support from the Swiss NSF, the NCCR Nanoscience Basel, and the FP7-ICT project “ELFOS”.

References

1. C.M. Papadimitriou, *Computational Complexity* (Addison-Wesley, Reading, 1994)
2. D.P. DiVincenzo, Fortschr. Phys. **48**, 771 (2000)
3. D. Deutsch, R. Jozsa, Proc. R. Soc. Lond. Ser. A, Math. Phys. Sci. **439**, 553 (1992)
4. R. Cleve, A. Ekert, C. Macchiavello, M. Mosca, Proc. R. Soc. Lond. Ser. A, Math. Phys. Sci. **454**, 339 (1998)
5. L.K. Grover, in *Proceedings of the 28th Annual ACM Symposium on the Theory of Computing*, (1996), p. 212
6. P. Shor, SIAM J. Comput. **26**, 1484 (1997)
7. D. Deutsch, Proc. R. Soc. Lond. A **400**, 97–117 (1985)
8. J. Church, Am. J. Math. **58**, 435 (1936)
9. A.M. Turing, Proc. Lond. Math. Soc. **442**, 230 (1936)
10. M.A. Nielsen, I.L. Chuang, *Quantum Computation and Quantum Information* (Cambridge University Press, New York, 2000)
11. W.K. Wootters, W.H. Zurek, Nature **299**, 802 (1982)
12. A. Barenco, C.H. Bennett, R. Cleve, D.P. DiVincenzo, N. Margolus, P. Shor, T. Sleator, J.A. Smolin, H. Weinfurter, Phys. Rev. A **52**, 3457 (1995)
13. D. Loss, D.P. DiVincenzo, Phys. Rev. A **57**, 120 (1998)
14. A. Imamoglu, D.D. Awschalom, G. Burkard, D.P. DiVincenzo, D. Loss, M. Sherwin, A. Small, Phys. Rev. Lett. **83**, 4204 (1999)

15. J.I. Cirac, P. Zoller, *Phys. Rev. Lett.* **74**, 4091 (1995)
16. Q.A. Turchette, C.J. Hood, W. Lange, H. Mabuchi, H.J. Kimble, *Phys. Rev. Lett.* **75**, 4710 (1995)
17. N.A. Gershenfeld, I.L. Chuang, *Science* **275**, 350 (1997)
18. A. Shnirman, G. Schön, Z. Hermon, *Phys. Rev. Lett.* **79**, 2371 (1997)
19. B.E. Kane, *Nature (London)* **393**, 133 (1998)
20. R. Vrijen, E. Yablonovitch, K.L. Wang, H.W. Jiang, A.A. Balandin, V. Roychowdhury, T. Mor, D.P. DiVincenzo, *Phys. Rev. A* **62**, 012306 (2000)
21. E. Knill, R. Laflamme, G.J. Milburn, *Nature (London)* **409**, 46 (2001)
22. F. Jelezko, J. Wrachtrup, *Phys. Status Solidi A* **203**, 3207 (2006)
23. R. Hanson, D.D. Awschalom, *Nature (London)* **453**, 1043 (2008)
24. P. Maletinsky, S. Hong, M.S. Grinolds, B. Hausmann, M.D. Lukin, R.L. Walsworth, M. Loncar, A. Yacoby, *Nat. Nanotechnol.* (2012). doi:[10.1038/nnano.2012.50](https://doi.org/10.1038/nnano.2012.50)
25. D.V. Bulaev, B. Trauzettel, D. Loss, *Phys. Rev. B* **77**, 235301 (2008)
26. M. Trif, V.N. Golovach, D. Loss, *Phys. Rev. B* **77**, 045434 (2008)
27. M.N. Leuenberger, D. Loss, *Nature (London)* **410**, 789 (2001)
28. J. Tejada, E. Chudnovsky, E. del Barco, J. Hernandez, T. Spiller, *Nanotechnology* **12**, 181 (2001)
29. F. Meier, J. Levy, D. Loss, *Phys. Rev. Lett.* **90**, 047901 (2003)
30. F. Troiani, A. Ghirri, M. Affronte, S. Carretta, P. Santini, G. Amoretti, S. Piligkos, G. Timco, R.E.P. Winpenny, *Phys. Rev. Lett.* **94**, 207208 (2005)
31. J. Lehmann, A. Gaita-Arino, E. Coronado, D. Loss, *Nat. Nanotechnol.* **2**, 312 (2007)
32. M. Trif, F. Troiani, D. Stepanenko, D. Loss, *Phys. Rev. Lett.* **101**, 217201 (2008)
33. E.M. Chudnovsky, L. Gunther, *Phys. Rev. Lett.* **60**, 661 (1988)
34. D.D. Awschalom, J.F. Smyth, G. Grinstein, D.P. DiVincenzo, D. Loss, *Phys. Rev. Lett.* **68**, 3092 (1992)
35. R. Sessoli, D. Gatteschi, A. Caneschi, M.A. Novak, *Nature (London)* **365**, 141 (1993)
36. L. Thomas, F. Lioni, R. Ballou, D. Gatteschi, R. Sessoli, B. Barbara, *Nature (London)* **383**, 145 (1996)
37. J.R. Friedman, M.P. Sarachik, J. Tejada, R. Ziolo, *Phys. Rev. Lett.* **76**, 3830 (1996)
38. W. Wernsdorfer, E. Bonet Orozco, K. Hasselbach, A. Benoit, D. Maillly, O. Kubo, H. Nakano, B. Barbara, *Phys. Rev. Lett.* **79**, 4014 (1997)
39. J. Tejada, X.X. Zhang, E. del Barco, J.M. Hernández, E.M. Chudnovsky, *Phys. Rev. Lett.* **79**, 1754 (1997)
40. E. del Barco, A.D. Kent, E.M. Rumberger, D.N. Hendrickson, G. Christou, *Phys. Rev. Lett.* **91**, 047203 (2003)
41. A. Chiolero, D. Loss, *Phys. Rev. Lett.* **80**, 169 (1998)
42. F. Meier, D. Loss, *Phys. Rev. Lett.* **86**, 5373 (2001)
43. D. Gatteschi, A. Caneschi, L. Pardi, R. Sessoli, *Science* **265**, 1054 (1994)
44. C. Sangregorio, T. Ohm, C. Paulsen, R. Sessoli, D. Gatteschi, *Phys. Rev. Lett.* **78**, 4645 (1997)
45. D. Gatteschi, R. Sessoli, A. Cornia, *Chem. Commun.* **725** (2000). doi:[10.1039/A908254I](https://doi.org/10.1039/A908254I)
46. D. Loss, D.P. DiVincenzo, G. Grinstein, *Phys. Rev. Lett.* **69**, 3232 (1992)
47. M.N. Leuenberger, D. Loss, *Phys. Rev. B* **61**, 1286 (2000)
48. M.N. Leuenberger, F. Meier, D. Loss, *Monatsh. Chem.* **134**, 217 (2003)
49. W. Wernsdorfer, R. Sessoli, *Science* **284**, 133 (1999)
50. M.N. Leuenberger, D. Loss, *Phys. Rev. B* **63**, 054414 (2001)
51. G. González, M.N. Leuenberger, *Phys. Rev. Lett.* **98**, 256804 (2007)
52. G. González, M.N. Leuenberger, E.R. Mucciolo, *Phys. Rev. B* **78**, 054445 (2008)
53. M. Trif, F. Troiani, D. Stepanenko, D. Loss, *Phys. Rev. B* **82**, 045429 (2010)
54. K.-Y. Choi, Y.H. Matsuda, H. Nojiri, U. Kortz, F. Hussain, A.C. Stowe, C. Ramsey, N.S. Dalal, *Phys. Rev. Lett.* **96**, 107202 (2006)
55. F.H.L. Koppens, C. Buizert, K.J. Tielrooij, I.T. Vink, K.C. Nowack, T. Meunier, L.P. Kouwenhoven, L.M.K. Vandersypen, *Nature (London)* **442**, 766 (2006)

56. S. Bertaina, S. Gambarelli, T. Mitra, B. Tsukerblat, A. Müller, B. Barbara, *Nature (London)* **453**, 203 (2008)
57. M. Borhani, V.N. Golovach, D. Loss, *Phys. Rev. B* **73**, 155311 (2006)
58. K.C. Nowack, F.H.L. Koppens, Yu.V. Nazarov, L.M.K. Vandersypen, *Science* **318**, 1430 (2007)
59. M.F. Islam, J.F. Noss, C.M. Canali, M.R. Pederson, *Phys. Rev. B* **82**, 155446 (2010)
60. J.F. Noss, M.F. Islam, C.M. Canali, M.R. Pederson, *Phys. Rev. B* **85**, 085427 (2012)
61. P.W. Anderson, *Phys. Rev.* **115**, 2 (1959)
62. T. Moriya, *Phys. Rev.* **120**, 91 (1960)
63. R. Winkler, *Spin-Orbit Coupling Effects in Two-dimensional Electron and Hole Systems* (Springer, Berlin, 2003)
64. G. Burkard, D. Loss, D.P. DiVincenzo, *Phys. Rev. B* **59**, 2070 (1999)
65. A. Ardavan, O. Rival, J.J.L. Morton, S.J. Blundell, A.M. Tyryshkin, G.A. Timco, R.E.P. Winpenny, *Phys. Rev. Lett.* **98**, 057201 (2007)
66. A. Schweiger, G. Jeschke, *Principles of Pulse Electron Paramagnetic Resonance* (Oxford University Press, New York, 2001)
67. F. Troiani, D. Stepanenko, D. Loss, *Phys. Rev. B* **86**, 161409 (2012)
68. W.A. Coish, D. Loss, *Phys. Rev. B* **70**, 195340 (2004)
69. D. Gatteschi, R. Sessoli, J. Villain, *Molecular Nanomagnets* (Oxford University Press, New York, 2006)

FUNDAMENTALS AND PROPERTIES OF MULTIFUNCTIONAL NANOMATERIALS

Edited by
Sabu Thomas, Nandakumar Kalarikkal,
and Ann Rose Abraham



Micro & Nano Technologies Series

***Fundamentals and Properties of
Multifunctional Nanomaterials***

This page intentionally left blank

Micro and Nano Technologies
***Fundamentals and Properties of
Multifunctional Nanomaterials***

Edited by
Sabu Thomas
Nandakumar Kalarikkal
Ann Rose Abraham



Elsevier

Radarweg 29, PO Box 211, 1000 AE Amsterdam, Netherlands
The Boulevard, Langford Lane, Kidlington, Oxford OX5 1GB, United Kingdom
50 Hampshire Street, 5th Floor, Cambridge, MA 02139, United States

Copyright © 2021 Elsevier Inc. All rights reserved.

No part of this publication may be reproduced or transmitted in any form or by any means, electronic or mechanical, including photocopying, recording, or any information storage and retrieval system, without permission in writing from the publisher. Details on how to seek permission, further information about the Publisher's permissions policies and our arrangements with organizations such as the Copyright Clearance Center and the Copyright Licensing Agency, can be found at our website: www.elsevier.com/permissions.

This book and the individual contributions contained in it are protected under copyright by the Publisher (other than as may be noted herein).

Notices

Knowledge and best practice in this field are constantly changing. As new research and experience broaden our understanding, changes in research methods, professional practices, or medical treatment may become necessary.

Practitioners and researchers must always rely on their own experience and knowledge in evaluating and using any information, methods, compounds, or experiments described herein. In using such information or methods they should be mindful of their own safety and the safety of others, including parties for whom they have a professional responsibility.

To the fullest extent of the law, neither the Publisher nor the authors, contributors, or editors, assume any liability for any injury and/or damage to persons or property as a matter of products liability, negligence or otherwise, or from any use or operation of any methods, products, instructions, or ideas contained in the material herein.

Library of Congress Cataloging-in-Publication Data

A catalog record for this book is available from the Library of Congress

British Library Cataloguing-in-Publication Data

A catalogue record for this book is available from the British Library

ISBN: 978-0-12-822352-9

For information on all Elsevier publications visit our website at
<https://www.elsevier.com/books-and-journals>

Publisher: Matthew Deans
Acquisitions Editor: Simon Holt
Editorial Project Manager: Chiara Giglio
Production Project Manager: Sojan P. Pazhayattil
Cover Designer: Christian J. Bilbow

Typeset by TNQ Technologies



Contents

Contributors	xvii
Editors' biographies	xxi
Contributors' biographies	xxiii
Foreword	lxi
Chapter 1: A glimpse into the fundamentals and properties of multifunctional nanomaterials	1
<i>Ann Rose Abraham, Nandakumar Kalarikkal, and Sabu Thomas</i>	
1. Fundamentals and properties of multifunctional nanomaterials: an overview	1
2. Conclusion.....	6

PART 1: Nanoscopic solids and transport properties

Chapter 2: Transport properties of nanoscopic solids as probed by spectroscopic techniques	9
<i>Dejan M. Djokić, Novica Paunović, Bojan Stojadinović, Dimitrije Stepanenko, Saša Lazović, and Zorana Dohčević-Mitrović</i>	
1. Introduction	9
2. Raman scattering	10
2.1 Short introduction to Raman scattering technique	10
2.2 Multiferroic BiFeO ₃ nanoparticles	13
3. Infrared reflection.....	21
3.1 Short introduction to infrared reflection technique	21
3.2 Doped nanocrystalline CeO ₂	24
4. Electron spin resonance	26
4.1 Short introduction to electron spin resonance technique	26
4.2 Carbon nanotubes.....	30
5. Concluding remarks	32
Acknowledgments.....	33
References.....	34

PART 2: Properties of liquid crystalline nanomaterials

**Chapter 3: Properties of multifunctional bionanomaterials of lipid
A-phosphate in liquid phases and quasi-crystalline structures 41**

Henrich H. Paradies, Chester A. Faunce, Hendrik Reichelt, and Kurt Zimmermann

1. Introduction	41
2. Experimental	47
2.1 Materials and preparation of the lipid-A-diphosphate samples	47
2.2 Methods	47
3. Results and discussion	50
3.1 Small-area electron diffraction profiles of various lipid A-diphosphate phases in aqueous solutions.....	50
3.2 Transmission electron microscopy images of the various lipid A-diphosphate derivatives.....	53
4. Conclusions	61
References.....	62

Chapter 4: Behavior of nanoparticles within liquid crystal phases 65

Apparao Gudimalla, Brigita Rožič, and Samo Kralj

1. Introduction	66
1.1 History of liquid crystals	66
1.2 Classifications of liquid crystals.....	67
1.3 Liquid crystals and nanoparticles.....	71
2. Experimental identification of liquid crystals.....	73
2.1 High-resolution calorimetry.....	73
2.2 Dielectric spectroscopy.....	74
2.3 Polarizing optical microscope	76
2.4 X-ray diffraction	77
2.5 Localized surface plasmon resonance	78
3. Nanoparticles synthesis and their dispersions in the host liquid crystals.....	78
3.1 Lyotropic liquid crystals.....	80
3.2 Thermotropic liquid crystals.....	82
3.3 Liquid crystal–decorated nanoparticles.....	84
4. Physical properties of liquid crystalline nanoparticles and their applications	84
4.1 Display applications.....	84
4.2 Other applications	86
5. Conclusion.....	87
Acknowledgments.....	88
References.....	88

PART 3: Properties of carbon-based nanomaterials

Chapter 5: Characteristics of carbon nanotubes and their nanocomposites 99

Piyush Kumar Sonkar, Narvadeshwar, and Pawan Kumar Gupta

1. Introduction	99
1.1 History of carbon nanotubes.....	101
1.2 Types of carbon nanotubes	101
1.3 Physical properties of carbon nanotubes.....	102
2. Functionalization of carbon nanotubes	105
3. Characterization tool for carbon nanotubes and their nanocomposites	107
3.1 Microscopic analysis.....	107
3.2 Raman spectroscopy	111
4. Applications of carbon nanotubes and their composites	113
5. Summary	114
Acknowledgments.....	114
References.....	114

Chapter 6: Morphology-correlated mechanical properties of ionic liquid-modified multiwalled carbon nanotubes/poly(vinyl chloride) nanocomposites 119

Elizabeth Francis and Sabu Thomas

1. Introduction	120
2. Experimental	121
2.1 Materials and methods.....	121
3. Characterization	123
3.1 Raman spectroscopy	123
3.2 Fourier Transform Infrared spectroscopy analysis	123
3.3 Thermal analysis	123
3.4 Morphology and microstructure	123
3.5 Mechanical properties.....	124
4. Results and discussion	124
4.1 Fourier Transform Infrared spectra of nanocomposites	124
4.2 Raman spectra of nanocomposites	126
4.3 Morphology	127
4.4 Thermal properties of CN _x , CN _x (12), CN _x (16) nanocomposites.....	131
4.5 Mechanical properties of MWCNT/PVC nanocomposites.....	132
4.6 Conclusion.....	139
References.....	140

Chapter 7: Fundamentals and properties of multifunctional graphene and graphene-based nanomaterials..... 143

Srinivasarao Yaragalla and K.B. Bhavitha

1. Introduction	143
-----------------------	-----

Contents

2. History and properties of graphene.....	145
3. Preparation methods of graphene.....	146
3.1 Top-down approach.....	146
4. Bottom-up approach.....	149
5. Multifunctional applications of graphene and graphene-based materials.....	149
5.1 Field effect transistors.....	149
5.2 Effective reinforcement in polymer nanocomposites	150
5.3 Role of graphene in energy storage devices	151
6. Graphene applications in sensors	153
7. Conclusions and future outlook.....	154
References.....	155

Chapter 8: Fundamental photophysical properties of fluorescent carbon dots and their applications in metal ion sensing and bioimaging 159

Soumita Mukhopadhyay, Tapan Kumar Si, and Nibedita Pradhan

1. Introduction	160
1.1 Historical overview	160
2. Synthesis approaches for fluorescent carbon dots preparation.....	161
2.1 Top-down approach.....	161
2.2 Bottom-up approach.....	161
3. Fundamental photophysical properties of carbon dots	170
3.1 Fluorescence mechanisms.....	170
4. Applications.....	173
4.1 Metal ion sensing.....	174
4.2 Subcellular imaging	181
4.3 RNA imaging	185
4.4 Glutathione imaging.....	186
4.5 Intracellular pH sensing.....	187
4.6 Intracellular reactive oxygen species imaging.....	188
4.7 Cancer imaging	188
4.8 Multimodal in-vivo imaging.....	189
4.9 Fluorescent carbon dot as super resolution imaging probe.....	192
5. Conclusion and future scope	196
Glossary	197
Acknowledgment	197
References.....	197

PART 4: Characteristics of magnetic nanomaterials

Chapter 9: Magnetic properties of doped germanium nanostructures..... 213

Amar S. Katkar

1. Introduction about dilute magnetic semiconductors materials in group IV elements.....	213
--	-----

2. Doped germanium nanostructures (synthesis and characterizations).....	215
2.1 Cr, Fe-doped Ge single crystals	215
2.2 Transition metal-doped group-IV semiconductors: R_xY_{1-x} , $R = Cr, Mn,$ Fe; $Y = Si, Ge$	215
2.3 $Ge_{1-x}Mn_x$ nanocolumns	215
2.4 $Ge_{1-x}M_x$ ($M_x = Mn, Fe, \text{ and } Co$) nanowires	218
2.5 $Ge_{0.95}Mn_{0.05}$ quantum dots	223
2.6 Cr-doped Ge nanotowers	225
2.7 Cr-doped Ge/ GeO_x core-shell nanowires	228
3. Conclusions	232
References.....	233
Chapter 10: Magnetic and electrochemical characteristics of carbon-modified magnetic nanoparticles	235
<i>Arun Thirumurugan, R. Udayabhaskar, T. Prabhakaran, Mauricio J. Morel, Ali Akbari-Fakhrabadi, K. Ravichandran, K. Prabhakaran, and R.V. Mangalaraja</i>	
1. Introduction	235
2. Carbon-modified magnetic nanoparticles.....	236
3. Magnetic characteristics of carbon-modified magnetic nanoparticles	239
4. Electrochemical characteristics of carbon-modified magnetic nanoparticles	240
5. Magnetic field—assisted electrochemical characteristics.....	242
6. Conclusion.....	246
Acknowledgment.....	247
References.....	247
PART 5: Properties of ferroelectric nanomaterials	253
Chapter 11: Effect of particle size on structural phase transitions of lithium-modified sodium niobates ($Li_xNa_{1-x}NbO_3$ $x = 0, 0.06$ and 0.12)	255
<i>S.K. Mishra, P.S.R. Krishna, and A.B. Shinde</i>	
1. Introduction	255
2. Experimental	258
3. Structural behavior of lithium-modified sodium niobate	260
3.1 Phase stability of pure sodium niobate at room temperature	260
3.2 Phase stability of compositionally modified sodium niobate at room temperature for different length scales (particle sizes)	261
3.3 Low temperature neutron diffraction study of sintered LNN06	264
3.4 Effect of particle size on structural phase transition from orthorhombic to rhombohedral phase below 300 K.....	266
4. Dynamical behavior of lithium-modified sodium niobate at elevated temperature.....	268
4.1 Factor group analysis of the Raman active modes.....	268
4.2 Temperature-dependent Raman spectra	269

Contents

5. Conclusion.....	272
References.....	273

Chapter 12: BiFeO₃-based multiferroic materials and their properties 275

Ashalata Puhan, Bhavya Bhushan, Arpan Kumar Nayak, and Dibyaranjan Rout

1. Introduction	276
2. Multiferroic materials	276
3. Types of multiferroics.....	277
3.1 Type-I multiferroics	278
3.2 Type-II multiferroic.....	279
4. Coupling in multiferroics.....	280
4.1 Magnetoelectric coupling.....	281
4.2 Piezoelectric coupling.....	281
4.3 Piezomagnetic coupling	282
5. Single phase multiferroic materials and their applications	282
6. BiFeO ₃	282
6.1 Crystal structure of BiFeO ₃	283
6.2 Ferroelectric property of BiFeO ₃	284
6.3 Dielectric property of BiFeO ₃	286
6.4 Magnetic property of BiFeO ₃	287
6.5 Optical property of BiFeO ₃	288
7. Application of BiFeO ₃	289
8. Motivations.....	290
9. Conclusions	291
Acknowledgments.....	291
References.....	291

PART 6: Properties of plasmonic nanomaterials

Chapter 13: Multifunctional plasmonic nanomaterials..... 297

Sudhir Cherukulappurath

1. Introduction	297
2. Plasmonic nanoparticles: theory, synthesis, and properties.....	298
3. Hybrid plasmonic nanomaterials	305
4. Plasmonic-semiconductor core-shell nanoparticles	306
5. Magnetic-plasmonic nanoparticles	307
6. Applications of magnetic core-plasmonic shell nanoparticles	312
7. Fluorescent-plasmonic nanoparticles.....	314
8. Fluorescent-magnetic-plasmonic nanoparticles.....	319
9. Graphene-plasmonic nanocomposites	319
10. Future prospects of multifunctional plasmonic nanomaterials.....	321
References.....	322

Chapter 14: Multifunctional gold nanoparticles for biosensing: effects of surface plasmon resonance, localized surface plasmon resonance, fluorescence, and aggregation 331

Shirsendu Mitra, Mitali Basak, and Dipankar Bandyopadhyay

1. Introduction	332
2. Synthesis of gold nanoparticles.....	335
2.1 Trisodium citrate or Turkevich method	335
2.2 Sodium Borohydride reduction	337
2.3 Mixed reducing agents.....	338
2.4 Brust–Schiffrin method.....	339
2.5 Ascorbic acid reduction	340
2.6 Green methods	342
3. Size control parameters	342
3.1 Molar ratio of reducing agents.....	343
3.2 Temperature.....	343
3.3 Rate of stirring	344
3.4 pH	344
4. Characterization of gold nanoparticles.....	345
4.1 UV-Visible spectroscopy.....	345
4.2 Dynamic light scattering.....	345
4.3 Electron microscopy	346
5. Colors of gold nanoparticles.....	347
6. Biosensing	348
6.1 Surface Plasmon Resonance.....	349
6.2 Localized surface plasmon resonance.....	352
6.3 Fluorescence quenching.....	355
6.4 Salt aggregation.....	357
7. Advantages and disadvantages	358
8. Summary	359
References.....	359

PART 7: Engineered nanomaterials for industrial applications

Chapter 15: The key role of metal nanoparticle in metal organic frameworks of UiO family (MOFs) for the application of CO₂ capture and heterogeneous catalysis 369

Thirunarayanan Ayyavu, Hemamalini Arasappan, Francisco Gracia, and Monica Soler

1. Introduction of metal organic frameworks.....	370
2. Interesting characteristic features and advantages of zirconium-based metal organic frameworks in porous materials.....	370
3. Designing strategies of zirconium-based metal organic frameworks (Zr-MOF).....	376
3.1 Modulated synthesis in Zr-MOFs.....	376
3.2 Isoreticular expansion of zirconium metal organic frameworks.....	377

Contents

3.3 Geometrical and spatial relationship properties of zirconium metal organic frameworks.....	378
3.4 Post synthetic functionalization of zirconium metal organic frameworks.....	379
4. Synthesis of zirconium metal organic frameworks	380
4.1 UiO-MOFs synthesis by conventional synthetic route	381
4.2 Solvothermal/hydrothermal method for synthesis of UiO-MOFs	381
4.3 Microwave-assisted synthesis of zirconium-based MOFs.....	382
4.4 Synthesis of zirconium-based metal organic frameworks by electrochemical process	382
4.5 Synthesis of zirconium-based MOFs by sonochemical method	384
4.6 Mechanochemical technique for synthesis of UiO-MOFs	384
4.7 Purification/activation	384
5. Characterization methods.....	386
5.1 Powder X-ray diffraction technique to confirm the crystal nature of the UiO-MOFs	386
5.2 Infrared spectroscopic method for confirmation of UiO-MOFs	387
5.3 Nitrogen adsorption-desorption isotherm at 77 K to calculate the textural properties of zirconium MOFs.....	387
5.4 Analysis of structural morphology of UiO-MOFs by scanning and field emission scanning electron microscopy (SEM and FESEM) as well as transmission electron microscopy	388
5.5 Thermogravimetric analysis to determine the structure of UiO-MOFs.....	389
5.6 Inductively coupled plasma optical emission spectroscopy for identification of atomic molecules of UiO-MOFs.....	390
6. Carbon dioxide capture, adsorption, and activation on the structure of UiO metal organic frameworks	390
7. Synthesis of nanomaterials based on the UiO-MOFs and their application for hydrogenation of CO ₂ and organic synthesis by heterogeneous catalysis	392
8. Conclusion.....	396
Acknowledgement	396
References.....	397

Chapter 16: Embracing nanotechnology concepts in the electronics industry..... 405

Mathew Chethipuzha, Ann Rose Abraham, Nandakumar Kalarikkal, Sabu Thomas, and S. Sreeja

1. Introduction	405
2. The top-down and bottom-down approaches toward nanoelectronics	407
3. Applications of nanomaterials in electronics industry	407
3.1 Nanomaterials in highly sensitive Internet of Things devices	408
3.2 Nanomaterials in transistors	409
3.3 Nanotechnology in printed electronics applications.....	417
3.4 Nanomaterials in stretchable bioelectronics devices	417
3.5 Nanomaterials in memory devices	418
4. Conclusion.....	418
References.....	419

Chapter 17: Conducting polyaniline-based nanocomposites as electromagnetic interference shielding materials..... 423

Muhammad Faisal

1. Introduction	423
2. Diversity in polyaniline	426
3. Concept of doping and charge carriers	428
3.1 Redox doping	430
3.2 Nonredox doping.....	431
4. Charge carriers in conducting polymers	431
5. Importance of composites.....	437
6. Electromagnetic interference shielding	439
6.1 Importance of electromagnetic interference shielding and shielding mechanisms	439
6.2 Electromagnetic interference shielding measurements.....	440
6.3 Scattering (S) parameters and shielding effectiveness	441
7. Preparation of polyaniline composite samples	443
8. Structural and morphological characterization	444
8.1 Structure characterization by X-ray diffraction analysis.....	444
8.2 Morphology by electron microscopy	447
8.3 Electromagnetic interference shielding studies.....	453
9. Conclusion.....	458
Acknowledgment	458
References.....	458

PART 8: Fundamentals of 2D nanomaterials

Chapter 18: Two-dimensional layered nanosheets: structure and unique properties..... 465

Abimannan Sethurajaperumal, Vanmathi Ravichandran, Arghya Banerjee, Anagha Manohar, and Eswaraiah Varrla

1. Introduction	465
2. Graphene	466
2.1 Stacking sequence and band structure of graphene.....	466
2.2 Twisted bilayer graphene.....	468
3. Molybdenum disulphide (MoS ₂)	472
3.1 MoS ₂ structure and its properties.....	472
3.2 MoS ₂ layer–dependent physical properties.....	473
3.3 Molybdenum disulphide (MoS ₂) polymorphs.....	473
4. Black phosphorus and physical properties.....	476
5. MXenes	480
5.1 MXene nanosheets	480
5.2 Crystal structure of MXenes.....	481
6. Boron nitride structure and properties	482

Contents

7. Layered double hydroxide	487
8. Phyllosilicates structure and properties	490
9. Concluding remarks	494
Acknowledgments.....	494
References.....	495
Chapter 19: MoS₂, a new perspective beyond graphene	499
<i>Levna Chacko, Aswini Poyyakkara, V.B. Sameer Kumar, and P.M. Aneesh</i>	
1. Introduction	499
2. Beyond graphene—molybdenum disulphide (MoS ₂)	501
3. Structural properties of MoS ₂	503
4. Optical properties of MoS ₂	509
5. Magnetic properties of MoS ₂	514
6. Applications of MoS ₂ nanoflakes.....	519
6.1 MoS ₂ for electrocatalytic applications	519
6.2 MoS ₂ for anti-angiogenic and anti-cancer theranostics.....	525
7. Conclusion.....	532
References.....	533
Chapter 20: Effect of defects and functionalization on mechanical and fracture properties of two-dimensional nanomaterials.....	543
<i>Bharat Bhushan Sharma and Avinash Parashar</i>	
1. Introduction	543
2. Classical mechanics-based molecular dynamics.....	547
3. Defect engineering.....	550
3.1 Effect of point defects	550
3.2 Effect of line defects or grain boundaries	555
4. Chemical functionalization	558
5. Conclusion.....	564
References.....	564
PART 9: The impact of nanomaterials on health and safety	
Chapter 21: Occupational health and safety measures of multifunctional nanoparticles in biomedical research and beyond	571
<i>Maya Nair, Anjali Chandra, Riyaz Basha, V. Gayathri, Matthew Moncus, Helen Orimoloye, Nandakumar Kalarikkal, Zara Soomro, and Jamboor K. Vishwanatha</i>	
1. Multifunctional nanoparticles in biomedical research and application	572
1.1 Liposomes	573
1.2 Proteoliposomes	574
1.3 Nanopolymers	575
1.4 Lipoprotein nanoparticles	575
1.5 Inorganic nanoparticles.....	575

1.6 Quantum dots	575
1.7 2D MXenes	576
2. Toxicity of nanoparticles	576
2.1 Adverse health effects from exposure to nanoparticles.....	577
2.2 Nanomaterials—primary health and safety concerns	580
3. Exposure to nanomaterials.....	581
3.1 Occupational exposure to nanomaterials.....	581
3.2 Nanomaterials exposure through consumer products	581
4. Occupational safety and health management systems for multifunctional nanoparticles.....	581
4.1 Challenges for regulating multifunctional nanoparticle	582
4.2 Risk assessment and risk management	583
4.3 Preliminary hazard assessment.....	583
4.4 Nanotechnology Research Center risk assessment and risk management.....	583
5. Minimize exposure to nanomaterials	585
5.1 Changing the form of the nanomaterial.....	585
5.2 Changing the work activity	585
5.3 Engineering control.....	586
5.4 Administrative control	586
5.5 Personal protective equipment.....	586
5.6 Challenges with personal protective equipment	586
6. Regulatory agencies for nanomedicine	588
6.1 US Nanotechnology Characterization Laboratory	588
6.2 European Nanotechnology Characterization Laboratory	588
7. Occupational health research in nanomaterials and nanotechnology	589
7.1 EUnetHTA—Europe Health Technology Assessment.....	589
7.2 The National Institute for Occupational Safety and Health/Centers for Disease Control and Prevention	590
7.3 Nanotechnology Research Center	590
7.4 NIOSH logic model	591
7.5 NIOSH partnerships.....	592
7.6 Nanotechnology Research Center—standards development organizations	593
7.7 NIOSH international activities	593
7.8 Organization for economic co-operation and development	594
7.9 Extramural nanotechnology research activities NIOSH	594
7.10 RIVAM — Dutch National Institute for public health and the environment.....	595
7.11 Nano Commons.....	595
7.12 Asia Nano Forum.....	596
7.13 Center for Research and Development Strategy, Japan Science and Technology Agency	596

Contents

8. World Health Organization guidelines on “protecting workers from potential risks of manufactured nanomaterials”	597
9. Conclusion.....	597
References.....	598
Index	611

Transport properties of nanoscopic solids as probed by spectroscopic techniques

Dejan M. Djokić¹, Novica Paunović¹, Bojan Stojadinović¹,
Dimitrije Stepanenko¹, Saša Lazović², Zorana Dohčević-Mitrović¹

¹Nanostructured Matter Laboratory, Institute of Physics Belgrade, University of Belgrade, Belgrade, Serbia; ²Biomimetics Laboratory, Institute of Physics Belgrade, University of Belgrade, Belgrade, Serbia

Chapter Outline

- 1. Introduction 9
- 2. Raman scattering 10
 - 2.1 Short introduction to Raman scattering technique 10
 - 2.2 Multiferroic BiFeO₃ nanoparticles 13
- 3. Infrared reflection 21
 - 3.1 Short introduction to infrared reflection technique 21
 - 3.2 Doped nanocrystalline CeO₂ 24
- 4. Electron spin resonance 26
 - 4.1 Short introduction to electron spin resonance technique 26
 - 4.2 Carbon nanotubes 30
- 5. Concluding remarks 32
- Acknowledgments 33
- References 34

1. Introduction

Nanoscale world is at the border between the quantum realm at the smaller dimensions and the classical one at larger. At the quantum side of this divide, systems under consideration consist of few particles and the properties of the sample often do not average into well-behaved quantities with deviations from the mean value much smaller than the mean value itself. So standard assumptions of both the classical physics and the standard statistics can break down within the nanoscale domain. This occurrence impacts the methods for probing the transport at the nanoscale.

Noncontact measurements of transport can offer distinct advantages. Macroscopic contacts necessary for the standard transport measurements often disturb the system since they are immensely larger than it. The structure of the contacts needs to impact the system as little as possible, requiring cooling to very low temperatures. Thermal noise introduced by contacts is hard to distinguish from the quantum noise that is an interesting property of the probed system.

Experiment is always performed on an object composed of nonidentical units and averaging of the properties does not automatically occur within the measurement apparatus. Moreover, the most interesting properties are often encoded into distribution of the results of measurements, and not exclusively in their mean values. Quantum side of the breakdown is somewhat different. The quantum transport theory deals with universality of the transport. In the quantum limit, as most transparently seen in the Landauer formula for conductivity, the whole variety of the transport behavior boils down to the number and transmitivities of transport channels. The variety of quantum behavior in transport appears due to macroscopic quantum phenomena or lies hidden in the variability of nominally identical nanoscale systems.

To probe the rich variety of transport phenomena at the nanoscale, it is preferable to look at the properties of conducting quasiparticles than to look at the integral characteristics of a collection of them. Quasiparticles are most easily accessed through spectroscopic techniques, like Raman spectroscopy, electron spin resonance (ESR), and infrared reflection (IRR) spectroscopy. Resonant nature of excitations and response detection in spectroscopy offer us a way to discriminate between constituents of the nanoscale system and look exclusively at the processes that are in resonance with the appropriate driving. Therefore the noncontact spectroscopic measurements give us an opportunity to see the nanoscale world in more detail.

This chapter is partitioned in three sections which are organized as follows. In the first section, we provide a short introduction to the Raman scattering technique followed with a review on an indirect finding of the two different variable range hopping (VRH) transport mechanisms based on the analysis of the temperature dependent electronic Raman background of nanocrystalline BiFeO_3 [1]. The subsequent section tackles a summary on how both particle size decreased and Nd doping influence the Plasmon–phonon interaction and optical conductivity in CeO_{2-y} nanocrystals investigated by IRR spectroscopy [2]. Finally, in the third section, the main aspects of conduction ESR have been briefly introduced in which terms the temperature evolution and character of transport properties of single-walled carbon nanotubes have been elaborated [3].

2. Raman scattering

2.1 Short introduction to Raman scattering technique

In solid state spectroscopy, the inelastic scattering of photons by lattice vibrations (LVs) is known as Raman effect. The photon energy can be lost or gained in such processes, which

is accomplished by the phonon creation or annihilation, and termed in literature as Stokes or anti-Stokes Raman excitation, respectively. Brillouin Raman scattering (RS), however, stands for a particular case of RS that concerns the scattering by acoustic phonons of very low frequencies, unlike common Raman which involves optical phonons. The theory of Raman spectroscopy can be found elsewhere. Nevertheless, for a rather comprehensive elaboration the reader is further referred to seminal Mitra's work [4], some of which fragments we will rely on in what follows.

Following the first principles of electromagnetism, the incident electromagnetic field of the photons is coupled with the phonons via dipole moments that are induced by the phonon field. The electronic 3×3 polarizability tensor α_{mn} is modulated by the variation of the lattice due to the normal vibration of frequency ω_p and can be expanded in terms of the time dependent atomic displacement components $u_p = u_p(0)e^{i\omega_p t}$ as

$$\alpha_{mn} = \alpha_{mn}^{(0)} + \sum_p \alpha_{mn,p}^{(1)} u_p + \frac{1}{2} \sum_p \sum_q \alpha_{mn,pq}^{(2)} u_p u_q + \dots \quad (2.1)$$

where

$$\alpha_{mn,p}^{(1)} = \left(\frac{\partial \alpha_{mn}}{\partial u_p} \right)_{u_p=0}, \quad \alpha_{mn,pq}^{(2)} = \left(\frac{\partial^2 \alpha_{mn}}{\partial u_p \partial u_q} \right)_{u_p=0, u_q=0} \dots \quad (2.2)$$

If \vec{E} denotes the electric field of incident electromagnetic radiation with frequency ω ,

$$\vec{E} = \vec{E}(0)e^{i\omega t}, \quad (2.3)$$

then the induced dipole moment can be written as

$$\vec{M} = \hat{\alpha} \vec{E}, \quad (2.4)$$

which ultimately yields induced dipole moment along p mode

$$\vec{M}_p = \hat{\alpha}^{(0)} \vec{E}_0 e^{i\omega t} + \hat{\alpha}^{(1)} \vec{E}_0 e^{i(\omega \pm \omega_p)t} u_p(0) + \hat{\alpha}^{(2)} \vec{E}_0 e^{i(\omega \pm 2\omega_p)t} u_p^2(0) + \dots \quad (2.5)$$

First term in Eq. (2.5) represents nothing but elastic Rayleigh scattering process. The energy of the electromagnetic radiation remains unchanged in this case. The derivative of the electronic polarizability in the second term in Eq. (2.5) gives rise to the first-order RS processes when incident photon $(\hbar \vec{k}_1, \hbar \omega_1)$ is absorbed or created to create or destroy a phonon $(\hbar \vec{k}, \hbar \omega)$. The final photon, with both different wave vector and frequency $(\hbar \vec{k}_2, \hbar \omega_2)$ from the incident one, gets emitted in such a way that the energy and the momentum are totally conserved. Reduced Planck's constant is denoted as \hbar .

In doped semiconductors and disordered metals, spectral recoil of light in RS consistently comprises a number of distinctive peaks generated by optically active phonons, as well as, an extended frequency continuum which is in direct relationship with electronic response [6]. This continuous spectral background originates from low-energy electronic excitations, which reflects the charge carrier scattering rate, and is familiarly known in literature as the Raman electronic background [1,7–11]. Falkovsky [7] was first to provide a theoretical foundation for the spectral profiles of Raman electronic background in “dirty” metals. The effects of electronic excitations in Raman are usually observed at low-energy scales and are attributed to scattering by phonons or impurities involving finite momentum transfers ($k \neq 0$) as a result of the finite penetration depth of light in materials. Later on, Zawadowski and Cardona [8] proposed a Feynman diagrammatic approach to estimating the Kubo spectral response function within the scope of ladder approximation [12] at $q \approx 0$. Most importantly, these authors were first to recognize an intimately related link between the nonresonant electronic excitations seen in Raman with the carrier transport.

As with nonresonant RS electronic response, the related Feynman diagrams (see Fig. 2.1) are composed of wavy lines denoting photon propagators. Their initial and final (momentum, energy) are respectively $(\hbar \vec{k}_1, \hbar \omega_1)$ and $(\hbar \vec{k}_2, \hbar \omega_2)$. An electron-hole pair of (momentum: $\vec{k} = \vec{k}_1 - \vec{k}_2$, energy: $\omega = \omega_1 - \omega_2$), scattered by phonons and/or impurities, become generated by the incoming photon propagator. Phonon propagator, given in dashed line (Fig. 2.1), can be excited by the electron/hole inside a pair and is further captured by its counterpart (hole/electron), as is enforced by the ladder approximation. At last, upon summing up all the dominating ladder-like diagrams, Raman differential cross section due to the purely electronic response [9,11], reads as

$$\frac{d^2\sigma}{d\omega d\Omega} \propto \frac{1}{1 - \exp(-\hbar\omega/k_B T)} \times \frac{\omega\tau}{1 + (\omega\tau)^2}. \quad (2.6)$$

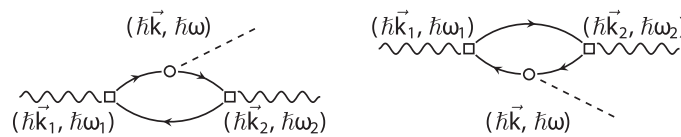


Figure 2.1

Raman scattering of light (wavy lines) due to phonons (dashed lines). Electron-hole formations (solid lines) represented via loops in the Feynman diagrams of third order (first order Raman scattering). Processes involving electron and hole contributions are given in left and right diagrams, respectively. Vertex \square represents electron-photon interaction, while vertex \circ represents electron-phonon interaction as is given in Ref. [5]. *The drawing is adapted from D.M. Djokić, B. Stojadinović, D. Stepanenko, Z. Dohčević-Mitrović, Probing charge carrier transport regimes in BiFeO₃ nanoparticles by Raman spectroscopy, Scr. Mater. 181 (2020) 6–9. <https://doi.org/10.1016/j.scriptamat.2020.02.008>.*

At a particular value of the effective scattering rate, $1/\tau$, the proportionality factor in Eq. (2.6) is a function of different variables depending on the type of the experimental setup [10]. The temperature-dependent Bose-Einstein factor and expression resembling Drude function are respectively given as the second and third term in the product of Eq. (2.6), while $1/\tau$ involves two terms in the sum as follows

$$1/\tau = 1/\tau_0 + Dq^2. \quad (2.7)$$

$1/\tau_0$ stands for the charge carrier scattering rate due to phonons/impurities in $q \rightarrow 0$ limit, which is concerned with nothing but bulk channels. The second term (Dq^2), however, gives rise to the effects of processes nonconserving momenta, very often pronounced in nanocrystals [1]. It is safe to neglect the bulk term ($1/\tau_0$) if there is no experimental evidence for the electronic Raman background in the case of bulk materials. D is the diffusion constant which is, based on the Einstein relation, related to electric conductivity σ in the following manner

$$D = \sigma / (g(\varepsilon_F) e^2), \quad (2.8)$$

where $e = 1.6 \times 10^{-19}$ C. The average value of the electronic density states close to the Fermi level [9] is denoted with $g(\varepsilon_F)$.

2.2 Multiferroic BiFeO₃ nanoparticles

Crystalline bismuth ferrite stands for a multiferroic material increasingly attracting the attention among the researchers and is also one of few materials to provide both ferroelectric ($T_C \approx 1100$ K) and antiferromagnetic ($T_N \approx 643$ K) properties at room temperature [13] and even higher. It is important to know that BiFeO₃ has proven undemanding to obtain in ambient conditions. BiFeO₃ is classed as rhombohedrally distorted ABO₃ perovskite structure (space group $R3c$) with lattice parameter $a_{\text{rh}} = 3.965$ Å, a rhombohedral angle α_{rh} of 89.30–89.48°, and ferroelectric polarization along $[111]_{\text{pseudocubic}}$ direction at room temperature [14]. Primitive unit cell consists of two unit formulas and contains 10 atoms. This structure can be represented as two distorted perovskite unit cells, connected along the main pseudocubic diagonal $[111]$ to form a rhombohedral unit cell, as is given in Fig. 2.2A. Bi³⁺ ions are situated at A lattice sites and are surrounded by 12 oxygen atoms. On the other hand side, Fe³⁺ ions are located at B lattice sites, and they are surrounded by six oxygen atoms with which it forms a FeO₆ octahedron. In this configuration, Bi³⁺ and Fe³⁺ ions are shifted along $[111]$ direction, and two oxygen octahedrons are rotated around $[111]$ direction in the opposite directions by 14° that can be seen from the position of the green octahedrons in Fig. 2.2B. This means that the Fe-O-Fe angle deviates from 180° to amount nearly 154–156° [16,17]. The unit cell can also be described in a hexagonal frame of reference, where the hexagonal

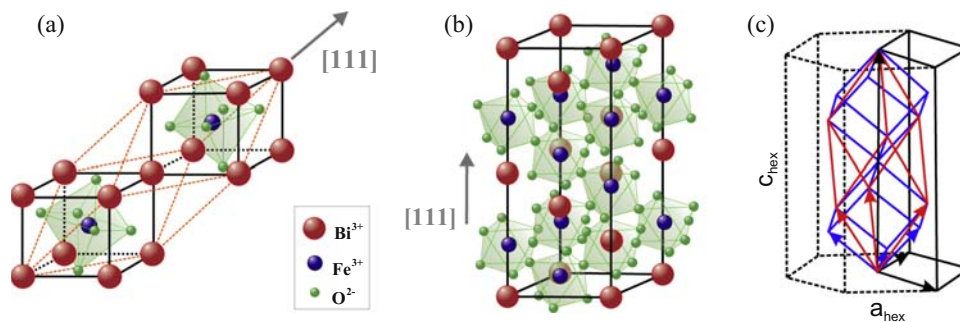


Figure 2.2

Schematic representation of (A) rhombohedral structure framed by orange dashed lines, (B) hexagonal perovskite structure of BiFeO_3 with $[111]$ ferroelectric polarization direction given in gray arrow, and (C) hexagonal cell (black), rhombohedral (red), and pseudocubic (blue) unit cell with corresponding unit vectors drawn in arrows. The figure is to a rather large extent reworked from J.-G. Park, M.D. Le, J. Jeong, S. Lee, *Structure and spin dynamics of multiferroic BiFeO_3* , *J. Phys. Condens. Mat.* 26 (2014) 433202. <https://doi.org/10.1088/0953-8984/26/43/433202>.

c -axis is aligned parallel to the diagonals of the perovskite cube. In other terms, $[001]_{\text{hexagonal}} \parallel [111]_{\text{pseudocubic}}$. The corresponding hexagonal lattice parameters (Fig. 2.2C) are $a_{\text{hex}} = 5.579 \text{ \AA}$ and $c_{\text{hex}} = 13.869 \text{ \AA}$ [14,18].

Bulk BiFeO_3 is a semiconductor with literature values of the bandgap determined by optical measurements at room temperature in the range from 2.1 to 2.8 eV. Several authors claim that BiFeO_3 has a direct bandgap transition at about 2.1–2.8 eV [19–22]. There are, however, published studies in which it has been shown that BiFeO_3 has an indirect bandgap transition of about 0.4–1.0 eV, quite smaller as compared to the values obtained for the direct transition [23]. Density functional theory calculations [24,25] have corroborated an indirect energy transition of about 2.1 eV, while in the room temperature absorption spectra recorded on BiFeO_3 thin film, the transition at approximately 2.17 eV has been observed [26].

Finally, according to Catalan and some of the references therein [16], based on two-probe DC resistivity measurements carried out on high-quality bulk samples of BiFeO_3 , the log resistivity value undergoes two slopes in Arrhenius law with increasing temperature. Actually, it has been found that the activation energy of the charge carriers decreases from nearly 1.3 down to nearly 0.6 eV as the material is heated above T_N with the anomaly around it. However, one does not expect such type of conducting behavior when the scale of the crystal moves down to several nanometers. Indeed, in the case of defective nanoparticles with a core/shell structure [1], the nanoparticle shell may have metallic and/or semiconducting features, while the nanoparticle core prominently features insulating properties. This casts a shadow over models that are commonly applied in pristine bulk materials to fit the resistivity data in systems with disorder and/or decreased dimensions.

At a scale ranging down to nanometers, BiFeO₃ has proven very prospective for a potential use in satellite communications, electrically accessed magnetic memory, commercial applications for photovoltaics and alternative sensors [16]. Most essentially, the electric resistance of BiFeO₃ is found to be a key parameter that should comply with the prime industrial requirements. Accomplishing high-electric conductivity value in this nanoscopic compound from its powders is one of the major assets and is perceived as a very promising in development of the novelty. Moreover, it proves quite demanding to identify the charge carrier transport, as well as, to distill electric conductivity value using the contact probes themselves invasively [27,28]. On the other hand, RS tool is widely known as a local and highly informative experimental probe capable of assessing the origin and dynamics of charge carriers in conducting materials. This makes Raman technique a reliable, yet noninvasive, means for investigating the transport properties of materials that are treated with utmost delicacy.

Fairly recent temperature-dependent RS study, carried out on the multiferroic BiFeO₃ nanoparticles of high purity and relied on the temperature evolution electronic Raman background [1], has explored an exciting prospect of extracting the relevant piece of information about the electric transport in this nanoscopic compound. μ -RS measurements were recorded over the temperature range of 80–723 K, while the related spectra were gathered at the backscattering arrangement with solid state 532 nm Nd:YAG laser as excitation at sub-mW laser powers on the sample itself. There were more than 13 optical phonon modes (symmetry: A_1 and E) detected in the experiment, while the spectra were decomposed with Lorentzian lineshape profiles, as is presented in Fig. 2.3 at four different temperatures. The entire number, together with frequency positions, of the optically active phonon modes of BiFeO₃ nanoparticles detected with Raman were found exactly the same with those observed in temperature-dependent RS spectra undertaken for bulk crystalline BiFeO₃ [29]. However, the authors [1] properly commented on the emerged splittings of a number of few polar LO+TO phonon modes, which naturally appear in the case of BiFeO₃ nanoparticles [30,31]. As with bulk, the prediction based on the factor group analysis turns out to be in accordance with the experiment implying 13 ($4A_1 + 9E$) optically active modes in phonon Raman spectra [32].

In contrast to Raman spectra recorded for on bulk BiFeO₃, Raman active optical modes pertinent to BiFeO₃ nanoparticles were evidenced to seat on quite a broad spectroscopic profile (Fig. 2.3 shaded in light gray). Such a spectroscopic feature has a pronounced temperature dependence and is familiarly known as Raman electronic background. In literature, indeed there are spectroscopic backgrounds akin to one studied in Ref. [1] such as nonresonant Raman continuous profile observed in metal-oxide thin films [33]. However, the related profile is quite shapeless, moreover with strong intensity, and is ascribed to entirely electronic RS recoil independent of bands due to the phonons. This Raman electronic background emerges as a result of the surface roughness at atomic scale.

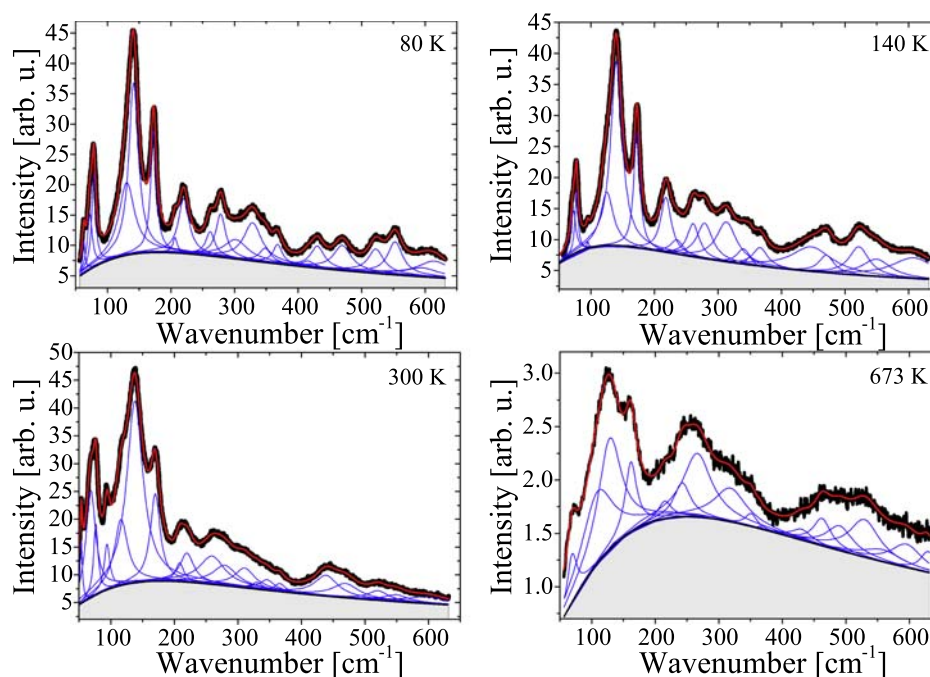


Figure 2.3

Raman scattering spectra given for four representative temperatures (data points presented in black). The spectra are composed of a continuous electronic background (shaded in light gray) and Lorentzian phonon peaks (lines in blue). The overall fitting line is drawn with red line. The figure is adopted from the published work D.M. Djokić, B. Stojadinović, D. Stepanenko, Z. Dohčević-Mitrović, *Probing charge carrier transport regimes in BiFeO₃ nanoparticles by Raman spectroscopy*, *Scr. Mater.* 181 (2020) 6–9. <https://doi.org/10.1016/j.scriptamat.2020.02.008>.

In addition, it has been reported that, in extremely small metallic particles [34] and metallic thin film islands with adsorbents [35], RS due to the particle-hole pair excitations brings about the emergence of the phononless continuous electronic background. This can be explained in terms of the momentum conservation violation generated in the presence of the electronic states at surface. Furthermore, even in the bulk hole-doped manganese perovskites, the broad electronic Raman response associated with the scattering by conduction electrons has been determined to cause a drastic change at the phase transition, as shown by Liu et al. [36]. The evolution of the effects of electron correlations in this compound could be assessed computably with temperature.

The authors of Ref. [1] have fittingly cast the surface states situated at particle boundaries in the role of localization centers via which the conduction can run efficiently. In terms of energy, these states are located near the vicinity of the Fermi level and they are, in general, unequally distributed to evolve with both spatial and energy gap between them. Therefore, the charge carrier conduction mechanism in which the hopping energy varies

with the hopping range can be safely modeled for description of the transport over an extended temperature range in disordered semiconductors and/or amorphous solids, such as nanoscaled materials. Commonly, exceptionally high-electric resistivity values are observed in such systems. As such, these values serve as a definite fingerprint to rule out any conventional metallic/semiconducting type of conductivity mechanism intrinsic to (semi)conductors. VRH mechanism, nonetheless [37], stands for a rather viable transport mechanism in nanoparticles with no other alternative acceptable, as was reported in Ref. [1] for BiFeO₃ nanoparticles. Two different types of VRH charge carrier transport mechanisms in 3D have been probed in a contactless way using temperature-dependent Raman spectroscopy, and it has been evidenced that these two are affected by different degrees of the electron correlation strengths on the opposite sides of the antiferromagnetic phase transition. Below the transition temperature, the transport undergoes the mechanism explained by Efros and Shklovskii [38], whereas at high temperatures, the charge carrier transport adheres to the traditional Mott VRH theory [37].

Here we provide a brief account of the Mott and Efros–Shklovskii laws based on a concise analysis from a seminal paper by Arginskaya and Kozub [39]. The central focus of this study was on a considerable diversity of theoretical results emerging from calculations for the exponential prefactors in various VRH expressions, as well as, the crossover from VRH conductivity of Mott type in which the density of electronic states at Fermi level is $g(\varepsilon \approx \varepsilon_F) = \text{const}$ toward VRH conductivity running via states separated by a Coulomb gap when $g(\varepsilon \approx \varepsilon_F) \propto \varepsilon^2$. Aharony et al. [40] have made an attempt to obtain the universal analytic expression for the temperature dependence of conductivity, $\sigma(T)$, in the crossover region from Mott to Efros–Shklovskii law. In general terms, temperature dependence of the VRH conductivity $\sigma(T)$ can be written down as

$$\sigma(T) = \sigma_n \exp\left(-\frac{T_n}{T}\right)^n, \quad (2.9)$$

where n might take on 1/4 or 1/2 in 3D with respect to the law chosen, Mott’s or Efros–Shklovskii’s. Constant factors σ_n and T_n depend on the preferred of the two models. However, the common feature of most of the relevant studies in the field of VRH boils down to simplistic approaches in estimating the exponential prefactor σ_n . As a traditional rule, σ_n is generally assumed to have no temperature dependence.

Factors σ_n and T_n , which are given in Eq. (2.9), can be computed straightforwardly by optimizing the correlation linking the energy and spatial separation between the lattice sites. Once an electric field is applied, hopping in the direction of the field is rather preferred at different probabilities with respect to both distance and energy separation. As with the 3D free electron case, in original Mott paper [37], it was in a simplified way presented that the hopping energy is inversely proportional to the cube of the hopping distance, while the hopping frequency ν for a given temperature T was found to depend on

two following parameters: r as the spatial distance between the sites in units of localization length ξ and W as their typical hopping energy separation. Namely,

$$\nu = \nu_0 \exp\left(-\frac{2r}{\xi} - \frac{W}{k_B T}\right), \quad (2.10)$$

where $\nu \equiv \nu_0$ for both $r = 0$ and $W = 0$, whereas $k_B = 1.38 \times 10^{-23}$ J/K stands for Boltzmann constant. The hopping frequency characterizes the relative number of directed charge carrier hops due to the electric field. Indeed, in noncrystalline systems, the variables r and W are not randomly independent so that one can be combined into a single parameter by minimizing the total exponent in (Eq. 2.10). In the actual fact, the hopping from one site to another with a lower energy/distance occurs at high rate. However, reaching both low energy/distance sites at the same time remains utterly impossible. The same reasoning applies for the large energy/distance sites that altogether justifies the application of variation method and thence the term “variable” in VRH.

Variable hopping processes translate a charge carrier by a range r within a time $\sim 1/\nu$, but at a preferred W value that maximizes the electric current via hopping. This proportionality squarely leads to the VRH expression for conductivity which is given in (Eq. 2.9). Yet, to relate r with W or vice versa, one has to further assume that most of the mobile carriers come from a narrow energy window near the Fermi level of width $\sim k_B T$. In such a way, the carrier density n_c of spin $S = 1/2$ which as the other factor prominently figures in the expression for the conductivity and can be computed by integration as

$$n_c = 2 \int_{\epsilon_F}^{\epsilon_F + k_B T} g(\epsilon) d\epsilon, \quad (2.11)$$

where $g(\epsilon)$ measures the total number of states (dN) per both energy (dE) and volume unit (V), each of which is double degenerated ($2S + 1 = 2$).

One must emphasize that the wise choice of $g(\epsilon)$ leads to the correct expression for the exponent T_n , which differs by switching from 3D Mott ($n = 1/4$) to Efros–Shklovskii regime ($n = 1/2$). Experimental measurements in disordered systems do reveal that the electron density of states (DOSs) may strongly vary in the vicinity of Fermi level, and it seems reasonable to suggest that the theoretical concept of uniform DOSs near the Fermi level is certainly insufficient to describe conduction mechanisms which account for the Coulomb gap, as there is a jump in the electron DOSs due to Coulomb interactions between localized states. In general, one can write down

$$k_B T_n = \begin{cases} c_p / (g(\epsilon_F) \xi^3), & \text{for } n = 1/4 \\ e^2 / (4\pi\epsilon_0 \epsilon_r \xi), & \text{for } n = 1/2 \end{cases} \quad (2.12)$$

where $k_B = 1.38 \times 10^{-23}$ J/K and $\epsilon_0 = 8.85 \times 10^{-12}$ F/m, while ξ stands for the localization length of electron wave function of the surface states. c_p represents the percolation constant varying from 5 to 20. ϵ_r corresponds to the relative permittivity constant. Nevertheless, even when the DOSs is not constant, the 3D Mott VRH conductivity pattern is fully recovered if presented like Eq. (2.9), but is rather referred to as the 3D Efros–Shklovskii VRH [38] when n is, in particular, equal to 1/2. In Ref. [41], a few temperature dependencies of the hopping conductivity, which come under exponent 1/4 or 1/2, are presented and the reader is further redirected to this reference to properly infer the validity of use of VRH at high temperatures in disordered materials.

Nanoscaled BiFeO₃ puts itself forward as a suitable candidate for exploring the crossover from 1/2 to 1/4 exponent VRH conductivity as demonstrated in Ref. [1] based on the Raman spectra. More interesting is the fact that crystalline BiFeO₃ nanoparticles do not only undergo a crossover but even a pronounced phase transition at ~ 640 K below which Coulomb correlations take place to form the antiferromagnetic ordering. Above the transition temperature, however, these correlations become overwhelmed by the temperature fluctuations through the concrete manifestation of the metallic-like paramagnetic state.

There is a presence of localized surface states occupying the energies near the Fermi level in the BiFeO₃ nanomaterial. These states through a mediation back the VRH transport even over a broad range of temperature. Temperature variations of $\ln(1/\tau)$, which is proportional to $\ln(\sigma)$ based on the Einstein relation from Eq. (2.8) are linearized against T^{-n} in Fig. 2.4A with $n = 1/2$ and Fig. 2.4B with $n = 1/4$, in the strongly correlated ($T < T_N$) and paramagnetic phase ($T > T_N$), respectively. Relying on the calculation for $\epsilon_r \approx 28$ from the impedance dielectric spectroscopy of BiFeO₃ nanoparticles [42] and following (12) one can find that $\xi \approx 7$ nm, while the DOSs $g(\epsilon_F)$ in the high-temperature phase nearly amounts 2.1×10^{18} localized states per (eV \times cm³). The result $\xi \approx 7$ nm is physically meaningful since $\xi < \langle \ell \rangle$, where the average particle size $\langle \ell \rangle \approx 66$ nm has been computed from the Gaussian particle size distribution recorded by Scanning Electron Microscopy at room temperature on BiFeO₃ (Fig. 2.4C and D). Finally, $\rho = 1/\sigma \approx 4\pi^2\tau / (\langle \ell \rangle^2 e^2 g(\epsilon_F)) \approx 350$ mΩcm, which stands for an extraordinarily high value that is not commonly encountered in conventional metals. This value goes beyond the maximum resistivity value (~ 1 mΩcm) limited by the Mott-Ioffe-Regel criterion [43,44], which categorizes crystalline BiFeO₃ nanoparticles into a family of bad conductors and ultimately suggests that the conduction bands are vanishing. This eliminates any possibility for the fixed thermally activated transport generic to intrinsic semiconductors to dominate over 3D VRH.

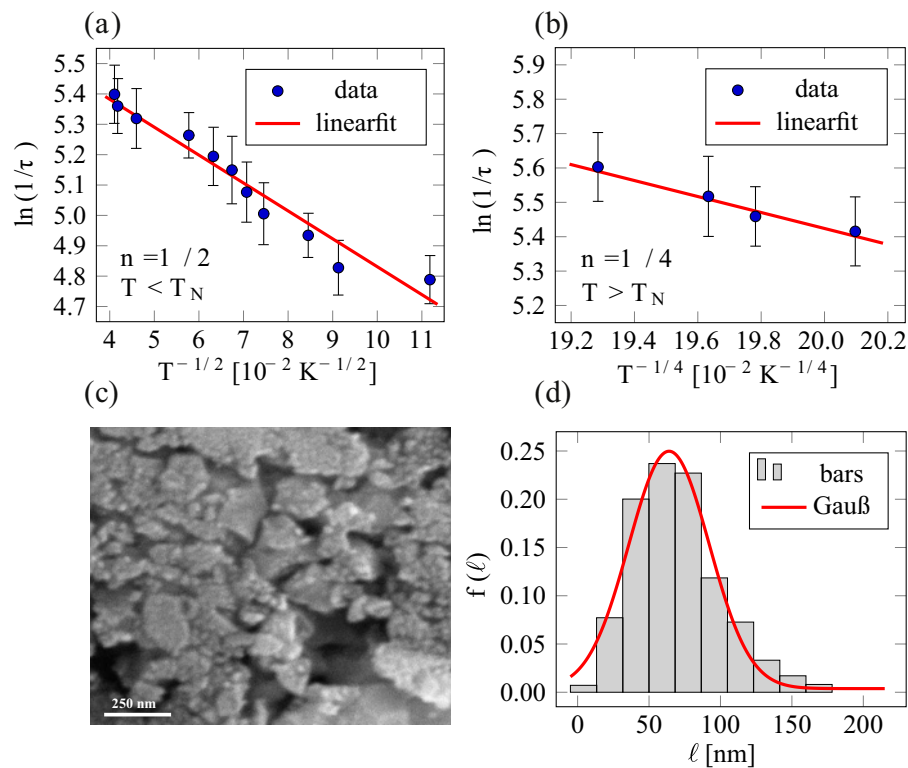


Figure 2.4

The dependence (T^{-n}) versus ($\ln(1/\tau)$) in both paramagnetic phase (subfigure (A), $n = 1/2$) and antiferromagnetic phase (subfigure (B), $n = 1/4$) with the linear fitting curves given in red.

The surface morphology of the nanocrystalline BiFeO_3 particles made with TESCAN SM-300 (subfigure (C)) and the corresponding histogram of the distribution of the particle size given in gray, fitted by the Gauß distribution (red line), where (64 ± 2) nm is mean value and (28 ± 2) nm is standard deviation (subfigure (D)). The frequency of occurrence is labeled as $f(\ell)$. The entire figure is taken from D.M. Djokić, B. Stojadinović, D. Stepanenko, Z. Dohčević-Mitrović, *Probing charge carrier transport regimes in BiFeO_3 nanoparticles by Raman spectroscopy*, *Scr. Mater.* 181 (2020) 6–9.

<https://doi.org/10.1016/j.scriptamat.2020.02.008>.

In certain disordered semiconductors, Ioffe and Regel [45], as well as Mott [46], have altogether realized that conduction states pertinent to such systems fail to survive due to the indefinite reduction in free mean path of carriers that scatters by. The key argument is that it can never become shorter than the typical interatomic spacing. In this case, the concept of carrier velocity cannot be properly formulated, and the entire coherent quasiparticle motion is lost. The notion of a minimum metallic conductivity is actually in accordance with a minimum mean free path.

Generally, the choice of 3D VRH ought to be provisionally accepted as an assumption. In the case of BiFeO₃ nanoparticles, the existence of the Mott VRH mechanism has already been deduced from the DC/AC measurements. These results are presented in Ref. [27]. Furthermore, the assumption about the validity of VRH is substantiated by the fact that the estimated resistivity value ultimately exceeds the Mott-Ioffe-Regel maximum (350 mΩcm ≫ 1 mΩcm). This implies that the conduction band energy sector tends to fade away leaving no room for the fixed thermally activated transport to prevail, which typically requires a markedly high density of conduction band states. Therefore, the BiFeO₃ nanoparticles are safe to be termed as bad conductors that retain metallic behavior, through qualitative features such as temperature evolution. Quantitatively, however, the bad conductors very much resemble the electric insulators as was observed in Ref. [1]. Specifically, the BiFeO₃ nanoparticle shell exhibits metallic behavior whereas the core insulator one, which is a case in defective nanoparticles with a core/shell structure.

3. Infrared reflection

3.1 Short introduction to infrared reflection technique

Infrared solid state spectroscopy stands for one of the most powerful and versatile techniques meant for optically probing a diverse family of materials in a contactless manner. The IRR response can assume either a purely electronic or a purely LV character. The two cases have distinctly different approaches to the quantitative treatment of the interaction processes between the radiation field and matter. The latter has conclusively proven powerful for analyzing propagating vibrations with which crystal structures can be revealed in ionic crystals and polar semiconductors. This analytical probe is highly useful even for systems poor in the degree of crystallinity, which is oftentimes encountered in nanoscopic matter.

In the long-wave limit ($q \approx 0$), optically active vibrations of an ionic bipartite lattice encapsulate the motion of one type of atoms relative to that of the other sublattice, yet both in spatial phase. The natural concomitants of such motions comprise strong electric dipoles of the material that can, accordingly, be directly coupled with the external electric field at a given polarization angle of the incident electromagnetic radiation. The theory of the IRR response originating from the interaction between the radiation field and the matter is purely phenomenological and can be found elsewhere [4,47,48], based on Maxwell's and the macroscopic equations describing the vibrations in a polar material. The reflective IRR spectroscopic recoil begins with a singularity in the dielectric function observed at the transverse optical (TO) frequency of the polar phonon mode. The singularity occurs as the radiation field of the incident electromagnetic wave couples with the TO phonon mode. Coulombic force effects in the polar crystal shift the LO mode to higher energies in contrast to the TO mode. The TO mode has a complex pole of the

complex dielectric response function $\tilde{\varepsilon}(\omega)$, whereas the LO mode is associated with a complex zero of $\tilde{\varepsilon}(\omega)$. Consequently, the incident infrared electromagnetic waves at frequencies over the so-called *reststrahlen* TO-LO window are dispersed in such a way that they fail to propagate through the condensed medium, but undergo reflection. In an ideal polar crystal with undamped oscillators, the frequency selective reflectivity amounts exactly 100%, but the reality is rather followed with the oscillator damping. Formally, the reflectivity is given by the Fresnel formula

$$R(\omega) = \frac{|\tilde{n}(\omega) - 1|^2}{|\tilde{n}(\omega) + 1|^2} = \frac{(n(\omega) - 1)^2 + \kappa^2(\omega)}{(n(\omega) + 1)^2 + \kappa^2(\omega)}, \quad (2.13)$$

where $R(\omega)$ is the frequency-dependent fraction of light intensity reflected. Complex frequency dependent index of refraction, $\tilde{n}(\omega)$, is related to the complex dielectric response as

$$\tilde{n}(\omega) = n(\omega) - i\kappa(\omega) = \sqrt{\tilde{\varepsilon}(\omega)}. \quad (2.14)$$

The frequency dependent real part, $n(\omega)$, and imaginary part, $\kappa(\omega)$ as the extinction coefficient, of the complex refractive index $\tilde{n}(\omega)$ satisfy the following relationships

$$\varepsilon_1(\omega) = n(\omega)^2 - \kappa(\omega)^2 \quad \text{and} \quad \varepsilon_2(\omega) = 2n(\omega)\kappa(\omega), \quad (2.15)$$

where finally

$$\tilde{\varepsilon}(\omega) \equiv \varepsilon_1(\omega) + i\varepsilon_2(\omega). \quad (2.16)$$

For this reason, it is of uppermost importance to model, as well as, parametrize $\tilde{n}\varepsilon(\omega)$ that properly describe the system probed by the IRR technique.

IRR signal of poorly conductive ionic crystals with large splitting between TO and LO frequencies is commonly fitted with a complex dielectric function given by the following expression

$$\tilde{\varepsilon}(\omega) = \varepsilon_\infty \prod_j \frac{\omega_{\text{LO}j}^2 - \omega^2 + i\omega\gamma_{\text{LO}j}}{\omega_{\text{TO}j}^2 - \omega^2 + i\omega\gamma_{\text{TO}j}}, \quad (2.17)$$

where $\omega_{\text{LO}j}$ and $\omega_{\text{TO}j}$ are longitudinal and transverse frequencies of the j -th oscillator, respectively, while $\gamma_{\text{TO}j}$ and $\gamma_{\text{LO}j}$ are their energy dampings, and ε_∞ corresponds to the high-frequency dielectric constant ($\omega \rightarrow \infty$). This model presents four tunable parameters for each TO/LO mode and is employed for description of purely phononic spectra. The model is familiarly known as the LV model, or habitually, four-parameter factorized form of the dielectric function. Its major disadvantage consists in the fact that it considers no contribution from the itinerant electronic excitations, neither single particle nor collective [49].

However, a great deal of semiconductors has a sizable portion of itinerant charge carriers. Accordingly, the full description of the infrared optical reflectivity data of such materials has to allow for both phonon and electronically collective (plasmon) excitations. The cohabitation between the phonons and plasmons brings inexorably about a somewhat pronounced interaction between the plasmons and LO phonons. This effect becomes the most striking if the plasma frequency ω_p lies situated close to the LO phonon energy. In this case, the complex dielectric function [50] can be factorized to read as follows

$$\tilde{\varepsilon}(\omega) = \varepsilon_\infty \frac{\prod_{j=1}^{m+n} (\omega^2 + i\omega\gamma_{\text{LO}j} - \omega_{\text{LO}j}^2)}{\omega^m \prod_{j=1}^m (\omega + i\gamma_{Pj}) \prod_{j=1}^n (\omega^2 + i\omega\gamma_{\text{TO}j} - \omega_{\text{TO}j}^2)}, \quad (2.18)$$

where $\omega_{\text{TO}j}$ and $\gamma_{\text{TO}j}$ are frequencies and damping of the TO modes, respectively. γ_p represents the plasma damping rate. The equation directly expresses the coupled plasmon-LO phonon frequencies $\omega_{\text{LO}j}$ and damping rates $\gamma_{\text{LO}j}$. This model is in literature termed as the coupled plasmon-phonon (CPP) model.

In conducting oxides [48], on the other hand side, the Drude model can be employed with no coupling for fitting the infrared reflectivity spectra. The plasmon contribution to the complex dielectric function is expressed through the Drude term so that $\tilde{\varepsilon}(\omega)$ is composed of two additive terms in the following manner

$$\tilde{\varepsilon}(\omega) = \varepsilon_\infty \left(\prod_j \frac{\omega_{\text{LO}j}^2 - \omega^2 + i\omega\gamma_{\text{LO}j}}{\omega_{\text{TO}j}^2 - \omega^2 + i\omega\gamma_{\text{TO}j}} - \frac{\omega_p^2}{\omega(\omega - i\gamma_p)} \right). \quad (2.19)$$

The first product term is concerned with the pure phonon contribution, while the second term represents the contributions originating from the collective electronic excitations—plasmons. The $\omega_{(\text{TO}/\text{LO})j}$ and $\gamma_{(\text{TO}/\text{LO})j}$ are (TO/LO) frequencies and the related damping rates of the decoupled phonon modes. The ω_p and γ_p are the plasma frequency and its daping rate. This model brings us a material advantage in decoupling the phonon from the plasmon contributions, and is called the decoupled plasmon-phonon (DPP) model. Besides the aforementioned “classical” Drude term, sometimes the so-called Double-damped Drude term is used, as is given in

$$\tilde{\varepsilon}(\omega) = \varepsilon_\infty \left(\prod_j \frac{\omega_{\text{LO}j}^2 - \omega^2 + i\omega\gamma_{\text{LO}j}}{\omega_{\text{TO}j}^2 - \omega^2 + i\omega\gamma_{\text{TO}j}} - \frac{\omega_p^2 + i(\gamma_p - \gamma_0)\omega}{\omega(\omega - i\gamma_0)} \right). \quad (2.20)$$

The difference between the dynamic damping (γ_p) at plasma frequency and the static damping (γ_0) at zero frequency represents particular distinctiveness of this model. The second term in the additive form of $\tilde{\varepsilon}(\omega)$ turns into the classical Drude term once

$\gamma_P = \gamma_0$. The use of this model, which is also called DPP, provides more flexibility. In fact, a rather precise description of the parametrized complex dielectric function is offered by the model in numerical fittings based on it.

As with nanomaterials, the related IRR spectra can be properly analyzed using the Bruggeman effective medium approximation [51]. The basic Bruggeman model includes the influence of porosity as

$$\left(\frac{\tilde{\epsilon}(\omega) - \tilde{\epsilon}_{\text{eff}}(\omega)}{\tilde{\epsilon}(\omega) + 2\tilde{\epsilon}_{\text{eff}}(\omega)} \right) \tilde{f} + \left(\frac{1 - \tilde{\epsilon}_{\text{eff}}(\omega)}{1 + 2\tilde{\epsilon}_{\text{eff}}(\omega)} \right) (1 - \tilde{f}) = 0. \quad (2.21)$$

A decrease of the powder volume fraction as compared to the ambient air leads to a decrease in the reflectivity values, and thence the IRR features may become significantly broadened if there is a greater air fraction in the powder. For the binary material with a great degree of inhomogeneity, constituted of the material $\tilde{\epsilon}(\omega)$ and air ($\epsilon_{\text{air}} = 1$) with the volume fractions \tilde{f} and $1 - \tilde{f}$, respectively, the empirical relation for the complex effective dielectric function $\tilde{\epsilon}_{\text{eff}}(\omega)$ must obey the above-written equation.

3.2 Doped nanocrystalline CeO₂

As one of the most stable oxide of cerium, cerium dioxide CeO₂ is considered to be highly important functional material with outstanding applications in many various fields. It crystallizes into a fluorite face centered cubic structure with space group $Fm\bar{3}m$ (No. 225) to form a simple cubic oxygen suba lattice where the cerium ions occupy alternate cube centers (see Fig. 2.5A) [52]. In terms of Wyckoff positions, Ce atoms are located at the centers of the tetrahedrons (4a) (0,0,0) of which corners are populated with

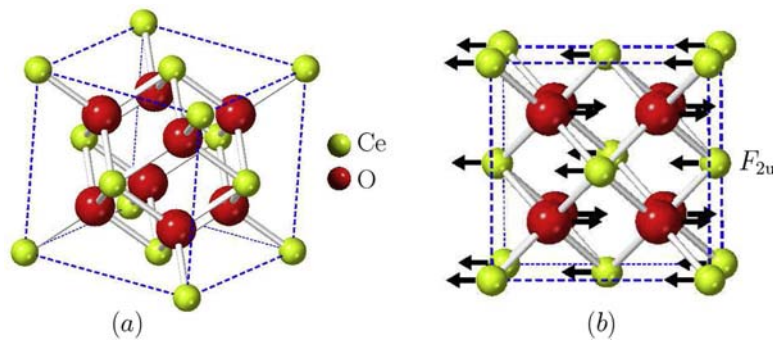


Figure 2.5

The fluorite face centered cubic crystal structure of CeO₂ (A) and its normal mode of the infrared active lattice vibrations of (B). Ce ions are denoted in green, while O ions are denoted in red.

oxygen ions (8c) (1/4, 1/4, 1/4). Observing the existence of the center of inversion, the structure has exactly one IRR (F_{2u}) and one Raman (F_{2g}) active mode [32], both of which are triple degenerated. As is shown in Fig. 2.5B, the normal mode of the infrared optically active vibrations consist of motions of both Ce and O atoms, but in the opposite directions.

Nanocrystalline CeO_2 is distinguished by its enhanced electric conductivity, size lattice relaxation, as well as, many other advantages to bulk CeO_2 . As to what has been reviewed in Ref. [53], decreasing particle size of crystalline CeO_2 particles down to nanoceria dioxide crystals results in the formation of oxygen vacancies which can be further employed as descriptors for determining the valence state of Ce in the nanoparticles. Actually, the large surface to volume ratio, then the inclination toward the oxygen consumption, and basically, freeing Ce because of the reversible transition between Ce^{3+} and Ce^{4+} ions altogether lead to enormous catalytic capacity of this material. Nanoscaled CeO_2 is furthermore found applicable to the active area of research for renewable energy, solid oxide fuel cells, water and air purification, optical glass polishing and decolorizing, UV ray filters, and many others [53].

Doped nanocrystalline CeO_2 , however, deserves a special attention as the optimal doping with Cu or Nd has proven efficient in inducing the semiconductor-to-metallic state crossover [2,52] in nanoceria dioxide. Moreover, electrons localized at the vacancies may behave like free charge carriers to contribute drastically to the electrical conductivity [54]. This originates from the presence of free charge carriers, which are numbered in the nanoceria lattice, as the number of oxygen vacancies becomes increased by Nd content [55].

Following Ref. [2], the IRR spectroscopy has been applied to nondestructively investigate the mechanism of the influence of the plasmon due to the enhanced conductivity upon the phonon spectra with increasing Nd content in nanocrystalline CeO_2 . This material is a polar semiconductor so that both phonon and plasmon excitations can be registered in the IRR spectra, whereby the plasmon-phonon coupling mechanism can be explored, while the extent to which the system acquires metallicity can be assessed. Radović et al. [2] have recorded the infrared reflectivity spectra on pure and Nd-doped CeO_{2-y} nanopowders at ambient temperature in far-infrared region from 100 up to 700 cm^{-1} .

Fig. 2.6 shows the IRR spectra of undoped and Nd-doped CeO_{2-y} nanopowders fitted with the two models: coupled plasmon-phonon and decoupled plasmon-phonon with double-damped Drude term. The concentration of the dopant is increased from 0% to 25%. The IRR spectra markedly differ from those done on bulk CeO_2 , as the bulk reststrahlen region is split into two extended TO-LO modes over $200\text{--}550\text{ cm}^{-1}$ range with decreasing crystallite size. The splitting is more pronounced in samples with rather small crystallite sizes and is accompanied with the redshift of the two LO modes, as well. Also, one can

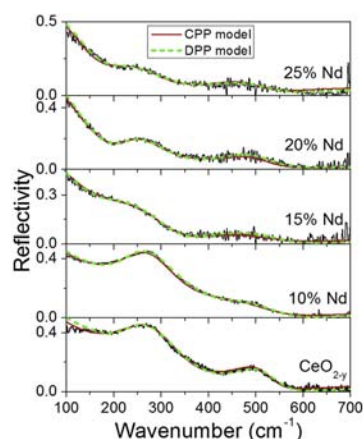


Figure 2.6

Infrared reflectivity spectra of undoped and Nd-doped CeO_{2-y} nanopowders involving the two theoretical fits based on coupled plasmon-phonon and decoupled plasmon-phonon model. *The credits for the figure are given to M. Radović, Z. Dohčević-Mitrović, N. Paunović, S. Bošković, N. Tomić, N. Tadić, I. Belča, Infrared study of plasmon-phonon coupling in pure and Nd-doped CeO_{2-y} nanocrystals, J. Phys. D Appl. Phys. 48 (2015) 065301–065306. <https://doi.org/10.1088/0022-3727/48/6/065301>.*

notice that with the raise of the dopant concentration, the low energy Drude tail and the screening of the phonon modes became more and more prominent, due to the strong presence of the free charge carriers. In the actual fact, increasing Nd content in the nanoceria dioxide lattice can generate a huge number of oxygen vacancies [2], while the plasmon-phonon interaction in the Nd-doped samples gets stronger.

Following the fits based upon both models applied (Fig. 2.6), all the plasmon modes registered in all nanoceria dioxide samples exhibit a frequency decrease with Nd doping, as can be seen from Fig. 2.7. The shift in the plasma frequency toward lower energies with increasing Nd concentration occurs owing to the weighted effective charge carrier mass, as there is no dopant impact on the free carrier concentration [2]. In fact, the plasma frequency is inversely proportional to the effective electron mass. This feature, together with the enhanced plasmon-phonon coupling with Nd doping, affords us a better insight into the transport properties of crystalline nanoceria based on the infrared-derived optical conductivity [48].

4. Electron spin resonance

4.1 Short introduction to electron spin resonance technique

ESR exemplifies a very sensitive and informative experimental technique, based on the use of magnetic field, which continues to find countless applications not only in solid state and

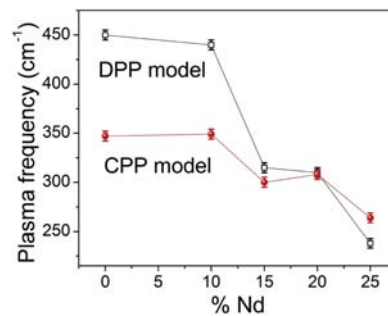


Figure 2.7

Evolution of the plasma frequency with the increased Nd dopant concentration as inferred from the two models: coupled plasmon-phonon and decoupled plasmon-phonon. *The credits for the figure are given to M. Radović, Z. Dohčević-Mitrović, N. Paunović, S. Bošković, N. Tomić, N. Tadić, I. Belča, Infrared study of plasmon-phonon coupling in pure and Nd-doped CeO_{2-y} nanocrystals, J. Phys. D Appl. Phys. 48 (2015) 065301–065306. <https://doi.org/10.1088/0022-3727/48/6/065301>.*

nano, but also in biomedical and environmental sciences. By means of ESR spectroscopy, one is able to directly probe electron spin response at resonance that certainly makes ESR as one of the most powerful probe to investigate magnetic properties in various compounds. More interestingly, ESR stands for both noninvasive and contactless tool with ability to analyze accurately the nature and dynamics of charge carriers in conductive systems no matter how their geometry welcomes electrical leads and contacts in an electrical circuit.

Familiarly known as CESR in abbreviated term, conduction electron spin resonance has captivated much scientific attention for its capacity to measure the electrical conductivity of systems from bulk over microsized down to nanoscopic conducting materials. In the actual fact, in the conducting systems, the free electron motion exerting eddy current leaves an impact upon the recorded signal at resonance through asymmetry as the definite signature. This was originally recognized by Feher and Kip [56], Dyson [57] who put forward that asymmetric CESR lineshapes originate as linear combinations due to the two facts: (1) the attenuation of the AC field through the skin depth and (2) the capability of itinerant electrons to diffuse backward and forward through the skin depth region in many instances between consecutive spin flips that is only critical to transmission-based CESR techniques. In the case of transmissive CESR, magnetization can penetrate far deeply into metals unlike the AC magnetic field. This gives an extra contribution to enhancing the asymmetry of the signals at resonance [58,59].

Dating back to the 1950's, Freeman John Dyson is the first in the field to be credited with fully deriving the asymmetric CESR profiles. For the obvious reasons, such CESR lines are referred in literature to as Dysonians of which asymmetry extent is oftentimes quantified using A/B ratio (see the inset in Fig. 2.8), as common signature of metallicity in CESR experiments.

As with CESR operating in the reflection mode, Chapman et al. [61] developed an approach based on Dyson's theory to grasp both on- and off-resonance signal for the various crystal shapes, such as flat plates, long cylinders, and spheres. This allows the prediction of the asymmetric nature of CESR absorption profiles depending on geometry of the conducting samples with different size. Furthermore, Platzman and Wolf [62] examined spin waves excitations at resonance in paramagnetic metals that are described within the frame of Fermi-liquid theory. Their extended theory boils down to Dyson's in the limit of short momentum relaxation times. Dyson's theory was additionally generalized to involve various shapes of conducting crystals at desirable resonant magnetic field directions [63–65]. Later on, Kaplan pointed out that there is a substantial discrepancy between Dyson's theory and experimental results recorded in CESR based on the reflection mode [66]. Actually, CESR becomes recoiled rather with electric than magnetic component of the frequency-dependent electromagnetic field. The component of electric field is known to get easily coupled with the free electron momentum across the surface via relativistic spin-orbit interaction. This fact finds its application in the quantum mechanical density matrix method, which ultimately brings about the rather general form of CESR signal as [67]:

$$\chi''(\omega)\cos\phi + \chi'(\omega)\sin\phi. \quad (2.22)$$

Terms χ'' and χ' represent the absorptive and dispersive parts of the CESR signal. The magnitudes of their contributions are measured with $\cos\phi$ and $\sin\phi$, respectively, both of which disappear in the limit of highly conductive samples, where ϕ is the signal phase. Eq. (2.22) does represent a particular manifestation of Dysonian, which falls into the range of the so-called “NMR limit” [68,69]. In that case, the electron diffusion rate is considerably slower as compared to the spin relaxation rate, and there is no need to consider other limits so as to reasonably infer CESR spectra of usual metallic samples. Spin dynamics itself as regards this case can lead to nothing but Lorentzian-profiled absorptions (χ''), unlike the situations with reduced dimensionality or motionally narrowed signals [70,71].

In a recent CESR study [60], the authors have favored Kaplan's approach, made for analyzing the CESR lineshape, to impart a valuable piece of information on the conductivity of samples with different geometries. Key lengths and points of CESR lines, necessary for simplification of a fitting procedure of CESR lineshape, have been established in this account to analytically derive, as well as, grasp the geometry independent asymmetry ratio limit $A/B \rightarrow (5 + 3\sqrt{3})/4$, encountered in literature as universal 2.55 limit, when the CESR is carried out on extremely conducting samples. A/B ratio value markedly evolves once nano- or micro-sized metallic samples start to agglomerate into larger ones that makes the CESR technique especially helpful in

monitoring the extent to which the clustering takes place [72,73]. Moreover, in Ref. [60], the phase dependence of the asymmetry ratio A/B is given as

$$A/B = \frac{\left(1 + 2\cos\frac{2\phi}{3}\right) \left(3\cos\left(\frac{\pi}{6} - \frac{\phi}{3}\right) + \sin\phi\right)}{4\cos\left(\frac{\pi}{6} - \frac{\phi}{3}\right) \left(1 + \sin\left(\frac{\pi}{6} - \frac{2\phi}{3}\right)\right)^2}, \quad (2.23)$$

which can be further employed to relate A/B with the conductivity. Namely, Chapman et al. [61] introduced the parameter $\eta \equiv d/\delta$, where d represents the characteristic length of the sample (thickness or diameter), while δ is the skin depth at given resonant frequency. It is exactly this quantity that is in correlation with the sample conductivity. The absorptive and dispersive parts of the CESR signal in Ref. [61] are respectively $x(\eta)$ and $y(\eta)$ so that $y(\eta)/x(\eta)$ exactly corresponds to $\tan\phi$ in Ref. [60]. According to Ref. [61], $x(\eta)$ and $y(\eta)$ for the three relevant geometries look like

$$\begin{aligned} \text{Plate} \Rightarrow & \begin{cases} x(\eta) = \frac{\sinh(\eta) + \sin(\eta)}{2\eta(\cosh(\eta) + \cos(\eta))} + \frac{1 + \cosh(\eta)\cos(\eta)}{(\cosh(\eta) + \cos(\eta))^2}, \\ y(\eta) = \frac{\sinh(\eta) - \sin(\eta)}{2\eta(\cosh(\eta) + \cos(\eta))} + \frac{\sinh(\eta)\sin(\eta)}{(\cosh(\eta) + \cos(\eta))^2}. \end{cases} \quad (2.24) \\ \text{Cylinder} \Rightarrow & \begin{cases} x(\eta) = 1 - \frac{2(\text{Ber}(\vartheta)\text{Ber}'(\vartheta) + \text{Bei}(\vartheta)\text{Bei}'(\vartheta))(\text{Ber}(\vartheta)\text{Bei}'(\vartheta) - \text{Ber}'(\vartheta)\text{Bei}(\vartheta))}{(\text{Ber}^2(\vartheta) + \text{Bei}^2(\vartheta))^2}, \\ y(\eta) = \frac{(\text{Ber}^2(\vartheta) - \text{Bei}^2(\vartheta))(\text{Bei}'^2(\vartheta) - \text{Ber}'^2(\vartheta)) - 4\text{Ber}(\vartheta)\text{Bei}(\vartheta)\text{Ber}'(\vartheta)\text{Bei}'(\vartheta)}{(\text{Ber}^2(\vartheta) + \text{Bei}^2(\vartheta))^2}, \\ \text{where } \vartheta \equiv \eta/\sqrt{2}. \end{cases} \quad (2.25) \end{aligned}$$

$$\begin{aligned} \text{Sphere} \Rightarrow & \begin{cases} \frac{4}{9}x(\eta) = \frac{8 + \eta^4}{\eta^4} - \\ \frac{8(\sinh(\eta) + \sin(\eta))}{\eta^3(\cosh(\eta) - \cos(\eta))} + \frac{8\sinh(\eta)\sin(\eta)}{\eta^2(\cosh(\eta) - \cos(\eta))^2} + \frac{\sinh(\eta) - \sin(\eta)}{\eta(\cosh(\eta) - \cos(\eta))} - \frac{\sinh^2(\eta) - \sin^2(\eta)}{(\cosh(\eta) - \cos(\eta))^2}, \\ \frac{4}{9}y(\eta) = \\ \frac{8(\sinh(\eta) - \sin(\eta))}{\eta^3(\cosh(\eta) - \cos(\eta))} - \frac{4(\sinh^2(\eta) - \sin^2(\eta))}{\eta^2(\cosh(\eta) - \cos(\eta))^2} + \frac{\sinh(\eta) + \sin(\eta)}{\eta(\cosh(\eta) - \cos(\eta))} - \frac{2\sinh(\eta)\sin(\eta)}{(\cosh(\eta) - \cos(\eta))^2}. \end{cases} \quad (2.26) \end{aligned}$$

This set of the three dependencies allows us to compute A/B versus $\log \eta$ as is presented in Fig. 2.8. Oftentimes, A/B can be expanded in the form of the linear approximation with respect to either η or is proportional to the conductivity of the probed spins. The latter approximation works well in the case of the carbon nanotubes [3] of which CESR-based charge carrier transport is going to be discussed in detail throughout the upcoming section.

4.2 Carbon nanotubes

As a building brick that takes fascinating variety of forms such as diamond, fossil fuels, and graphite, together with innumerable compounds derived from it, carbon stands for one of the most impressive elements in the periodic table. Increased focus of renewed scientific interest in carbon has stepped into the realm of novel carbon-based materials, specifically known as the carbon allotropes at nanoscopic level, such as carbon nanotubes. These were first discovered as multiwalled forms by Iijima in 1991 [74] initiating the golden era of the physics and chemistry of carbon nanostructures. Carbon nanotubes are distinguished by their outstanding electronic, mechanical, and transport properties revealing uncorrelated (semi)conducting nature of the tubes in relation to the curvature and chirality. They also prove suitable for various applications which span from the use as light and electron emitters [75] up to optical biosensors for life sciences and biomedicine [76].

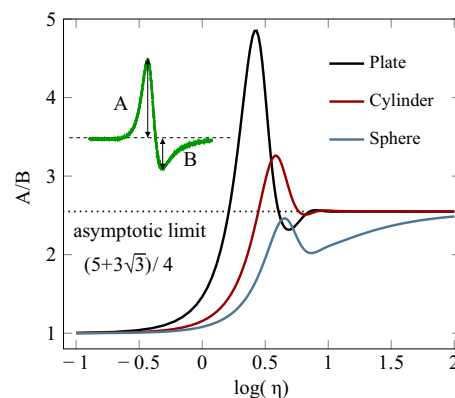


Figure 2.8

Asymmetry ratio A/B dependence on $\log(\eta)$ regarding the three relevant geometries: infinite plate (black), long cylinder (dark red), and sphere (dark blue). All the three curves converge to the asymptotic A/B ratio of $(5+3\sqrt{3})/4$ at $\eta \rightarrow \infty$. The inset represents graphically the A/B ratio in an arbitrarily selected CESR line. *The figure is adopted from D.M. Djokić, D. Stepanenko, Z. Dohčević-Mitrović, Extreme conduction electron spin resonance: $A/B \rightarrow (5+3\sqrt{3})/4$, the universal limit of lineshape asymmetry ratio, J. Magn. Magn. Mater. 491 (2019) 165616. <https://doi.org/10.1016/j.jmmm.2019.165616>.*

Even with the aid of nanoscaled technologies, making ideal electric contacts to adequately probe nanotube conductivity remains a perplexing puzzle. Electron backscattering, imbalanced injection of incident electron modes, and high-ohmic contact resistance are identified as the chief culprits at minuscule dimensions. However, nanotubes with large diameters have the added advantage of favoring low-ohmic contact resistance in a four-probe electric measurement [77]. This made them perfectly suited for the investigation of quantum interference caused by the Aharonov–Bohm effect specific by the pronounced magneto-resistance oscillations as a function of magnetic flux [78].

Despite their short diameters, transport electric properties of multiwalled nanotubes oftentimes remain consistent with theoretical models used to describe disordered conductors in $2D$. This might be explained by the fact that the electron wavelength is quite smaller than the nanotube diameter [79]. On the other hand side, one-dimensional essence of carbon nanotubes becomes already evident through specific heat and thermal lattice conductivity measurements since the phonon wavelength exceeds typical nanotube diameters [80], unlike the before-mentioned electron wavelength. Moreover, according to Ref. [81], it has been demonstrated that the electric transport in single walled carbon nanotubes exhibit a dependence in agreement with Luttinger liquid models.

Temperature and power-dependent CESR on an ensemble of metallic SWCNTs have been performed to infer their transport properties based on the insights into the spin dynamics [3]. The powder-form samples comprised acid-purified laser-oven SWCNTs which were prepared using the standardized annealing procedure, while the related CESR spectra were recorded as a function of temperature from 3.4 K to the ambient temperature at the X-band spectrometer. To yield a rather detailed insight into the transport mechanism, the authors of Ref. [3] studied the temperature evolution of the asymmetry Dysonian line shape parameter, $\alpha \equiv A/B$, which is to the first order approximation proportional to the conductance of the probed electron spins. These can relax by interaction with itinerant electrons that are present in metallic SWCNTs. In addition, the spin dephasing rate at resonance narrows with increasing temperature, which is a signature of the motional narrowing, a phenomenon that is particular to metallic systems.

Temperature dependence of the natural logarithm of conductivity, $\ln(\sigma)$ which in this case boils down to $\ln(\alpha)$, is oftentimes plotted versus n -th root of inverse temperature [41]. Exponent n provides information on the charge carrier transport mechanism and when n approaches $1/4$, it leaves a hallmark of 3D Mott VRH transport mechanism [37].

As shown in Fig. 2.9, the Dysonian asymmetry parameter tends to follow a three-dimensional variable-range hopping behavior at low T . From the scaling relationships in Eq. (2.12), the localization length of the electronic wave function, ξ , is roughly estimated to be ~ 100 nm, whereas the DOSs $g(\varepsilon_F)$ amounts $\sim 10^{19}$ localized states per $(\text{eV} \times \text{cm}^3)$

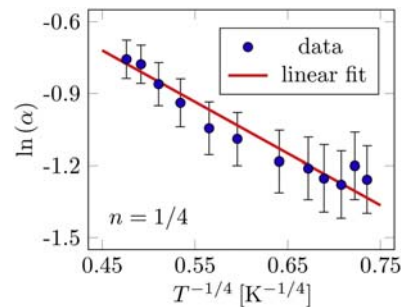


Figure 2.9

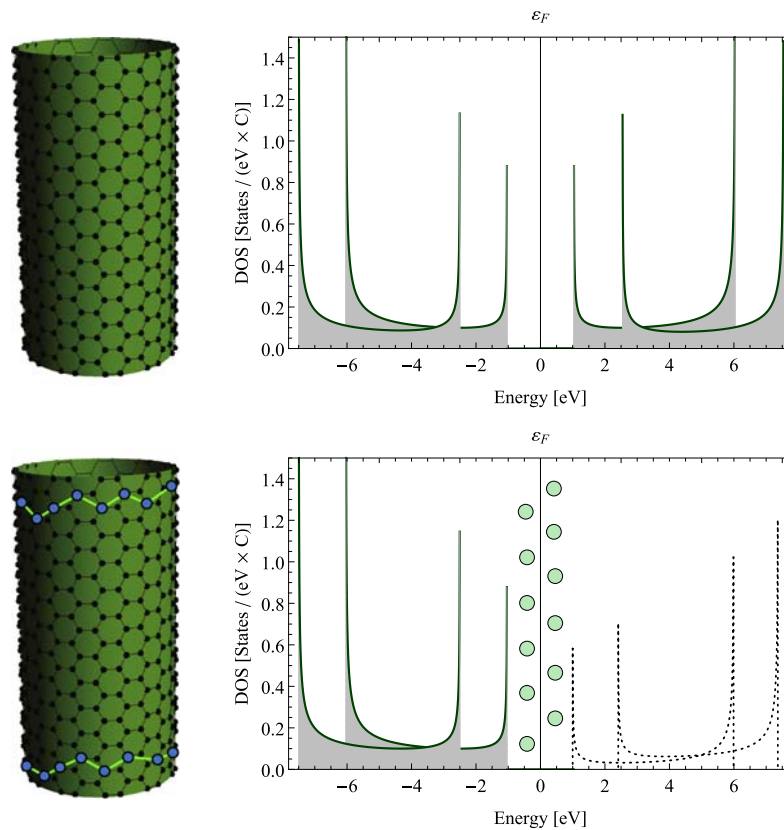
Natural logarithm of the asymmetry parameter, $\alpha \equiv A/B$, graphed versus the fourth root of inverse temperature. The logarithm is found to undergo the 3D VRH mechanism. *The data are taken from W.D. Rice, R.T. Weber, P. Nikolaev, S. Arepalli, V. Berka, A.L. Tsai, J. Kono, Spin relaxation times of single-wall carbon nanotubes, Phys. Rev. B 88 (2013) 041401–041405. <https://doi.org/10.1103/PhysRevB.88.041401>.*

around the Fermi energy. The traditional four-point probe transport measurements on the similarly prepared SWCNT samples [3] have, to some extent, corroborated the present picture of the CESR observed 3D VRH at low T .

As with nanoscopic systems such as SWCNTs, one can even venture to state that the VRH conduction mechanism, owing to the localized edge/surface states positioned around Fermi level, may extend even over a wide range of temperatures [1]. At high temperatures, the conduction mechanism in bulk systems commonly runs intrinsically via thermal activation through conduction bands. On the other hand side, there are, as a rule, defect states across the nanotube surface, effectively making its pristine length quite short and comparable to nanoscaled dimensions (Fig. 2.10). In this case, the overlaps between the orbitals decrease to cause the bands to become less dense. This leads to the band splittings to eventually open up wide gaps at rather high energies. Bands that are high in energy have, therefore, tendency to fade away so does the conduction band, as contrary to an ideally pristine SWCNT. It is thus reasonable to adopt that VRH mechanisms may apply up to somewhat higher temperatures in defected nanotubes. Certainly, the intrinsic thermally activated transport via conduction band can be ignored comparing to the VRH due to the evanescent DOSs, as is given in Fig. 2.10.

5. Concluding remarks

In summary, noncontact measurements of transport have been evidenced to offer various advantages to studying novel nanoscopic materials such as: multiferroic crystalline BiFeO_3 nanoparticles, doped nanocrystalline CeO_2 used for fuel cell applications, as well as,


Figure 2.10

Plots of the electronic density of states versus energy for an ideally pristine (upper part) and a defected semiconducting SWCNT (lower part), computed using the tight-binding model. The electronic states of the defects forming the effective SWCNT edges are given in *green circles*. They are distributed around Fermi level at zero energy above which the DOS perishes gradually as the energy goes higher.

single walled carbon nanotubes exploited for molecular electronics and spintronics. The transport properties of these novel multifunctional materials have been reviewed in this chapter in the light of noninvasive spectroscopic techniques which involve: RS, IRR, and ESR. Through brief introductions made at the beginning of each section, these three contactless spectroscopic tools have been described in detail.

Acknowledgments

The authors greatly acknowledge funding provided by the Institute of Physics Belgrade, through the grant by the Ministry of Education, Science, and Technological Development of the Republic of Serbia.

References

- [1] D.M. Djokić, B. Stojadinović, D. Stepanenko, Z. Dohčević-Mitrović, Probing charge carrier transport regimes in BiFeO₃ nanoparticles by Raman spectroscopy, *Scripta Mater.* 181 (2020) 6–9, <https://doi.org/10.1016/j.scriptamat.2020.02.008>.
- [2] M. Radović, Z. Dohčević-Mitrović, N. Paunović, S. Bošković, N. Tomić, N. Tadić, I. Belča, Infrared study of plasmon-phonon coupling in pure and Nd-doped CeO_{2-y} nanocrystals, *J. Phys. D Appl. Phys.* 48 (2015) 065301–065306, <https://doi.org/10.1088/0022-3727/48/6/065301>.
- [3] W.D. Rice, R.T. Weber, P. Nikolaev, S. Arepalli, V. Berka, A.L. Tsai, J. Kono, Spin relaxation times of single-wall carbon nanotubes, *Phys. Rev. B* 88 (2013) 041401–041405, <https://doi.org/10.1103/PhysRevB.88.041401>.
- [4] S.S. Mitra, *Infrared and Raman Spectra Due to Lattice Vibrations*, Springer US, 1969, pp. 333–451, https://doi.org/10.1007/978-1-4757-1123-3_14.
- [5] M. Cardona, *Light Scattering in Solids I - Introductory Concepts*, Springer-Verlag, Berlin, 1983.
- [6] L.A. Falkovsky, Investigation of semiconductors with defects using Raman scattering, *Phys. Usp.* 47 (2004) 249–272, <https://doi.org/10.1070/pu2004v047n03abeh001735>.
- [7] L.A. Falkovsky, Raman scattering of light by electrons in a metal with impurities, *Sov. Phys. JETP* 68 (1989) 661–663.
- [8] A. Zawadowski, M. Cardona, Theory of Raman scattering on normal metals with impurities, *Phys. Rev. B* 42 (1990) 10732–10734, <https://doi.org/10.1103/PhysRevB.42.10732>.
- [9] T.P. Devereaux, Theory for the effects of impurities on the Raman spectra of superconductors, *Phys. Rev. B* 45 (1992) 12965–12975, <https://doi.org/10.1103/PhysRevB.45.12965>.
- [10] E.Y. Sherman, O.V. Misochko, Raman scattering in metals with disorder: beyond the zero-momentum approximation, *J. Phys. Condens. Matter* 15 (2003) 3751–3758, <https://doi.org/10.1088/0953-8984/15/22/309>.
- [11] T.P. Devereaux, R. Hackl, Inelastic light scattering from correlated electrons, *Rev. Mod. Phys.* 79 (2007) 175–233, <https://doi.org/10.1103/RevModPhys.79.175>.
- [12] A.A. Abrikosov, L.P. Gorkov, I.E. Dzyaloshinsky, *Quantum Field Theoretical Methods in Statistical Physics*, Pergamon Press, Oxford, 1965.
- [13] H. Zhang, K. Kajiyoshi, Hydrothermal synthesis and size-dependent properties of multiferroic bismuth ferrite crystallites, *J. Am. Ceram. Soc.* 93 (2010) 3842, <https://doi.org/10.1111/j.1551-2916.2010.03953.x>.
- [14] F. Kubel, H. Schmid, Structure of a ferroelectric and ferroelastic monodomain crystal of the perovskite BiFeO₃, *Acta Crystallogr. B* 46 (1990) 698, <https://doi.org/10.1107/S0108768190006887>.
- [15] J.-G. Park, M.D. Le, J. Jeong, S. Lee, Structure and spin dynamics of multiferroic BiFeO₃, *J. Phys. Condens. Mat.* 26 (2014) 433202, <https://doi.org/10.1088/0953-8984/26/43/433202>.
- [16] G. Catalan, J.F. Scott, Physics and applications of bismuth ferrite, *Adv. Mater.* 21 (2009) 2463–2485, <https://doi.org/10.1002/adma.200802849>.
- [17] C.-H. Yang, D. Kan, I. Takeuchi, V. Nagarajan, J. Seidel, Doping BiFeO₃: approaches and enhanced functionality, *Phys. Chem. Chem. Phys.* 14 (2012) 15953, <https://doi.org/10.1039/C2CP43082G>.
- [18] J.D. Bucci, B.K. Robertson, W.J. James, The precision determination of the lattice parameters and the coefficients of thermal expansion of BiFeO₃, *J. Appl. Cryst.* 5 (1972) 187–191, <https://doi.org/10.1107/S0021889872009173>.
- [19] J.F. Ihlefeld, N.J. Podraza, Z.K. Liu, R.C. Rai, X. Xu, T. Heeg, Y.B. Chen, J. Li, R.W. Collins, J.L. Musfeldt, X.Q. Pan, J. Schubert, R. Ramesh, D.G. Schlom, Optical band gap of BiFeO₃ grown by molecular-beam epitaxy, *Appl. Phys. Lett.* 92 (2008) 142908, <https://doi.org/10.1063/1.2901160>.
- [20] Y. Xu, M. Shen, Structure and optical properties of nanocrystalline BiFeO₃ films prepared by chemical solution deposition, *Mater. Lett.* 62 (2008) 3600, <https://doi.org/10.1016/j.matlet.2008.04.006>.

- [21] A. Kumar, R.C. Rai, N.J. Podraza, S. Denev, M. Ramirez, Y.-H. Chu, L.W. Martin, J. Ihlefeld, T. Heeg, J. Schubert, D.G. Schlom, J. Orenstein, R. Ramesh, R.W. Collins, J.L. Musfeldt, V. Gopalan, Linear and nonlinear optical properties of BiFeO₃, *Appl. Phys. Lett.* 92 (2008) 121915, <https://doi.org/10.1063/1.2901168>.
- [22] J. Allibe, K. Bougot-Robin, E. Jacquet, I.C. Infante, S. Fusil, C. Carrétéro, J.-L. Reverchon, B. Marcilhac, D. Creté, J.-C. Mage, A. Barthélémy, M. Bibes, Optical properties of integrated multiferroic BiFeO₃ thin films for microwave applications, *Appl. Phys. Lett.* 96 (2010) 182902, <https://doi.org/10.1063/1.3402763>.
- [23] M. Shariq, D. Kaur, V.S. Chandel, M.A. Siddiqui, Investigation on multiferroic properties of BiFeO₃ ceramics, *Mater. Sci. Poland* 31 (2013) 471, <https://doi.org/10.2478/s13536-013-0128-2>.
- [24] S.J. Clark, J. Robertson, Band gap and Schottky barrier heights of multiferroic BiFeO₃, *Appl. Phys. Lett.* 90 (2007) 132903, <https://doi.org/10.1063/1.2716868>.
- [25] H. Wang, Y. Zheng, M.-Q. Cai, H. Huang, H.L. Chan, First-principles study on the electronic and optical properties of BiFeO₃, *Solid State Commun.* 149 (2009) 641, <https://doi.org/10.1016/j.ssc.2009.01.023>.
- [26] S.R. Basu, L.W. Martin, Y.H. Chu, M. Gajek, R. Ramesh, R.C. Rai, X. Xu, J.L. Musfeldt, Photoconductivity in BiFeO₃ thin films, *Appl. Phys. Lett.* 92 (2008) 091905, <https://doi.org/10.1063/1.2887908>.
- [27] A. Mukherjee, M. Banerjee, S. Basu, N.T.K. Thanh, L.A.W. Green, M. Pal, Enhanced magnetic and electrical properties of Y and Mn co-doped BiFeO₃ nanoparticles, *Physica B: Cond. Matt.* 448 (2014) 199–203, <https://doi.org/10.1016/j.physb.2014.03.082>.
- [28] S. Ruby, S.S.R. Inbanathan, Structural properties and electrical conduction mechanisms of Bi^{0.9}Sm^{0.05}Tb^{0.05}FeO₃ thin film, *Appl. Surf. Sci.* 449 (2018) 10–14, <https://doi.org/10.1016/j.apsusc.2017.11.231>.
- [29] H. Fukumura, H. Harima, K. Kisoda, M. Tamada, Y. Noguchi, M. Miyayama, Raman scattering study of multiferroic BiFeO₃ single crystal, *J. Magn. Magn. Mat.* 310 (2007) e367–e369, <https://doi.org/10.1016/j.jmmm.2006.10.282>.
- [30] J. Hlinka, J. Pokorny, S. Karimi, I.M. Reaney, Angular dispersion of oblique phonon modes in BiFeO₃ from micro-Raman scattering, *Phys. Rev. B* 83 (2011) 020101–020104, <https://doi.org/10.1103/PhysRevB.83.020101>.
- [31] J. Bielecki, P. Svedlindh, D.T. Tibebe, S. Cai, S.-G. Eriksson, L. Börjesson, C.S. Knee, Structural and magnetic properties of isovalently substituted multiferroic BiFeO₃: insights from Raman spectroscopy, *Phys. Rev. B* 86 (2012) 184422–184437, <https://doi.org/10.1103/PhysRevB.86.184422>.
- [32] D.L. Rousseau, R.P. Bauman, S.P.S. Porto, Normal mode determination in crystals, *J. Raman Spectrosc.* 10 (1981) 253–290, <https://doi.org/10.1002/jrs.1250100152>.
- [33] A. Otto, J. Timper, J. Billmann, G. Kovacs, I. Pockrand, Surface roughness induced electronic Raman scattering, *Surf. Sci.* 92 (1980) L55–L57, [https://doi.org/10.1016/0039-6028\(80\)90237-X](https://doi.org/10.1016/0039-6028(80)90237-X).
- [34] R. Monreal, F. Flores, Y. Gao, T. López-Ríos, Raman scattering by electron-hole pairs at metal surfaces, *Europhys. Lett.* 4 (1987) 115–120, <https://doi.org/10.1209/0295-5075/4/1/019>.
- [35] C.Y. Chen, E. Burstein, S. Lundquist, Giant Raman scattering by pyridine and en adsorbed on silver, *Solid State Commun.* 32 (1979) 63–66, [https://doi.org/10.1016/0038-1098\(79\)90998-0](https://doi.org/10.1016/0038-1098(79)90998-0).
- [36] H.L. Liu, S. Yoon, S.L. Cooper, S.-W. Cheong, P.D. Han, D.A. Payne, Probing anisotropic magnetotransport in manganese perovskites using Raman spectroscopy, *Phys. Rev. B* 58 (1998) R10115–R10118, <https://doi.org/10.1103/PhysRevB.58.R10115>.
- [37] N.F. Mott, E.A. Davis, *Electronic Processes in Non-crystalline Materials*, Oxford University Press, 1979.
- [38] A.L. Efros, B.I. Shklovskii, Coulomb gap and low temperature conductivity of disordered systems, *J. Phys. C Solid State Phys.* 8 (1975) L49–L51, <https://doi.org/10.1088/0022-3719/8/4/003>.
- [39] N.V. Arginskaya, V.I. Kozub, Potential influence of pre-exponential factors on the temperature dependence of variable-range hopping conductivity, *Soviet JETP* 79 (1994) 466–472.
- [40] A. Aharony, Y. Zhang, M.P. Sarachik, Universal crossover in variable range hopping with Coulomb interactions, *Phys. Rev. Lett.* 68 (1992) 3900–3903, <https://doi.org/10.1103/PhysRevLett.68.3900>.

- [41] L. Zuppiroli, L. Forró, Hopping conductivity in polaronic situations, *Phys. Lett. A* 141 (1989) 181–185, [https://doi.org/10.1016/0375-9601\(89\)90785-8](https://doi.org/10.1016/0375-9601(89)90785-8).
- [42] B. Stojadinović, Faculty of Physics, University of Belgrade, 2018 (Ph.D. thesis).
- [43] O. Gunnarsson, M. Calandra, J.E. Han, *Colloquium: saturation of electrical resistivity*, *Rev. Mod. Phys.* 75 (2003) 1085–1099, <https://doi.org/10.1103/RevModPhys.75.1085>.
- [44] N.E. Hussey, K. Takenaka, H. Takagi, Universality of the Mott-Ioffe-Regel limit in metals, *Philos. Mag. A* 84 (2004) 2847–2864, <https://doi.org/10.1080/14786430410001716944>.
- [45] A. Ioffe, A. Regel, Non-crystalline, amorphous and liquid electronic semiconductors, *Prog. Semicond.* 4 (1960) 237–291.
- [46] N.F. Mott, Conduction in non-crystalline systems IX. The minimum metallic conductivity, *Philos. Mag. J. Theor. Exp. Appl. Phys* 26 (4) (1972) 1015–1026, <https://doi.org/10.1080/14786437208226973>.
- [47] F. Gervais, Infrared dispersion in several polar-mode crystals, *Opt. Commun.* 22 (1977) 116–118, [https://doi.org/10.1016/0030-4018\(77\)90260-7](https://doi.org/10.1016/0030-4018(77)90260-7).
- [48] F. Gervais, Optical conductivity of oxides, *Mater. Sci. Eng. R Rep.* 39 (2002) 29–92, [https://doi.org/10.1016/S0927-796X\(02\)00073-6](https://doi.org/10.1016/S0927-796X(02)00073-6).
- [49] R.F. Wallis, M. Balkanski, *Many-body Aspects of Solid State Spectroscopy*, Elsevier Science Ltd, Amsterdam, the Netherlands, 1986.
- [50] A.A. Kukharskii, Plasmon-phonon coupling in GaAs, *Solid State Commun.* 13 (1973) 1761–1765, [https://doi.org/10.1016/0038-1098\(73\)90724-2](https://doi.org/10.1016/0038-1098(73)90724-2).
- [51] D.A.G. Bruggeman, Berechnung verschiedener physikalischer Konstanten von heterogenen substanzen. I. Dielektrizitätskonstanten und Leitfähigkeiten der Mischkörper aus isotropen Substanzen, *Ann. Phys.* 416 (7) (1935) 636–664, <https://doi.org/10.1002/andp.19354160705>.
- [52] Z.V. Popović, M. Grujić-Brojčin, N. Paunović, M.M. Radonjić, V.D. Araújo, M.I.B. Bernardi, M.M. de Lima, A. Cantarero, Far-infrared spectroscopic study of CeO₂ nanocrystals, *J. Nanopart. Res.* 17 (2015) 23–30, <https://doi.org/10.1007/s11051-015-2859-y>.
- [53] A. Younis, D. Chu, S. Li, Cerium oxide nanostructures and their applications, in: *Functionalized Nanomaterials*, 2016, pp. 52–68, <https://doi.org/10.5772/65937>. Ch. 3.
- [54] P. Jasinski, T. Suzuki, H.U. Anderson, Nanocrystalline undoped ceria oxygen sensor, *Sensor. Actuator. B Chem.* 95 (2003) 73–77, [https://doi.org/10.1016/S0925-4005\(03\)00407-6](https://doi.org/10.1016/S0925-4005(03)00407-6).
- [55] X. Han, J. Lee, H.-I. Yoo, Oxygen-vacancy-induced ferromagnetism in CeO₂ from first principles, *Phys. Rev. B* 79 (2009) 100403–100406, <https://doi.org/10.1103/PhysRevB.79.100403>.
- [56] G. Feher, A.F. Kip, Electron spin resonance absorption in metals. I Experimental, *Phys. Rev.* 98 (1955) 337–348, <https://doi.org/10.1103/PhysRev.98.337>.
- [57] F.J. Dyson, Electron spin resonance absorption in metals. II. Theory of electron diffusion and the skin effect, *Phys. Rev.* 98 (1955) 349–359, <https://doi.org/10.1103/PhysRev.98.349>.
- [58] M.I. Azbel, V.I. Gerasimenko, I.M. Lifshitz, Paramagnetic resonance and polarization of nuclei in metals, *Sov. Phys. JETP* 5 (1957) 986–996.
- [59] M.I. Azbel, V.I. Gerasimenko, I.M. Lifshitz, On the theory of paramagnetic resonance in metals, *Sov. Phys. JETP* 8 (1959) 480–487.
- [60] D.M. Djokić, D. Stepanenko, Z. Dohčević-Mitrović, Extreme conduction electron spin resonance: $A/B \rightarrow (5+3\sqrt{3})/4$, the universal limit of lineshape asymmetry ratio, *J. Magn. Magn. Mater.* 491 (2019) 165616, <https://doi.org/10.1016/j.jmmm.2019.165616>.
- [61] A.C. Chapman, P. Rhodes, E.F.W. Seymour, The effect of eddy currents on nuclear magnetic resonance in metals, *Proc. Phys. Soc. B* 70 (1957) 345–360, <https://doi.org/10.1088/0370-1301/70/4/301>.
- [62] P.M. Platzman, P.A. Wolff, Spin-wave excitation in nonferromagnetic metals, *Phys. Rev. Lett.* 18 (1967) 280–283, <https://doi.org/10.1103/PhysRevLett.18.280>.
- [63] H.R. Webb, Electron-spin-resonance line shape in spherical metal particles, *Phys. Rev.* 158 (1967) 225–233, <https://doi.org/10.1103/PhysRev.158.225>.
- [64] J.H. Pifer, R. Magno, Conduction-electron spin resonance in a lithium film, *Phys. Rev. B* 3 (1971) 663–673, <https://doi.org/10.1103/PhysRevB.3.663>.

- [65] A.H. Kahn, Theory of microwave eddy currents and paramagnetic resonance in materials of intermediate conductivity, *Phys. Rev. B* 16 (1977) 64–72, <https://doi.org/10.1103/PhysRevB.16.64>.
- [66] J.I. Kaplan, J. Reuben, Electron spin resonance line shapes of paramagnetic species on surfaces, *J. Phys. Chem.* 86 (1982) 4465–4466, <https://doi.org/10.1021/j100220a001>.
- [67] A.G. Marshall, D.C. Roe, Dispersion versus absorption: spectral line shape analysis for radiofrequency and microwave spectrometry, *Analyt. Chem.* 50 (1978) 756–763, <https://doi.org/10.1021/ac50027a023>.
- [68] L. Walmsley, G. Ceotto, J.H. Castilho, C. Rettori, Magnetic field modulation frequency, sample size and electromagnetic configuration effects on the spin resonance spectra of graphite intercalation compounds, *Synth. Met.* 30 (1989) 97–107, [https://doi.org/10.1016/0379-6779\(89\)90645-0](https://doi.org/10.1016/0379-6779(89)90645-0).
- [69] L. Walmsley, Translating conduction-electron spin-resonance lines into lorentzian lines, *J. Magn. Reson. A* 122 (1996) 209–213, <https://doi.org/10.1006/jmra.1996.0196>.
- [70] M. Oshikawa, I. Affleck, Electron spin resonance in $S=1/2$ antiferromagnetic chains, *Phys. Rev. B* 65 (2002) 134410–134437, <https://doi.org/10.1103/PhysRevB.65.134410>.
- [71] J.P. Joshi, S.V. Bhat, On the analysis of broad Dysonian electron paramagnetic resonance spectra, *J. Magn. Res.* 168 (2004) 284–287, <https://doi.org/10.1016/j.jmr.2004.03.018>.
- [72] K.W. Blazey, K.A. Müller, F. Blatter, E. Schumacher, Conduction electron spin resonance of Caesium metallic clusters in zeolite X, *Europhys. Lett.* 4 (1987) 857–861, <https://doi.org/10.1209/0295-5075/4/7/017>.
- [73] J.J. van der Klink, H.B. Brom, NMR in metals, metal particles and metal cluster compounds, *Prog. Nucl. Magn. Reson. Spectr.* 36 (2) (2000) 89–201, [https://doi.org/10.1016/S0079-6565\(99\)00020-5](https://doi.org/10.1016/S0079-6565(99)00020-5).
- [74] S. Iijima, Helical microtubules of graphitic carbon, *Nature* 354 (1991) 56–58, <https://doi.org/10.1038/354056a0>.
- [75] L. Forró, C. Schönenberger, *Physical Properties of Multi-Wall Nanotubes*, Springer Berlin Heidelberg, Berlin, Heidelberg, 2001, pp. 329–391, https://doi.org/10.1007/3-540-39947-X_13.
- [76] D.M. Djokić, A. Goswami, Quantum yield in polymer wrapped single walled carbon nanotubes: a computational model, *Nanotechnology* 28 (2017) 465204, <https://doi.org/10.1088/1361-6528/aa8f38>.
- [77] A. Bachtold, M. Henny, C. Terrier, C. Strunk, C. Schönenberger, J.-P. Salvetat, J.-M. Bonard, L. Forró, Contacting carbon nanotubes selectively with low-ohmic contacts for four-probe electric measurements, *Appl. Phys. Lett.* 73 (1998) 274–276, <https://doi.org/10.1063/1.121778>.
- [78] A. Bachtold, C. Strunk, J.-P. Salvetat, J.-M. Bonard, L. Forró, T. Nussbaumer, C. Schönenberger, Aharonov-Bohm oscillations in carbon nanotubes, *Nature* 397 (1999) 673–675, <https://doi.org/10.1038/17755>.
- [79] L. Langer, V. Bayot, E. Grivei, J.-P. Issi, J.P. Heremans, C.H. Olk, L. Stockman, C. Van Haesendonck, Y. Bruynseraede, Quantum transport in a multiwalled carbon nanotube, *Phys. Rev. Lett.* 76 (1996) 479–482, <https://doi.org/10.1103/PhysRevLett.76.479>.
- [80] W. Yi, L. Lu, Z. Dian-lin, Z.W. Pan, S.S. Xie, Linear specific heat of carbon nanotubes, *Phys. Rev. B* 59 (1999) R9015–R9018, <https://doi.org/10.1103/PhysRevB.59.R9015>.
- [81] M. Bockrath, D.H. Cobden, J. Lu, A.G. Rinzler, R.E. Smalley, L. Balents, P.L. McEuen, Luttinger-liquid behaviour in carbon nanotubes, *Nature* 398 (1999) 598–601, <https://doi.org/10.1038/17569>.

Мнистарство просвете науке и технолошког развоја
Матични научни одбор за физику
Датум: 05.07.2022. године
Београд

**Институт за физику у Београду
Др Дејан Ђокић, научни сарадник**

Прегревица 118
11080 Београд

Поштовани др Ђокићу,

Матични научни одбор за физику је на својој седници од 24. јуна 2022. године разматрао Ваш захтев за признавање и категорисање публикације "Transport properties of nanoscopic solids as probed by spectroscopic techniques" аутори Дејан М. Ђокић, Новица Пауновић, Бојан Стојадиновић, Димитрије Степаненко, Саша Лазовић, Зорана Д. Дохчевић-Митровић из 2021. године у монографији „Fundamentals and Properties of Multifunctional Nanomaterials“, издавач Elsevier.

Одбор је једногласно донео одлуку да се наведена публикација категорише као истакнута монографија међународног значаја, а Ваш допринос као монографска студија у оквиру ове монографије, која се на основу Прилога 1 Правилника о стицању истраживачких и научних звања категорише као публикација категорије М13.

С поштовањем,

Председник Матичног научног одбора за физику



др Антун Балаж, научни саветник

Date: Thu, 17 Dec 2015 08:17:30 -0500
Message-Id: <9145035825034@ejpww6.nature.com.nature.com>
To: dimitrije.stepanenko@ipb.ac.rs
Subject: NATURE: Decision on Nature manuscript XXXXXXXXX
From: k.ziemelis@nature.com
Reply-To: k.ziemelis@nature.com

Dear Colleague,

Thank you for your help with the manuscript entitled "XXXXXXXXXXXXXXXXXXXX" by XXXXXXXXXX and colleagues. We have now received all of the referees' reports, which I have attached below for your information. In the light of these various comments, we have decided to offer publication of a suitably revised version of the manuscript. Please treat this information as strictly confidential.

Thank you again for your help and I hope that we can call upon your advice in the future.

Yours sincerely,

Karl Ziemelis
Physical Sciences Editor, Nature
Nature's author and policy information sites are at
www.nature.com/nature/submit/.

Date: Mon, 4 Jun 2018 07:44:28 -0400
Message-Id: <49152811266867@ejpwwl.nature.com.nature.com>
To: dimitrije.stepanenko@ipb.ac.rs
Subject: Decision made for XXXXXXXXXX
From: Maria.Maragkou@nature.com
Reply-To: Maria.Maragkou@nature.com
X-AV-Checked: ClamAV using ClamSMTP

Dear Dr. Stepanenko,

Thank you for reviewing the manuscript "XXXXXXXXXXXXXXXXXX" for Nature Materials. In the light of the various comments we received, we have decided to offer publication of a suitably revised version of the manuscript. Please treat this information as strictly confidential.

Thank you again for your help and I hope that we can call upon your advice in the future.

Best wishes,

--
Maria Maragkou
Senior Editor
<i>Nature Materials</i>

Date: Wed, 4 Jan 2017 10:41:45 -0500
Message-Id: <72148354450562@ejpww16.nature.com.nature.com>
To: dimitrije.stepanenko@ipb.ac.rs
Subject: Final Decision made for XXXXXXXX
From: scientificreports@nature.com
Reply-To: scientificreports@nature.com

Dear Dr. Stepanenko:

Thank you for your help with manuscript XXXXXXXX, "XXXXXXXXXXXXXXXX", which you recently reviewed for Scientific Reports.

For your records, the decision for this manuscript, based partly on your input, was Accept. A full copy of the comments to authors is appended, below.

Your assistance and participation in the review process for Scientific Reports is greatly appreciated.

Best regards,

Manuscript Administration
Scientific Reports
4 Crinan Street
London N1 9XW
E-mail: scientificreports@nature.com

Date: Mon, 18 Jun 2018 18:00:47 -0400
Message-Id: <70152935924718@buildmts-www5.nature.com.nature.com>
To: Dimitrije.Stepanenko@ipb.ac.rs
Subject: Final Decision made for XXXXXXXXX
From: npjq@nature.com
Reply-To: npjq@nature.com
X-AV-Checked: ClamAV using ClamSMTP

Dear colleague,

Thank you very much for reviewing the paper entitled "XXXXXXXXXXXX" for npj Quantum Information. Having considered the collective advice that we have received, the editor has taken the Revise decision. Please treat this information as strictly confidential.

For your information, the full complement of reviewers' reports is appended below, which I hope will provide some insight into the views of the other referees.

We appreciate the time you have taken to review this manuscript and submit your report. I hope that we may call upon your advice in the future.

Best regards,

Manuscript Administration
npj Quantum Information
4 Crinan Street
London N1 9XW
E-mail: npjq@nature.com

Date: Mon, 9 Jul 2018 18:40:03 -0400
Message-ID: <1067306010.1531176003841.JavaMail.tomcat@prism-jobs-4-245>
From: prl@aps.org
Reply-To: prl@aps.org
To: dimitrije.stepanenko@ipb.ac.rs
Subject: Review_request STEPANENKO XXXXXXXXX

Re: XXXXXXXX
XX
XX

Dear Dr. Stepanenko,

We would appreciate your review of this submission to Physical Review Letters.

Please let us know promptly if you will be able to send a report and, if so, by when.

Do the authors make a convincing case for their claims?

Please address the Physical Review Letters criteria of impact, innovation, and interest in your report.

Thank you for your help.

Yours sincerely,

Robert Garisto
Editor
Physical Review Letters
Email: prl@aps.org
<https://journals.aps.org/prl/>
twitter @RobertGaristo

"Every 80 seconds someone cites a PRL"

Celebrating 125 Years of the Physical Review
<https://journals.aps.org/125years> #PhysRev125

We ask that you download the manuscript and return your report via:

<https://referees.aps.org/r/XXXXXXX>

Alternatively, you may send your completed Referee Response Form by email to prl@aps.org. If you use email, either reply to this message or give as the subject "Report STEPANENKO XXXXXXXXX".

...

Date: Tue, 8 May 2018 09:43:17 -0400
Message-ID: <1714919704.1525786997025.JavaMail.tomcat@prism-jobs-4-245>
From: prb@aps.org
Reply-To: prb@aps.org
To: dimitrije.stepanenko@ipb.ac.rs
Subject: Resub_review_request STEPANENKO XXXXXXXXXX

Dear Dr. Stepanenko,

We would appreciate your review of this manuscript, which has been submitted to Physical Review B.

Comments from the editor:

XXXXXXXXXXXXXXXX

Thank you for your help.

Yours sincerely,

Manolis Antonoyiannakis
Associate Editor
Physical Review B
Email: prb@aps.org
<http://journals.aps.org/prb/>

Celebrating 125 Years of the Physical Review
<https://journals.aps.org/125years> #PhysRev125

We ask that you download the manuscript and return your report via:

<https://referees.aps.org/r/XXXXXXXX>

Alternatively, you may send your completed Referee Response Form by email to prb@aps.org. If you use email, either reply to this message or give as the subject "Report STEPANENKO XXXXXXXX".

DANI FIZIKE KONDENZOVANOG STANJA MATERIJE

10 – 12 septembar 2013
Srpska akademija nauka i umetnosti
www.cond-mat.ipb.ac.rs

Utorak, 10 Septembar

10:00 – 10:40	Ivan Božović, Brookhaven National Laboratory (USA) <i>Novi rezultati u fizici visoko-temperaturnih superprovodnika</i>
10:40 – 10:50	diskusija
10:50 – 11:00	pauza
11:00 – 11:40	Zoran Radović, Fizički fakultet <i>Biharmonijska zavisnost Josephsonove struje od faze u superprovodnim spojevima sa nehomogenim feromagnetom</i>
11:40 – 11:50	diskusija
11:50 – 12:00	pauza
12:00 – 12:40	Antun Balaž, Institut za fiziku <i>Proučavanje dipolnih Bose-Einstein kondenzata u anizotropnim slabim potencijalima sa neuređenošću</i>
12:40 – 12:50	diskusija
13:00 – 15:00	pauza za ručak
15:00 – 15:40	Darko Tanasković, Institut za fiziku <i>Kvantni kritični transport u blizini Mottovog metal-izolator prelaza</i>
15:40 – 15:50	diskusija
15:50 – 16:00	pauza
16:00 – 16:40	Mihajlo Vanević, Fizički fakultet <i>Kvantno proklizavanje faze u mezoskopskim superprovodnim žicama</i>
16:40 – 16:50	diskusija

Sreda, 11 Septembar

10:00 – 10:40	Milica Milovanović, Institut za fiziku <i>Geometrijski opis frakcionih Chernovih izolatora</i>
10:40 – 10:50	diskusija
10:50 – 11:00	pauza
11:00 – 11:40	Ivanka Milošević, Fizički fakultet <i>Termalne osobine helikalnih ugljeničnih nanotuba</i>
11:40 – 11:50	diskusija
11:50 – 12:00	pauza

– nastavak, Sreda 11 Septembar –	
12:00 – 12:40	Zoran Popović, Institut Vinča <i>Dinamički Jahn-Tellerov efekat u grafenu sa šupljinskim defektom</i>
12:40 – 12:50	diskusija
13:00 – 15:00	pauza za ručak
15:00 – 15:40	Željko Šljivančanin, Institut Vinča <i>Modelovanje atomske strukture djelimično oksidisanog grafena</i>
15:40 – 15:50	diskusija
15:50 – 16:00	pauza
16:00 – 16:40	Nenad Vukmirović, Institut za fiziku <i>Priroda nosilaca naelektrisanja u organskim kristalima</i>
16:40 – 16:50	diskusija
16:50 – 17:00	pauza
17:00 – 17:40	Zoran Mišković, University of Waterloo (Canada) <i>Interakcija grafena sa naelektrisanim česticama</i>
17:40 – 17:50	diskusija

Četvrtak, 12 Septembar

10:00 – 10:40	Velimir Radmilović, Tehnološko-metalurški fakultet <i>Šta znamo o klizanju bez trenja na atomskom nivou?</i>
10:40 – 10:50	diskusija
10:50 – 11:00	pauza
11:00 – 11:40	Nataša Bibić, Institut Vinča <i>Modifikacija tankih slojeva metala i keramika primenom jonskih snopova</i>
11:40 – 11:50	diskusija
11:50 – 12:00	pauza
12:00 – 12:40	Đorđe Spasojević, Fizički fakultet <i>Analiza spening lavina u dvodimenzionalnom neravnotežnom Izingovom modelu na temperaturi $T=0$</i>
12:40 – 12:50	diskusija
13:00 – 15:00	pauza za ručak
15:00 – 15:40	Dimitrije Stepanenko, Institut za fiziku <i>Kvantni računari bazirani na kvantnim tačkama i spin-orbit interakciji</i>
15:40 – 15:50	diskusija
15:50 – 16:00	pauza
16:00 – 16:40	Nenad Švrakić, Institut za fiziku <i>Pokrivanje i pakovanje u ravni: egzaktni i numerički rezultati za mešavine superdiskova</i>
16:40 – 16:50	diskusija

XIX Symposium on
Condensed Matter Physics
SFKM 2015

Book of Abstracts



Spin-electric Coupling in Molecular Magnets

Dimitrije Stepanenko

Center for Condensed Matter Physics and New Materials, Institute of Physics Belgrade

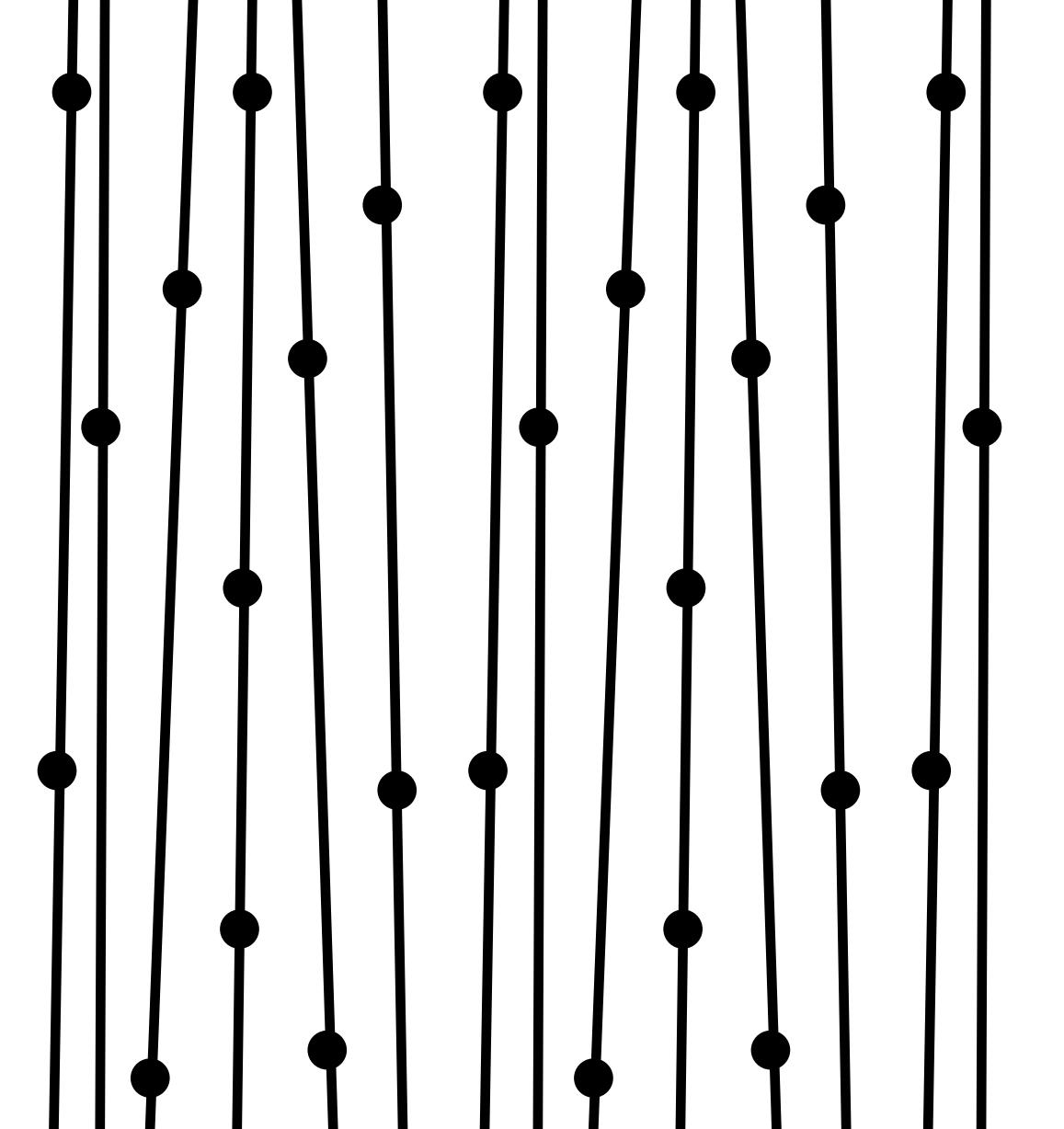
Abstract. Molecular magnets behave as large spins at low energies. They show hysteresis controlled by quantum tunneling of magnetization, long spin coherence times, and spin texture in the ground state. Coupling of molecular spins to an external electric fields would provide a superior mechanism for their control and manipulation. In triangular low-spin antiferromagnets with broken inversion symmetry it is the chirality of spin texture that couples to electric fields. We show that the chirality has long coherence time, and that it allows for a controllable superradiant phase transition.

Hyperfine-induced decoherence in a triangular spin cluster varies across independent two-level subsystems that encode a qubit. Electrically controllable eigenstates of spin chirality show decoherence times that approach milliseconds, two orders of magnitude longer than those estimated for the eigenstates of the total spin projection and of the partial spin sums. The robustness of chirality is due to its decoupling from components of both the total spin and individual spins in the cluster.

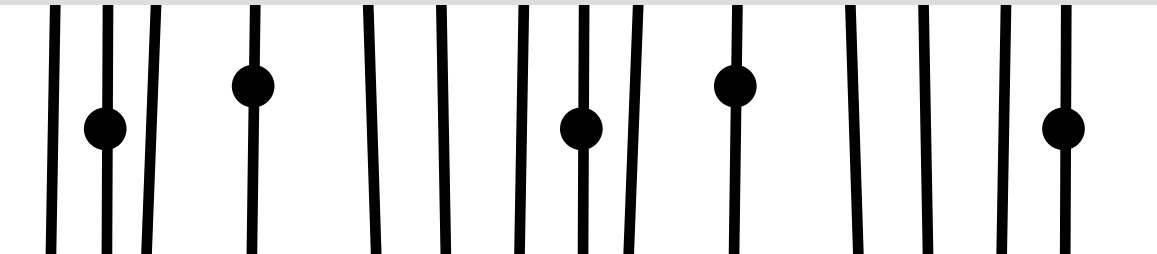
A crystal of triangular molecular antiferromagnets coupled to a resonant cavity shows superradiant phase transition. The critical coupling strength for transition depends on the external magnetic field, in sharp contrast to the standard case of two-level emitters, where the critical coupling was set by the structure of emitter alone. The source of modification is traced to the entanglement of spin and chirality in the low-energy states of the cluster.

REFERENCES

1. Trif, M., Troiani, F., Stepanenko, D., and Loss, D., *Phys. Rev. B* **82**, 045429 (2010).
2. Troiani, F., Stepanenko, D., and Loss, D., *Phys. Rev. B* **86**, 161409(R) (2012).
3. Stepanenko, D., Trif, M., Tsyplatyev, O., and Loss, D, arXiv:1502.04075



PROGRAMME



Thursday 11th April

08:00 - 09:00	<i>Registration</i>	Rectory building University of Belgrade
---------------	---------------------	---

Chairs: Yang Ye & Marina Soković

09:00 - 09:15	<p>Welcome Remarks Petar MARIN Vice Rector University of Belgrade, Serbia</p>
09:15 - 09:25	<p>Opening speech Mladen ŠARČEVIĆ Minister Ministry of Education, Science and Technological Development, Serbia</p>
09:25 - 09:35	<p>Keynote Speech Jing WANG Full-time Deputy Director Office for advancing Shanghai's Science and Innovation Center Development, China</p>
09:35 - 09:50	<p>An introduction of Chinese Academy of Sciences (CAS) and CAS Shanghai Branch Ronghui QU Vice President Chinese Academy of Sciences, Shanghai Branch, China</p>
09:50 - 10:00	<p>Opening speech Marina SOKOVIĆ Principal Research Fellow, IBISS, Serbia</p>
10:00 - 10:10	<i>Signing Ceremony</i>
10:10 - 10:20	<i>Group photography</i>
10:20 - 11:00	<i>Coffee break</i>

Section 1 Natural products in food quality

Moderators: Lijiang Xuan & Marina Soković

11:00 - 11:15	Exploitation of essential oils and hydrosol for the preservation of fresh produce: Quality and Safety issues Nikos TZORTZAKIS , Cyprus
11:15 - 11:30	Polyphenolic profile of honeys from Serbia Živoslav TEŠIĆ , Serbia
11:30 - 11:45	The Role of Mushrooms as Functional Food and Dietary supplements Miomir NIKŠIĆ , Serbia
11:45 - 12:00	Bio-based products from lactic acid bacteria Aleksandra ĐUKIĆ-VUKOVIĆ , Serbia
12:00 - 12:15	Slaughterhouse blood: from wasted by-product of meat industry to added-value products Branko BUGARSKI , Serbia
12:15 - 12:25	Hypericin in traditional herbal medicine Hyperici oleum? Veronika STOILKOVSKA , R. North Macedonia
12:25 - 12:35	Polysaccharides from <i>Inonotus obliquus</i> cultivated mycelium and sterile conk and mycelial cultivation with sea buckthorn press cake Gabriele BELTRAME , Finland
12:35 - 12:50	A viewpoint of encapsulation technologies for value - added food Viktor NEDOVIĆ , Serbia
12:50 - 14:00	Lunch Garden, Rectory building

Section 2 Medicinal plants and fungi

Chairs: Ana Ćirić & Yang Ye

14:00 - 14:15	Research on Health Effects of Sea Buckthorn at University of Turku Baoru YANG , Finland
14:15 - 14:30	Investigations of selected groups from the Balkan flora - fundamental and applicative aspects Petar MARIN , Serbia
14:30 - 14:45	Pharmacognostic overview of some <i>Gentiana</i> , <i>Gentianella</i> and <i>Swertia</i> species from Central Balkan Katarina ŠAVIKIN , Serbia
14:45 - 15:00	Drought and salinity stress due to Climate Change alter the physiology and biochemistry of Medicinal and Aromatic plants Antonios CHRYSARGYRIS , Cyprus
15:00 - 15:10	Ethnobotanical study of medicinal plants traditionally used in South-East Serbia (Pčinja district) Jelena ŽIVKOVIĆ , Serbia
15:10 - 16:00	<i>Coffee break</i>
16:00 - 16:15	Organic mushroom growing technology – challenge for the science and practice Ivanka MILENKOVIĆ , Serbia
16:15 - 16:30	Cultivation of arnica (<i>Arnica montana</i> L.) in various fertilization and propagation models Dejan PLJEVLJAKUŠIĆ , Serbia
16:30 - 16:45	Valuable sources of natural compounds in the Mediterranean: the case of Greek flora Spyridon PETROPOULOS , Greece
16:45 - 17:00	Legalization of Medical Cannabis in Macedonia - how far we have reached Gjoshe STEFKOV , R. North Macedonia
17:00 - 19:00	<i>Dinner</i> Garden, Rectory building

Friday 12th April

Section 3 Bioactive natural products

Chairs: Katarina Šavikin & Gjoshe Stefkov

09:00 - 09:15	Identification of bioactive diterpenoids from traditional Chinese medicines Yang YE , China
09:15 - 09:30	Nutritive and therapeutic properties of selected wild growing mushrooms from Serbia Jovana PETROVIĆ , Serbia
09:30 - 09:45	Utilizing the indigenous biosynthetic capacity of medicinal and aromatic plants through optimization of tissue culture conditions Kalina DANOVA , Bulgaria
09:45 - 10:00	Edible and medicinal fungi inhibit enzymes linked to diabetes type-2 therapy Dejan STOJKOVIĆ , Serbia
10:00 - 10:15	Comparative study of antiproliferative potential of three different plant species Danijela DRAKULIĆ , Serbia
10:15 - 10:30	Iridoids of <i>Centaurium</i> and <i>Nepeta</i> species: exploring their diversity, metabolism, ecophysiological roles and bioactivities Danijela MIŠIĆ , Serbia
10:30 - 11:30	Coffee break
11:30 - 11:45	Plant and mushroom extracts as potential intervening supplements in diabetes and diabetic complications Jelena ARAMBAŠIĆ JOVANOVIĆ , Serbia
11:45 - 12:00	Phytochemical investigations of <i>Salvia transsylvanica</i> , <i>Salvia glutinosa</i> , and <i>Salvia officinalis</i> from Romania and their bioactivities Andrei MOCAN , Romania
12:00 - 12:15	Freeze dried <i>Salvia officinalis</i> methanolic extract incorporated into nanostructured lipid carriers for Alzheimer's disease treatment Elena MARKOVA , R. North Macedonia
12:15 - 12:30	The pygidial gland secretions of ground beetles (Insecta: Coleoptera: Carabidae): antimicrobial and antitumour activity of the natural products Srećko ĆURČIĆ , Serbia
12:30 - 14:00	Lunch Garden, Rectory building

Section 4 Drug discovery

Chairs: Viktor Nedović & Jasmina Glamočlija

14:00 - 14:15	13-year-R&D and 13-year-postmarketing, a long and risky road to be a blockbuster in clinic Lijiang XUAN , China
14:15 - 14:30	C–H Activation: a Late Stage Functionalization Tool for Drug Discovery Huixiong DAI , China
14:30 - 14:45	Quantifying randomness in real interaction networks and examples in biology Marija MITROVIĆ DANKULOV , Serbia
14:45 - 15:00	High throughout antimycobacterial drug screening platform and study of mechanisms of action of antimycobacterial drugs Tianyu ZHANG , China
15:00 - 15:15	GPCR–targeted Drug Discovery Xin XIE , China
15:15 - 16:00	<i>Coffee break</i>
16:00 - 16:15	Bavachinin, a novel natural pan-PPAR agonist, exhibits unique synergism with synthetic PPAR- α -and - γ activators Yiming LI , China
16:15 - 16:30	Discovery of hits/lead compounds based on natural product-like libraries generated from chromones Chunhao YANG , China
16:30 - 16:45	Spin textures in molecular magnets and designed polypeptides Dimitrije STEPANENKO , Serbia
16:45 - 17:00	Concluding remarks Yang YE, Marina SOKOVIĆ
18:00	<i>Closing ceremony</i> Gala dinner, Restaurant Vizantija

Saturday 13th April

10:00	<i>Excursion</i>	<i>Roman city and legionary fort Viminacium, Smederevo</i>
-------	------------------	--

Citation Report

Stepanenko, Dimitrije (Author)

Analyze Results

Create Alert

Export Full Report

Publications

23

Total

From 1996 to 2024

Citing Articles

711

Total

697

Without self-citations

Times Cited

893

Total

868

Without self-citations

38.83

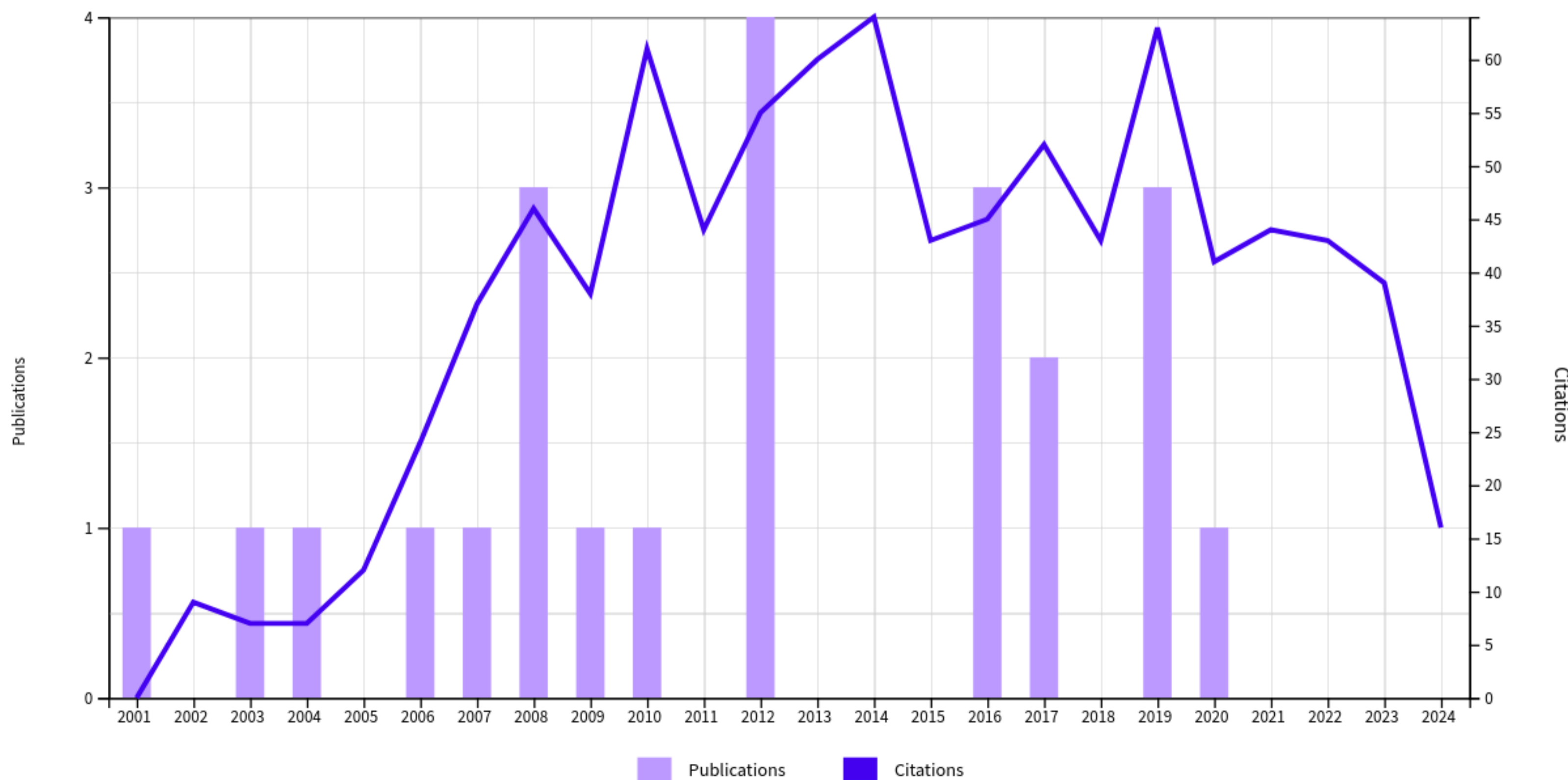
Average per item

12

H-Index

Times Cited and Publications Over Time

DOWNLOAD



Stepanenko, Dimitrije

[University of Belgrade, Belgrade, Serbia](#)

[57190883044](#)

[Connect to ORCID](#)

[View more](#)

938

Citations by **744 documents**

25

Documents

12

h-index [View *h*-graph](#)

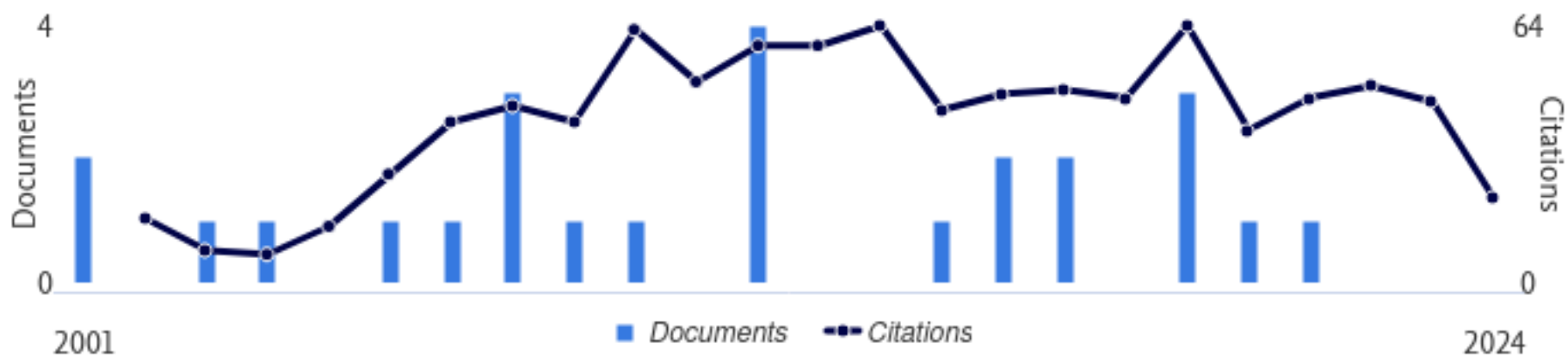
[View all metrics >](#)

[Set alert](#)

[Edit profile](#)

[More](#)

Document & citation trends



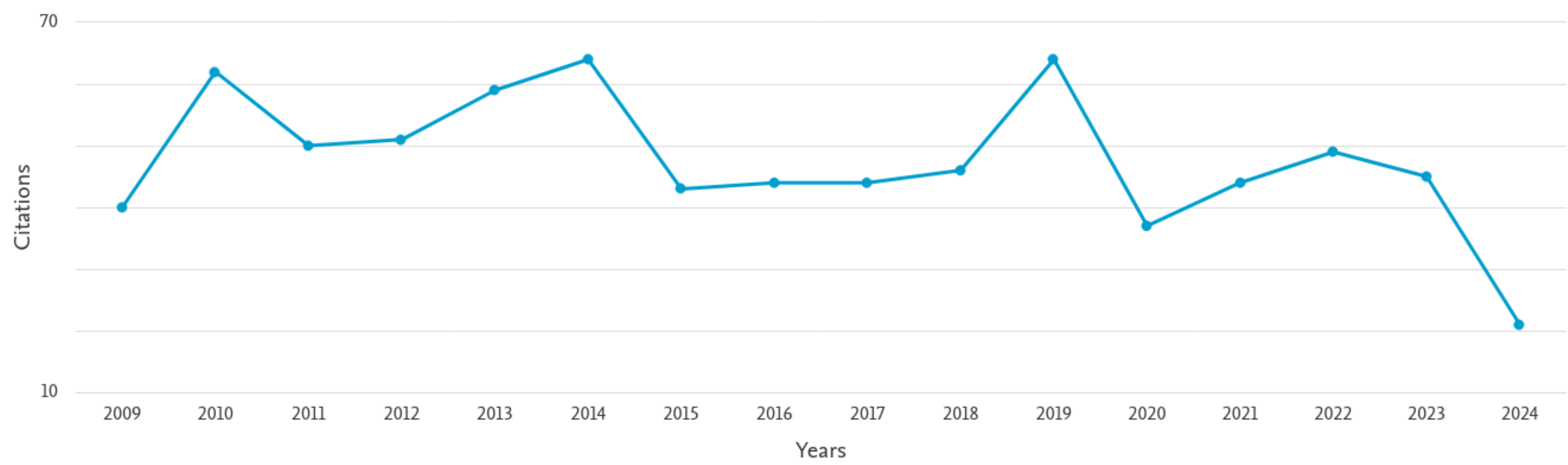
[Analyze author output](#)

[Citation overview](#)

25 Cited Documents from "Stepanenko, Dimitrije" [+ Add to list](#)

Author ID:57190883044

Date range: to Exclude self citations of selected author Exclude self citations of all authors Exclude citations from books [Update](#)



Sort on: [Date \(newest\)](#)

Page

Documents	Citations	<2009	2009	2010	2011	2012	2013	2014	2015	2016	2017	2018	2019	2020	2021	2022	2023	2024	Subtotal	>2024	Total	
	Total		147	40	62	50	51	59	64	43	44	44	46	64	37	44	49	45	21	763	0	910